Modelling the sources, variability and fate of freshwater in the Bellingshausen Sea, Antarctica

Heather Christine Regan

supervised by
Dr. Paul Holland
Prof. Michael Meredith
Dr. Jennifer Pike

August, 2017

A thesis submitted in accordance with the requirements for the award of the degree of
Doctor of Philosophy

Cardiff University
School of Earth and Ocean Sciences

DECLARATION

This work has not been submitted in substance for any other degree or award at this or any other university or place of learning, nor is being submitted concurrently in candidature for any degree or other award.

Signed.....(candidate) Date .....

STATEMENT 1

This thesis is being submitted in partial fulfilment of the requirements for the degree of .....(insert MCh, MD, MPhil, PhD etc, as appropriate)

Signed.....(candidate) Date .....

STATEMENT 2

This thesis is the result of my own independent work/investigation, except where otherwise stated, and the thesis has not been edited by a third party beyond what is permitted by Cardiff Universitys Policy on the Use of Third Party Editors by Research Degree Students. Other sources are acknowledged by explicit references. The views expressed are my own.

Signed.....(candidate) Date .....

STATEMENT 3

I hereby give consent for my thesis, if accepted, to be available for photocopying and for inter-library loan, and for the title and summary to be made available to outside organisations.

Signed.....(candidate) Date .....

STATEMENT 4

I hereby give consent for my thesis, if accepted, to be available for photocopying and for inter-library loans **after expiry of a bar on access previously approved by the Academic Standards & Quality Committee**.

Signed.....(candidate) Date .....

Abstract

During the second half of the twentieth century, the Antarctic Peninsula exhibited a rapid increase in air temperatures. This was accompanied by a reduction in sea ice extent, increased precipitation and a dramatic retreat of glaciers associated with an increase in heat flux from deep ocean water masses. Isotopic tracers have been used previously to investigate the relative importance of the different freshwater sources to the adjacent Bellingshausen Sea, but the data coverage is strongly biased toward summer and unambiguous determination of the different meteoric water contributions remains challenging. Here a high-resolution model is used to investigate the ocean's response to the observed changes in its different freshwater inputs (sea ice melt/freeze, precipitation/evaporation, iceberg melt, ice shelf melt and glacier melt). By developing the code to enable tracing of the sources and pathways of the individual components of the freshwater budget, it is shown that sea ice dominates the seasonal changes in freshwater content, but all sources contribute approximately equally to annual-mean freshwater fluxes and interannual freshwater flux anomalies. Ice shelf melting is shown to be the largest contributor to freshwater content on the annual mean. Decadal trends in the salinity and stratification of the ocean are investigated, and a 20-year surface freshening trend is found to be predominantly driven by decreasing autumn sea ice growth. By partitioning the freshwater in this way, insight is gained into the long-term freshwater balance and variability, and therefore the potential effects of a changing climate.

Author's Note

The chapters from this thesis are summarised in the following paper submitted to *Deep-Sea Research Part I*:

Regan, H., Holland, P., Meredith, M. and Pike, J. (Submitted) Sources, variability and fate of freshwater in the Bellingshausen Sea, Antarctica.

The code development from Chapter 3, allowing ice-shelf meltwater to be traced in the model, is used in the following paper submitted to *Journal of Geophysical Research: Oceans*:

Kimura, S., Jenkins, A., **Regan, H.**, Holland, P., Assmann, K., Whitt, D., van Wessem, M., van de Berg, W., Reijmer, C. and Dutrieux, P. (Submitted) Oceanographic controls on the variability of ice-shelf basal melting and circulation of glacial meltwater in the Amundsen Sea Embayment, Antarctica.

Acknowledgements

I'd like to thank my supervisors Paul, Mike and Jenny for their hard work in helping me in my journey to become an ocean modeller dealing with the real world, and especially for the opportunities I have had throughout my PhD. This includes my incredible trip to Antarctica on the JR299 cruise, for which I also thank my fellow scientists for making the experience so enjoyable and informative. I'm particularly grateful to Paul and his encouragement and invaluable input during the seemingly endless days of model blowups and equations.

I also need to mention the support of my parents and sister Melanie, who have managed to put up with my PhD woes over the last 4 years. Also the support of the PhD and postdoc community at BAS, without which I wouldn't have reached this point. In particular, thanks to the 4th year girls for the company while writing up at the weekends. Special thanks go to Jim for always being at the end of the phone to offer advice and reassurance. Thanks also to Tom for keeping me sane with lunchtime runs towards the end. I'd also like to thank everyone I've met in Cambridge over the past few years, notably Ashleigh, for always being there for me with wine, and Vicky, Paul, Ryan and Jan (amongst many others) for showing me the importance of adventures.

I would also like to acknowledge the NERC studentship (NE/L501633/1) that funded my research and has enabled me to produce this thesis.

Contents

Commonly used acronyms

AABW	Antarctic Bottom Water
AAIW	Antarctic Intermediate Water
AASW	Antarctic Surface Water
ACC	Antarctic Circumpolar Current
BS	Bellingshausen Sea
CDW	Circumpolar Deep Water
GCM	General Circulation Model
GM	Gent-McWilliams parameterisation
GVIIS	George VI Ice Shelf
ISOMIP	Ice Shelf Ocean Model Intercomparison Project
LCDW	Lower Circumpolar Deep Water
LTER	Long Term Ecological Research
MITgcm	Massachusetts Institute of Technology General Circulation Model
P-E	Precipitation minus Evaporation
PF	Polar Front
RaTS	Rothera Time Series
SAF	Sub-Antarctic Front
SF	Southern ACC Front
UCDW	Upper Circumpolar Deep Water
wAP	west Antarctic Peninsula
WW	Winter Water

Chapter 1

Introduction

Until the late 1990s the Antarctic Peninsula (AP) warmed more rapidly than any other region in the Southern Hemisphere, with air temperatures increasing by nearly 3°C (Turner et al.; 2005a). Over the same period, the summer surface ocean in the adjacent Bellingshausen Sea (BS) warmed and salinified (Meredith and King; 2005). Unlike elsewhere in Antarctica, the Bellingshausen and Amundsen seas have seen an overall decrease in sea ice duration (Stammerjohn et al.; 2012) and extent (Parkinson and Cavalieri; 2012) over the satellite era, with changes focussed on the summer (Holland; 2014). Furthermore, along the AP, 87% of glaciers have retreated since records began (Cook et al.; 2005) in conjunction with mid-depth ocean warming (Cook et al.; 2016), and ice mass loss (Wouters et al.; 2015) and thinning (Paolo et al.; 2015) observed in the southern BS ice shelves.

While atmospheric circulation changes and warming are thought to be significant drivers, they cannot fully explain the glacial ice loss, and recent observations suggest that atmospheric warming has halted at some sites (Turner et al.; 2016). Recent indications are that the ocean is playing an important role (Wouters et al.; 2015; Cook et al.; 2016), highlighting the complexity of the forcings in the Bellingshausen Sea region. With this in mind, this introduction will provide an overview of studies into the region, firstly considering the Bellingshausen Sea in the context of the Southern Ocean, before summarising the oceanography of the Bellingshausen Sea at the regional level, and looking in detail at the importance of freshwater changes. It will then analyse different approaches to studying the region, and the questions that remain. This will form the basis of research into **modelling the sources, variability and fate of freshwater in the Bellingshausen Sea, Antarctica**.

1.1 The Southern Ocean

The Southern Ocean plays a vital role in the global climate system. It serves as the junction of the three main ocean basins, through which water masses are transported and modified due to two key circulation features. The first, the global thermohaline circulation, is the mechanism by which circulation below wind-driven upper layers is driven by density differences (Carter et al.; 2008). It transports heat, salt, nutrients and gases around the

world's oceans by a) warming at low latitudes, with the resulting temperature gradient driving flow to the poles, b) sinking of dense water at high latitudes, c) equatorward flow of deep, salty water, and d) deep water upwelling through the thermocline to the surface (Wyrtki; 1961). Figure 1.1 shows how the Southern Ocean is a key component in

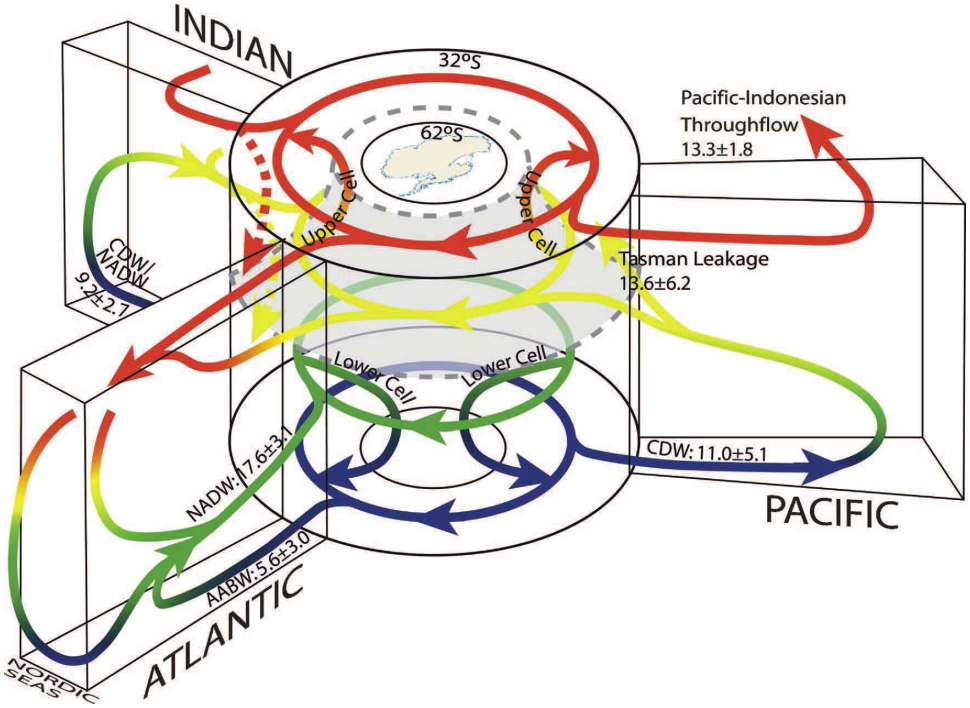

Figure 1.1: The role of the Southern Ocean in global circulation, taken from Lumpkin and Speer (2007). Surface waters are shown in red while deeper currents are shown in blue.

closing the global thermohaline circulation. It allows deep waters to transfer between or rise up from ocean basins, and contributes dense, salty Antarctic Bottom Water (AABW), which is formed in high sea-ice production regions from high salinity shelf water which sinks and, thus, completes the global overturning.

At the surface, the fully circumpolar ocean with no land barrier to obstruct flow results in a strong, predominantly wind-driven eastward current circling Antarctica, called the Antarctic Circumpolar Current (ACC) (Talley et al.; 2011a), the second key circulation feature of the Southern Ocean (the first being the global thermohaline circulation). It connects surface and deep ocean waters via tilted isopycnals, allowing for exchange of ocean properties (Böning et al.; 2008). These tilting isopycnals result in significant upwelling of deep waters that are able to rise without changing their density, sustaining the global overturning budget. As a consequence, over half of the global ocean's properties result from air-sea interactions in the Southern Ocean (Fyfe and Saenko; 2005), including draw-down of CO_2, and thus it is a key system to consider when investigating oceanic control of climate.

The ACC transports a yearly average of 134±11.2 Sverdrups (10^6 m^3 s^{-1}) of water around Antarctica, reaching depths of 4 km in places and 500-1000 km in width (Fyfe and

Saenko; 2005). It contains four fronts, the Subantarctic Front (SAF), Polar Front (PF), southern ACC front (SACCF) and Southern Boundary (SB) (Orsi et al.; 1995), as shown in Figure 1.2 from Meredith and Brandon (2017), each characterised by strong current cores and/or marked transitions in water mass properties. They vary greatly with latitude on their near-circumpolar path, and have been observed to shift by as much as 100 km in 10 days (Nowlin and Klinck; 1986). The Polar Front is defined as the northernmost limit of surface waters from the Antarctic shelf regions while the SAF is the northern limit of the Southern Ocean, steered by topography (Cunningham; 2005).

The surface waters of the ACC are the result of upwelling of Upper Circumpolar Deep Water (UCDW) and air-sea interactions around the coast of Antarctica which form Antarctic Surface Water (AASW). The AASW flows northwards through Ekman transport before sinking at the SAF as Antarctic Intermediate Water (AAIW) (Cunningham; 2005). Deep water masses from the ocean basins to the north, such as North Atlantic Deep Water (NADW) or its form after mixing with other ocean deep waters, Lower Circumpolar Deep Water (LCDW), rise towards the surface along the isopycnals, where they are transformed into surface or dense waters (Rintoul et al.; 2001). The poleward limit of UCDW is generally defined as the southern limit of the ACC (Orsi et al.; 1995). From the south, significant brine rejection predominantly in the high sea-ice production Weddell and Ross seas causes the formation of brine-enriched dense water (High Salinity Shelf Water, HSSW) which sinks to form Antarctic Bottom Water (AABW) before flowing northwards at depth.

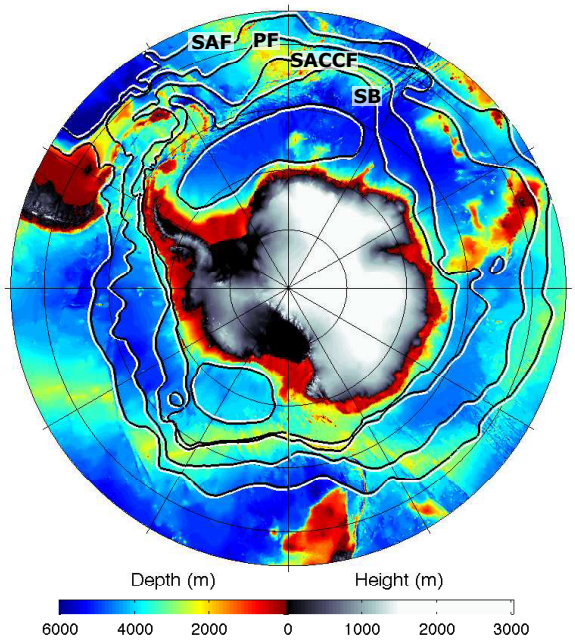

Figure 1.2: Map of Antarctica from Meredith and Brandon (2017), showing surrounding shelf bathymetry and the fronts from north to south: SAF, PF, SACCF, and SB.

1.2 The Bellingshausen Sea and its water masses

The contribution of Antarctic shelf seas-derived water masses to the Southern Ocean circulation varies greatly depending on geographical location and the associated climatic and oceanographic conditions. The Bellingshausen Sea extends to 62°S at Drake Passage, the furthest north of any part of the Antarctic continent, and is situated to the east of the Amundsen Sea (Figure 1.3). The majority of the shelf varies from 200 to 700 metres deep (Hofmann et al.; 1996), with some troughs exceeding 1000 metres. The continental boundary is characterised by islands, narrow inlets, and ice shelves where mesoscale processes are dominated by bathymetric effects that control flow (Hofmann et al.; 1996). Around Alexander Island, for example, cyclonic circulation is forced by winds encouraging downwelling and flow around the coast (Savidge and Amft; 2009). This can control the supply of sediments from elsewhere (Leventer et al.; 1996; Barbara et al.; 2013), which is an important consideration when interpreting past records (explored further in section 1.5).

The Bellingshausen Sea continental shelf break lies close to the SF (Figure 1.2, Meredith and Brandon (2017)) and this exposes it to deep ACC water masses which are able to flood the shelf as they shoal upwards due to northward Ekman transport of surface layers (Hofmann et al.; 1996). The dominant form of this inflow of Circumpolar Deep Water (CDW) transported into the Bellingshausen Sea is UCDW (e.g. Martinson et al.; 2008) with temperatures and salinities exceeding 0°C and 34.6 psu (practical salinity units) respectively (Dinniman et al.; 2011), though LCDW exists in deep troughs such as Marguerite Trough as a salinity maximum of 34.74 psu (Klinck et al.; 2004).

The Bellingshausen Sea experiences a strong influence from the atmosphere. Summer solar insolation and enhanced freshwater fluxes result in Antarctic Surface Water formation, a surface layer which has salinities around 34 psu and temperatures around 1°C, though this can reach 2.5°C near the PF where outcrops of deeper water occur (Carter et al.; 2008). AASW varies greatly seasonally and is widespread around the whole coast of Antarctica (Clarke et al.; 2007), with freshwater inputs in spring increasing stratification and nutrient injection, and thus biological production (Swann et al.; 2013). In the winter, brine rejection salinifies the mixed layer, deepening it to create a Winter Water (WW) layer, the remnant of which persists as a subsurface temperature minimum into summer (Klinck et al.; 2004).

In comparison with more mid-latitude regions, the depth of shelf seas in Antarctica is generally greater and therefore the usual vertical homogeneity (Mastumoto et al.; 2001) is disrupted due to decreased influence of wind mixing near the sea bed (Hofmann et al.; 1996). Figure 1.4 (Petty et al.; 2013) shows a schematic of the differing shelf regimes. The top panel shows the Weddell Sea, where High Salinity Shelf Water (HSSW) formation is a key process, and the lower panel shows the structure of the Amundsen and Bellingshausen seas as the two locations where Circumpolar Deep Water (CDW) from the ACC is able to bring warm, salty water onto the shelf in large amounts. Whilst under the pycnocline the structure is similar in both regimes (Jacobs and Comiso; 1997), brine rejection from sea ice

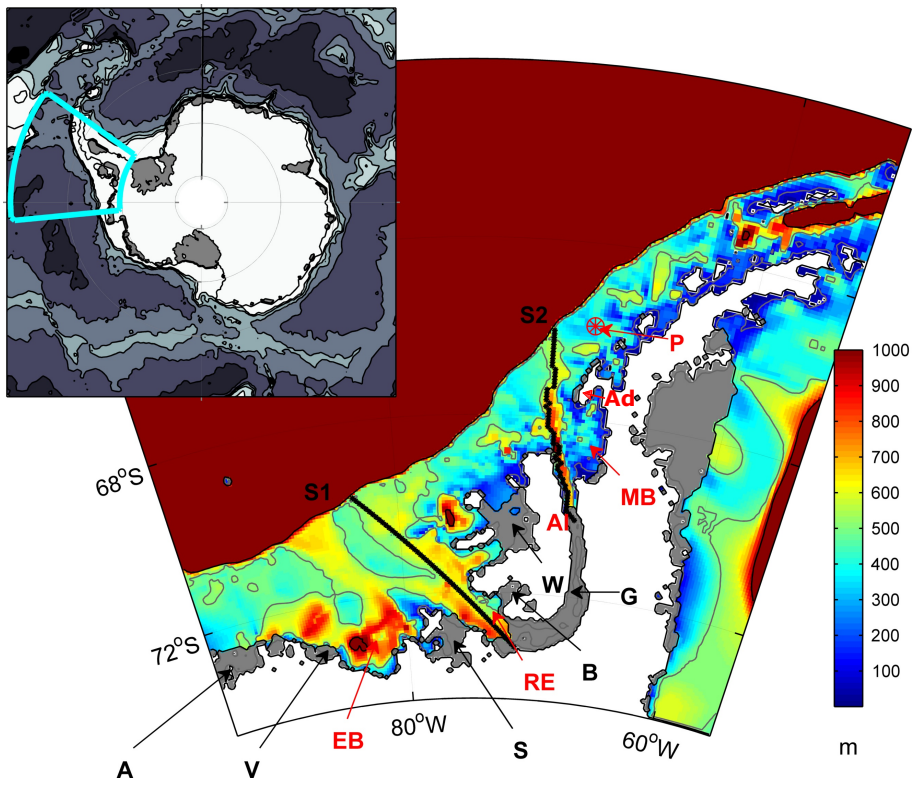

Figure 1.3: Model domain. Coloured is BEDMAP2 bathymetry, with contours shown at 100, 500, and 1000 metres. Ice shelves are shown in grey, with underlying bathymetry contours shown. Also provided in red are key locations, where EB = Eltanin Bay, RE = Ronne Entrance, AI = Alexander Island, MB = Marguerite Bay, Ad = Adelaide Island, and P = Palmer Long Term Ecological Research (LTER) grid point 400.1 (http://pal.lternet.edu), used for validation. Ice shelves on the west Antarctic Peninsula are shown with black arrows, where A = Abbot, V = Venable, S = Stange, B = Bach, W = Wilkins and G = George VI Ice Shelf. Sections through Belgica Trough leading to Ronne Entrance (S1) and Marguerite Trough (S2) are also shown (black). Inset shows the Bellingshausen Sea and model domain (blue) in relation to the Southern Ocean and Antarctic Ice Sheet. M_map tool by (Pawlowicz; 1997) was used for plotting.

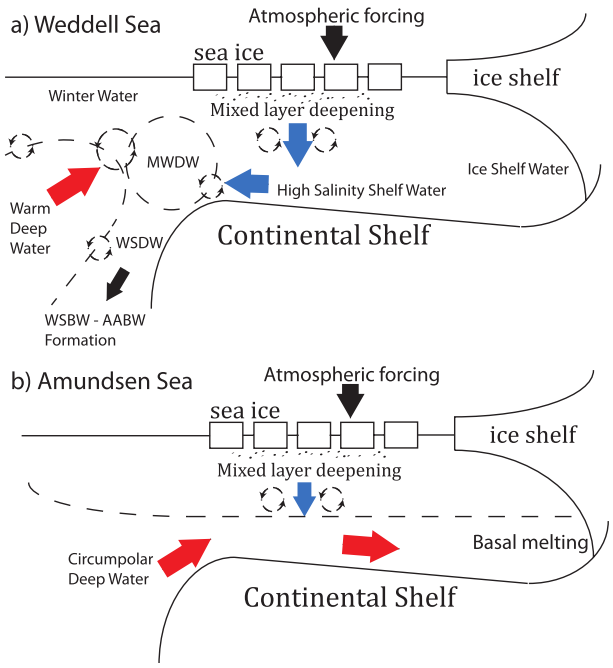

Figure 1.4: Schematic of water masses and main mechanisms of heat and salt transfer via interactions with the atmosphere and cryosphere for a) the Weddell and Ross seas, and b) the Amundsen and Bellingshausen seas, taken from Petty et al. (2013).

formation is not significant enough to reach the sea bed in the Bellingshausen Sea (Smith and Klinck; 2002) and create HSSW. This means that AABW formation does not occur here, attributable to differences in atmospheric forcing between the two regions (Petty et al.; 2013).

The presence of CDW in the Bellingshausen and Amundsen seas is aided by the lack of a significant gyre hindering on-shelf flow (Clarke et al.; 2007), their proximity to the SF (Klinck and Dinniman; 2010), and the action of regional wind forcing (Dinniman et al.; 2012). Eddies at the edge of the ACC produce frontal jets to transfer energy onto the shelf (Klinck et al.; 2004), with deep troughs enabling waters to spill onto and across the shelf from the ACC (Dinniman and Klinck; 2004). This flow is further enabled by upwelling and Rossby waves at the shelf break (St-Laurent et al.; 2013), and is thought to be episodic in nature (Klinck et al.; 2004). It has also been suggested that the absence of HSSW allows for CDW to flood the shelf, where elsewhere it may act as a barrier (Talbot; 1988).

Whilst the water mass structure in the Bellingshausen Sea is relatively well understood, the present incomplete knowledge concerning the on-shelf flow of CDW reflects the general understanding of the shelf circulation east of 120 °W (Grotov et al.; 1998). The schematic in Figure 1.5, from Meredith et al. (2010), shows the known (solid) and hypothesised (dotted) surface currents (green) and those at depth (red); little is known about the region to the west of George VI Ice Shelf (GVIIS) (Holland et al.; 2010). Hofmann et al. (1996) suggest that the prevalent wind from the northeast, combined with the northward ACC

at the shelf break, would result in a general clockwise circulation if no other forcings were present. This is seen around Adelaide Island, with a clockwise surface current enhanced by surface wind patterns that continue west into the Amundsen Sea (Talbot; 1988), and bathymetrically-influenced cyclonic gyres (Savidge and Amft; 2009). Thus there is a large contribution from both winds and bathymetry, like the adjacent Amundsen Sea (Thoma et al.; 2008). CDW from the ACC flows through Belgica and Marguerite troughs, with a generally northward flow under GVIIS (Jenkins and Jacobs; 2008). A seasonal coastal current, the Antarctic Peninsula Coastal Current (APCC), flows westward, driven by a combination of winds and buoyancy forcing, the latter enhanced by the meltwater input to the near-coastal ocean in the summer season. The pathway of the APCC around islands is poorly understood (Moffat et al.; 2008) and it may form a branch of a larger gyre (Klinck et al.; 2004).

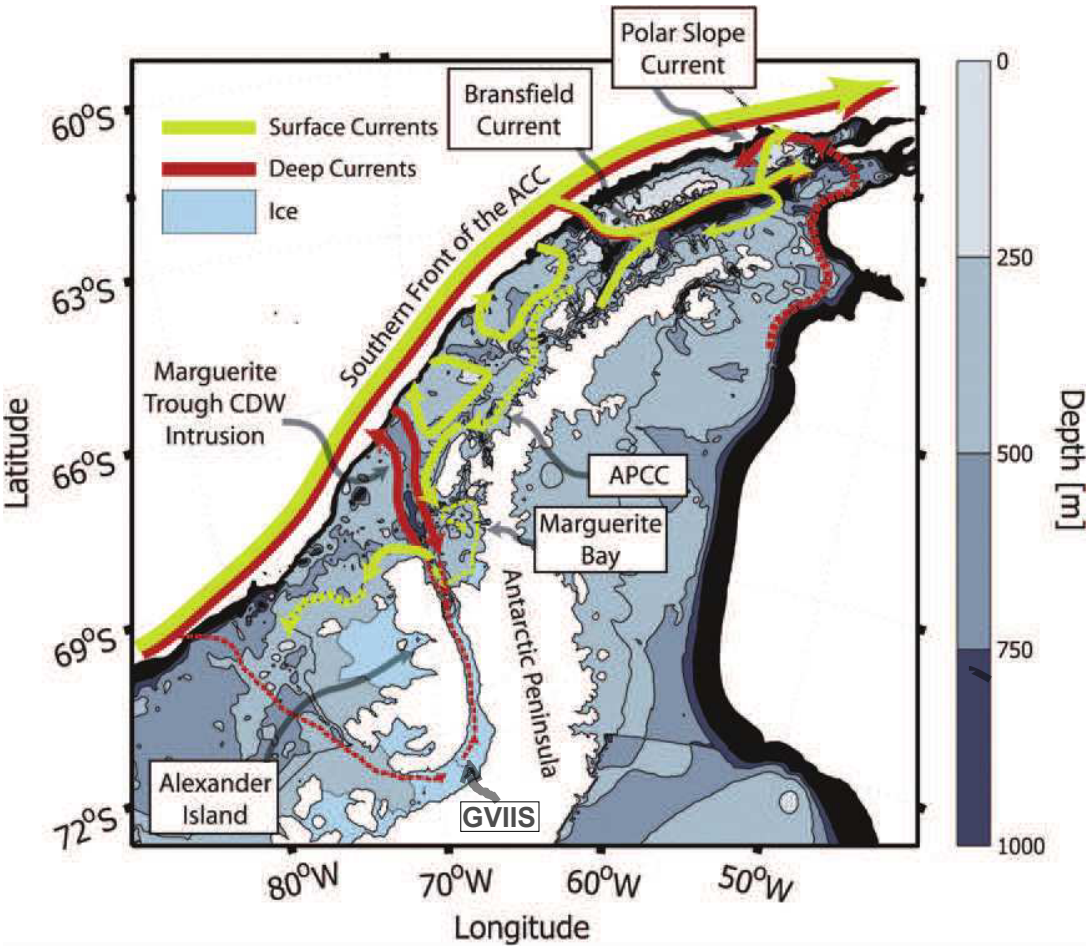

Figure 1.5: Known circulation features of the Antarctic Peninsula shelf, adapted from (Meredith et al.; 2010). Green arrows show surface currents while red arrows show deep currents. Pathways that are uncertain are shown with dotted lines. The Antarctic Peninsula Coastal Current (APCC) and George VI Ice Shelf (GVIIS) are labelled along with other key features.

1.3 Climate change in the Bellingshausen region

Bordered by the Antarctic Peninsula (AP), the most northerly point of continental Antarctica, the Bellingshausen Sea experiences the warmest air temperatures in Antarctica (Lennon et al.; 1982). More interannual variability and warming is seen here than elsewhere, thought to be related to sea ice trends and ocean circulation (King; 1994). This shows a strong coupling of air-sea-ice interactions, meaning that the region is sensitive to change in any of these components. Average winter temperatures vary significantly; for example, 1979-2007 July temperatures at the Faraday/Verdnasky station in the north of the peninsula have ranged from a -12.6°C average in cold years to -4.6°C in years of reduced sea ice (Turner et al.; 2013a). This large range results in a complex system with ocean and cryosphere responding on different timescales. High interannual variability, explaining a recent hiatus in warming after from the 2000s (Turner et al.; 2016), could not account for an increase of air temperatures over the last 50 years to the late 1990s (Turner et al.; 2005a) along with precipitation (Thomas et al.; 2008).

In conjunction with changes to air temperatures, it has been suggested, though not proven, that the ACC is moving poleward (Sokolov and Rintoul; 2009) and warming, alongside more poleward winds (Gille; 2008). This suggests that the BS, being adjacent to the southern bound of the ACC, is potentially vulnerable to change in the future. Across Antarctica, a surface ocean warming of over 1°C has been observed, alongside summer salinification uniquely in the west Antarctic Peninsula (wAP) region (Meredith and King; 2005), whilst in the northern BS the CDW layer has thickened and warmed in recent decades (Martinson et al.; 2008). Changes to water mass properties can have a significant effect on currents that are driven by density gradients, suggesting that circulation of deep waters may change. This could have far-reaching effects on the global thermohaline circulation as well as local changes, affecting upwelling and vertical mixing of nutrients for biological production and heat supply to the coast.

The cryosphere has seen significant changes in recent years. Eighty-seven percent of glaciers have retreated since records began (Cook et al.; 2005), with an acceleration ice loss from the southern peninsula glaciers since the 2000s (Wouters et al.; 2015). It has been suggested that the ocean is the cause (Cook et al.; 2016; Wouters et al.; 2015), and studies have shown that a thickening CDW layer can increase basal melt rates (Holland et al.; 2010), showing a direct link between the ocean and cryosphere. Sea ice extent has also been in decline in the region (Parkinson and Cavalieri; 2012). Despite the causes being unclear, the result is a change to the freshwater inputs into the region. The importance of freshwater in the Bellingshausen Sea is explored below.

1.4 Freshwater

Freshwater is disproportionately important in polar regions. Firstly, density differences drive baroclinic flow, and whilst temperature variation plays a role, salinity is dominant in governing buoyancy at high latitudes. The linear equation of state, for small changes

to T and S and ignoring pressure effects,

$$\rho \approx \rho_0 + \alpha(T - T_0) + \beta(S - S_0)\big), \tag{1.1}$$

describes the density of seawater, ρ, in terms of a reference density, ρ_0, in-situ temperature T and salinity S and their reference values T_0 and S_0. α and β are the thermal expansion coefficient and haline contraction coefficient respectively, which can be expressed as

$$\alpha = \rho^{-1} \frac{\partial \rho}{\partial T} \tag{1.2}$$

and

$$\beta = \rho^{-1} \frac{\partial \rho}{\partial S} \tag{1.3}$$

(e.g. Talley et al.; 2011b). Note here that often the sign of α in Equations (1.1) and (1.2) is negative to reflect the fact that density decreases with a temperature increase (e.g. Roquet et al.; 2015). While typically temperature change has the most effect on density globally, α, or thermal expansion, depends on temperature to first order (Roquet et al.; 2015) so is much lower at cold temperatures whilst β is relatively constant throughout the ocean (Roquet et al.; 2015). Thus any changes to freshwater flux, and hence the salinity term in Equation 1.1, have a great effect on the overall density of the water. This means that the upper layers of the ocean at high-latitudes are salt-stratified (Carmack; 2007).

The Bellingshausen Sea is a region where atmosphere, ocean and cryosphere all interact. While the atmospheric inputs of precipitation, evaporation and river runoff occur globally, their effect at the poles is lessened due to the low air temperatures reducing heat transfer and water vapour in the air (Rooth; 1982) and the freezing of surface water acting as a barrier. Over very long periods, snow accumulation on land forms ice sheets, and their extension over the ocean results in ice shelf formation which routinely calve to create icebergs. All of these sources are formed originally from precipitation and thus are termed meteoric water. The remaining freshwater source in the Bellingshausen Sea is sea ice, formed from the ocean waters due to the seasonal warming and cooling of the surface ocean. In Marguerite Bay, Meredith et al. (2008) found the surface mixed layer waters were mainly comprised of CDW, with freshwater content from meteoric sources (notably glacial melt) contributing up to 5% and sea ice melt only adding up to 1% of total water volume. However, knowledge of the regional variation in this budget is limited (Dierssen et al.; 2002). Given that 1955-1998 saw a freshening in the upper Southern Ocean (Carter et al.; 2008), the dependence of water-column structure on salinity means that it is important to understand how different components affect the system in order to predict its behaviour in the future. A schematic of the components contributing to freshwater is shown in Figure 1.6. The remainder of this section will look at these sources in more detail, their significance in the freshwater budget, and their variability.

1.4.1 Sea ice

Sea ice is an important feature of the Bellingshausen Sea. It controls water masses (Ishman and Sperling; 2002) and greatly affects the heat and salt budget (Hofmann et al.; 1996).

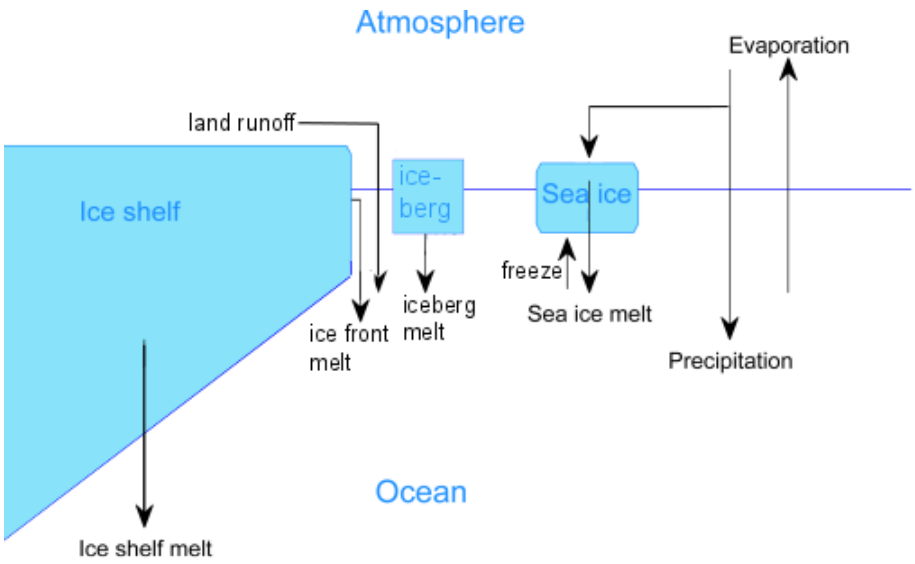

Figure 1.6: Diagram showing the freshwater inputs into the Bellingshausen Sea.

It is thought that the degree of upper ocean stratification is controlled dominantly by ice production (Meredith et al.; 2004), which has consequences for circulation, primary production, and various other physico-chemical processes. Sea ice is formed from the fresh AASW layer when cooling (predominantly from air temperatures in autumn) exceeds heat flux to the air-ocean interface, freezing the top of the water column. This results in an average ice thickness and ice concentration of 0.9 m and 81%, thickening to 2.14 m with a concentration of 53% in summer (Worby et al.; 2008) as the large areas of thinner ice melt away. Unlike Antarctic regions that form bottom water, the Bellingshausen Sea is thought to be a region of net ice melt due to warm air temperatures and heat from the CDW below (Smith et al.; 1999) but is one of the few regions to contain multiyear ice (Zwally et al.; 2002). Dynamical controls through local wind effects have a strong influence on melting and advection of sea ice into the region (Hofmann et al.; 1996), with a thickening towards the coast and further south (e.g. Xie et al.; 2013) that suggests a spatial gradient in its resulting meltwater. However, advection of melt into the region can disrupt this pattern, and coastal polynyas resulting from winds (Klinck et al.; 2004) or vertical exchange of heat (Jacobs and Comiso; 1993) can increase the complexity of sea ice distribution.

In the summer, melting sea ice along with surface heating of the exposed ocean enhance stratification (Barbara et al.; 2013), while in winter, densification from brine rejection along with increased mixing due to turbulence driven by strong winds deepens the winter water layer (Meredith et al.; 2004). This deepening results in mixing with saline CDW waters (Carter et al.; 2008). Seasonal shifts in wind direction cause divergence/convergence, and shorter wind events result in leads, polynyas and shifts in the pack ice (Watkins et al.; 1998). These changes can have a significant effect on the ocean. Extensive sea ice cover acts as a barrier to atmospheric exchanges, reducing heat loss and stabilising the water column (Goosse and Fichefet; 1999). In years with reduced winter sea

ice cover, the reverse occurs, and winter mixed layers deepen through increased exposure to the atmosphere (Venables et al.; 2013), which can happen during anomalous years or by large-scale atmospheric circulation changes causing high winter air temperatures and strong winds (Meredith et al.; 2004). The anomalously low winter sea ice allows for more air-sea interaction, deepening the mixed layer (Venables et al.; 2013). Holland et al. (2010) suggest that because the ice edge remains more on the continental shelf, more brine rejection occurs in the Bellingshausen Sea than in the deep ocean, also serving to deepen the mixed layer. This deepening can cause increased mixing with CDW below, transferring heat up the water column and increasing ice shelf basal melting (Holland et al.; 2010). The following summer can then experience less stratification due to the deeper mixed layer and reduced spring sea ice melt, which allows heat to be mixed down further, remaining into the following autumn and providing conditions less conducive to sea ice formation (Venables et al.; 2013). This creates a significant feedback system, demonstrating that there is a time-varying element to consider when interpreting discrete observations.

Sea ice experienced a loss in areal extent from 1979-2010 (Parkinson and Cavalieri; 2012), with around 20% loss in extent from 1979-1998 (Zwally et al.; 2002) in the Bellingshausen Sea. In conjunction with this, the sea ice season reduced by 3 months from 1979-2010 (Stammerjohn et al.; 2012). There are a number of mechanisms by which sea ice cover can vary between years. Sea ice is at the interface of air-sea interactions, and thus is sensitive to changes to these. Air temperatures on the peninsula have been rising until recently (Turner et al.; 2016), notably in winter (Turner et al.; 2005a). This alters the heat supply to the surface of the ocean and sea ice. Increased precipitation (Thomas et al.; 2008) contributes to a thickening of surface snow on sea ice, lowers surface ocean salinities, and stabilises the water column, thus creating conditionsand stabilising effects that favour formation of sea ice (Manabe et al.; 1992); thus increased freshwater input can act to offset the melting effect of increased air temperatures (Marsland and Wolff; 2001). The complexity of the feedbacks is increased by the weight of increased snow causing snow flooding. The snow distribution is determined by wind direction, resulting in increased surface albedo and insulation of the surface from cold air (Massom et al.; 2001). A trend towards northerly winds thickening ice at the coast and reducing thickness at the northern ice edge from autumn to spring (Holland et al.; 2014) has occurred in conjunction with ice loss in summer and autumn (Zwally et al.; 2002).

Stammerjohn et al. (2012) suggest that the interannual variability seen at the northern limit of the ice pack is too great to depend on atmospheric effects alone. Increased upper water temperatures, particularly in summer (Meredith and King; 2005), can result in a net thinning from basal melt which counters increased precipitation at the surface (Lewis et al.; 2011). Previous studies have suggested that heat stored from vertical exchange with CDW or warmer surface waters from solar radiation or advection could cause melting of sea ice that propagates along the current pathway (Jacobs and Comiso; 1993). Changes to both heat flux and stratification from salinity variations could alter sea ice melting in the area. Decreasing winter sea ice extent can result in higher summer surface salinities (Meredith

and King; 2005), suggesting a complex feedback between ocean and ice that is not confined to an instantaneous response. However, changes to salinity cannot easily be decomposed into changes in CDW, sea ice and other freshwater sources, meaning that cause and effect are difficult to deduce.

1.4.2 Precipitation and Evaporation

Meteoric water, derived from the atmosphere, is input to the ocean either directly via precipitation or via accumulation over land and incorporation into glacial systems, subsequently entering the ocean following melting of the resulting ice. Precipitation itself is important both as a source of meteoric-based ice and by its own inputs to the ocean, particularly north of the PF (Tiwari et al.; 2013). Snowfall is the dominant form, with rain generally being an order of magnitude lower except for in some specific areas, and strongly seasonal (van Wessem et al.; 2016a). The former requires more latent heat to melt, thus precipitation can introduce freshwater with varying properties into the surface ocean. In Bransfield Strait to the north of the region, it is thought that precipitation minus evaporation (P-E) accounts for at least two thirds of the total freshwater input balancing the salt input from CDW, showing that P-E could be a significant source of freshwater in some areas (Hofmann et al.; 1996). This, along with melting glaciers and winds that cause downwelling, means that the west Antarctic Peninsula (wAP) region creates favourable conditions for a buoyancy-driven coastal current - the APCC - to form (Moffat et al.; 2008), something that may be enhanced if any of these increase. However, P-E varies in significance based on region, indicating the importance of understanding local inputs and their effects.

At Faraday station in the northern AP, the number of days experiencing precipitation has increased by over 12 days per decade since 1951 (Turner et al.; 2005b). This is in conjunction with an increase in net snow accumulation, thought to be due to an increase in precipitation (Thomas et al.; 2008). Atmospheric circulation mainly determines the precipitation changes due to warmer air being brought to the peninsula (Meredith et al.; 2008). While orographic effects cause a lot of precipitation to occur near the coast (Meredith et al.; 2013), it also falls into the ocean out as far as the shelf break (van Wessem et al.; 2016a). This snowfall can accumulate on top of sea ice and be moved as the ice is advected under the influence of winds and currents. Therefore sea ice distribution plays a big role in the effect of precipitation on the ocean, meaning its effects could be affected by declining sea ice extent.

1.4.3 Surface melt and glacial discharge

Net surface melting from marine-terminating glaciers and land-based ice is thought to be small in the Antarctic Peninsula (Hofmann et al.; 1996), as despite high rates of melting, most meltwater refreezes before reaching the ocean (van Wessem et al.; 2016a). However, the duration of conditions enabling melt has lengthened since records began, with associated increases in runoff expected (Vaughan; 2006). While contributions from surface runoff

are insignificant, meltwater from oceanic subsurface or ice-front melting is the dominant contributor to meteoric water in Marguerite Bay (Meredith et al.; 2008), though with meltwater concentrations showing strong interannual variability (Meredith et al.; 2016).

Glaciers are important for supplying nutrients to the water column, with effects seen out to 100 km offshore (Dierssen et al.; 2002); the resulting elevated iron concentrations have been identified up to 3500 km from the source (de Jong et al.; 2012). In Ryder Bay, south of Adelaide Island (Figure 1.3), glacial melt is thought to be a key input to the surface ocean in summer once the sea ice has melted and the associated sea ice melt flux has therefore reduced from its highest values, bringing iron with it (Annett et al.; 2015). This enhancement occurs earlier if sea ice is lost (Dierssen et al.; 2002). Localised inputs of glacial melt can cause cyclonic circulation to overlie more persistent anticylonic features (Martinson et al.; 2008), with vertical mixing through buoyant freshwater melt at depth enhancing circulation away from the coast along the pycnocline or surface ocean (Cook et al.; 2016). Thus small-scale flows, in addition to the APCC, can be generated from glacial inputs. Since 87% of glaciers on the wAP have retreated since 1940 (Cook et al.; 2005), with thinning in the south (Wouters et al.; 2015), it is important that the glacial discharge is quantified and understood given its importance in the freshwater budget.

1.4.4 Icebergs

Icebergs can result from calving of ice shelves or, on a smaller scale, from glacier calving. This can inject cold, fresh water into surface layers or at depth, often thousands of kilometres from the calving site and years after the original calving event (Tournadre et al.; 2016). Iceberg trajectories usually follow coastal currents, with deviations due to bathymetry (Gladstone et al.; 2001). While giant iceberg melt inputs large amounts of freshwater in the Southern Ocean, it varies spatially and temporally (Silva et al.; 2006), and there is modelling and observational evidence to suggest that there is no strong advection of large icebergs into or out of the Bellingshausen Sea (Tournadre et al.; 2015; Merino et al.; 2016). The majority of large icebergs break into smaller icebergs rather than shrinking from basal melt (Tournadre et al.; 2015), suggesting significant advection before injection of meltwater and therefore nonlocal input of freshwater. Basal melt of ice shelves and iceberg calving along the peninsula are comparable (Rignot et al.; 2013; Depoorter et al.; 2013), and 2002-2012 saw twice the amount of iceberg melting as calving of icebergs (Tournadre et al.; 2015). This suggest that the freshwater flux from resulting small icebergs is not insignificant.

Tournadre et al. (2016) found a large concentration of icebergs in the Bellingshausen Sea, reducing out to the ACC from the coast, much of which was held in sea ice and therefore limited in its open water motion and break down. Iceberg meltwater is generally thought to increase sea ice cover by shallowing winter mixed layers and enhancing stratification, therefore reducing heat mixed up from depth (Merino et al.; 2016). However, recent studies suggest that, unlike in the rest of the Southern Ocean, sea ice extent and iceberg

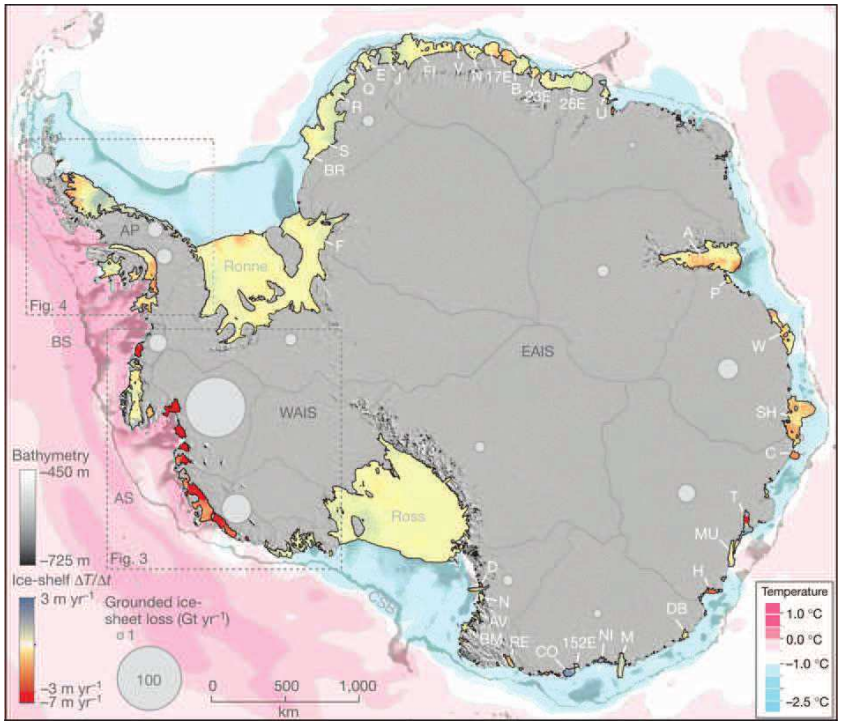

Figure 1.7: Figure showing the ice shelf thickness change occurring along the west Antarctic Peninsula between 2003-2008 in the context of the rest of Antarctica. Also shown are the annual average temperatures at the sea bed, showing the presence of CDW in the Bellingshausen and Amundsen seas (Pritchard et al.; 2012).

volume are not correlated in the Bellingshausen Sea (Tournadre et al.; 2015). Merino et al. (2016) suggest that meltwater injection around Antarctica actually increases sea surface temperatures due to changes in heat transport of the ACC, which outweighs the local addition of cool, fresh iceberg meltwater. This is significant given the potential changes to the ACC.

1.4.5 Ice shelves

There are several small ice shelves on the west Antarctic Peninsula (Figure 1.3), namely (west to east) Abbot, Venable, Stange, Bach, Wilkins, and George VI, with all decreasing in size since the 1900s (Cook and Vaughan; 2010). The geometry of GVIIS, the largest on the peninsula at 450 km long and ranging from 110 metres to 475 metres thick (Talbot; 1988), is unusual in that it acts as a bridge between mainland and Alexander Island, and the ocean below has a northward throughflow (Jenkins and Jacobs; 2008). GVIIS melt rates increase when the CDW layer thickens and comes into contact with the ice base (Holland et al.; 2010), which can result in mixing of ice shelf meltwater and CDW into the mixed layer, creating warm, fresh waters reaching the surface due to buoyancy (Jenkins; 1999) rather than creating a subsurface plume (Potter and Paren; 1985). If the ice base is shallower than the warm waters, an ice shelf is more dependent on surface processes

and upper water column changes (Holland et al.; 2010), which can result in a change in significance of processes over time as ice shelf geometry changes.

Ice shelves and icebergs, resulting from calving of ice shelves, differ from surface inputs in that they release cool, fresh water at various depths in the water column. This can serve to alter the stratification, often stabilising the water column where convection would otherwise happen from sea ice formation (Hellmer; 2004), where the meltwater advects depending on its own density compared to the ambient water. Basal melt can result in a positive feedback, strengthening circulation on the shelf, shallowing the mixed layer and therefore allowing CDW to thicken, exposing the ice shelf to more warm water (Nakayama et al.; 2014a). However, in some cases the cool meltwater can limit the effect of the CDW and serve to reduce further melting (Hattermann and Levermann; 2010). Ice shelf basal melt rates are also affected by winds, for example via changed upwelling (Carter et al.; 2008) increasing on-shelf flow of warm CDW. Dinniman et al. (2012) found that, perhaps counterintuitively, stronger winds actually caused a net loss of heat at depth under GVIIS due to increased mixing of the CDW, cancelling the effects of increased CDW transport onto the shelf, and therefore reducing melt rate. Thus the atmospheric forcing can affect processes at depth and non-locally.

Increased melting of Bellingshausen Sea ice shelves can be seen in Figure 1.7. Ice shelf melting on the AP is a) dominated by basal melt, and b) experiencing high melt rates in the Bellingshausen Sea (e.g. Rignot et al.; 2013; Depoorter et al.; 2013), and whilst this is thought to stabilise the water column, a modelling study by Hellmer (2004) found that removal of the ice shelf meltwater freshwater source reduced sea ice thickness, resulting in warmer and saltier waters on the shelf. This means that the effects of changes to ice shelf melting are not fully understood. The fact that meltwater from the Bellingshausen Sea has been found to contribute to freshening in the Ross Sea (Nakayama et al.; 2014a) is further evidence of the need for understanding ice shelf processes in the region.

1.4.6 Summary

The freshwater budget plays an important role in the Bellingshausen Sea. The intrusion of saline CDW is balanced by freshwater inputs from precipitation and ice (Hofmann et al.; 1996). Cyclonic circulation on the shelf is thought to be amplified by freshwater-induced buoyancy effects (Savidge and Amft; 2009), and a summer coastal current enhanced by runoff and precipitation is observed (Moffat et al.; 2008) in the absence of sea ice, suggesting that along-shelf circulation is dependent on the freshwater balance. Biological consequences of the freshwater are also profound, with increased meltwater increasing phytoplankton blooms (Dierssen et al.; 2002). In addition to spatial variation in freshwater flux, temporal changes can be rapid and episodic (Silva et al.; 2006). All freshwater components have different responses to seasonal and longer-term warming, and their effects are often apparent on different timescales. As meteoric inputs are expected to rise (Meredith et al.; 2008) and sea ice is declining (Parkinson and Cavalieri; 2012), a thorough understanding of each is required. Key ways of achieving this are explored in

the next sections.

1.5 Methods

In previous sections the oceanography of the Antarctic Peninsula has been discussed with emphasis on freshwater behaviour and importance in the ocean. This section will focus on methods for understanding the freshwater balance of the region and how they can be collected and interpreted, highlighting methods for past and present eras.

1.5.1 In-situ observations of freshwater

Whilst many studies look at changes to salinity and fluxes into the ocean, separation of a freshwater component from total freshwater content in the ocean is difficult. As a partial solution to this, a very useful indicator of freshwater for both the past (palaeo-era) and the present (contemporary era) is the ratio of stable oxygen isotopes. This ratio is defined as the following:

$$\delta^{18}\mathrm{O}_{sample} = \frac{\mathrm{R}_{sample} - \mathrm{R}_{standard}}{\mathrm{R}_{\ standard}} \times 1000 \tag{1.4}$$

where $\mathrm{R}=\frac{^{18}\mathrm{O}}{^{16}\mathrm{O}}$ (Rohling; 2007). The two main isotopes of oxygen in seawater are ^{18}O and ^{16}O, and their content varies due to evaporation and condensation causing fractionation at the surface (Epstein and Mayeda; 1953), but the behaviour of the isotopes away from the surface is as a conservative tracer (Meredith et al.; 2008). High latitudes have much less ^{18}O in atmospheric water vapour than lower latitudes; evaporation mainly occurs at low latitudes so by the time moisture reaches the polar regions most of the heavier ^{18}O has already been lost through rain-out (Rohling; 2007). By the same argument, evaporation preferentially takes up the lighter ^{16}O isotope, depleting the ^{18}O content of the resulting precipitation further. Thus a lower δ^{18}O content of water in the polar regions is an indicator of meteoric water (Meredith et al.; 2013). As previously discussed, this comprises glacial meltwater and precipitation (Delaygue et al.; 2000). δ^{18}O has been used as a tracer of water masses, for example, those interacting with ice shelves in the Weddell Sea, to enable diagnosis of meteoric water contribution to bottom water (Schlosser et al.; 1990).

The calculation of δ^{18}O content of seawater samples can be used to infer the isotopic ratio of the meteoric water input to the ocean, with values as low as -57‰when calculated against the standard in Equation 1.4 (Rohling; 2007). However, sea ice forms from ocean water and acquires a δ^{18}O signature very similar to that of the water from which it formed, and thus while its salinity falls below 10 psu (Eicken; 1992), its formation has little effect on the oxygen isotope ratio of the surrounding sea water, resulting an average enrichment of δ^{18}O of 2.57±0.10‰ (Rohling; 2007). It is known that two water masses can have the same salinity but different δ^{18}O values (Epstein and Mayeda; 1953). This fact can be exploited when used in conjunction with salinity to deduce relative contributions of sea ice melt and meteoric water to the freshwater present via a simple mass balance of

freshwater, f, salinity, S, and δ^{18}O, δ, such that

$$\begin{aligned} f_{cdw} + f_{si} + f_m &= 1, \\ S_{cdw} f_{cdw} + S_{si} f_{si} + S_m f_m &= S, \\ \delta_{cdw} f_{cdw} + \delta_{si} f_{si} + \delta_m f_m &= \delta, \end{aligned} \tag{1.5}$$

where the water column is partitioned into *cdw* (CDW contribution), m (meteoric water contribution) and *si* (sea ice melt) (Meredith et al.; 2008).

The composition of freshwater in Marguerite Bay (Meredith et al.; 2008, 2010) and the wider west Antarctic Peninsula (Meredith et al.; 2013) has been investigated in recent decades through analysing δ^{18}O of seawater. Comparing data from individual stations shows the need for an understanding of how specific sites represent the broader region. Measurements in the northern BS show a general dominance of meteoric water in coastal areas, though years of weak precipitation and/or extreme sea ice can show comparable quantities of sea ice melt (Meredith et al.; 2016). Over time there has been a decline in meteoric water in the surface waters adjacent to Adelaide Island (northern Marguerite Bay) due to deepening winter mixed layers (Meredith et al.; 2013), despite increased glacial discharge (Pritchard and Vaughan; 2007) and snowfall (Thomas et al.; 2008) in the BS. However, interannual variability in freshwater inputs from different sources and strong regional structure in their injection locations can complicate the interpretation of data on wider temporal and spatial scales (Meredith et al.; 2016), highlighting the importance of understanding the three-dimensional spatial variance of freshwater composition over time.

1.5.2 Palaeoceanographic records

Since freshwater inputs can be observed in the δ^{18}O signature of surface waters (Meredith et al.; 2013), a common source of isotopic composition of sea water in the past is planktonic shells, for example, $CaCO_3$ in foraminifera (Rohling; 2007), or SiO_2 frustules of diatoms, with the assumption that fractionation is constant or small between species (Swann et al.; 2013). This can be used in conjunction with other data from sediment cores, such as the ratio of known meltwater species to known open ocean species (Leventer et al.; 1996), to infer melting conditions at a particular site. Deglaciation, inferred through higher productivity of coastal species (e.g. Maddison et al.; 2005) and confirmed by low δ^{18}O values in foraminifera, are interpreted as subglacial meltwater discharge due to a warmer climate (Khim et al.; 2001). Conversely, higher δ^{18}O indicates less glacial discharge, or more global ice, while significant iceberg calving events are shown by abrupt changes in δ^{18}O (Pike et al.; 2013). Shorter-term seasonal differences determined by sea surface temperature and salinity changes deduced from the ecological preferences of species present (Pike et al.; 2008), and fluctuating behaviour of diatom assemblages, can suggest short-term atmospheric change (Pike et al.; 2013), and combining with δ^{18}O has shown that there has been significant variability in glacial discharge in the past at the wAP (Swann et al.; 2013).

One issue with glacial meltwater is that it is formed of precipitation from when the ice

was formed, and therefore the isotope ratio reflects the large-scale past climate rather than the present day climate (Rohling; 2007). The fact that iceberg calving is shown by abrupt changes in δ^{18}O (Pike et al.; 2013) means that incomplete or sparse data could result in longer term interpretations being made that reflect the sampling strategy. If glaciers are not present the errors are constrained somewhat (Epstein and Mayeda; 1953), making the Antarctic Peninsula particularly susceptible to problems compared to regions with less glacial meltwater. Diatom frustule δ^{18}O does not easily constrain sea ice processes due to δ^{18}O being affected more by P-E than sea ice (Craig and Gordon; 1965). Schmidt et al. (1997) showed that the fractionation of isotopes preserved in diatoms in sediment records resulted in different δ^{18}O values to those obtained from sea water, highlighting limitations of the method. Over time, the response of δ^{18}O to glacial discharge will change depending on how far away the ice sheet is (Swann et al.; 2013), something that must be considered; a lower diatom frustule δ^{18}O signal may mean a spatial rather than climate shift. This local nature of changes causes many potential problems, with some suggesting nonlocal calibrations and monitored patterns are preferred to inferences from small scale results (Schmidt et al.; 2007), highlighting the need for multiple data sources on larger scales and more continuous recording. Some large-scale climate shifts are consistent across different regions (Noon et al.; 2003) but confidence in understanding small-scale processes and how they can be extrapolated to larger-scale shelf behaviour is not high.

1.5.3 Satellite data

Increasingly, satellite observations are becoming a key tool in monitoring change in oceanographic fields such as the ACC (Meredith and Hogg; 2006), atmospheric patterns and clouds, and cryospheric changes. For example, satellite altimetry data has been used to monitor surface changes of ice shelves and conclude that basal melting is a significant portion of total ice shelf melting in the Bellingshausen Sea (Rignot et al.; 2013), with recent studies quantifying melt rates across Antarctica (e.g. Depoorter et al.; 2013; Rignot et al.; 2013). Glacial changes have been tracked by looking at sea surface height anomalies (Rye et al.; 2014), and satellite imagery has also tracked large iceberg calving, another freshwater parameter hard to quantify (Tournadre et al.; 2016).

Sea ice areal coverage is of particular interest in polar regions as it is one of the main limiting factors in gaining direct in-situ observations. In the Bellingshausen and Amundsen seas, the first satellite records from 1973 onwards have been key in identifying the reduction in sea ice extent (that opposes the increasing extent in the rest of Antarctica (Jacobs and Comiso; 1997)) which can be attributed to changes to seasonal trends in ice advection (Holland; 2014) caused by trends in local wind direction (Holland and Kwok; 2012). Seasonality can also be explored through continuous satellite products, concluding that the sea ice season has shortened (Parkinson; 2004), with each month showing a decrease in sea ice extent (Parkinson and Cavalieri; 2012) and strong trends of ice loss in summer and autumn acting as a response to changes in spring melting (Holland; 2014).

A significant barrier to using satellites to infer sea ice change is that while sea ice

area can be calculated, the thickness is significantly harder to infer and therefore changes to ice volume are only poorly determined, despite this being a key factor in calculating changes to resulting meltwater. Given that winds can pile up sea ice at the coast, it could be that changes to the wind are reducing extent but thickening the ice resulting in no volume change. Ice thickness has been estimated by various methods, including using calculations based on buoyancy and empirical formulae, and these observations suggest that thickness in the Bellingshausen Sea does increase in summer when extent reduces. However, variability in ice extent tends to dominate calculated ice volume, suggesting that thickness variability is not significant (Xie et al.; 2013). The calculations carried out by Xie et al. (2011) and Xie et al. (2013) also require a calculation of snow depth which, while shown to be similar to ship-based in-situ measurements, adds another assumption into the derivation. So while satellite observations can shed new light on the spatial and temporal evolution of the cryosphere, quantifying freshwater flux from these is still problematic.

1.5.4 Models

There are a number of geographical areas poorly characterised by observations due to sparse data with discrete points in space and time, and lack of understanding of how the processes affecting them behave and interact on different scales. The remainder of this section will discuss the benefits and limitations of using models as a tool, and detail studies carried out to investigate the Bellingshausen Sea region.

Modelling studies involve some choices to be made to create a setup that is both fit for purpose and within computational constraints. For example, the complexity of the model can range from simple box models investigating the interplay between a few processes, up to global General Circulation Models (GCMs) and beyond to cover Earth System Models that involve complex physics and explicitly calculate interactions between different spheres (such as the cryosphere and ocean).

The small internal Rossby radius of deformation associated with Antarctic regions implies narrow currents (Hofmann et al.; 1996), providing a minimum resolution requirement. Model resolution and bathymetry are important for modelling realistic ice shelf melt rates (Holland et al.; 2010) and CDW inflow (Dinniman et al.; 2003), suggesting that the approximation of the Antarctic coastline in global climate models (Hellmer; 2004) is problematic. Additionally, low-resolution studies often have to sacrifice ice shelf freshwater flux (e.g. Yin et al.; 2011), or greatly simplify to only the largest ice shelves. For example, Hattermann and Levermann (2010) do not include any ice shelves from the Amundsen and Bellingshausen seas, despite their basal melt rates being the highest in Antarctica.

It is impossible to explicitly calculate every process occurring with available computational power, and therefore parameterisations are used for sub-grid processes. Caution must be taken, as sub-grid processes can directly affect freshwater pathways. Losch (2008) suggests that overestimated basal melt rates of ice shelves were due to a combination of low resolution and poor parameterisation. Small-scale processes affect freshwater inputs, such as the role of vertical mixing on basal melt (Dinniman et al.; 2012) and sea ice formation,

and eddies in modelling the summer coastal current. Liu (2003) used sensitivity studies to test various mixing schemes and identify their weaknesses, finding that sea ice cover is very responsive to parameterisations on small scales. This demonstrates that limitations can be identified and tested, and high-resolution studies such as a study by Dinniman et al. (2011) with overestimated melt rates suggests that the limiting factor is not always resolution.

While ocean models are able to couple to atmosphere, sea ice and ice shelf models, it is not always feasible to do this. While some have suggested that models coupling the ocean to the atmosphere are necessary to accurately model the effects of their physical interactions (Bintanja et al.; 2013), such coupled models do not currently estimate Antarctic sea ice correctly, predicting a decline in extent in areas of Antarctica where growth is observed (Turner et al.; 2013b). This could cause issues given that dense water formation from sea ice is a key component of the global circulation, and therefore using data-derived atmospheric reanalyses and focusing computational resources on improving physics elsewhere in Antarctic models may be more suitable.

The difficulty with representing a realistic ocean is problematic for freshwater processes. Ice shelf basal melt is very important in stratification; a potential scenario in the absence of ice shelves is less stabilisation and advection by coastal currents, reduced sea ice formation, and denser waters flooding deep basins (Hellmer; 2004). Comparative studies, using the same model setup for different regions, allows diagnosis of different regional controls, such as the finding that there is more mixing of CDW onto the Ross Sea shelf than the Bellingshausen Sea (Dinniman et al.; 2011). Both Holland et al. (2010) and Dinniman et al. (2012) employ high-resolution models of the Bellingshausen Sea to investigate ice shelf melting, finding that GVIIS is susceptible to changes in CDW. However, Dinniman et al. (2012) suggest increased winds at the shelf break result in more mixing of the water column, reducing the heat of the CDW and therefore lessening its effect despite an increase in its volume. Holland et al. (2010), meanwhile, attribute the difference to sea ice changes at the surface across the whole of the Bellingshausen Sea, highlighting the feedbacks between different freshwater sources. Hattermann and Levermann (2010) suggest that local influence of freshwater input is weak, with shelf break processes being affected by iceberg melting (Gladstone et al.; 2001). This suggests that location of freshwater input may be less important than magnitude of flux, thus validating studies that use a uniform iceberg melt flux along the coast (e.g. Holland et al.; 2014), but also emphasises the nonlocal effects of multiple freshwater forcings and their individual importance.

Attempts to understand the geographical importance of freshwater flux and water masses have been carried out in the past. Nakayama et al. (2014a) use a passive tracer to track ice shelf meltwater, allowing a full interrogation of the temporal variation of meltwater and flux pathways, rather than just the end result. In a similar study, Dinniman et al. (2011) used a tracer to follow the path of CDW, a technique which is often employed to monitor water masses using stable isotopes and salinity (e.g. Delaygue et al.; 2000; Mathieu et al.; 2002). The former used tracers to study past climates; observations from

ice cores allow model validation where the climate is vastly different to the present day, allowing the assumptions and tuning of the model from present-day validations to be tested. This example highlights how useful the combined effort of models and observations can be in investigating the behaviour of freshwater and processes on the shelf. However, instantaneous release of a bulk of tracer does not provide insight into the steady-state of the traced fields over a given time period, just their pathway, and thus no realistic quantification can be gained. Age tracers can be used to give some temporal information on a release, although this does not directly relate to observational records of δ^{18}O and other measurements that just provide the current state of the ocean.

1.6 Aims of the research

There are multiple drivers of ocean circulation and transport on the Antarctic Peninsula shelf, and these vary locally and over time. While winds and large scale atmospheric events are certainly factors in driving variability, the ocean's effects and feedbacks are currently poorly understood. The ocean is affected by freshwater inputs from both sea ice and meteoric sources, the balance of which is variable but the overall effect of which is thought to be becoming more significant.

Oxygen isotope data can be used to identify the relative contributions of sea ice and meteoric water sources at a particular location and time, through the fact that freshwater has a different salinity to seawater and the δ^{18}O value of seawater is greatly affected by meteoric water but not by changes in sea ice. If enough data points existed, a comprehensive picture could be built of the freshwater behaviour in the ocean system. However, data is sparse and generally more easily obtained in summer, something that is problematic since the ocean system has very seasonal behaviour. This paucity of data makes interpretation difficult, particularly in the past.

It is clear that the changes to the freshwater budget of the Bellingshausen Sea could have profound changes on its circulation and associated feedbacks, both regionally and beyond, but there are still many questions surrounding the quantification of the variation in the freshwater flux and content. Motivated by this, the aim of this thesis is to develop a new model of the Bellingshausen Sea to investigate the temporal and spatial variation in each freshwater source, and their overall importance in the freshwater budget. This will be achieved by developing a novel method of tracking freshwater.

Chapter 2 will describe the development of a high resolution model of the Bellingshausen Sea. This will include tests of different forcings and optimising these to create the most realistic setup.

Chapter 3 will detail development of a new method of tracking freshwater sources from their input source. This will utilise the current passive tracer capability and develop this for use with individual sources. Full testing with a coarse resolution model and implementation in the high resolution model will be described.

Chapter 4 will validate the model, and then explore the spatial variation of modelled

freshwater on the Antarctic Peninsula shelf and the associated composition in particular areas.

Chapter 5 will investigate the temporal variation in modelled freshwater composition. This will include focus on sea ice trends and variations to ice shelf melting.

Chapter 6 will discuss the implications of these results in the context of the wider Bellingshausen Sea oceanography, and future directions that the research could take.

Chapter 2

Model setup

This chapter describes the model used in the research, the Massachusetts Institute of Technology general circulation model (MITgcm), and its governing equations. It then details the various inputs and settings used to create a model applicable to the Bellingshausen Sea, some developments made to improve the accuracy of the model output, and some issues that were overcome in the development stages. Note that from this point onwards throughout the remainder of the thesis, where maps are plotted using a projection, the open-source toolkit m_map (https://www.eoas.ubc.ca/ rich/map.html, (Pawlowicz; 1997)) has been used.

2.1 The MITgcm

The MITgcm is an open-source general circulation model that can be used for both atmosphere and ocean studies at a range of scales. It has a sea ice component (Losch et al.; 2010) and ice shelf model (Losch; 2008) that are described in more detail in Sections 2.6.3 and 2.6.4. It is capable of hydrostatic and non-hydrostatic computations. To make these less computationally intense, the configuration (as described in this section) is run in its hydrostatic mode; De Rydt et al. (2014) have shown that this has little effect on the results even in a much higher resolution simulation.

The MITgcm is based on the Boussinesq Navier-Stokes equations. Equations (2.1)-(2.5) show the incompressible, hydrostatic horizontal and vertical momentum equations (conservation of momentum), the continuity (conservation of mass) equation and governing equations for heat and salt respectively (Marshall et al.; 1997a,b):

$$\frac{D\vec{\mathbf{v}}_h}{Dt} + \left(2\vec{\Omega} \times \vec{\mathbf{v}}\right)_h + \frac{\nabla_h p}{\rho_c} = F_{\vec{\mathbf{v}}_h}, \tag{2.1}$$

$$\frac{\partial p}{\partial z} = -\rho g, \tag{2.2}$$

$$\nabla \cdot \vec{\mathbf{v}} = 0, \tag{2.3}$$

$$\frac{\partial \Theta}{\partial t} = -\nabla \cdot (\mathbf{v}\Theta) + F_\Theta, \tag{2.4}$$

$$\frac{\partial S}{\partial t} = -\nabla \cdot (\mathbf{v}S) + F_S, \tag{2.5}$$

where $\vec{\mathbf{v}}$ is the velocity vector, h relates to horizontal components, $\vec{\Omega}$ is the rotation of the Earth, z is the vertical coordinate, p is pressure, ρ_c is the reference density, and F_n is dissipation and external forces affecting n for $n = \vec{\mathbf{v}}_h$, Θ, and S. Θ and S are potential temperature and salinity respectively. Note passive tracers will be dealt with in Chapter 3.

The equation of state used is that of McDougall et al. (2003) (Figure 2.1), the form of which is shown in Equation (2.6) with density, ρ, being a function of salinity S (psu), potential temperature θ (°C) and pressure p (dbar).

$$\rho(S, \theta, p) = \frac{P_1(S, \theta, p)}{P_2(S, \theta, p)}. \tag{2.6}$$

Here

$$\begin{aligned} P_1(S,\theta,p) =& 9.997 \times 10^2 + 7.352 \times 10^0 \theta - 5.459 \times 10^{-2} \theta^2 + 3.984 \times 10^{-4} \theta^3 \\ &+ 2.969 \times 10^0 S - 7.233 \times 10^{-3} S\theta + 2.124 \times 10^{-3} S^2 + 5.188 \times 10^{-6} pS \\ &+ 1.040 \times 10^{-2} p + 1.040 \times 10^{-7} p\theta^2 - 3.240 \times 10^{-8} p^2 - 1.239 \times 10^{-11} p^2 \theta^2 \end{aligned} \tag{2.7}$$

and

$$\begin{aligned} P_2(S,\theta,p) =& 1.000 + 7.286 \times 10^{-3} \theta - 4.608 \times 10^{-5} \theta^2 + 3.684 \times 10^{-7} \theta^3 + 1.808 \times 10^{-10} \theta^4 \\ &+ 2.147 \times 10^{-3} S - 9.270 \times 10^{-6} S\theta + 4.765 \times 10^{-6} S^{\frac{3}{2}} \\ &- 1.783 \times 10^{-10} S\theta^3 + 1.634 \times 10^{-9} S^{\frac{3}{2}} \theta^2 \\ &+ 5.308 \times 10^{-6} p - 3.032 \times 10^{-16} p^2 \theta^3 - 1.279 \times 10^{-17} p^3 \theta. \end{aligned} \tag{2.8}$$

Note that η is the height of the free surface above the top model cell (z=0). When a surface forcing, G, is applied to the model, the formulation for a free surface, η, for $\eta \ll H$, H being the depth of the water column, is

$$\begin{aligned} G &= \frac{\partial \eta}{\partial t} + \nabla_h \cdot \left(\int_{-H}^{0} \bar{\mathbf{v}}_h \right) dz \\ &= \frac{\partial \eta}{\partial t} + \nabla_h \cdot (H \bar{\mathbf{v}}_h) \end{aligned} \tag{2.9}$$

for a linear free surface, where h is the horizontal direction and v_h is the horizontal velocity (Marshall et al.; 1997a). Here ∇_h is the horizontal divergence. The model uses a real freshwater flux as opposed to a virtual salt flux, meaning that all freshwater inputs relate to a sea level rise rather than just a change to the salt content. The code version used in this study is checkpoint c62r.

2.2 Grid and domain

To investigate the whole Antarctic Peninsula region, the domain has been chosen to extend from the southern ice shelves to the southern tip of Chile, including the Antarctic Circumpolar Current (ACC) in order to allow for shelf break processes to be influenced by general circulation. It ranges from the Abbot Ice Shelf in the west to Joinville Island, the easternmost large island at the tip of the peninsula, to the east. When selecting the location of the boundaries, the resulting number of grid cells in each direction was considered so that it could be easily divided up into smaller tiles for parallel computing. This

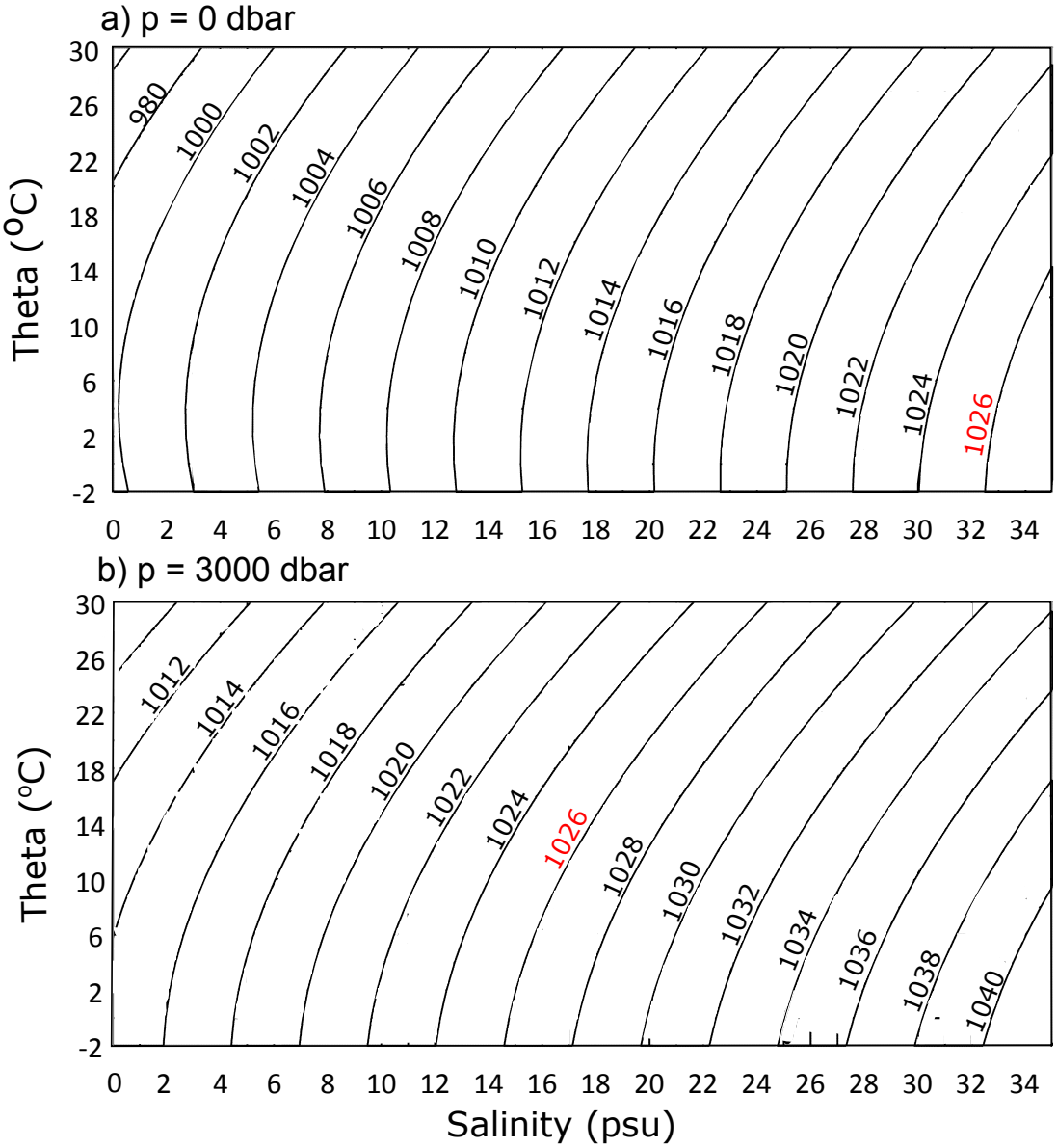

Figure 2.1: Θ-S diagram showing density contours (kg/m^3) calculated from the McDougall et al. (2003) 25-term equation (2.6), shown for a) ρ(S,Θ,0) and b) ρ(S,Θ,3000). Red marker indicates $\rho = 1026\ kg/m^3$ in each plot, to show the variation.

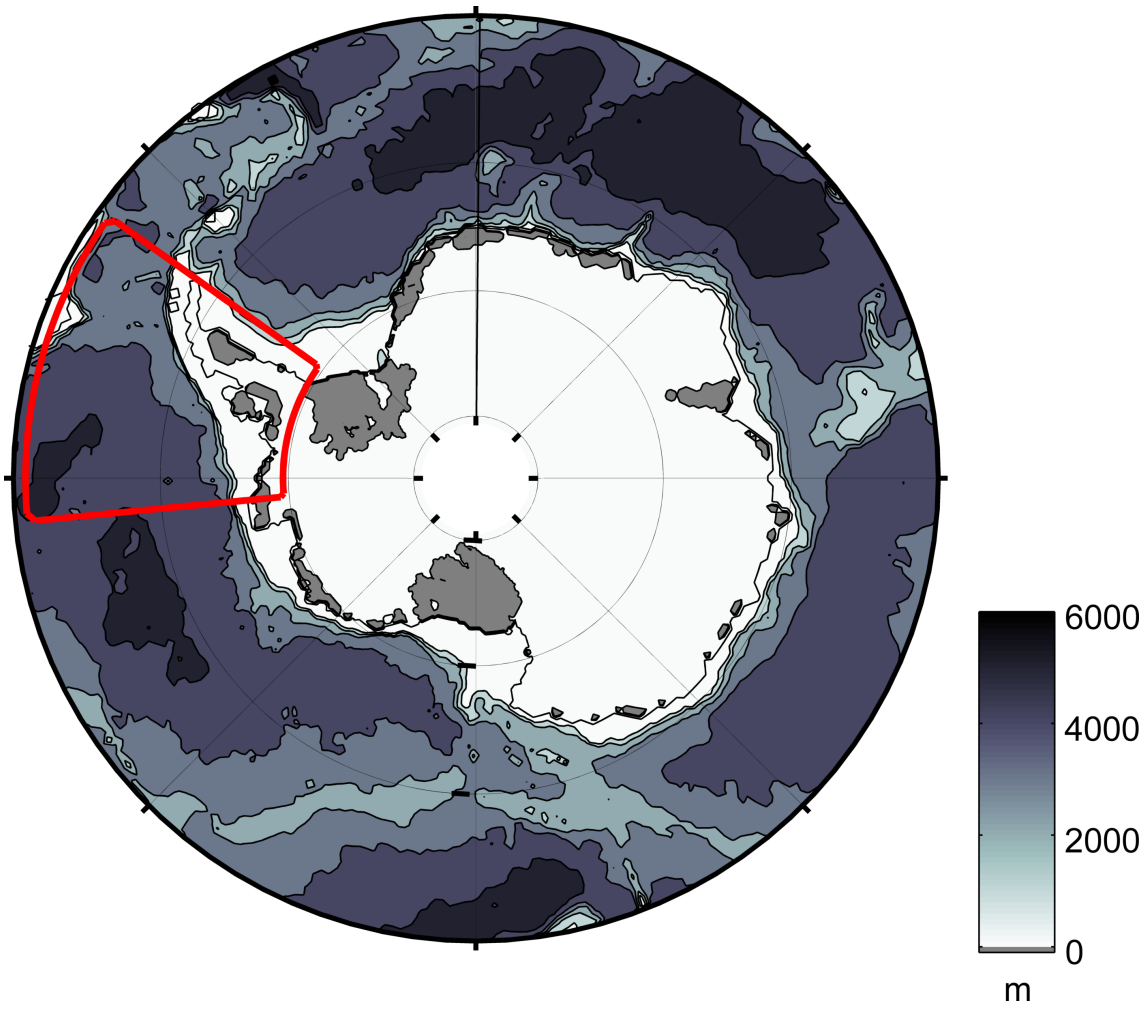

Figure 2.2: Bathymetry of the Southern Ocean. Ice shelves are shown in grey, and model domain is shown in red.

results in it spanning the range (74.4 °S, 265 °W) to (55.0 °S, 304.4 °W) (Figure 2.2). When selecting the location of the eastern boundary, the edge of the grid was chosen to intersect one of the islands at the northeastern tip of the peninsula rather than creating a poorly resolved narrow channel, as this could cause numerical issues. It is noted that the Weddell Sea is outside of the domain, fed only by the eastern boundary and Bransfield Strait which at this resolution only contains a few grid cells in its width, so few conclusions can be drawn from its behaviour.

The model uses a curvilinear grid in the horizontal and a z-level vertical coordinate system (e.g. Losch; 2008) with 50 levels selected. The horizontal resolution has been set to 0.2 degrees longitude, with latitude spacing set to result in square grid cells, resulting in a regular grid spacing of around 5.98 kilometres in the south of the domain and 12.75 kilometres in the north. This resolution is the highest computationally feasible resolution, given that test runs are required, but does not resolve eddies (explored below).

Chassignet et al. (1996) suggest that density-based vertical coordinates are preferable to depth-based coordinate systems, which fail to accurately represent dense water masses over long timescales. Dinniman et al. (2012) instead use a terrain-following vertical coordinate system which allows for investigations at the shelf break as it handles large gradients imposed by the continental slope better than a depth-based coordinate system would. In order to reduce the impact of this issue, depth-based coordinates employ partial cells to resolve sub-grid cell steps. Models usually have closely spaced grids nearer the surface (e.g. Dinniman et al.; 2012; Holland et al.; 2010) to resolve the sharp gradients and increased exchanges occurring at the air-ice-ocean interface. Some models use hybrid grids to resolve different regions, such as the terrain-following shelf and depth-level open ocean setup used by Nakayama et al. (2014a), to optimise accuracy of activity on different scales.

In this setup, the selection of 50 z-levels enables resolving the complex topography without resulting in a large run time. Because the model is used to study freshwater inputs, most of which occur at the surface, the vertical resolution ranges from 10 metres in the first 100 metres and becomes coarser with depth. This spacing is shown in Figure 2.3. To further increase the representation of the vertical structure, both the sea bed and the base of ice shelves have their depth controlled by partial cells at the interface with the ocean (Adcroft et al.; 1997). These are fractions of the raw grid height that can represent intermediate values between the 50 defined levels so that the topography is better represented and large steps in the gradient between two adjacent cells are avoided. The minimum size of these partial cells has been set to 0.25 of the cell thickness at the depth of the interface; this still allows realistic representation without causing numerical problems from the cells becoming too thin.

To justify the choice of the minimum cell fraction, Figure 2.3 shows the sea bed profiles for the minimum partial cell fraction ('hFacMin' = h_f) of 0.1, 0.2, 0.25, 0.5 and 1. At h_f = 0.1 or 0.2, the model crashed due to large velocities within very small cells on the shelf break. At a $h_f = 1$, the deep ocean especially is very step-like and causes some sharper gradients as it is limited to the 50 prescribed depth levels which are over 400 metres apart

at depth. This happens to a lesser extent in shallow regions where vertical spacing is smaller, but there are still flat areas where the profile has been smoothed creating more of a plateau. At $h_f = 0.5$, the sea bed topography is still represented poorly at depth but recreates the profiles of lower h_f more successfully on the shelf. There is little deviation between $h_f = 0.1$, 0.2 and 0.25, providing confidence in the selection of the latter.

2.3 Parameterisations

The baroclinic Rossby radius of deformation (e.g. Chelton et al.; 1998) is

$$R = \frac{c_m}{f} \tag{2.10}$$

where c_m, the phase speed, is

$$c_m = \frac{1}{m\pi} \int_{-H}^{0} N(z) dz. \tag{2.11}$$

Here m is the mode, $f = 2\Omega \sin\theta$ is the Coriolis parameter with $\Omega = 2\pi/86400\ \mathrm{s}^{-1}$ the Earth rotation rate and θ the latitude, H is the water depth and N is the Brunt-Väisälä frequency. Here $N = \sqrt{-\frac{g}{\rho}\frac{\partial \rho}{\partial z}}$, where g is the gravitational constant and ρ is the water density (e.g. Chelton et al.; 1998). This is the length scale which eddies act on, which is small at high latitudes due to its dependence on the Coriolis parameter. Thus a high resolution is required to fully resolve eddies. Equation (2.11) shows that radius is dependent on the depth of the water column, meaning that shelf seas will have a lower Rossby radius of deformation. Inoue (1985) found that a section across Drake Passage had R=17.3 km in the north and 7.7 km in the south, close to the model grid size, suggesting that 0.2° does not fully resolve eddies everywhere. This is highlighted in Figure 2.4, which provides and estimate of the first mode of the Rossby radius for the model domain calculated from long-term mean salinity, temperature and depth, using the GSW toolbox (McDougall and Barker; 2011) and the assumption that N is constant (e.g. Gill; 1982; Nurser and Bacon; 2014).

Given that the north of the domain has a grid spacing of over 12 km, 0.2° is not high enough resolution to resolve eddies. To account for this, the Gent-McWilliams and Redi parameterisation (Redi; 1982; Gent and McWilliams; 1990; Gent et al.; 1995) is used. The implementation of this in MITgcm is described by Gnanadesikan et al. (2006), and uses default parameters, with diffusivity limited to 600 $\mathrm{m}^2\mathrm{s}^{-1}$ and slope-clipping set to a minimum of 0.01 to avoid numerically-unstable gradients, as described by Large et al. (1997).

Vertical mixing processes are dealt with by the nonlocal K-Profile Parameterization (KPP) scheme of Large et al. (1994). Background vertical diffusivity of heat and salt is set to 10^{-5} m^2 s^{-1}. Viscosity terms use the Leith (1996) calculation of eddy viscosity in the horizontal, and a coefficient of 10^{-4} m^2 s^{-1} in the vertical (these appear in the last term of equations 2.4 and 2.5; more information can be found at mitgcm.org). The advection is dealt with by using a 3^{rd} order flux-limited scheme. Higher order (nonlinear) flux limiting

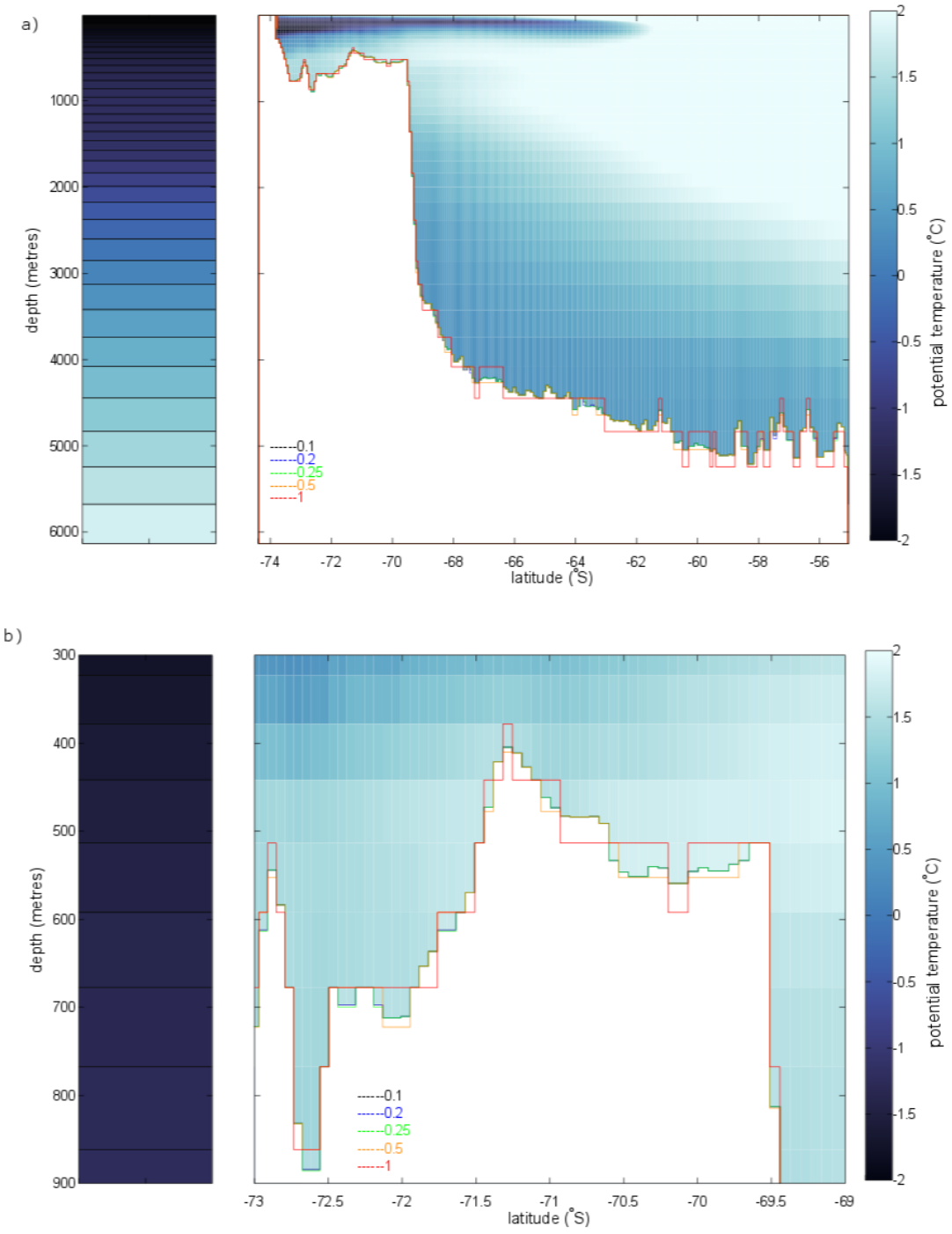

Figure 2.3: Vertical section from south to north through 278 ^{o}W for a) full depth and b) 300 to 900 metres deep from 73°S to 68°S, showing the profile of the sea bed for different values of the minimum partial cell ('hFacMin' = h_f) value. Bars on the left show the vertical grid spacing. Sea bed profiles for $h_f = 0.1$ (black), 0.2 (blue), 0.25 (green), 0.5 (orange) and 1 (red) are overlain onto the January 1979 potential temperature field from the run with $h_f = 0.1$.

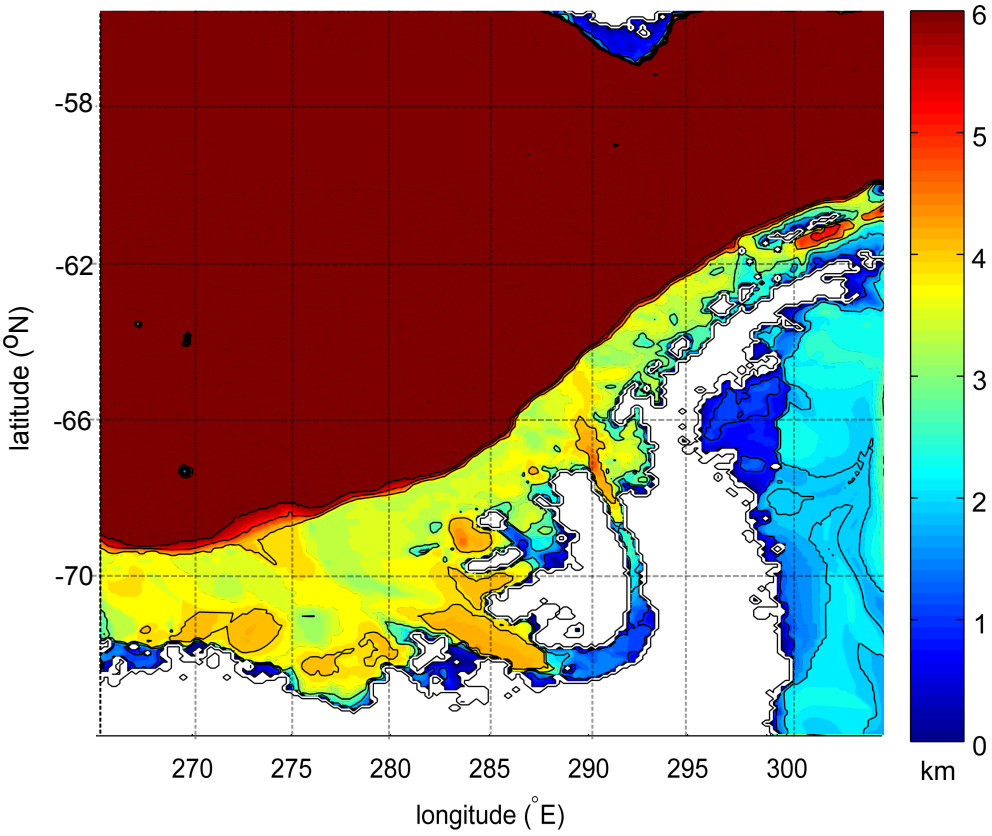

Figure 2.4: Estimate of Mode 1 of the Rossby radius of deformation (in kilometres) for the Bellingshausen Sea region, calculated using long-term mean ocean properties from the model output and the GSW toolbox from McDougall and Barker (2011).

schemes are useful with sea ice as they do not create false extrema or overshoots and they preserve the sharp gradients that often occur with sea ice (Losch et al.; 2010).

2.4 Boundary and initial conditions

Initial conditions for temperature and salinity are taken from the World Ocean Atlas (Boyer et al.; 2009). At the surface, the cold atmosphere and freshwater inputs result in a cool, fresh layer which remains into depth level 15 (162.49 metres) due to a deep mixed layer (e.g. Figure 2.3). By level 20 (323 metres) this is replaced by a warmer, salty layer of CDW. Since measurements in the region are sparse, missing data is interpolated, which can result in errors. Figure 2.5 shows that this has resulted in some cold, salty water being placed under GVIIS from the Weddell Sea. On running the model, this water is lost almost immediately to be replaced by more reasonable values in line with the rest of the shelf at depth, and is comparable to starting with warmer water there, suggesting that the small region of unrealistic values does not affect the run after spin up time. The model is also started with sea ice initial conditions (Figure 2.6), extracted by the same method as the boundary conditions, described below.

All atmospheric variables are provided from the 0.75° resolution version of the ERA Interim reanalyses (Dee et al.; 2011) at 6-hourly intervals. This is a reanalysis dataset produced by the European Centre for Medium-Range Forecasts (ECMWF), and is based on observations taken around the globe which are assimilated into a global model to produce a high-resolution atmospheric dataset. Using a reanalysis such as this allows a consistent group of variables to be applied to the model, at high temporal resolution and reasonable spatial resolution. When selecting this atmospheric reanalyses, tests were carried out with the Regional Atmospheric Climate MOdel (RACMO) and Climate Forecast System Reanalysis (CFSR), two other atmospheric datesets produced by the Royal Netherlands Meteorological Institute (KNMI; at 5.5 km resolution, utilising physics from ECMWF (van Meijgaard et al.; 2008)) and the National Center for Atmospheric Research (NCAR; at approximately 0.3 ° resolution (Saha et al.; 2010)) to identify the most suitable forcing to use when continuing to set up the model. In the early stage of the model configuration when these tests were carried out, ERA-Interim was the only model that did not cause widespread convection to the sea bed that did not recover.

The Bellingshausen Sea model is run from 1979-2014. In order to adjust the initial state to balance the inputs on each boundary (described below), the model requires some "spin-up" time. Some model studies choose to repeat the initial year of time-varying forcing (atmospheric data in this case) a number of times to spin the model up so that all of the years of time-varying data can be used after this. However, implementing this caused the model to deviate too far from realistic conditions and then required more time with realistic forcing to recover. For this reason the model is run with the full time-varying forcing and the first ten years from 1979-1989 are classed as spin up instead and will not be used for results. Figure 2.7 demonstrates that this 10-year period is long enough to

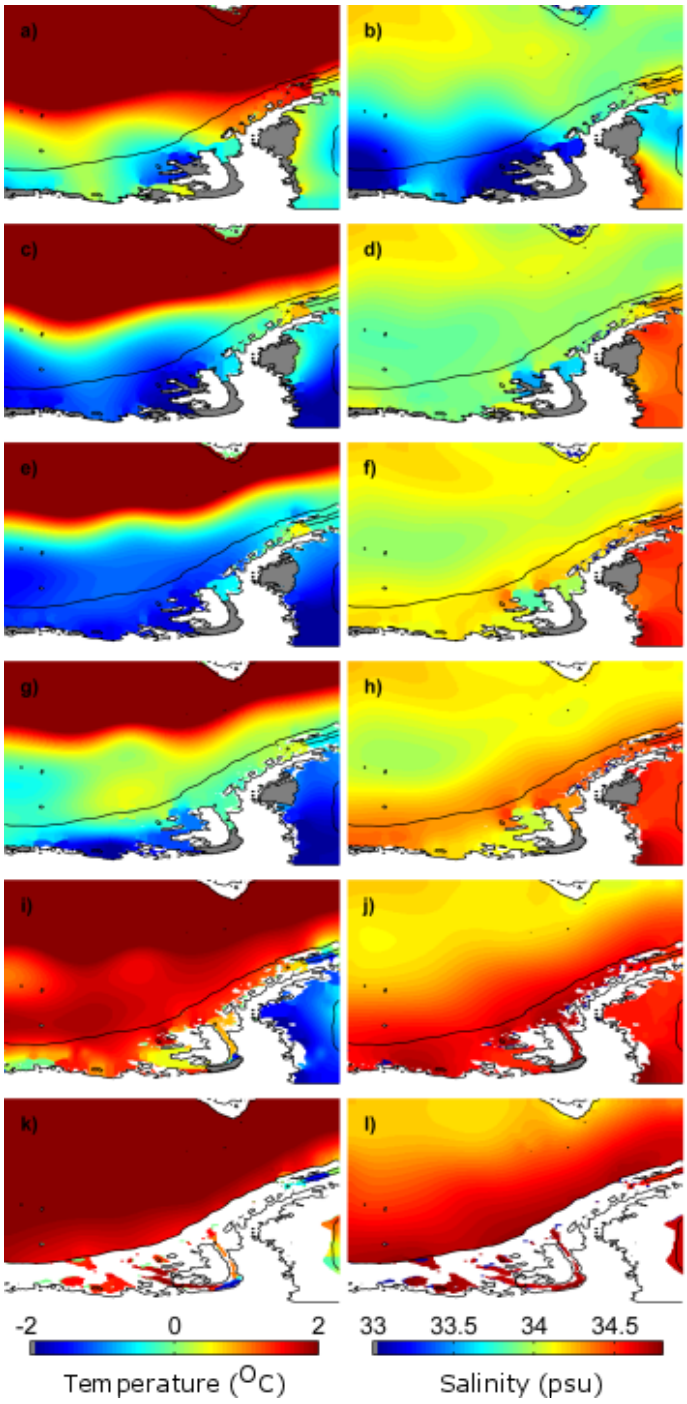

Figure 2.5: Initial conditions for potential temperature (left) and salinity (right) shown for depth levels from the surface to depth level 25, corresponding to (from top) 10 metres, 50 metres, 100.15 metres, 162.49 metres, 323.18 metres and 677.31 metres respectively, covering the majority of the shelf depth. Plotted from model input after being interpolated from World Ocean Atlas data (Boyer et al.; 2009) onto the model grid. White areas indicate land and sea bed, while grey areas show ice shelves.

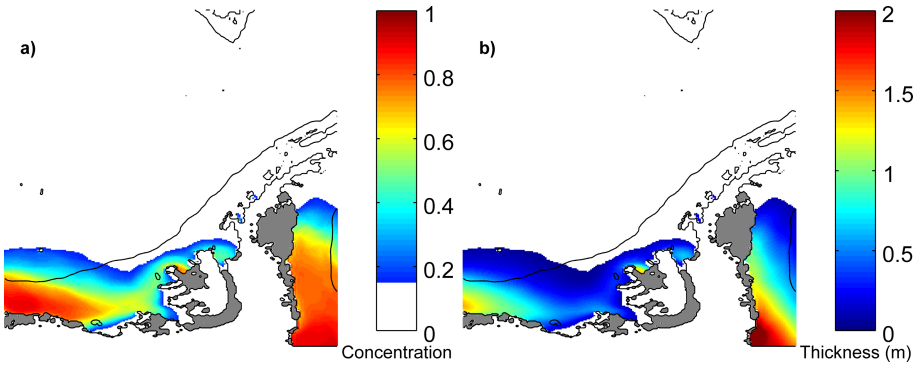

Figure 2.6: Sea ice a) concentration and b) thickness initial conditions for model runs, taken from the average January sea ice fields of Holland *et. al.* (2014) from 1990-1999. Ice shelves are grey and land is shown in white. The shelf break (1000 metre isobath) is shown by a black contour.

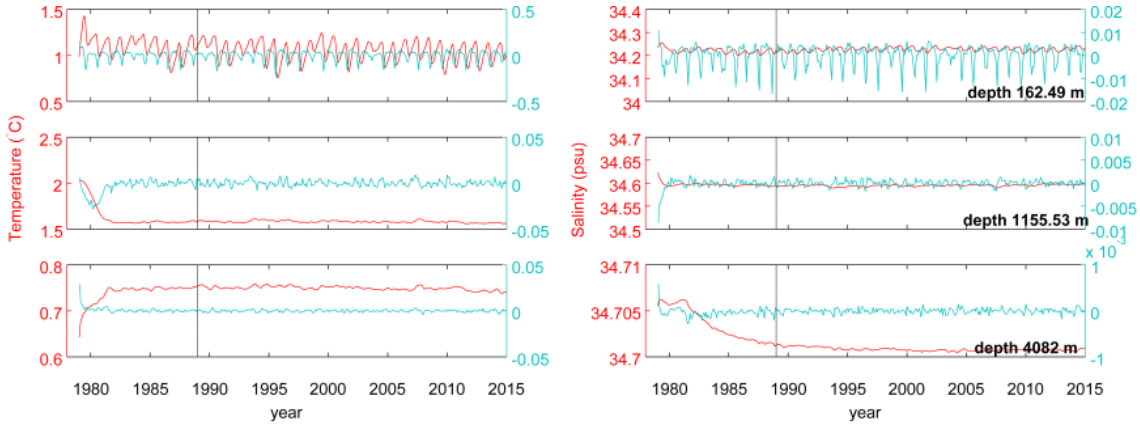

Figure 2.7: Horizontally-averaged temperature (first column) and salinity (second column) shown in red, with the associated difference between each month in blue, for depth levels 15 (top), 30 (second row), and 45 (third row). A vertical line is shown at 1989, before which the results are classed as spin-up time.

allow the temperature and salinity to adjust. After around three years the two fields reach their steady state values at intermediate depths. Shallower profiles have more variation since they have more interaction with the surface at the base of the mixed layer. Near the sea bed in the deep ocean, steady state takes longer to reach, with 4082 metres (level 45) showing a large decline in salinity that only becomes steady (with the time differential fluctuating around zero) in the late 1980s. While these deep areas are found off the shelf, which is of less interest here, it is important to represent them as they link to the ACC and on-shelf flow, and thus selecting 1989 as the start of results as opposed to a shorter spin-up time linked to intermediate depths is suitable.

The Bellingshausen Sea model prescribes open boundary conditions on the western, eastern and northern boundaries, setting the value of temperature, salinity and ocean velocities, along with sea ice area, thickness and velocities. Boundary condi-

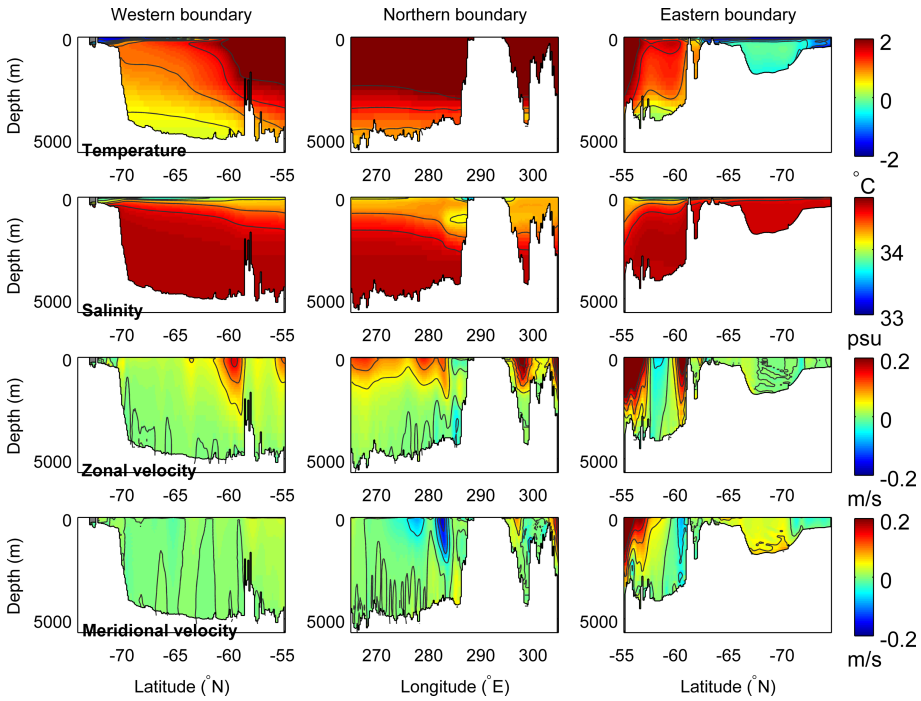

Figure 2.8: Ocean boundary conditions taken from the average annual fields of Holland et al. (2014) from 1990-1999 and interpolated onto the model grid. Shown are (left-right) western, northern and eastern boundary conditions for (top-bottom) temperature, salinity, zonal velocity and meridional velocity.

tions are taken from a 0.25° circumpolar model in MITgcm limited by 30° S and using RTOPO bathymetry (Holland et al.; 2014). Note that the Bellingshausen Sea model uses BEDMAP2 bathymetry (Fretwell et al.; 2013), described later. As such, there is a slight discrepancy between the bathymetry of the two models in addition to the resolution. The nearest latitude/longitudes are found and ocean properties linearly interpolated onto the model grid and bathymetry, averaging monthly output over the range 1990-1999 to obtain climatological monthly boundary conditions. The annual averages of these are shown for ocean properties (Figure 2.8) and sea ice (Figure 2.9; note that these have undergone modifications, described below). Features to note are the strong stratification of temperature and salinity in the south, with isopycnals sloping down away from the shelf further north, and the dominance of the ACC to the north of the domain. Using a circumpolar model such as this to derive boundary conditions allows for the ACC to force the model.

Adjustments needed to be made to some of the boundary conditions due to problems with sea-level rise. Freshwater fluxes from the surface and ice-shelf base are applied as volume fluxes to the ocean, so any net imbalance between these and the boundary conditions causes sea-level to rise or fall. This is resolved by varying the boundary flows very slightly via adjusting the eastern and western velocities to apply uniform convergence or divergence. Because the sea level rise is essentially monotonic on an interannual basis, a number of runs were performed with different adjustments and compared after 1 year to determine the value which resulted in a negligible change in sea level. It was not compu-

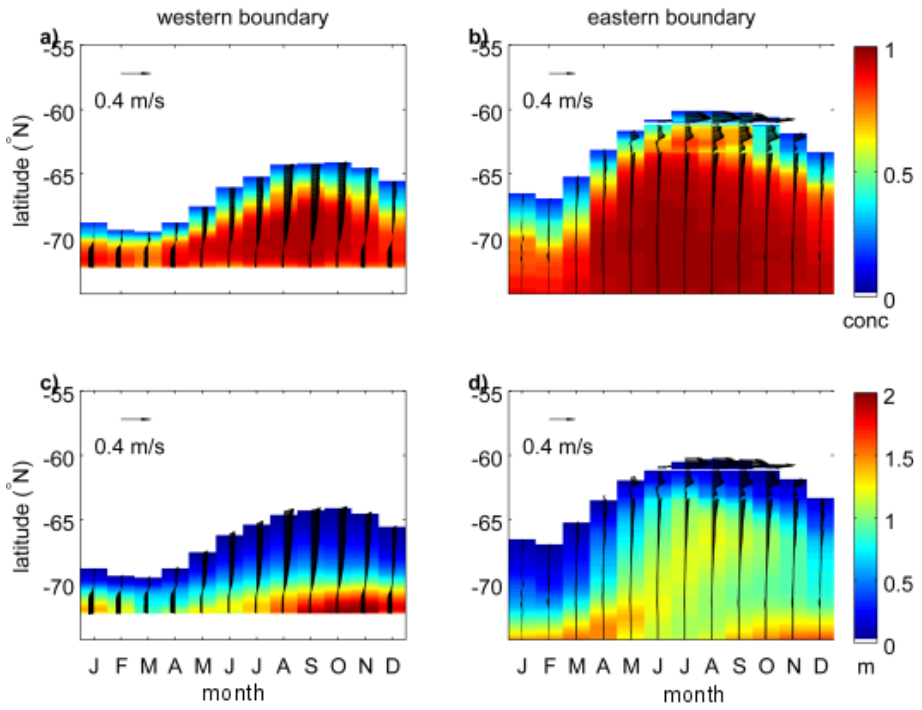

Figure 2.9: Sea ice boundary conditions shown in the form of Hovmöller plots, with cells from south to north on the x axis and months on the y axis. Sea ice concentration (top row) and thickness (bottom row) are overlain with sea ice velocity vectors through the boundary, with the monthly vector components displayed at the base of the row. Positive arrows indicate an eastward flow. Sea ice fields where concentration is less than 15% are masked.

m/s added	raw output: total rise after 12 months (m)	average rise after 12 months (m)
-1 × 10^{-4}	*18.7215*	*9.7381*
-1 × 10^{-5}	*4.459*	*2.3186*
0	*2.8822*	*1.4974*
1 × 10^{-5}	0.4872	0.2619
1.8 × 10^{-5}	0.0121	0.0143
1.9 × 10^{-5}	-0.1453	-0.0681
2 × 10^{-5}	-0.3031	-0.1506
2.5 × 10^{-5}	*-1.0934*	*-0.5635*
3 × 10^{-5}	*-1.8858*	*-0.9745*
1 × 10^{-4}	*-12.9521*	*-6.7367*

Table 2.1: Total adjustments made to the eastern and western zonal velocities in m/s spread out across every model point, the resulting sea level rise after one year, and the average sea level rise over the first year.

tationally feasible to run these simulations for the full 36 years. Large values ($\pm 1 \times 10^{-4}$) were used initially, with intermediate values tested until a sign reversal was seen in the sea level rise after 12 months and the average sea level rise over the first year. The results of this are shown in Table 2.1.

Those model setups which resulted in an monotonically increasing or decreasing average sea level rise over the first year (column 2, Table 2.1), such that the rise exceeded the seasonal cycle, were immediately discounted (shown in italic in Table 2.1); these coincided with those that exceeded a change of 1 metre or more by the end of the year. Values between these were then tested by running the model for 3 years until a low average rise was obtained (noting that this depends on the net flux in, which is not constant with time). The current configuration of the model requires an addition of 1.8651×10^{-5} m/s, resulting in a total sea level rise of 4.7 metres over the simulation. This is reasonable given the long run-time of the simulation.

A sponge layer of 5 grid cells is applied at each boundary so that there is not a sharp gradient between the ocean fields and the boundary conditions. For the velocities, the restoring resulting from the sponge layer relates to a timescale of one day at the boundary and 20 days at the edge of the sponge layer.

The sea ice boundary conditions also required adjustment to allow the model to run for the full 36 years. Using the raw output from interpolation resulted in model instability near the coast on the western boundary, due to convergence and thickening of sea ice. Figure 2.10, showing sea ice fields for the August 1990-1999 average, shows that the chosen location of the boundary is adjacent to a NW-SE coastline where velocities are high in certain months. In particular, the meridional velocity is anomalously high here compared to the rest of the coastline. Additionally, a slight eastward current one cell wide next to the coast is being represented in the interpolation, as shown in Figure 2.11a. This allows for the potential of high velocities immediately by the coast assigned during interpolation,

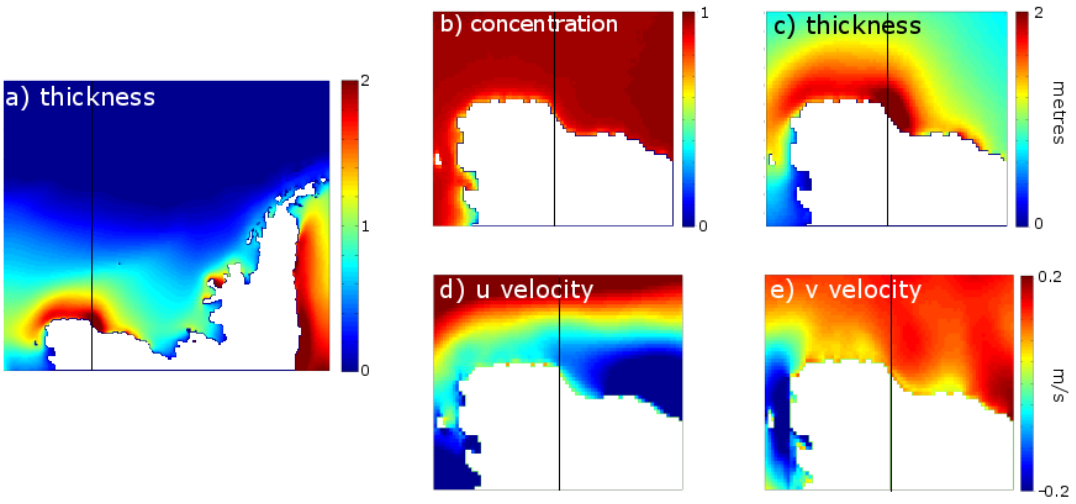

Figure 2.10: a) 1990-1999 August average sea ice thickness from Holland et al. (2014) before interpolation onto the model grid. Vertical line indicates the boundary of the Bellingshausen Sea model, through which interpolation is conducted. Panels b)-e) show a close up of the coastline adjacent to the western boundary in terms of sea ice area, thickness, zonal velocity and meridional velocity respectively. Here a positive value means eastward for zonal velocities and northward for meridional velocities.

which could result in convergence of sea ice due to the misalignment of the coastlines. To resolve this problem, a number of tests were carried out, with the resulting modified boundary condition shown in Figure 2.11b.

To achieve a boundary condition that prevented convergence on the western boundary, the cell-wide sea ice velocity that opposed the ocean velocity was replaced by setting all sea ice velocities south of the maximum westward velocity to that value. A gridcell-wide current would not be resolved and Figure 2.10 demonstrates that it is a very narrow current of low flow trapped by the choice of interpolation location. Additionally, all velocities where sea ice concentration is less than 15% have been masked, as per the usual handling of sea ice data (e.g. Holland et al.; 2010).

While adjustment of the western boundary condition allowed the model to run for longer, it still crashed after a number of years. In the code, there are some testing options which come with the caveat that accuracy on the boundary is less good due to the change in settings. The setting chosen allows the model to proceed with the maximum of the prescribed value on the boundary and the calculated value at the edge of the model domain. This means that if the sea ice velocity is larger than the prescribed value it takes the calculated velocity, therefore avoiding a convergence of sea ice due to boundary conditions that are too restrictive. The results of these experiments are shown in Figure 2.12, with the August zonal velocity map overlain with velocity vectors and an inset showing in detail what happens at the boundary. This option provides the best solution

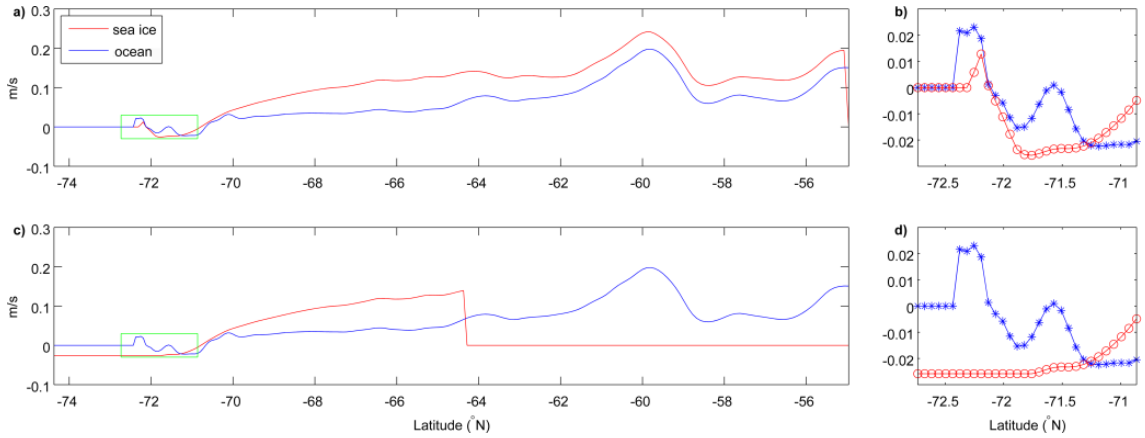

Figure 2.11: Line plots showing the zonal-velocity boundary conditions on the western boundary for the ocean (blue) and sea ice (red) in August, corresponding to the black line in Figure 2.10. a) shows the raw output from Holland et al. (2014), and c) shows the modified sea ice zonal velocity so that convergence problems are avoided. b) and d) show the problem area (green box in a and c) in more detail. The sea ice velocity is set to zero north of -64 N as the climatology shows sea ice less than 15% here.

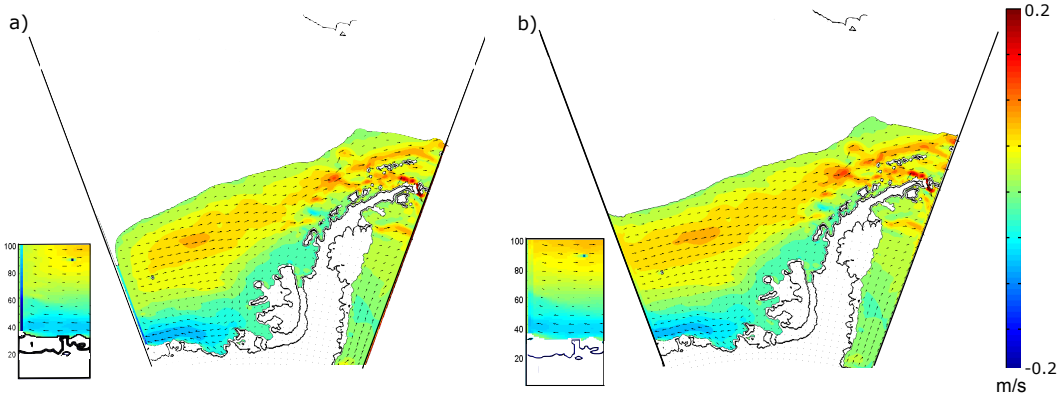

Figure 2.12: August average sea ice zonal velocity with velocity vectors overlaid for the a) non-convergence condition and b) calculated, rather than prescribed sea ice velocities. Insets show in detail the processes occurring at the boundary for each case.

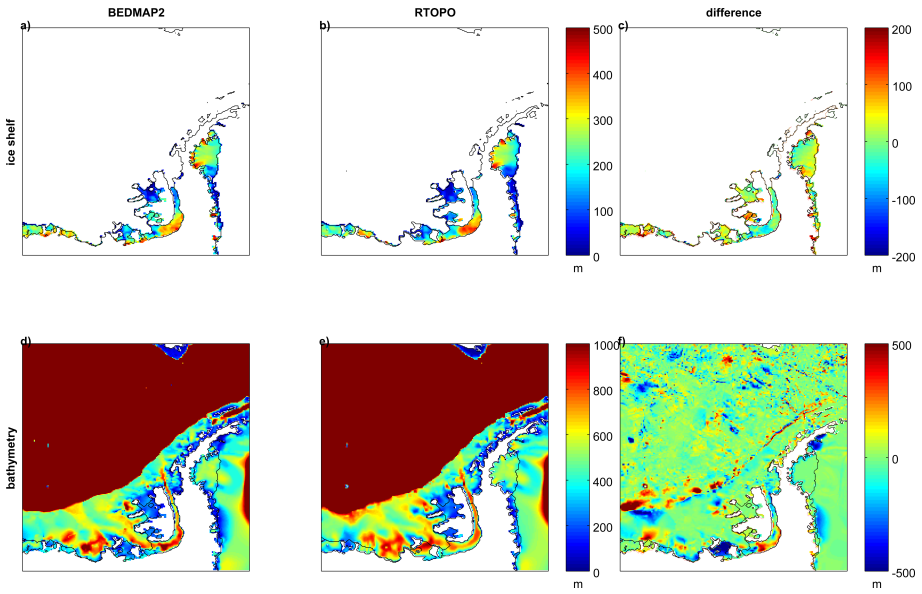

Figure 2.13: Comparison between the different ice shelf thickness (top) and bathymetry (bottom). BEDMAP2 (left), RTOPO (middle) and the difference between each dataset (right) is displayed on the model grid.

(the least modification required to the modelled value) and is used henceforth since it solves the numerical instability and does not result in severely misshaping the extent of the sea ice adjacent to the boundary. The final version of the monthly sea ice boundary conditions are shown in Figure 2.9, with velocity vectors highlighting the effect of the ACC at the northern limit of the sea ice extent and the westward coastal current. The gap during winter in the north of the eastern boundary is an island. Velocities are highest where sea ice extent and thickness is reduced.

No-slip conditions are applied at solid boundaries (the interface of ocean and land), meaning that at the boundary $\mathbf{u}$=0, i.e. there is no flow at the interface. At the interface between the ocean and ice shelves, a free slip condition is applied so that at y boundaries, $\frac{\partial u}{\partial y} = 0$, and at x boundaries, $\frac{\partial v}{\partial x} = 0$, i.e. there is no flow perpendicular to the wall. This is required for when drag coefficients are set.

2.5 Bathymetry

The Bellingshausen Sea model was first set up to use RTOPO bathymetry (Timmermann et al.; 2010). While developing the model, BEDMAP2 (Fretwell et al.; 2013) became available and so this has been implemented in order to have the most up to date bathymetry and sub-ice shelf cavity data available. BEDMAP2 data does not extend beyond 60° S so the northern part of the domain uses GEeneral Bathymetric Chart of the Oceans (GEBCO; www.gebco.net). The comparison between BEDMAP2 and RTOPO is seen for ice shelf thickness (top row) and bathymetry (bottom row) in Figure 2.13. It shows that BEDMAP2 now resolves cavities differently, with a deeper channel through GVIIS and shallower ice shelf cavities under the southern ice shelves, affecting the depth which CDW

can intrude into. The shelf break topography has also changed, with BEDMAP2 being steeper than RTOPO.

When the ice shelf profile was developed for the model grid from BEDMAP2, some ice shelves were being interpolated with very low thicknesses, smaller than the top grid cell of 10 metres. This resulted in very large sea level increases adjacent to these regions, causing numerical instability. Since this is an artefact of the interpolation method, any ice shelf thinner than one grid cell (10 metres) was removed from the field.

2.6 Freshwater inputs

The model is being used to study freshwater in the ocean, and therefore the freshwater inputs must be as realistic as possible. The methods of dealing with precipitation, evaporation, iceberg melt, ice front melt, surface melt, sea ice and ice shelf melt are explained below, along with adjustments carried out to improve their accuracy.

2.6.1 Precipitation and Evaporation

As mentioned in section 2.4, the model is run with ERA Interim reanalyses (Dee et al.; 2011). This results in the fields of atmospheric temperature at 2 metres, precipitation, zonal and meridional wind velocity at 10 metres, specific humidity at 2 metres, and long and short wave radiation being input to the model. As such, precipitation is input directly into the model, while evaporation E is calculated from the formulae in Large et al. (1994) so that

$$E = -\frac{1}{\rho_f}\tau q^* \tag{2.12}$$

where ρ_f is the density of freshwater. τ is calculated from input wind stress so that

$$\tau = -\rho < uw > \tag{2.13}$$

where ρ is the mean air density. Here

$$- < uw >= C_d W_s^2 \tag{2.14}$$

where C_d is the drag coefficient and W_s is the 10-m wind speed. This can be used to rearrange the equation for the friction velocity, u^*, where

$$u^* = (\tau/\rho)^{\frac{1}{2}} = | < uw > |^{\frac{1}{2}} \tag{2.15}$$

to express τ as

$$\tau = \rho(u^*)^2 = \rho C_d W_s^2. \tag{2.16}$$

q^* is calculated from the equations in Large and Pond (1982) and 2.15 such that

$$q^* = -\frac{< wq >}{u^*} = -\frac{C_e(q_s - q_a)}{\sqrt{(C_d)}} \tag{2.17}$$

where C_e is the Dalton number, q_s is the specific humidity at the surface, and q_a is the absolute humidity. The sea ice model handles separation of liquid and solid precipitation, by defining it as snow if the heat flux falls below zero.

2.6.2 Runoff - iceberg, ice shelf front and ice shelf surface melt

Surface melt of land-based ice, oceanic melting of ice cliffs, and iceberg calving/melting are not explicitly modelled in MITgcm and are instead collectively accounted for by a prescribed 'surface runoff' field. Note that freshwater should be input at depth, and latent heat of melting extracted also, but neither effect is included here. Liquid glacier-surface runoff is negligible (van Wessem et al.; 2016b), and ocean melting at the front of glaciers is taken to be small compared with the calving and subsequent melt of icebergs. Therefore these terms are collectively referred to as iceberg melt, though a fraction may come from ice front melting.

There are little data available to guide the choice of the prescribed iceberg melt, so assumptions are made about the amount. The model has been run with two such fields: Figure 2.14a shows 157.95 Gt/yr distributed uniformly around the coast, equivalent to 1000 Gt/yr of freshwater around the whole of Antarctica. Figure 2.14b shows an updated field of 130.50 Gt/yr taken from the amount of glacial discharge from the north of the peninsula found by van Wessem et al. (2016b). There is some evidence to suggest that the freshwater contribution from iceberg melt is localised (Gladstone et al.; 2001; Marsh et al.; 2015), with no strong advection of icebergs into or out of the region (Tournadre et al.; 2015; Merino et al.; 2016), meaning that iceberg melt is concentrated close to the southern coastline of the region, hence justifying an increase near the coast. In the absence of other data, the value from van Wessem et al. (2016b) is distributed around the coast uniformly, and linearly decreasing away from the coast to a limit of 100 km, thought to be the limit of freshwater runoff (van Wessem et al.; 2016b; Dierssen et al.; 2002). Both fields are temporally uniform. Sensitivity studies carried out in Chapter 4.5 test the chosen field.

2.6.3 Sea ice

The sea ice model used in MITgcm is a thermodynamic and dynamic sea ice model on an Arakawa C-grid, the same grid used by the MITgcm ocean component (Losch et al.; 2010). The elastic-viscous-plastic solver is used for ice dynamics, simulating a viscous-plastic rheology with an extra term to reduce computational cost (Kimmritz et al.; 2015). The thermodynamic component uses the 2-category model of Hibler (1980) to produce ice thickness and concentration. This employs the simple zero-layer thermodynamic ice model of Semtner (1976), which assumes that the temperature within the ice and snow follows a linear profile and ignores heat storage. The same setup was successfully employed to study sea ice trends (Holland et al.; 2014), giving confidence that the method is suitable. Snow flooding is also included, whereby snow that is depressed below sea level is flooded and converted to ice.

2.6.4 Ice shelf melt

The ice shelf model in MITgcm is a thermodynamic model with static pressure loading, developed by Losch (2008). It behaves in much the same way as interaction with the

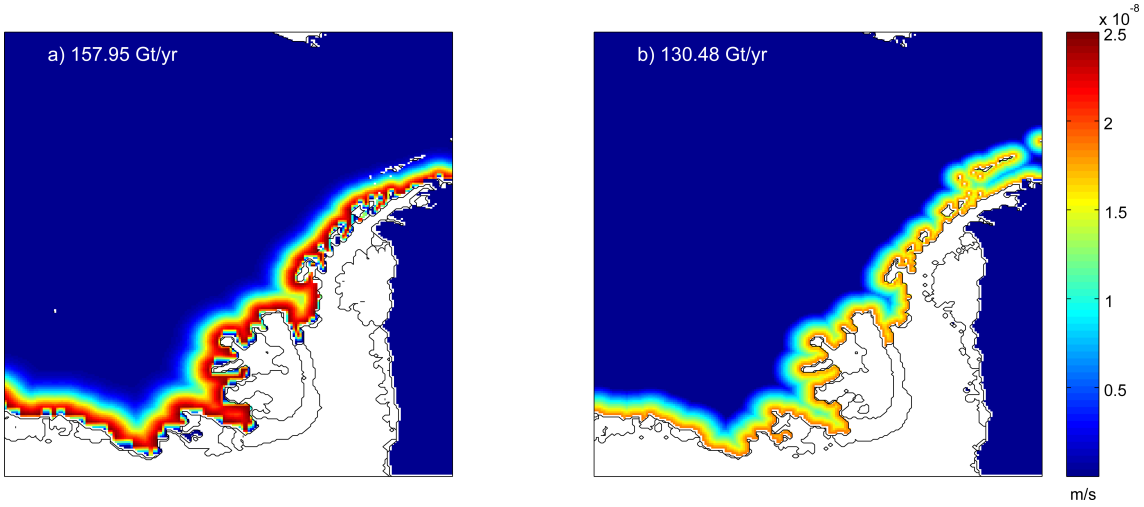

Figure 2.14: a) Old model runoff totalling 1000 Gt/yr spread uniformly around Antarctica with a characteristic distance as a half Gaussian distribution away from the coast, with the Weddell Sea section removed, showing it is equivalent to 157.95 Gt/yr in the Bellingshausen Sea. b) shows the new total calculated by van Wessem et al. (2016b), spread uniformly around the coast with a linear distribution decreasing away from the coast out to 100 kilometres.

sea bed in its treatment of topography, and requires input of ice shelf topography and a reference pressure load, both derived for this model from the BEDMAP2 products (Fretwell et al.; 2013). Basal melting/freezing, m (m/s), is based on solving the heat and salt balance equations described in Losch (2008), along with the freezing temperature of sea water shown in Holland and Jenkins (1999). These are based on the parameterization of the ice shelf-ocean boundary layer by Hellmer and Olbers (1989) and modifications of Jenkins et al. (2001), which are detailed in De Rydt et al. (2014):

$$\rho_O c_O \gamma_T (T - T_b) = m \rho_O L + \rho_I c_I \kappa_I \left(\frac{T_b - T_I}{H_I}\right), \tag{2.18}$$

$$\gamma_S (S - S_b) = -S_b m, \tag{2.19}$$

$$T_b = A S_b + B + C p_b. \tag{2.20}$$

Here ρ_O = 999.8 kg m^{-3} and ρ_I = 917 kg m^{-3} are the density of the ocean and the ice shelf respectively, c_O= 3994 J kg^{-1} K^{-1} and c_I = 2000 J kg^{-1}K^{-1} are the heat capacity of the sea water and ice shelf, κ =1.54$\times$10^{-6} m^2 s^{-1} is the heat diffusivity through the ice shelf, L =3.34$\times$10^5 $J\ kg^{-1}$ is the latent heat of fusion, H_I is the ice shelf draft and T_S = -20°C is surface temperature of the ice shelf. The freezing equation coefficients are set to A = -0.0575°C psu^{-1}, B = 0.0901°C and C = -7.61 $\times$ 10^{-4} °C Pa^{-1} (Holland and Jenkins; 1999). The variables T and S are the temperature and salinity of the ocean, T_I is the temperature of the ice shelf, and T_b, S_b and p_b are temperature, salinity and pressure at the interface of the ice shelf and ocean. Equations (2.18) and (2.19) are conservation equations and represent the turbulent transfer of heat and salt across the

boundary between the ocean and the ice shelf, and are functions of the heat/salt release resulting from melting. Once the melt rate has been calculated it is applied as a real freshwater flux, as for the other freshwater fluxes. Since vertical diffusivity of temperature through the ice cannot be assumed negligible like for salinity (Jenkins et al.; 2001), a second term describing the vertical diffusivity is also present in (2.18). Equation (2.20) constrains the temperature at the interface to be the freezing point and is therefore a function of the salinity at the boundary and the pressure exerted from above (Jenkins et al.; 2001).

In the c62r setup, the heat and salt exchange coefficients are set to $\gamma_T = 1 \times 10^{-4}$ m s^{-1} and $\gamma_S = 5.05 \times 10^{-3}\gamma_T$. These constant γ exchange coefficients mean that the heat and salt fluxes are only dependent on temperature, salinity and pressure. This is a very limiting assumption as it assumes a fixed turbulence at the interface, and therefore implicitly defines a fixed velocity, which is unrealistic. As such, this resulted in far too high melt rates - for example, the GVIIS melt rate after 10 years was 14.8 m/yr, much higher than the 3-5 m/yr suggested by Jenkins and Jacobs (2008).

To achieve more realistic ice shelf melt rates, the ice shelf melt component of the code was developed in line with De Rydt et al. (2014) so that the melting is dependent on both thermal driving and velocity via non-constant γ, where

$$\gamma_{T,S} = \frac{u_*}{\Gamma_{Turb}(u_*) + \Gamma_{Mole}^{T,S}}. \tag{2.21}$$

Here the friction velocity, $u_* = \sqrt{c_d u_o^2}$, is dependent on the dimensionless drag parameter $c_d = 0.0015$ in the default case and u_o is the ocean velocity adjacent to the base of the ice shelf. Γ terms describe the turbulent and molecular transfer parameters and are further described in Holland and Jenkins (1999). This development served to bring down the melt rates significantly to an average of 5.13 m/yr for George VI before tuning, but a side effect of reducing the freshwater content resulted in convection problems described in section 2.7. Tuning down of c_d to 0.001 was required in conjunction with testing other parameters in order to keep the ice shelf melt low while increasing stratification.

In the Bellingshausen Sea setup, the implementation of a boundary layer at the ice-ocean interface is not used. This is because it is incompatible with using a real freshwater flux input to the ocean. When calculating transfer of heat and salt at the ice-ocean interface, a boundary layer implementation uses the grid cells both directly below and one deeper than the ice shelf, with the depth extent limited by the partial cell height above. This means that small partial cells do not limit the effect on the ocean, as their vertical reach is extended into the cell below the interface. However, given that ice shelves are at depth, they experience coarser vertical spacing and therefore small partial cells should not have an adverse affect on the modelled melting.

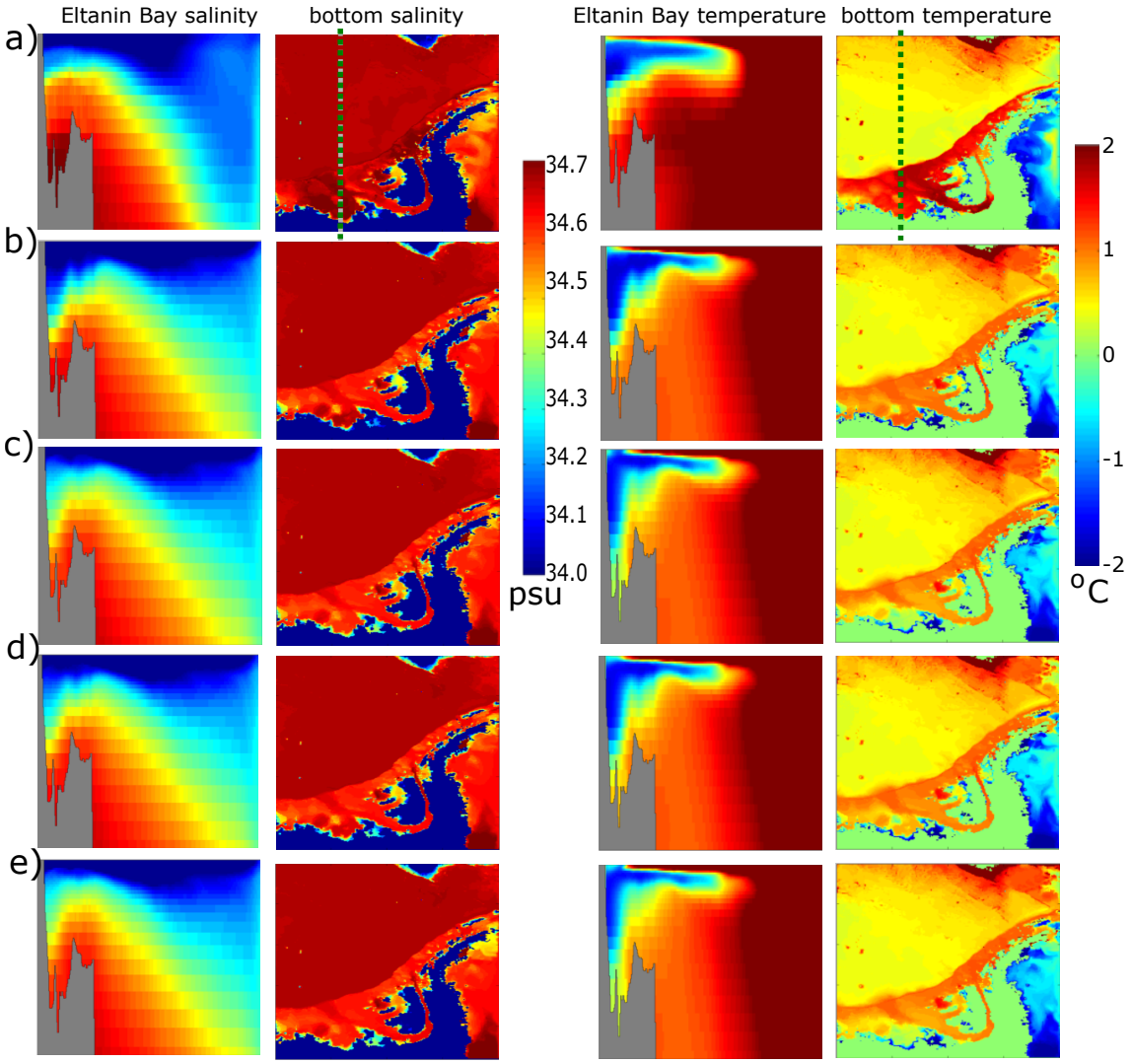

Figure 2.15: (l-r) Salinity section through Eltanin Bay, bottom salinity, temperature section through Eltanin Bay and bottom temperature for various model runs. Vertical line indicates the location of the section. a) and b) show the original model, after 1 month and 37 months respectively. c) shows the effect of the new code with ice shelf melting now dependent on velocity at the ice-ocean interface at month 37. Remaining plots in this figure and the next are based on this code. d) shows the result of increased ice shelf drag coefficient (0.005 instead of 0.001) and e) shows a doubling of the magnitude of the prescribed runoff, both at month 37. Other tests are shown in the next figure.

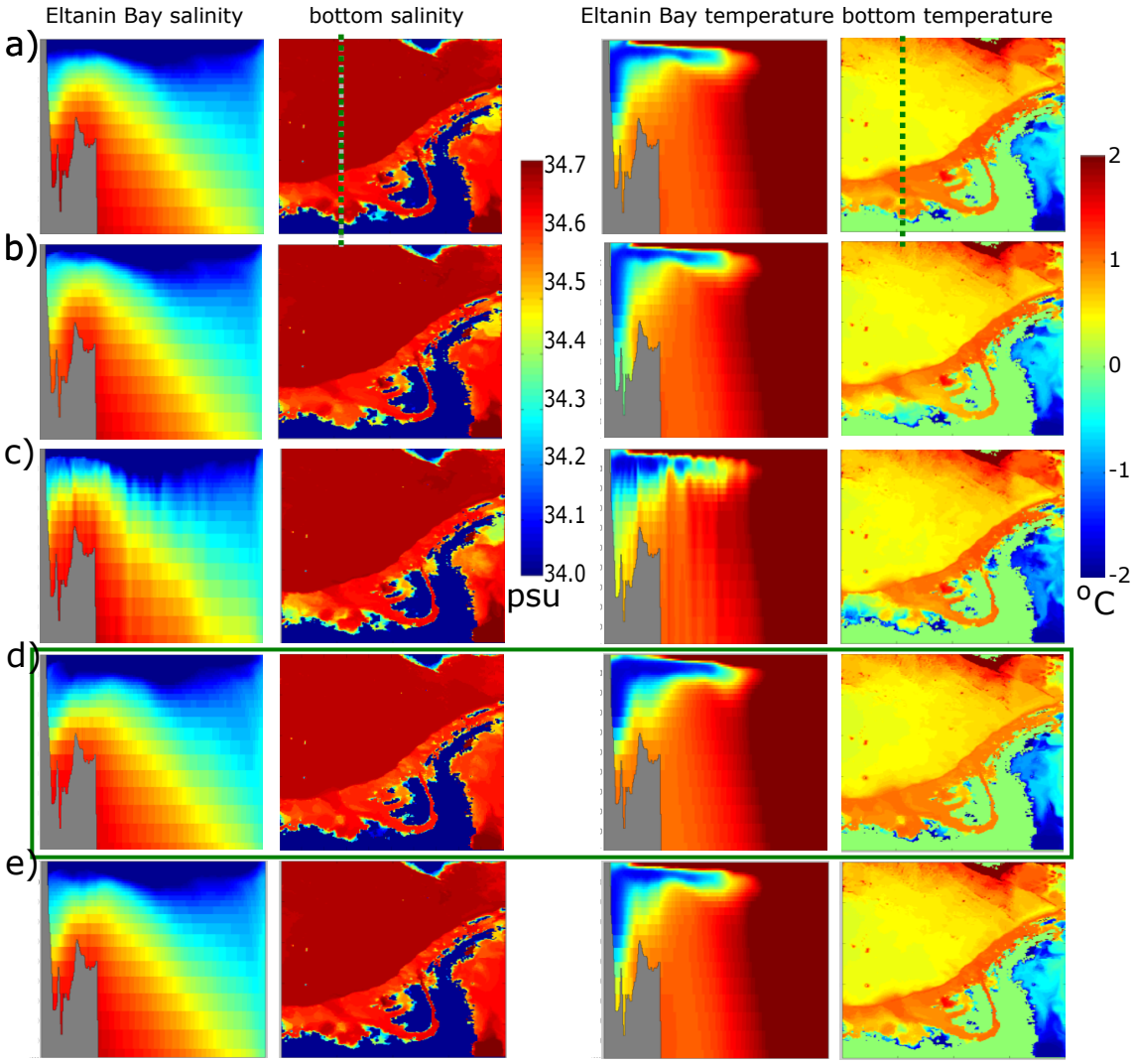

Figure 2.16: (l-r) Salinity section through Eltanin Bay, bottom salinity, temperature section through Eltanin Bay and bottom temperature for various model runs, following on from Figure 2.15. Vertical line indicates the location of the section. Rows show the result of a) a quadrupling of runoff, b) 10x less vertical mixing (from 10^{-5} to 10^{-6}), c) Gent-McWilliams parameterisation turned off, d) sea ice drag coefficient reduced by a factor of 3, and e) initial conditions of sea ice thickness set to equal one anywhere that the area is > 0.001. The chosen simulation is highlighted in green.

2.7 Convection problems

It was discovered that different ice shelf melt rates resulted in non-local effects on the stratification of the Bellingshausen Sea, specifically in the Eltanin Bay region of the domain. This happens during the spinup phase over the course of the first few winters. A similar phenomenon was found by Holland et al. (2010), who suggested wintertime polynyas were destabilising the water column. This is an issue because the cold, brine-enhanced water is convected to the sea bed, and because it is much denser than the rest of the water column it remains there, thus deepening the mixed layer too much and affecting the water column structure for the remainder of the model run. While dense bottom water is formed around Antarctica, it is not thought to occur here. Figure 2.15 shows vertical sections through Eltanin Bay after 37 months from the original b) c62r ice shelf code, and c) the updated code where the melt rate depends on velocity, which served to reduce the melt rates, tuned to simulate realistic melt rates for George VI Ice Shelf. Note that salinity and temperature are shown, as opposed to density, to demonstrate the decoupling between the two fields when the convection occurs. Additionally, it highlights the fact that temperature indicates the issue the most despite salinity variations on the shelf generally being greater; this is particularly true in test cases where freshwater fluxes are enhanced.

Figure 2.15 shows that at month 1 (a), Eltanin Bay is salty and warm, indicating the presence of CDW. By month 37 (b), the mixed layer has deepened but still retains stratification. However, after 37 months with the new code (c) the water at the sea bed along the southern ice shelves has become colder and this cold water has reached the sea bed, suggesting unrealistic convection. Saline deep water has also been lost. Due to the reduced freshwater input, the vertical salinity gradient is weaker, allowing for convection and initiating overturning. To resolve this issue, a number of experiments were run to diagnose the cause more specifically, comparing January outputs after three years. These investigations are based on the findings of Kjellsson et al. (2015) and Holland et al. (2010).

Figure 2.15d shows the result of an increase in the ice shelf drag coefficient from 0.001 to 0.005. The motivation for this was to attempt to increase the ice shelf melting to try to recreate the oceanographic conditions of Figure 2.15a, so that stratification returns. While it does result in some stratification, the mixed layer by the coast is still too deep, suggesting that increasing ice shelf melt does not have a simple relationship in terms of its feedbacks. Additionally, the resulting melt rate is over double the upper bound found by Jenkins and Jacobs (2008).

One method often adopted is to increase the runoff field, justified by the fact that it is poorly understood. Doubling the runoff field (Figure 2.15e) does not provide enough surface freshwater to enhance stratification sufficiently, resulting in a regime like Figure 2.15c, while quadrupling the runoff field (Figure 2.16a) manages to maintain warm water at depth. While changing the input by this much is unrealistic, especially in a study that aims to simulate freshwater successfully, it demonstrates the forcing required to enable a stratified system.

Figure 2.16b reduces the background vertical mixing by a factor of 10, to 10^{-6} m^2

s^{-1}. However, due to the weaker salinity gradient the convection is still able to occur, and large areas of the seabed are flooded with cold water. Figure 2.16c instead tests the effect of turning the Gent-McWilliams (GM) parameterisation of eddies off; since some areas are at the limit of eddy resolving (Figure 2.4), some will not require the use of GM, and therefore it may be that the eddies being parameterised are having an adverse effect here. However, the result is both convecting and in an irregular, non-smooth stratification. The cold water extends further on the southern part of the shelf too, suggesting that GM should remain on.

The last tests that were carried out are related to sea ice. The motivation for exploring this is that sea ice seasonal variation can have a significant effect on the stratification of the water column, both in terms of enhancing freshwater at the surface and deepening the mixed layer in winter. Additionally, Holland et al. (2010) found wintertime polynyas to be a problem in the region where convection occurs. Figure 2.16d shows the effect of reducing the drag coefficient between the sea ice and the air (suggested by Holland et al. (2010)) by 2/3, and Figure 2.16e shows the result of setting initial sea ice thickness and concentration to 1 metre/100% everywhere that sea ice area > 0.001 (small enough to include all sea ice coverage, but large enough to remove artefacts of numerical errors in the north). While Figure 2.16e shows some convection, though to a lesser extent than before, the conditions in Figure 2.16d prevent it from happening and recreates a similar density structure to Figure 2.15b.

Table 2.2: Table showing average GVIIS melt rates at month 37 for each test case for solving the problem of excessive convection in Eltanin Bay.

Figure	melt rate (m/y)
2.15a	27.44
2.15b	15.67
2.15c	5.67
2.15d	10.18
2.15e	2.87
2.16a	2.94
2.16b	2.91
2.16c	4.18
2.16d	6.25
2.16e	6.01

The original run, Figure 2.15a, is not suitable since its ice shelf melting calculation only depends on temperature, so melting is far too high. Accordingly, a run is required that uses the new code without convecting and also has low melt rates. Table 2.2 shows the GVIIS melt rates for each case. The only run that satisfied the former without compromising the latter was reducing the air-sea ice drag coefficient (Figure 2.16d). Additionally, it does not change the freshwater inputs, which should be avoided if the results of freshwater investigations are to be believed, so this model run is taken forward and tuned for ice shelf

melt (noting that the ice shelf melt values in Table 2.2 are still within the spinup period and therefore will change, although previous model runs suggest 3 years is sufficient for finding the general magnitude).

2.8 Summary

This chapter demonstrates that a high resolution model of the Bellingshausen Sea has been created with realistic inputs and a setup that runs for the full time period of atmospheric forcing (at the time of creation). Chapter 1 identified a need to look in detail at the behaviour of individual freshwater sources, and whilst the model is capable of looking at input fluxes it cannot identify their fate from the salinity field alone. The next chapter will focus on addressing this problem.

Chapter 3

Model Development

The Bellingshausen Sea model described in Chapter 2 can give an overview of the oceanography of the region and the standard model output is able to provide information on total freshwater flux, ice shelf melt flux, and atmospheric inputs along with the resultant salinity. However, whilst the knowledge of different freshwater fluxes is useful, the spatial and temporal effects of their variation cannot be deduced as their evolution is not known once they enter the ocean. This chapter focuses on exploration, development and testing of a method to identify each source of freshwater and trace it upon entering the ocean, which allows the model to provide new insights into the freshwater distribution in the Bellingshausen Sea.

3.1 Definition of freshwater inputs

The standard model can produce output of total freshwater flux (F_T), the total surface freshwater flux, as well as the modelled ice shelf flux (F_{ISM}) and atmospheric inputs (calculated evaporation F_E, input precipitation F_P, and prescribed runoff F_R). However, the latter do not account for land or sea ice area, and therefore do not directly correspond to the amount of freshwater the Bellingshausen Sea receives. As a first step in the model development, diagnostics for these have been defined after the atmospheric variables have passed through the sea ice model to account for this, which essentially mask land as zeros and account for nonzero sea ice concentration in each grid cell.

One of the main model developments carried out is based around the fact that there is no way to directly output sea ice flux from the model. This is problematic when trying to determine what contributes to the total freshwater flux, as simply subtracting the atmospheric inputs from the total surface freshwater flux would include surface sea ice processes that may not reach the ocean. It would also make the sea ice flux definition susceptible to change and inconsistencies if the definition were to be transferred to a new version of the model where additional processes were included in the sea ice formation code. A schematic describing the chosen definition of sea ice melt (F_{SM}) is shown in Figure 3.1 (sign convention here is positive downwards, so that an increase in a field results in an increase in freshwater).

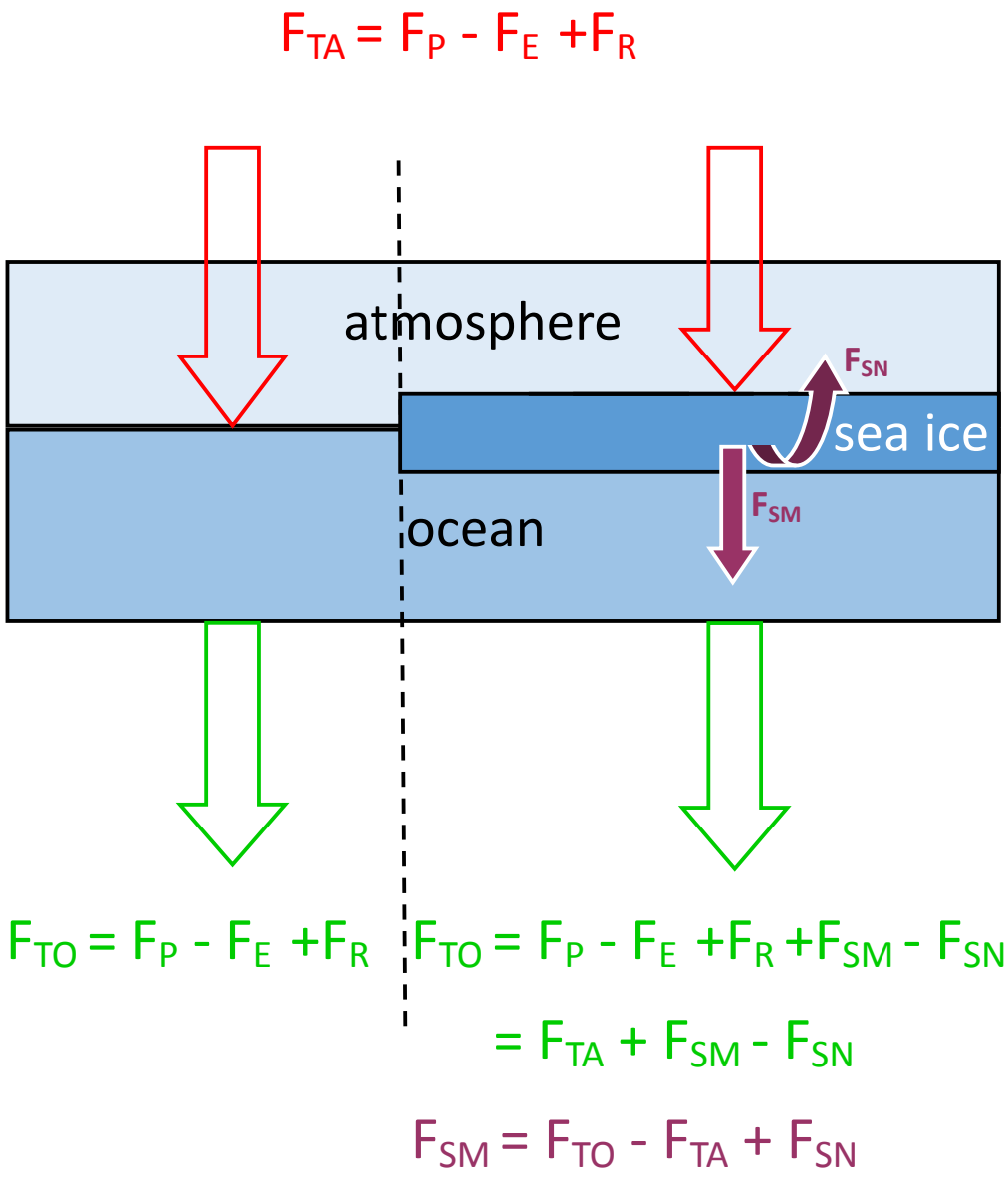

Figure 3.1: Schematic of the evolution of total freshwater flux in the model, from atmospheric inputs to including sea ice freshwater, and the resulting sea ice freshwater flux that can be derived from the known other fluxes.

The schematic shows the pathway of the total freshwater flux from the atmosphere, F_{TA}, through the sea ice model depending on when it interacts with sea ice (right) or not (left), and how this transfers into the total surface freshwater flux to the ocean, F_{TO}. If no sea ice is present, $F_{TO} = F_P - F_E + F_R$. If sea ice is present, the total freshwater flux from sea ice to the ocean, F_{SM}, is present, so that

$$F_{TO} = F_{TA} + F_{SM} - F_{SN} \tag{3.1}$$

where F_{SN} is precipitation that turns to snow on the sea ice surface and therefore does not affect the ocean freshwater content. The resulting sea ice flux is

$$F_{SM} = F_{TO} - F_{TA} + F_{SN}. \tag{3.2}$$

This calculation utilises current diagnostics in the *SEAICE* package of MITgcm, which calculates sea ice properties as well as taking atmospheric and ocean variables and modifying them according to the sea ice model, and is therefore more robust than manually selecting from the multitude of processes occurring in the sea ice model. A similar method to deduce sea ice freshwater flux has been used by Abernathey et al. (2016).

3.2 Development of ISOMIP test model

For the remainder of this chapter, frequent reference will be made to a test model based on a standard MITgcm setup called the Ice Shelf Ocean Model Intercomparison Project (ISOMIP), and developed according to the changes noted in this chapter. The configuration is a simple box with an ice shelf, as shown in Figure 3.2. It is a small model, covering 100 × 50 grid cells in the horizontal, (Δx=0.3°, Δy=0.1°) and 30 in the vertical, each of 30 metres high. As it is a simple design with a short run time, with ice shelf capability but no additional forcing, it is ideal for testing code changes relating to freshwater. In order to allow this testing, part of the ice shelf was removed to enable exposure to surface freshwater fluxes. In the simplest case, the model was run with only uniform surface forcing (in the form of runoff) in order to create a scenario where no advection or diffusion took place laterally (the freshwater stratifies the ocean, which remains stagnant). This allows direct comparison with an analytical solution. Figure 3.3 shows that adding 1 metre per day of freshwater to the model for 10 days to a grid cell results in a sea level rise of 10 metres in that grid cell (note that the model output is snapshots half way through each day). This demonstrates that the model has no lateral variability and so, with a known flux, its behaviour can be predicted. It is therefore suitable for testing addition of freshwater at the surface during development of tracers. In each of the following test plots, an individual location (x,y,z)=(20,20,1) (z numbered from the surface down) in the model is shown, along with predicted amounts from calculations based on additional code developments.

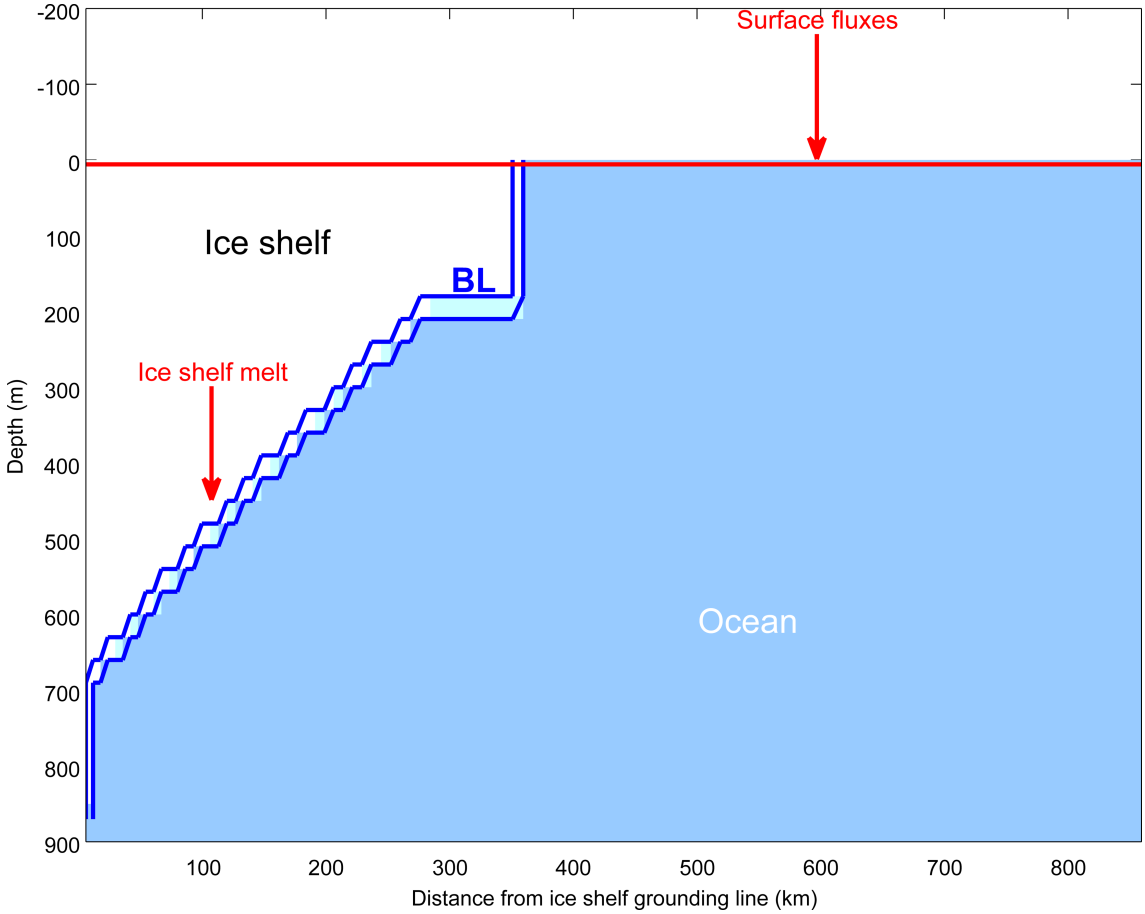

Figure 3.2: Vertical slice through the ISOMIP model setup (ice shelf shown in white), and the adapted setup for adding surface fluxes. The ice shelf boundary layer is shown in blue and the two types of flux, surface (precipitation, evaporation, iceberg melt and sea ice) and at depth (ice shelf melt) are also shown in red.

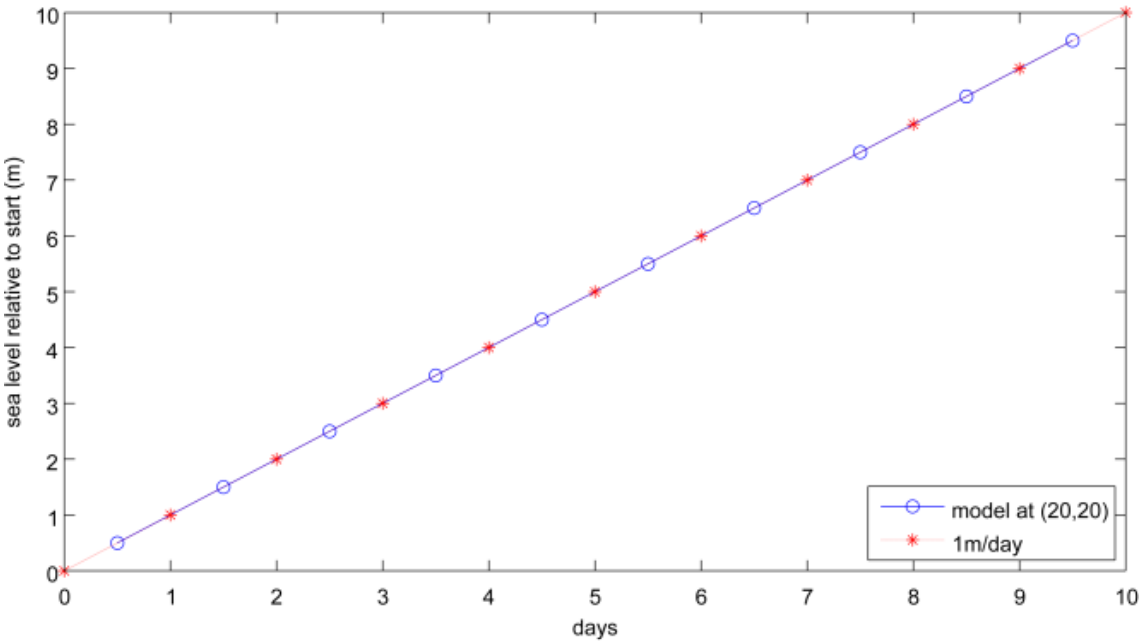

Figure 3.3: The amount of surface forcing, 1 metre per day, added per grid cell over the course of 10 days (red), and a comparison with the resulting sea level rise (blue) output as snapshots half way through each day. The plot is focused on location (20,20,1), though the input to each grid cell is uniform.

3.3 Passive tracers in MITgcm

Whilst identifying individual flux contributions to the ocean is a useful tool, it cannot provide information on the freshwater content, spatial distribution, and changes over time. Crucially, data from δ^{18}O measurements cannot be interpreted using these fluxes. The *ptracers* package in MITgcm allows passive tracers to be released into the ocean at user-defined locations and times, which then get carried in the ocean without affecting the active water column properties. This enables simulation of passive tracers in the ocean, such as chemical tracers (England and Maier-Reimer; 2001), which do not affect ocean dynamics but get carried in the currents (note that some, such as dissolved oxygen, have interactions with biological processes, especially at the surface (Jenkins and Jacobs; 2008)). Previous modelling studies have been used to trace ice-shelf meltwater (Nakayama et al.; 2014a) and on-shelf flow of CDW (Dinniman et al.; 2011) in the Bellingshausen Sea. However, these are generally based on an instantaneous release of a set amount of tracer rather than allowing for continuous addition from varying sources.

The *ptacers* capability in MITgcm has a setting whereby evaporation/precipitation can concentrate/dilute the surface concentration of each tracer by specifying the concentration of that tracer in the water added or removed. Open lateral boundaries can also affect the passive tracer, where the incoming concentration can be specified. Surface fluxes F (m/s)

affect the height of the ocean layer H, in metres, such that

$$\frac{\partial H}{\partial t} = F. \tag{3.3}$$

In the absence of any other forcing, a passive tracer in the ocean, of concentration ϕ, is affected by the flux F, of concentration ϕ_S, so that the total amount of integrated freshwater tracer

$$\frac{\partial (H\phi)}{\partial t} = \phi_S F. \tag{3.4}$$

By the product rule,

$$\frac{\partial (H\phi)}{\partial t} = H\frac{\partial \phi}{\partial t} + \phi\frac{\partial H}{\partial t} \tag{3.5}$$

and so, substituting Equations (3.3) and (3.4) into Equation (3.5) and rearranging,

$$\frac{\partial \phi}{\partial t} = \frac{F(\phi_S - \phi)}{H} \tag{3.6}$$

This expression is valid provided that the freshwater is also added as a material volume flux to the top grid cell. Tracers are subsequently advected and diffused in the same way as heat and salt.

It should be noted that in the calculation of tracers in the model, the cell height does not change (ΔH is fixed) as it is assumed that $\eta \ll H$. The model uses a real freshwater flux, as opposed to a virtual salt flux. This means that freshwater inputs will result in a change in volume. Thus the assumption in the model is valid for small perturbations to the sea surface, which is expected in the steady state scenarios being considered in the realistic model.

Assuming that F and ϕ_S are not functions of ϕ, i.e. $F \neq F(\phi)$ and $\phi_S \neq \phi_S(\phi)$, Equation 3.6 can be written as

$$\frac{\Delta \phi}{\Delta t} + \frac{F\phi}{\Delta H} = \frac{F\phi_S}{\Delta H}. \tag{3.7}$$

This is a first order ordinary differential equation in the form $\frac{d\phi}{dt} + P(t)\phi = Q(t)$ with solution $\phi = \frac{\int_0^t \mu Q(t)dt}{\mu}$ where $\mu = e^{\int_0^t P(t)dt}$. If F, H, and ϕ_S are constant with time, $\mu = e^{\frac{Ft}{H}}$. So

$$\begin{aligned} \phi &= \frac{\int_0^t e^{\frac{Ft}{H}} \frac{F\phi_S}{H} dt}{e^{\frac{Ft}{H}}} \\ &= \frac{\frac{F\phi_S}{H}\left[\frac{H}{F} e^{\frac{Ft}{H}}\right]_0^t}{e^{\frac{Ft}{H}}} \\ &= \phi_S(1 - e^{\frac{-Ft}{H}}). \end{aligned} \tag{3.8}$$

This analytical solution can be reproduced numerically using the ISOMIP box model shown in Figure 3.4, removing the ice shelf and applying a constant surface flux. From this point on, the assumption is that the initial tracer content in the ocean is 0, and the concentration in the surface flux, ϕ_S, is 1. To achieve test outcomes more quickly, an unrealistically large flux of F=1 metre per day for 10 days is used as the test case.

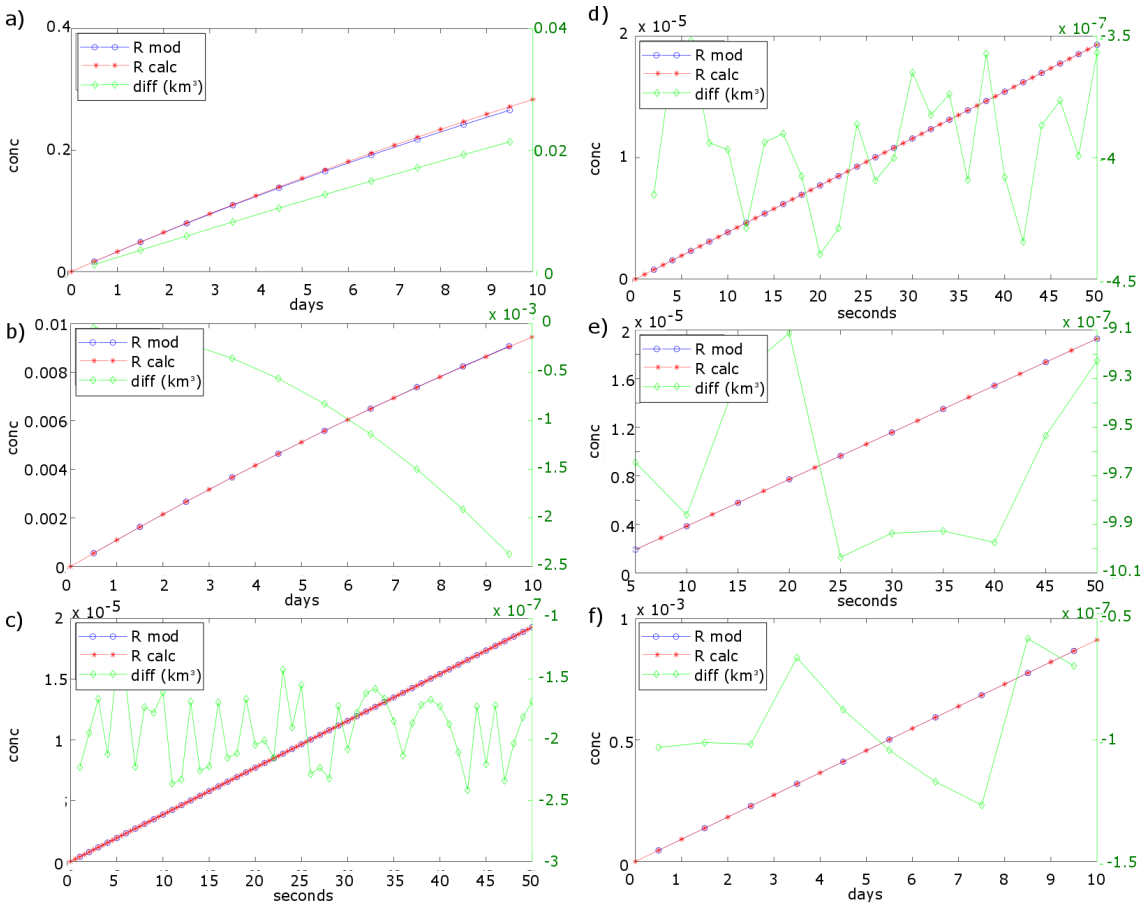

Figure 3.4: The concentration of freshwater tracer resulting from a surface forcing of 1 metre per day added per grid cell (blue), alongside the calculated amount of freshwater tracer from Equation 3.8 (red) in one grid cell ($(x, y, z) = (20, 20, 1)$), and the resulting relative error (green), for a) the surface, and b) the whole water column. Plots c)-e) show the first 50 seconds with the model timestep set to c) 1 second, d) 2 seconds and e) 5 seconds for a setup limited to 30 metres deep, with modelled concentration in blue, calculated in red and relative error in green. Plot f) shows a forcing of 1 metre per year and the resulting relative error over the whole 900 metres depth of the ISOMIP box model.

Adding this surface flux to the whole model grid results in the following concentration at the surface after 9.5 days:

$$\begin{aligned}\phi &= (1 - e^{\frac{-1\text{m/d}\times 9.5}{30\text{m}}}) \\ &= 0.2714.\end{aligned} \tag{3.9}$$

Note that 9.5 days is the last output of the model as snapshots in MITgcm are output halfway through the defined output frequency. A daily tracking of freshwater content versus calculated content can be seen in Figure 3.4a. This shows that the model is under-predicting the total amount at the surface, outputting a surface concentration of 0.2657. Figure 3.4b shows that if the total water column depth is used in the calculation, and then compared to the vertically-integrated model concentration, the relative error reduces significantly. This shows that vertical diffusion at the base of the surface grid cell reduced the tracer content at the surface from the expected value. However, there is still an error present - in the basic case, the relative error is around 10^{-3}.

Figures 3.4c-e show results from ISOMIP box model runs that were limited to 30 metres deep to avoid vertical diffusion through two deeper cells. Starting from the smallest timestep of 1 second and increasing it to 2 and 5 seconds, the relative error increases with increased timestep, suggesting a rounding error in the model and MATLAB calculations due to the small numbers. Whilst it is able to demonstrate the code behaves as expected, the unrealistically large forcing breaches the assumption of a fixed H. Given that the error is small compared to the magnitude of the flux despite this, and the flux is already unrealistically large, this is deemed acceptable and therefore further development based around this method can be conducted. This is backed by Figure 3.4f, which shows that if a more realistic forcing of 1 metre per year is added to the model, the relative error reduces to a much smaller value of less than 10^{-7} over the full 900 metres depth.

3.4 Developing code for surface fluxes

The original setup of the MITgcm code allows for the total surface freshwater input to be used to dilute or concentrate a passive tracer, and this has been used as a way of tracing the freshwater input. In order to trace multiple individual freshwater components, the surface fluxes defined in section 3.1 can be used as source terms to track the distribution of each component over time. In order to do this, Equation (3.6) must be modified.

Assuming two sources now rather than one, F_1 and F_2, the change in sea surface height, H, as the surface fluxes are added is

$$\frac{\partial H}{\partial t} = F_1 + F_2. \tag{3.10}$$

Now there are two input tracer concentrations, ϕ_{S1} and ϕ_{S2}. From this point onwards, these are always set to 1 to represent 100% freshwater, but could feasibly be given a different value. There are also two tracer concentrations in the ocean to keep track of, ϕ_1 and ϕ_2. The change in total volume of integrated freshwater tracer 1 (concentration ϕ_1)

equals the tracer flux

$$\frac{\partial(H\phi_1)}{\partial t} = \phi_{S1}F_1. \tag{3.11}$$

As before, using the product rule, this can be rewritten as

$$H\frac{\partial\phi_1}{\partial t} + \phi_1\frac{\partial H}{\partial t} = \phi_{S1}F_1 \tag{3.12}$$

so (3.10) can be used to obtain

$$H\frac{\partial\phi_1}{\partial t} + \phi_1(F_1 + F_2) = \phi_{S1}F_1 \tag{3.13}$$

Rearranging, and using the same argument for flux F_2, results in

$$\frac{\partial\phi_1}{\partial t} = \frac{1}{H}\bigg(F_1(\phi_{S1} - \phi_1) - F_2\phi_1\bigg) \tag{3.14}$$

$$\frac{\partial\phi_2}{\partial t} = \frac{1}{H}\bigg(F_2(\phi_{S2} - \phi_2) - F_1\phi_2\bigg). \tag{3.15}$$

By using the derivation as (3.8), the general solution for two tracers can be obtained for ϕ_1:

$$\phi_1 = \frac{\phi_{S1}F_1}{F_1 + F_2}(1 - e^{\frac{-(F_1+F_2)t}{H}}) \tag{3.16}$$

with a similar solution for ϕ_2. This again assumes $\eta \ll H$, such that H is steady with time.

This can therefore be extended for n fluxes. Modifying (3.10) such that

$$\frac{\partial H}{\partial t} = F_1 + \sum_{i=2}^{n} F_i, \tag{3.17}$$

then substituting into Equation 3.12 and rearranging, yields

$$H\frac{\partial\phi_1}{\partial t} + \phi_1(F_1 + \sum_{i=2}^{n} F_i) = \phi_{S1}F_1 \tag{3.18}$$

and so

$$\frac{\partial\phi_1}{\partial t} = \frac{1}{H}\bigg(F_1(\phi_{S1} - \phi_1) - \sum_{i=2}^{n} F_i\phi_1\bigg). \tag{3.19}$$

So for $j = 1, ..., n$,

$$\frac{\partial\phi_j}{\partial t} = \frac{1}{H}\bigg(F_j\phi_{Sj} - \sum_{i=1}^{n} F_i\phi_j\bigg). \tag{3.20}$$

Therefore for the total tracer concentration in the ocean

$$\phi_{tot} = \sum_{j=1}^{n} \phi_j, \tag{3.21}$$

with total flux

$$\sum_{j=1}^{n} F_j = F_{tot}, \tag{3.22}$$

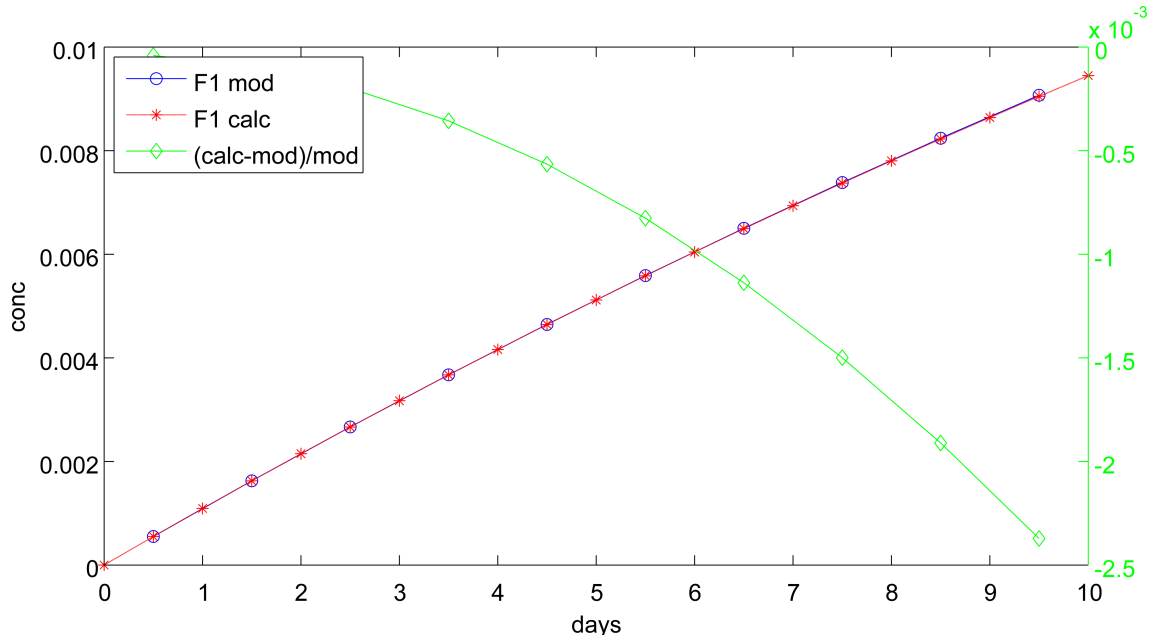

Figure 3.5: Plot showing the volume of freshwater tracer resulting from a surface forcing of 1 metre per day added per surface grid cell over the course of 10 days (blue), alongside the calculated amount of freshwater tracer from Equation 3.8 (red), and the resulting difference between the calculated and modelled volume (green).

and assuming $\phi_{S1} = \phi_{S2} = ... = \phi_{Stot} = 1$,

$$\begin{aligned}
\frac{\partial \phi_{tot}}{\partial t} = \sum_{j=1}^{n} \frac{\partial \phi_j}{\partial t} &= \sum_{j=1}^{n} \frac{1}{H}\left(F_j \phi_{Sj} - \phi_j \sum_{i=1}^{n} F_i\right) \\
&= \sum_{j=1}^{n} \frac{1}{H}\left(F_j \phi_{Stot} - \phi_j F_{tot}\right) \\
&= \frac{1}{H}\left(F_{tot}\phi_{Stot} - \phi_{tot}F_{tot}\right) \\
&= \frac{F_{tot}}{H}\left(\phi_{Stot} - \phi_{tot}\right).
\end{aligned} \tag{3.23}$$

A check on the implementation of this is shown in Figure 3.5, by adding $F_1 = 1$ m/day (with associated concentration $\phi_{S1} = 1$) and no other fluxes. It is equivalent to Figure 3.4a. This proves that if there is only one tracer present the code correctly calculates it as equivalent to the total freshwater tracer.

Figure 3.6 shows that when two tracers are added, in the form of 0.75 metres per day of runoff and 0.25 metres per day of precipitation, the tracers behave as expected compared with their flux and the difference between the calculated runoff and model runoff tracer (green line) remains small. Further, the total also behaves as expected, summing to 1 metre per day of total freshwater flux when compared to Figure 3.5.

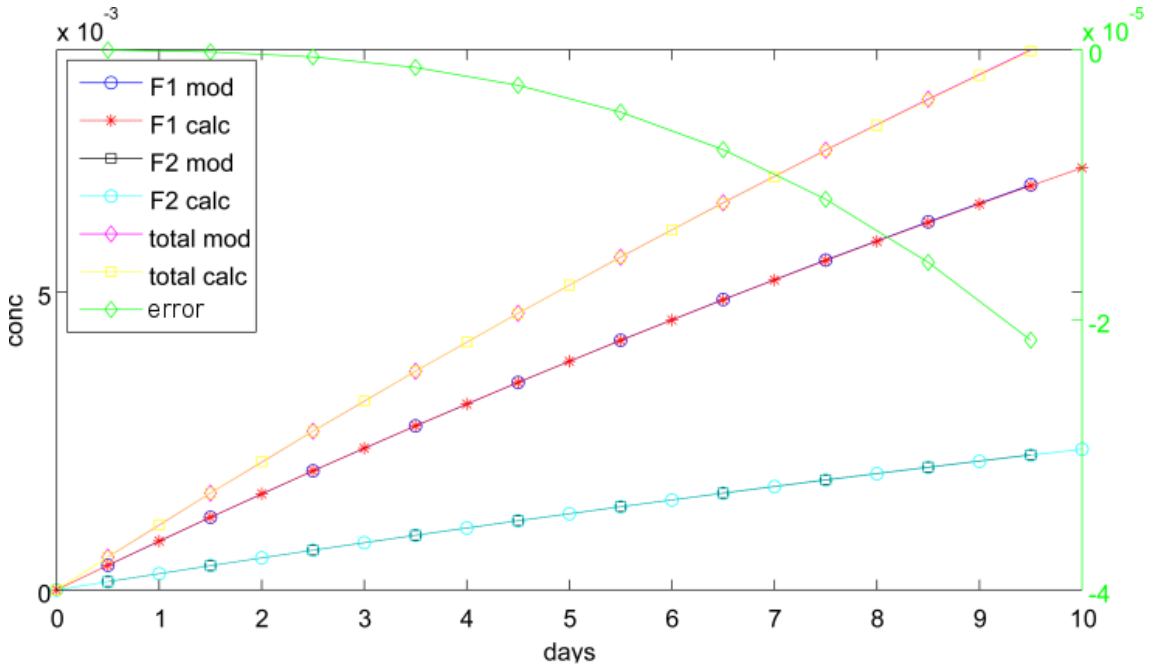

Figure 3.6: Plot showing the volume of freshwater tracer resulting from a surface forcing of 0.75 metres per day of runoff (blue) and 0.25 metres of precipitation added per surface grid cell over the course of 10 days (black), alongside the respective calculated amounts of freshwater tracers (red, cyan) and the resulting total modelled (magenta) and calculated (yellow) tracer amounts from Equation 3.8, and the resulting difference between the total calculated and modelled volumes (green).

3.5 Developing code for tracing fluxes at depth

So far, the total freshwater flux in the model has only been a result of surface fluxes, as in the standard MITgcm code. Since ice shelf melting is another component of the Bellingshausen Sea freshwater budget, and its meltwater could have effects on the stratification of the water column, it is important to include this in calculations. The ice shelf meltwater acts as a flux though the top of grid cells, and therefore behaves much like a surface flux, but its injection depth in the code needs to be modified so that the contribution to the tracer is through the relevant cell at depth. This is achieved by creating a new two-dimensional variable that tracks the depth of injection and then assigns the ice shelf flux to that depth when the passive tracers are forced with surface forcings.

Ice shelf melting is calculated interactively by the model, and therefore testing input at depth by manually prescribing it within the code would not fully test the new code. Instead, the tracer content is compared to modelled deviations in salinity as a result of the freshwater input. Figure 3.7 shows a) the ice shelf tracer, b) the salinity, c) the difference between the salinity at the beginning of the run (34.4 psu) and the time-evolving salinity, and d) this difference plotted against the ice shelf tracer values. As the only freshwater tracer which tracks the only source of change to salinity, the ice shelf melt should match in spatial distribution with the salinity. Figure 3.7d shows a set of points that do not lie on the same trend line as the rest, suggesting an issue with the code. Looking at panel (c), there is an extra row of salinity values changing below the ice shelf that do not appear in the ice shelf tracer.

Discrepancy between the modelled salinity and ice shelf tracer content occurs because in (3.6), the tracer concentration is spread over H, which is always equal to the cell height at the surface. But under ice shelves, the geometry is defined by applying partial cells at the interface, much like at the sea bed. For this reason, the partial cell fraction must be applied to H in the code to calculate the resulting tracer concentration. This results in little deviation from the trend line (Figure 3.8).

3.6 Issues encountered when moving back to Bellingshausen Sea model

The simple ISOMIP model was created so that testing could be done easily, both due to quick run times and the ability to analytically calculate fluxes in and out. However, the Bellingshausen Sea model is much more complex and the transition met with three main problems.

3.6.1 Negative tracers

During development of the ISOMIP model, no sea ice was included as it would complicate calculations. However, through adding this, along with an evaporation tracer, the possibility of negative tracers arose. When fluxes are negative (as happens when evaporation

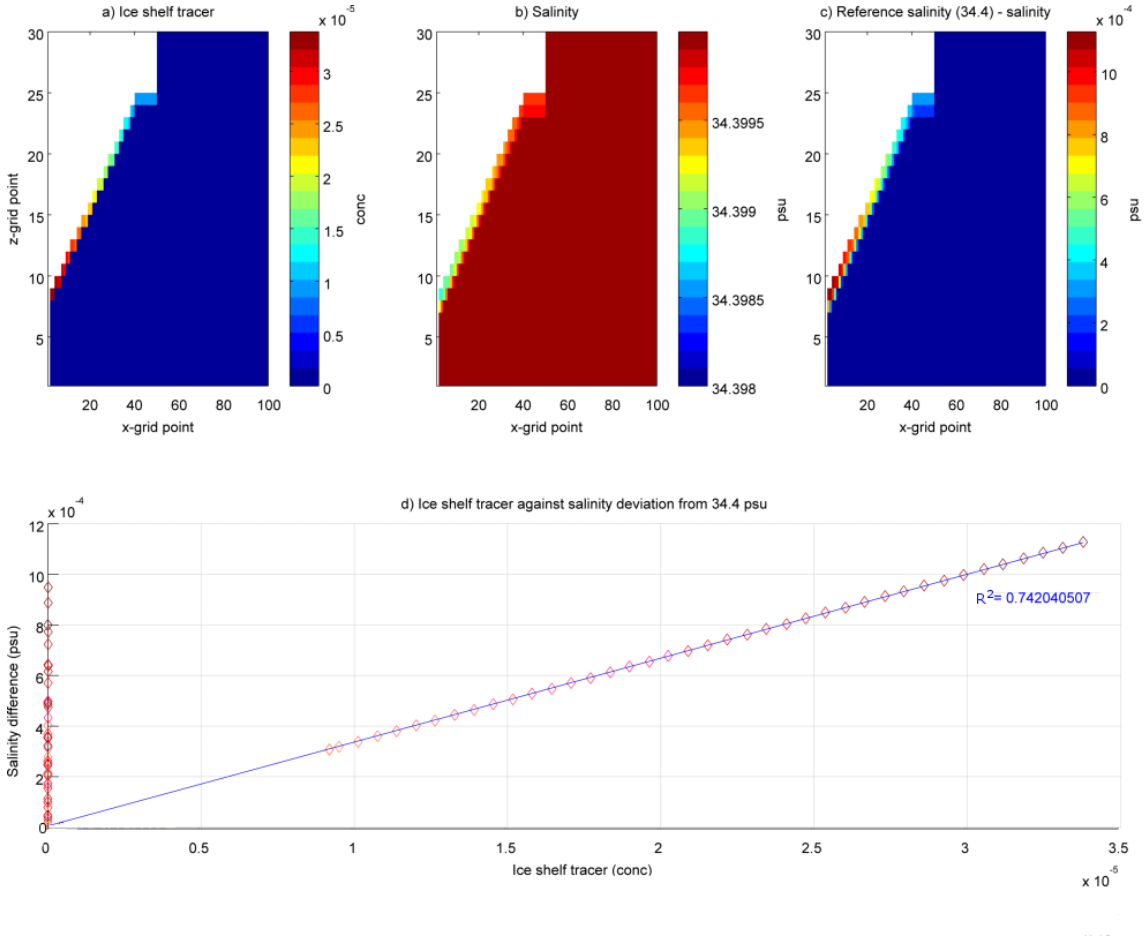

Figure 3.7: Plot showing a) concentration of ice shelf melt tracer after 10 timesteps with a run that has no surface forcing, b) corresponding salinity, c) the difference between the salinity at the start of the run, 34.4 psu, and the salinity after 10 timesteps, and d) a scatter plot of values from a) and c), where light red is near the surface and dark red points are at depth. Run where the standard code (3.6) for surface inputs is replicated for ice shelf melt injection, applied at the relevant depth level without further adjustment.

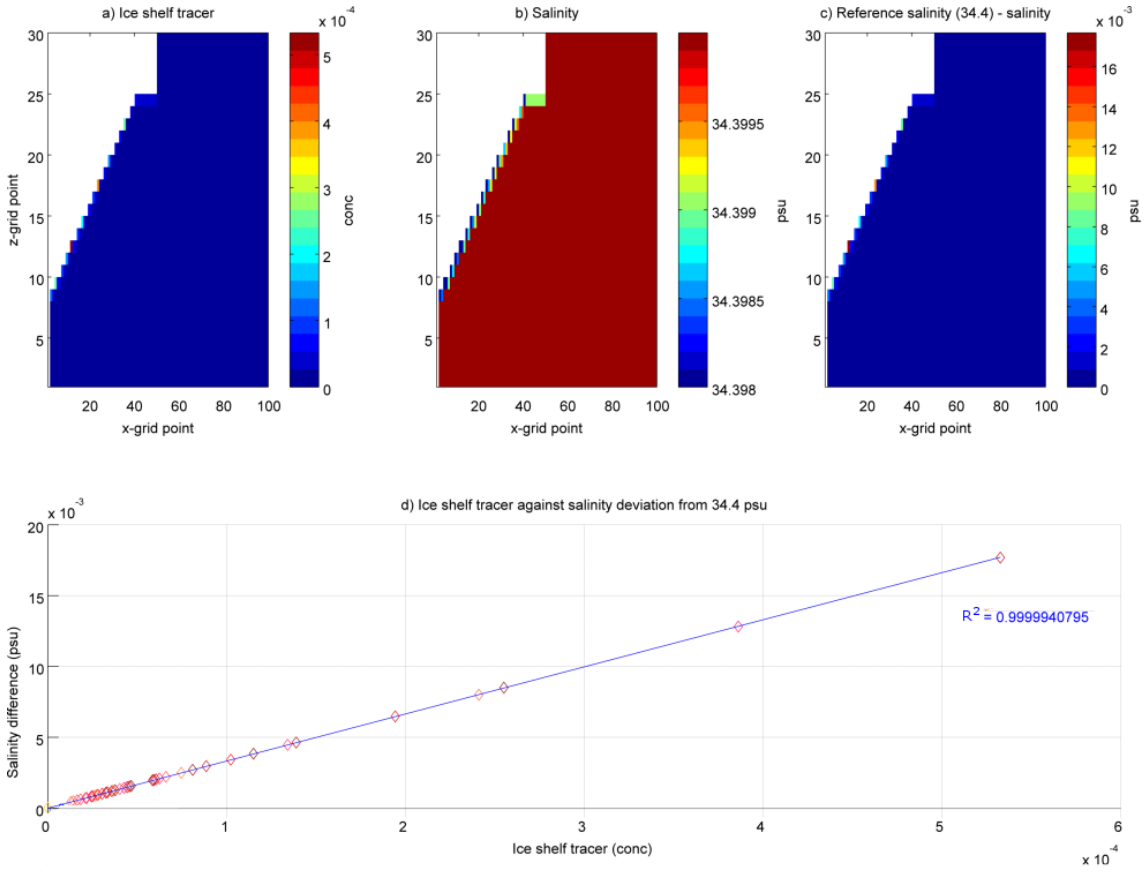

Figure 3.8: Plot showing a) concentration of ice shelf melt tracer after 10 timesteps with a run that has no surface forcing, b) corresponding salinity, c) the difference between the salinity at the start of the run, 34.4 psu, and the salinity after 10 timesteps, and d) a scatter plot of values from a) and c), where light red is near the surface and dark red points are at depth. Run considers partial cells below the ice shelf when calculating H in (3.6).

or sea ice freezing causes the surface to become more salty), negative tracer concentration can occur. Physically, it makes sense that the concentration of freshwater can decrease relative to an arbitrary initial concentration. In reality, negative contributions to freshwater are often the result of δ^{18}O analysis when using simple end-member calculations (e.g. Meredith et al.; 2016).

To check that the code is able to handle negative concentrations, a 10-day model run in the ISOMIP setup was created (Figure 3.9) with 1 metre per day precipitation (blue) and 1 metre per day evaporation (black) input everywhere, resulting in a net flux of zero (magenta). a) shows the forcing over the 10 days, b) shows the total concentration in the model, and c) shows the equivalent vertical metres of tracer content. The results show that over the 10-day period the net flux is zero, leading to a total tracer content of zero. This is comprised of 10 vertical metres of each individual tracer with opposing signs. This provides evidence that the negative concentrations (corresponding to a loss of freshwater volume) that are gained from sea ice and evaporation are suitable for the study and are dealt with correctly. The validation section (4.1) shows their interpretation in the context of observational data.

3.6.2 Boundary conditions

The application of boundary conditions means that tracers will be forced differently to temperature and salinity, and therefore behaviour at the boundary will be slightly different. Figure 3.10 shows the western boundary of four scenarios in the Bellingshausen Sea model where passive tracer boundary conditions have been applied. In Figure 3.10a, closed boundaries were used. The result is that the tracer builds up at the boundary as it is not advected away. After a period of time, the tracer would eventually fill the domain, as the net inflow would exceed the outflow. This is unrealistic in the ocean. Additionally, closed boundaries in the model are not an option as this would prevent the ACC from being forced through the domain. Therefore a boundary setting is required.

In open boundaries in MITgcm, fields being taken from the domain leave with their modelled values according to a Neumann boundary condition ($\frac{\partial \phi}{dn} = 0$, where n is normal to the boundary), while incoming fields adopt the prescribed boundary conditions. Figure 3.10b shows the result of not prescribing a boundary file for passive tracers. In this case, a Neumann boundary condition is applied on the inflow. This means the tracer exiting the domain does not change value, but where there is an eastward flow in the northwest of the domain, tracer is advected in according to the Neumann boundary condition, and thus large values can appear on inflows. Figure 3.10c shows the effect of the Dirichlet boundary condition on the inflow, where by setting the boundary tracer to 0, the tracer concentration in the sponge layer tends to 0, and inflowing water has a tracer concentration of 0. By choosing ϕ=0 on the boundary for incoming tracer, the model therefore only monitors local sources of freshwater. Figure 3.10d shows the result of setting the tracer concentration to 1 on the boundary.

The inflows have a great effect on the tracer concentration close to the western bound-

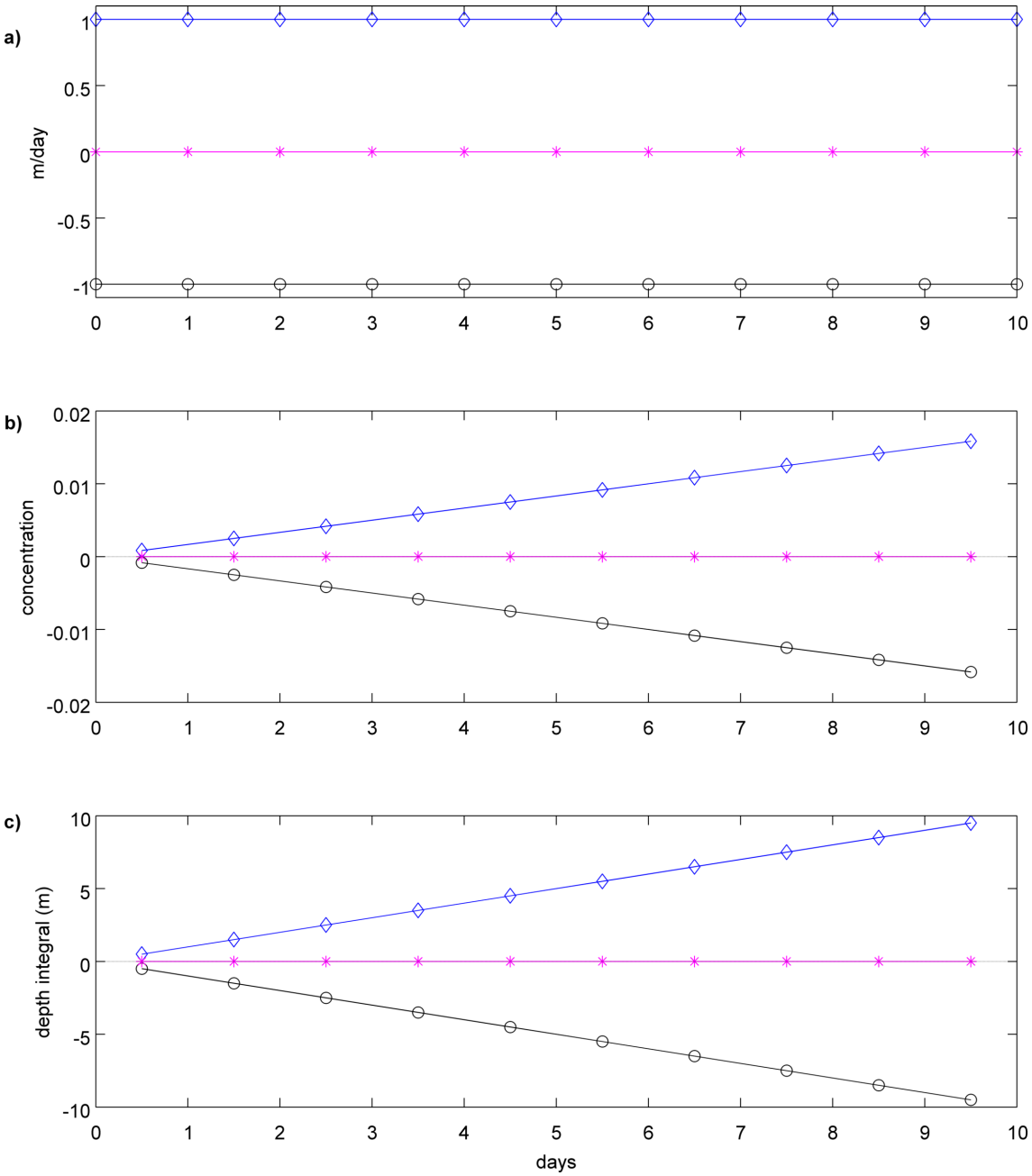

Figure 3.9: a) Forcing for a 10-day model run in the ISOMIP setup with 1 metre per day precipitation (blue) and 1 metre per day evaporation (black) everywhere, resulting in a net flux of zero (magenta). a) shows the forcing over the 10 days, b) shows the total concentration in the model, and c) shows the equivalent vertical metres of tracer content.

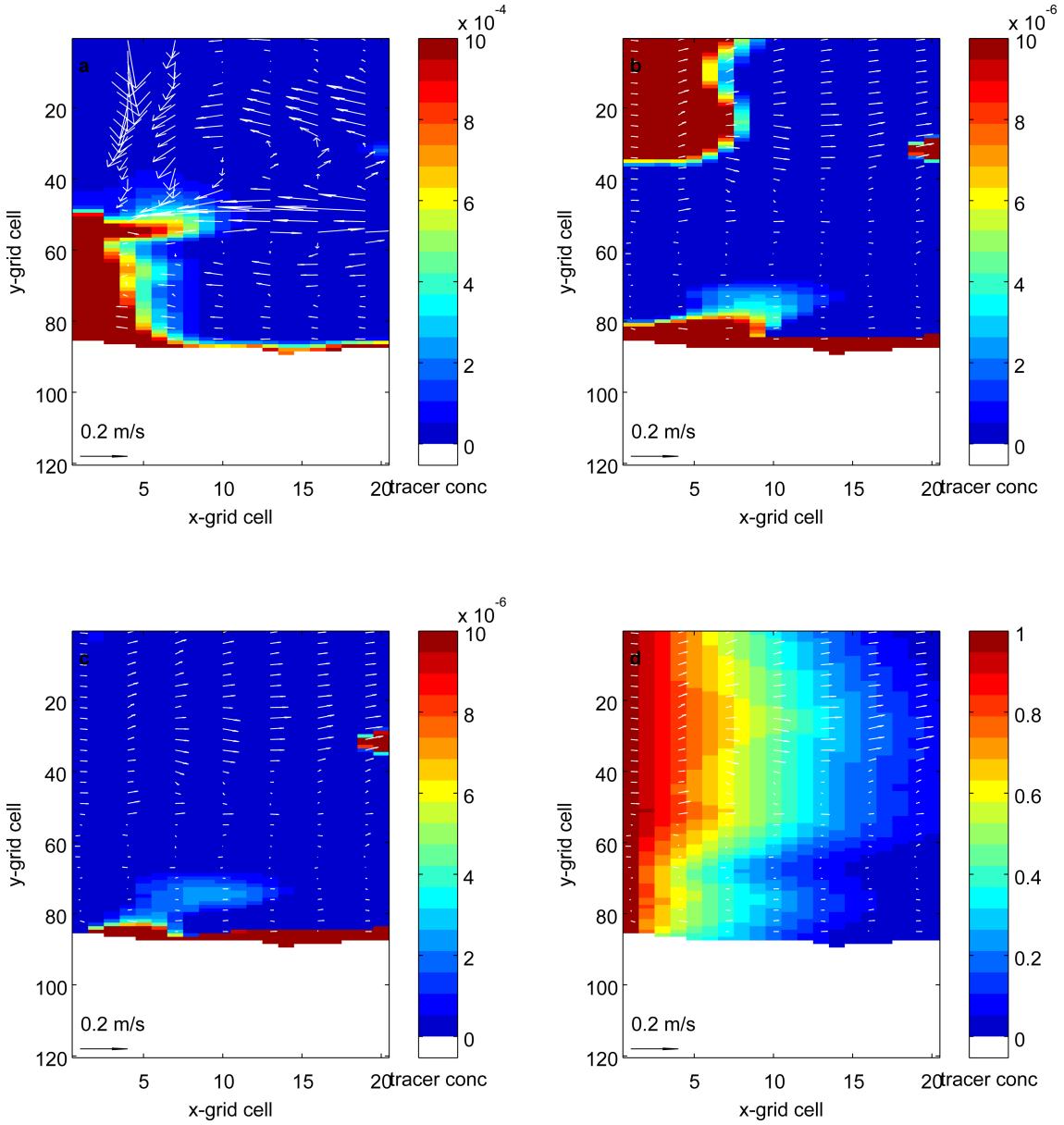

Figure 3.10: Bellingshausen Sea model surface output on the western boundary of total freshwater tracer after 6 months, overlaid by ocean velocities, for a) closed boundaries, b) no passive tracer boundary file set, with a Neumann boundary condition, c) passive tracers set to 0 on the boundary, therefore applying a Dirichlet boundary condition, and d) passive tracers set to 1 on the boundary. Note the differing colour schemes in order to highlight both the effect of the boundary and the tracer present in the model along the southern coastline.

ary. Using a dataset of tracer boundary conditions would be useful in representing non-local sources of freshwater, such as iceberg melt being advected into the region from the neighbouring Amundsen Sea. Carrying out such simulations would require a complete dataset, such as a global model, to fully represent each non-local freshwater source. It would be an avenue to explore in the future, but is beyond the scope of this study. Therefore the setting chosen to proceed with is ϕ=0 for inflows (option c), in order to fully control what is happening on the boundary and only represent tracer that has fluxed in through the surface inputs or ice shelves.

3.6.3 Numerical artefacts

On moving to the Bellingshausen Sea model, it was observed that tracers were able to become unrealistically large in some cells - particularly on the continental slope where small partial cells were adjacent to large cells with high ACC velocities. A number of approaches were tested in order to stop this from occurring, including smoothing the bathymetry to reduce sharp gradients and varying vertical diffusion parameters to see if the build-up of tracer could be prevented. However, the best solution was to increase the minimum partial cell fraction to the value described in the previous chapter. This is because it enabled bathymetric features to still be resolved (Chapter 2, Figure 2.3), without causing passive tracers to be advected into small partial cells at high speed and become trapped, enabling the model to run with original parameters but avoiding the instability.

3.7 Summary

This chapter details the identification of a requirement to track freshwater components for the study, and details how a method was investigated, implemented and tested. The Bellingshausen Sea model now has the capability to trace sources of freshwater from various sources and identify their fate over time. Chapter 4 will validate the model against available observations, before investigating the time-mean freshwater distribution of the Bellingshausen Sea.

Chapter 4

Spatial distribution of freshwater in the Bellingshausen Sea

In Chapter 1, it was acknowledged that whilst freshwater in the Bellingshausen Sea is important in governing the ocean circulation and feedbacks linked to ice-ocean interactions, there is little understanding of the region-wide spatial distribution of freshwater content and its composition. Based on the Bellingshausen Sea model designed in Chapter 2, and the code development from Chapter 3, the freshwater budget will now be investigated. The aims of this chapter are as follows:

4.1) Validate the physical model.

4.2) Provide an overview of the time-mean freshwater components' contributions to the overall freshwater content, in the context of individual fluxes and total salinity.

4.3) Understand the seasonality of freshwater fluxes and content, and how this affects the mean.

4.4) Investigate regional differences and associated variations in oceanography; deduce how much can be inferred of the wider shelf from individual locations.

4.5) Perform sensitivity analysis on iceberg melt field to quantify uncertainty in the freshwater flux and test the effect of changing the magnitude and distribution of surface fluxes.

4.1 Model validation

Validation of the model is difficult as available data is sparse in polar regions, both temporally and spatially, making any widespread comparisons difficult. This section aims to utilise the few available data to show how the modelled ocean, sea ice and ice shelves perform. As a reminder, Figure 4.1 shows the Bellingshausen Sea region in the context of the Southern Ocean, along with ice shelves and specific areas that will be referred to throughout the chapter.

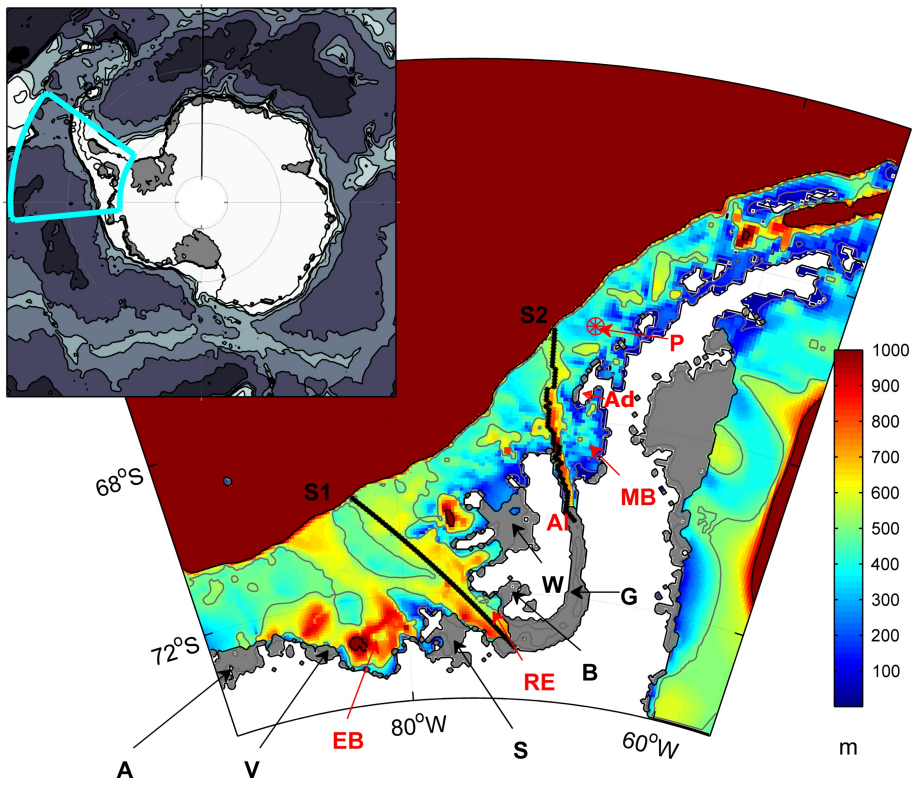

Figure 4.1: Model domain. Coloured is BEDMAP2 bathymetry, with contours shown at 100, 500, and 1000 metres. Ice shelves are shown in grey, with underlying bathymetry contours shown. Also provided in red are key locations, where EB = Eltanin Bay, RE = Ronne Entrance, AI = Alexander Island, MB = Marguerite Bay, Ad = Adelaide Island, and P = Palmer LTER grid point 400.1 (http://pal.lternet.edu), used for validation. Ice shelves on the west Antarctic Peninsula are shown with black arrows, where A = Abbot, V = Venable, S = Stange, B = Bach, W = Wilkins and G = George VI Ice Shelf. Sections through Belgica Trough leading to Ronne Entrance (S1) and Marguerite Trough (S2) are also shown (black). Inset shows the Bellingshausen Sea and model domain (blue) in relation to the Southern Ocean and Antarctic Ice Sheet.

4.1.1 Ocean model

Chapter 2 demonstrated that deviation from the World Ocean Atlas initial conditions can occur, particularly in cases where unrealistic convection is present (Chapter 2, Figures 2.15 and 2.16). Given that the model is initialised with World Ocean Atlas data averaged over the available time period, incorporating all available data, the long-term mean of the model should not deviate much from these values over time if it is simulating the region correctly. Figures 4.2 a and b show the average bottom salinity and temperature over the period 1989-2014 . These values are well within the bounds of CDW (1-2°C and 34.60-34.74 psu, Meredith et al. (2008)) that floods the shelf in reality but is hard to recreate in models (e.g. Nakayama et al.; 2014b; Holland et al.; 2010). Figure 4.3 demonstrates that the climatological potential temperature and salinity at the seabed deviate little from the starting conditions after spinup, and whilst these are slightly cooler and fresher than the initial conditions they are still within the bounds of CDW. This gives confidence in the ocean properties of the run over the full domain. The BS shelf is warmer and fresher than the ACC because of the shallower bathymetry. Warmer, saltier areas follow deeper bathymetry, highlighting areas where CDW intrudes onto the shelf from the ACC. Shallow areas immediately adjacent to the coast are cold and fresh, reflecting the proximity to the majority of freshwater inputs and surface influence. The model recreates the cold, salty deep waters of the Weddell Sea, although it should be noted that this region of the domain is greatly affected by boundary conditions and therefore simulating conditions here cannot be expected to be realistic.

The research is based around the Bellingshausen Sea shelf, and therefore shelf-wide comparisons of ocean properties can be performed to ensure its representation is realistic. A shelf-wide potential temperature-salinity diagram from World Ocean Atlas data (Boyer et al.; 2009) for each season (clockwise from top left: summer, autumn, winter, and spring) is shown in Figure 4.4, and can be compared to the equivalent for the model in Figure 4.5. The model does not reproduce CDW values with as large a range as the data, particularly in terms of its temperature and mixed waters, because it cannot simulate the influence of the Weddell Sea on Bransfield Strait in the north. This is demonstrated by a comparison of the annual average shelf properties if data further east than 298 °W is removed, as shown in Figure 4.6. However, it does capture the general distribution of water masses. Autumn and winter are best represented, with the overall shape of the diagram consistent, whereas the spread in other seasons is greater due to surface waters. A double peak is seen in summer in both the model and observations (Figures 4.5 and 4.6) due to both higher surface temperatures and warmer deeper waters, though the model does not capture the magnitude of the CDW temperature fully, relating to the difficulty of keeping warm, salty waters on the shelf in models. In general, the freshwater content in the model results in a larger density range in summer, and also a slightly lower surface density in winter. Less deep water resides in the high density band, although Figure 4.6 shows that this is mainly due to Bransfield Strait waters. Whilst this suggests potentially more stratification than in reality, the general trends below the very surface layer do match, giving confidence in

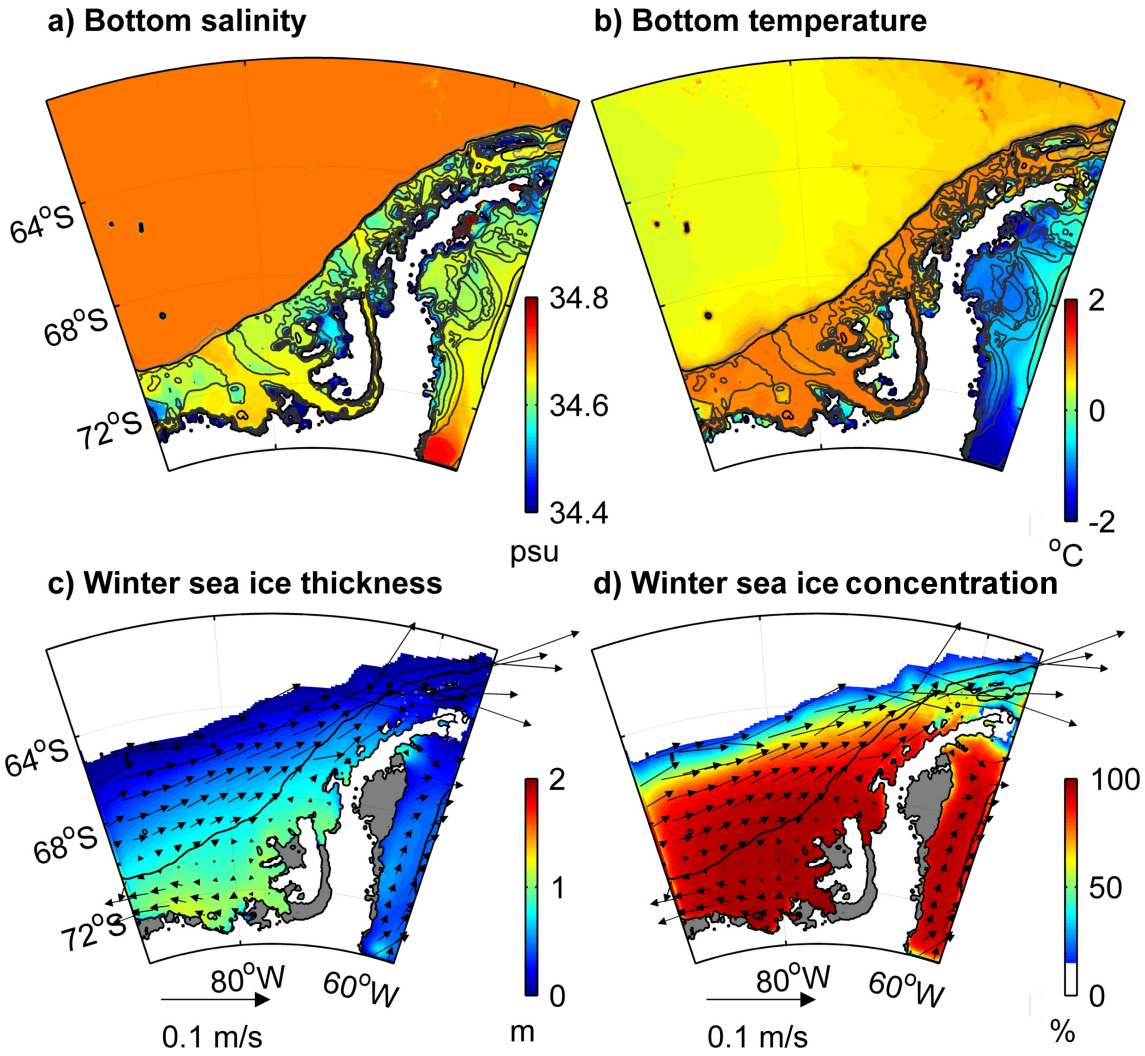

Figure 4.2: Annual mean over 1989-2014 for a) salinity and b) potential temperature at the seabed for the period 1989-2014. Bathymetry contours shown in grey at 100, 500, and 1000 metres, with the 1000 metre isobath shown in black. Mean winter (JAS) sea ice thickness (c) and concentration (d) is shown over the same period masked where sea ice concentration is below 15%, with ice shelves in grey. Vectors of ice velocity at 12 grid point intervals are also shown.

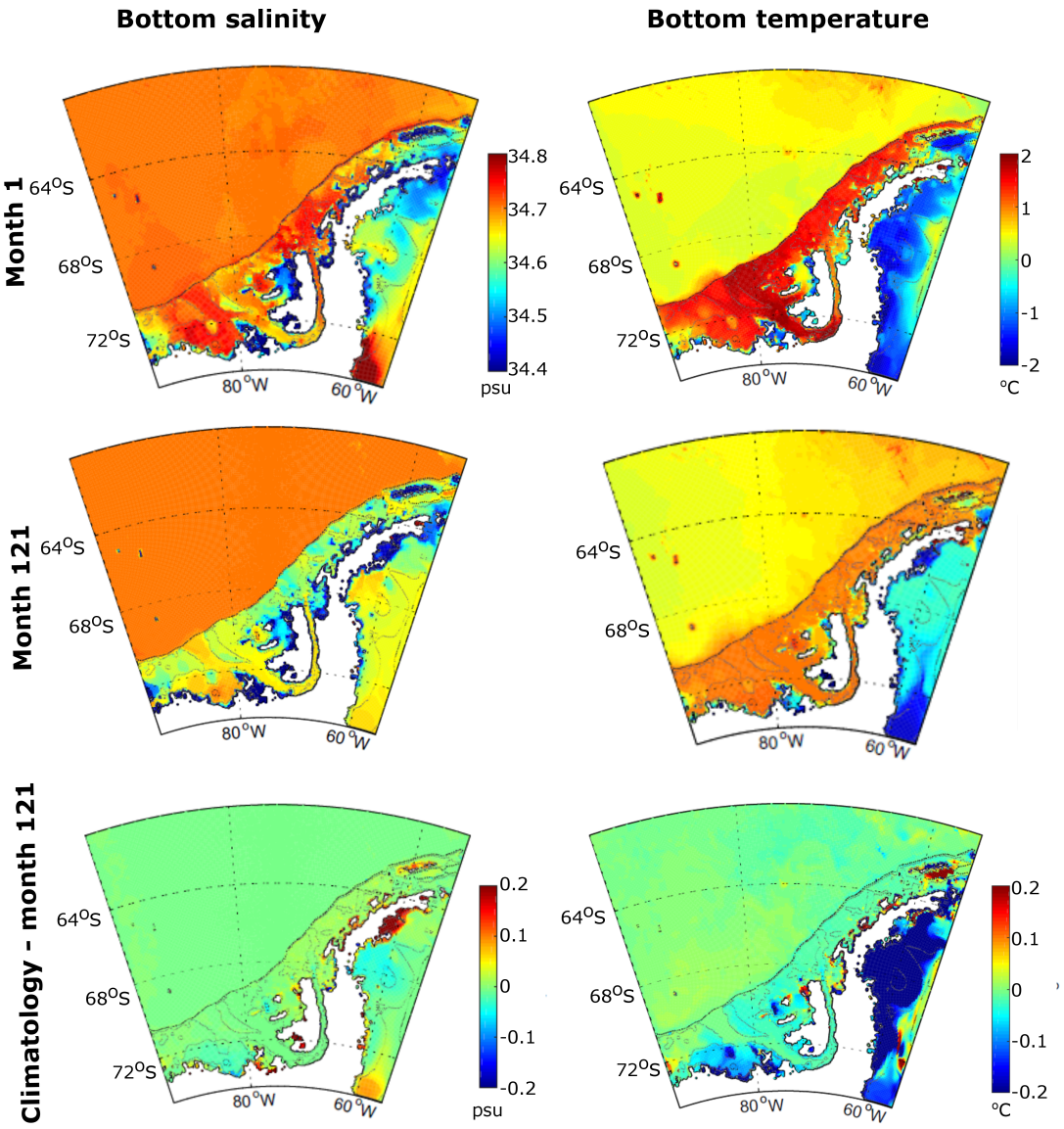

Figure 4.3: Annual mean over 1989-2014 for (left) salinity and (right) potential temperature at the seabed for (top) the first month, (second row) month 121, the first month after spinup, and (third row) the difference between the 1989-2014 climatology in Figure 4.2 and the first month after spinup. Bathymetry contours shown in grey at 100, 500, and 1000 metres, with the 1000 metre isobath shown in black.

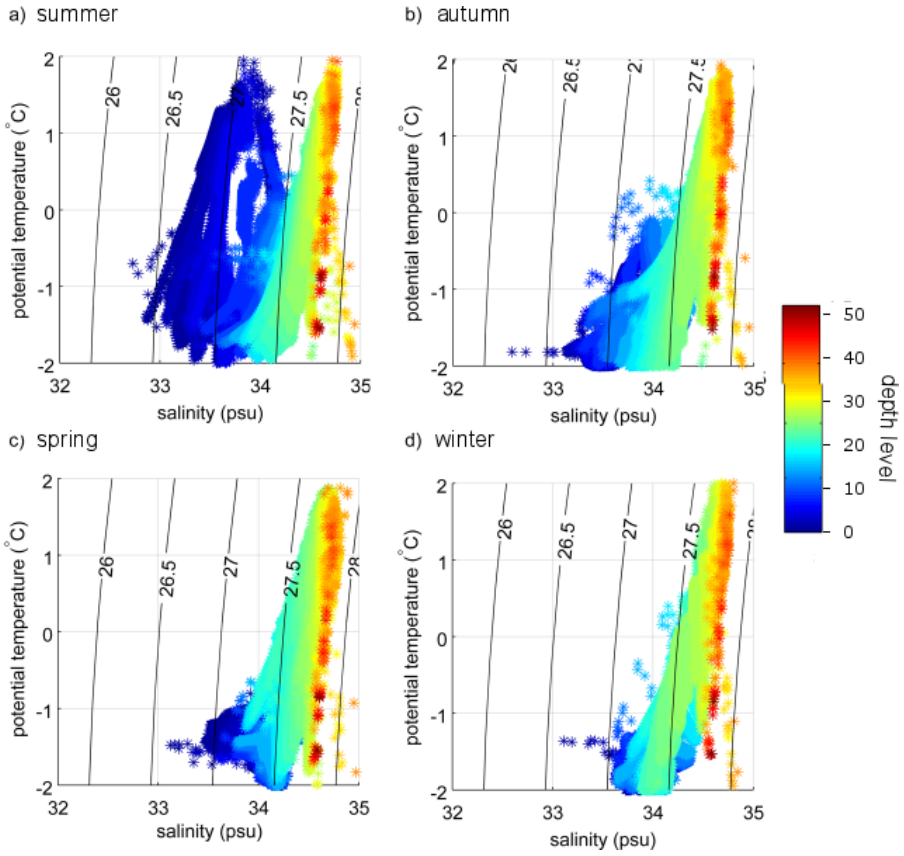

Figure 4.4: Potential temperature-salinity diagram for World Ocean Atlas data (Boyer et al.; 2009) for each season (clockwise from top left: a) summer, b) autumn, d) winter, and c) spring) on the shelf (less than 1000 metres). Surface waters are shown in blue, with deep waters in red, moving through the colour scale according to the depth level as indicated by the colour bar. Density contours (kgm^{-3}) calculated using MATLAB file exchange script *theta_sdiag* (Bhatt; 2009), utilising *sw_dens* (Meyer et al.; 2014).

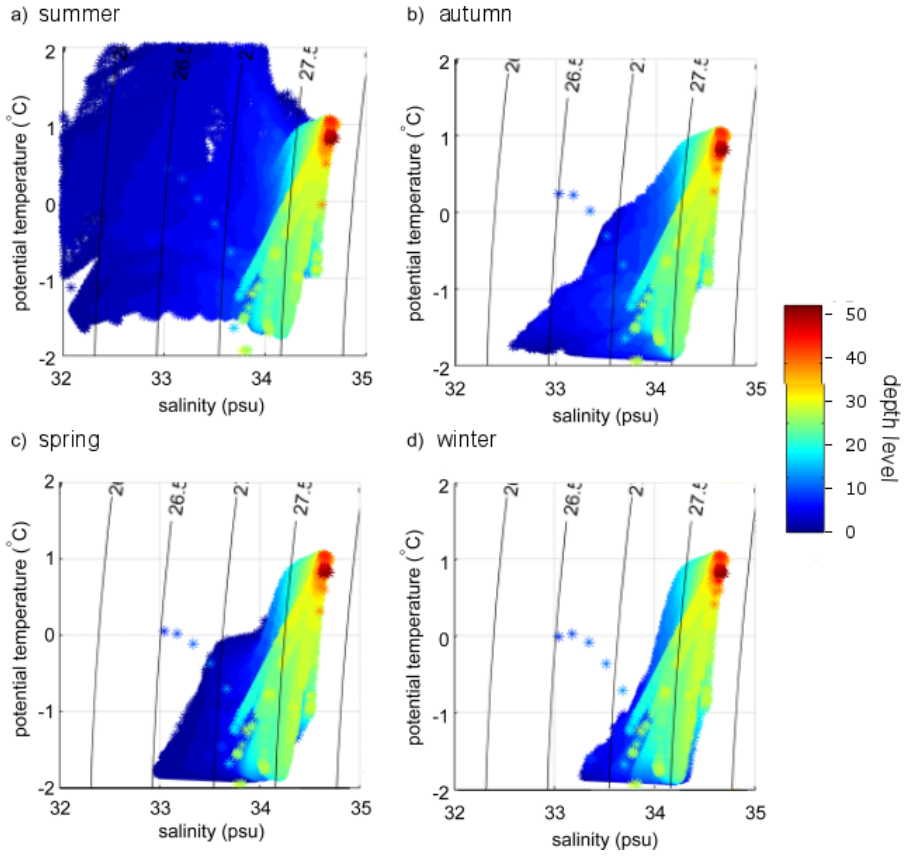

Figure 4.5: Potential temperature-salinity diagram for model output on the shelf, defined as areas less than 1000 metres, for each season (clockwise from top left:a) summer, b) autumn, d) winter, and c) spring) averaged over the period 1989-2014. Surface waters are shown in blue, with deep waters in red, moving through the colour scale according to the depth level as indicated by the colour bar. Density contours (kgm^{-3}) calculated using MATLAB file exchange script *theta_sdiag* (Bhatt; 2009), utilising *sw_dens* (Meyer et al.; 2014).

the model (see below).

Focussing on a point-comparison close to Palmer Station (65°52.6' S, 68°17.0' W), Figure 4.7 shows a vertical profile of salinity at location 65°52.6'S, 68°10.0' W reproduced from Meredith et al. (2016), along with the associated model output. The general behaviour is captured. In both the model and observations, most variation in salinity is seen in the top 50 metres of the water column, with less interannual variability at depth and a second increase with depth once the CDW layer is fully present. While the model is slightly too fresh right at the surface, as shown in the potential temperature-salinity diagrams, it does capture 2013-2014 quite well although 2011 and 2012 are not consistent.

Crucially for this study, these comparisons with CTD profiles are also able to validate the freshwater content. Figure 4.7b, c, e and f show the vertical profiles of derived sea ice melt and meteoric water content of location 65°52.6'S, 68°10.0' W (Figure 4.1, location P) reproduced from Meredith et al. (2016), along with the associated model output. The model underpredicts meteoric water content in the top 50 metres, and generally overpredicts sea ice meltwater at the surface. At depth there is net loss of sea ice meltwater in most years which the model is able to recreate successfully, though the interannual variability in the model at depth is less than in observations. The comparison is encouraging considering the difficulties inherent in modelling specific events using reanalysis forcing and relatively coarse model resolution, which can result in small-scale atmospheric features being smoothed. There are no error bars provided on the observations and therefore the uncertainty cannot be inferred, but it could be that the model performs within observational error.

4.1.2 Sea ice model

Figure 4.2c-d shows sea ice thickness and extent in winter. The sea ice velocity vectors show that the northern part of the winter sea ice extent is higher and heads northeastwards, while the southern end circulates round and heads west, in line with hypothesised general circulation in the region (e.g. Talbot; 1988; Holland and Kimura; 2016). In both seasons a lot of ice is lost through the boundaries. The model output is comparable to the winter and autumn extents shown in Holland et al. (2014), giving some confidence that it is correct. The sea ice concentration can be compared to satellite observations from Cavalieri et al. (1996). Figure 4.8 shows that in autumn and winter, there is good agreement between both the 15% northerly limit and the concentration gradient, although in general the model predicts high ice concentrations further north than the observations. The ice north of the peninsula exhibits less variation in the model than in the observations. A similar pattern is present in spring, with more concentrated ice predicted further north, resulting in a more northerly extent. However, in summer, the model generally loses too much ice.

In terms of ice thickness, the model produces maximum thicknesses of 1.24, 0.57, 0.90 and 1.24 metres and average thicknesses of 0.44, 0.15, 0.22 and 0.44 metres for spring-winter after removing values where the concentration is less than 0.15, the values on the boundary, and sea ice in the Weddell Sea. The maximum values fall within the bounds of

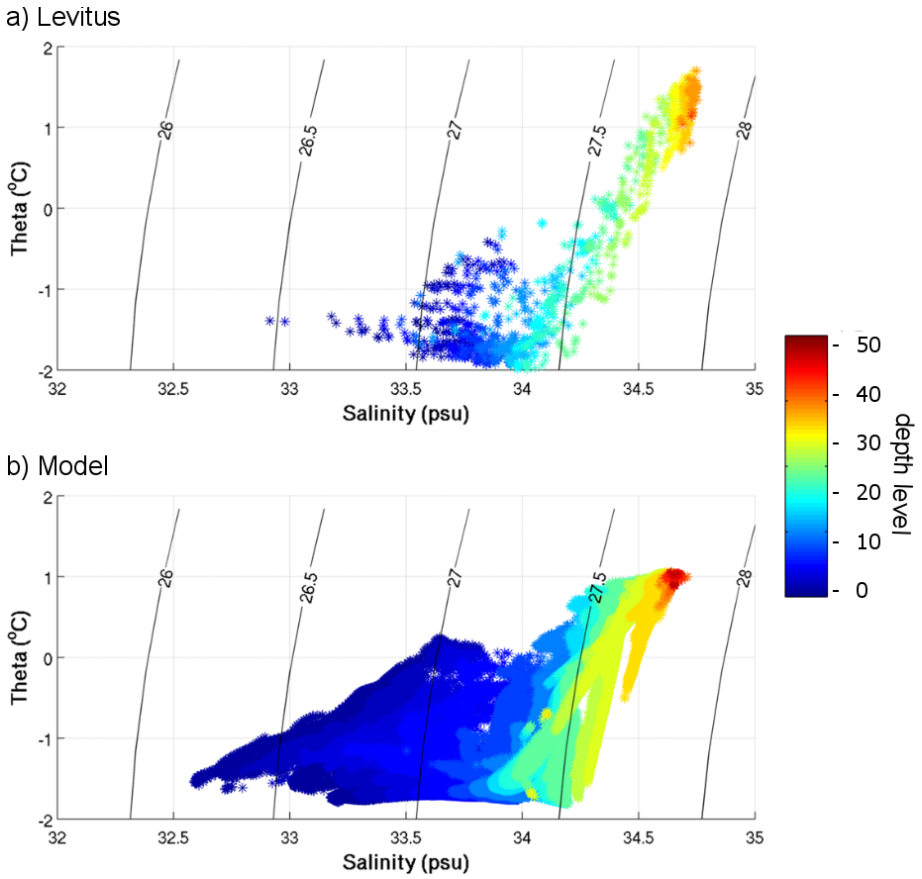

Figure 4.6: Potential temperature-salinity diagram for a) annual Levitus and b) annual model output on the shelf, defined as areas less than 1000 metres, for each season (clockwise from top left: a) summer, b) autumn, d) winter, and c) spring) averaged over the period 1989-2014. In this plot, all values east of 298 °W have been removed to remove the influence of Bransfield Strait. Surface waters are shown in blue, with deep waters in red, moving through the colour scale according to the depth level as indicated by the colour bar. Density contours (kgm^{-3}) calculated using MATLAB file exchange script *theta_sdiag* (Bhatt; 2009), utilising *sw_dens* (Meyer et al.; 2014).

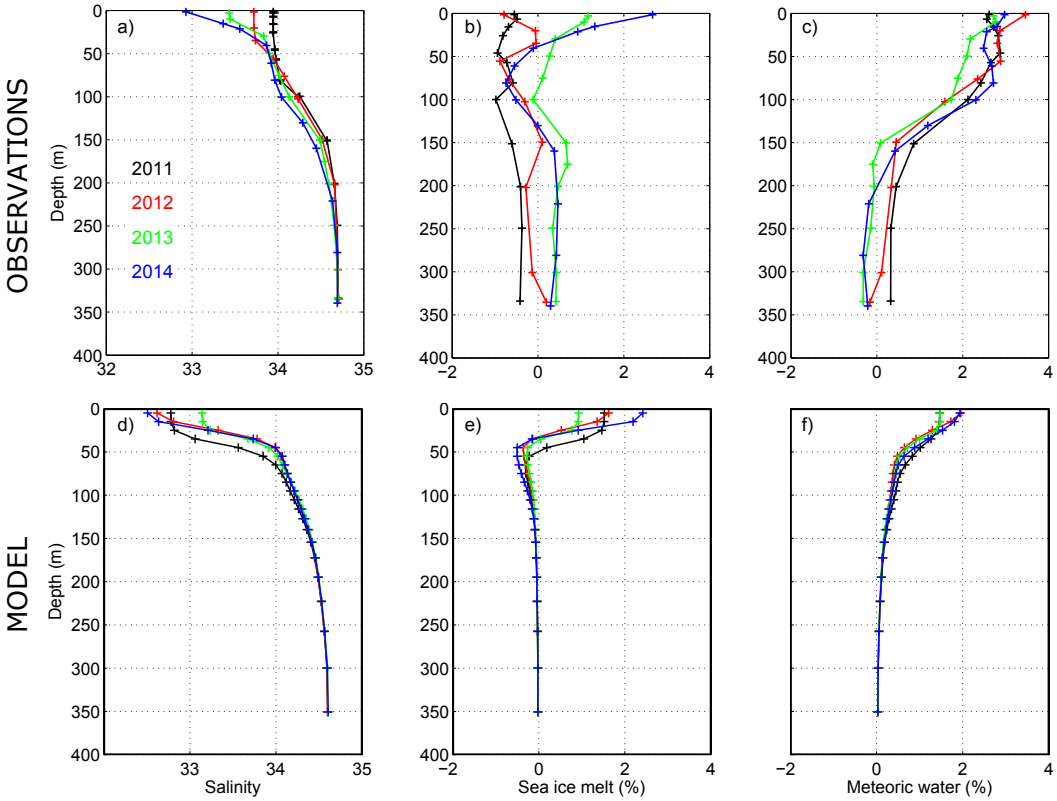

Figure 4.7: Salinity (a,d), sea ice melt (b,e) and meteoric water content (c,f) at 65°52.6' S, 68°17.0' W (see Figure 4.1). Top row (a-c) reproduced from Meredith et al. (2016) for validation purposes, with bottom row (d-f) showing the model equivalent for January 2011 (black), 2012 (red), 2013 (green) and 2014 (blue).

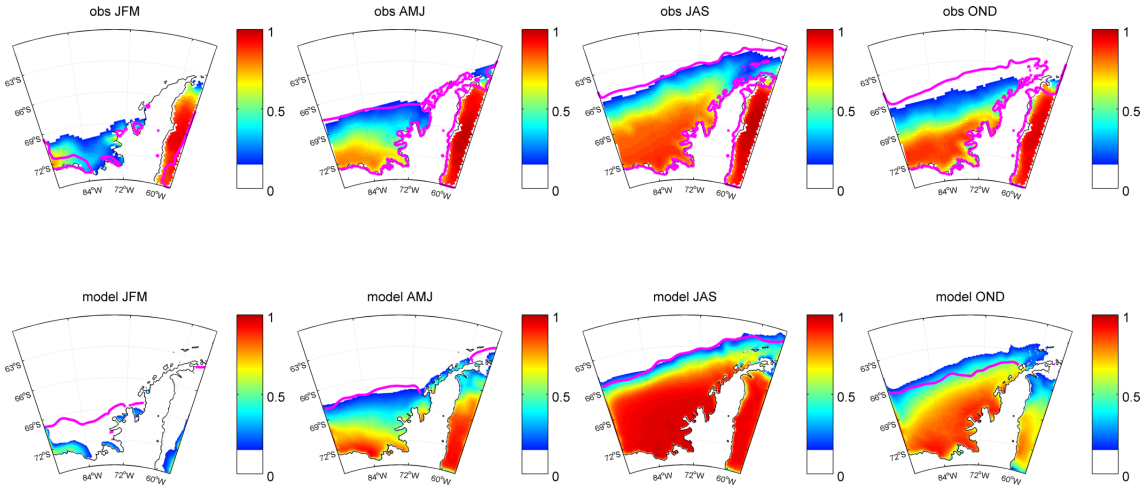

Figure 4.8: Sea ice concentration observations from Cavalieri et al. (1996) (top) and model (bottom) output for summer (JFM), autumn (AMJ), winter (JAS) and spring (OND), averaged over the time period 1989-2014. Ice below 15% has been removed. On the observations, the pink contour shows the 15% contour of the model for the same season, and vice versa.

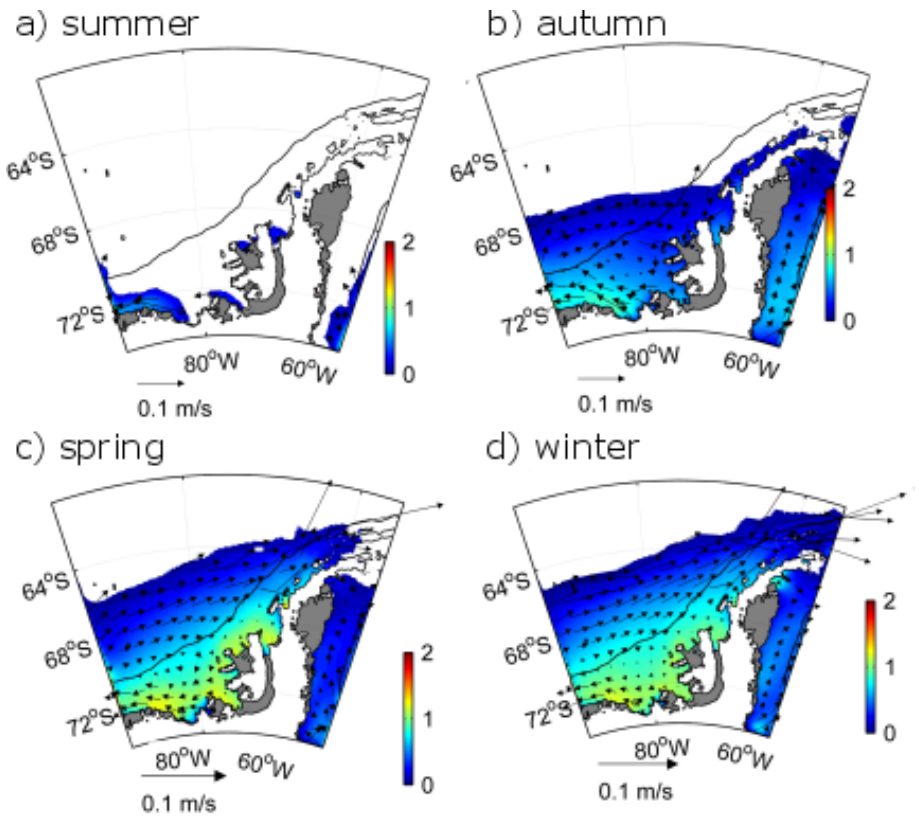

Figure 4.9: Sea ice thickness averages over 1989-2014 for (clockwise from top left) a) summer, b) autumn, d) winter and c) spring. Grey contours show the 0.2 metre intervals. Land, along with regions of no ice in the ocean, are shown in white, with ice shelves in grey. Thickness where sea ice concentration is less than 15% is masked.

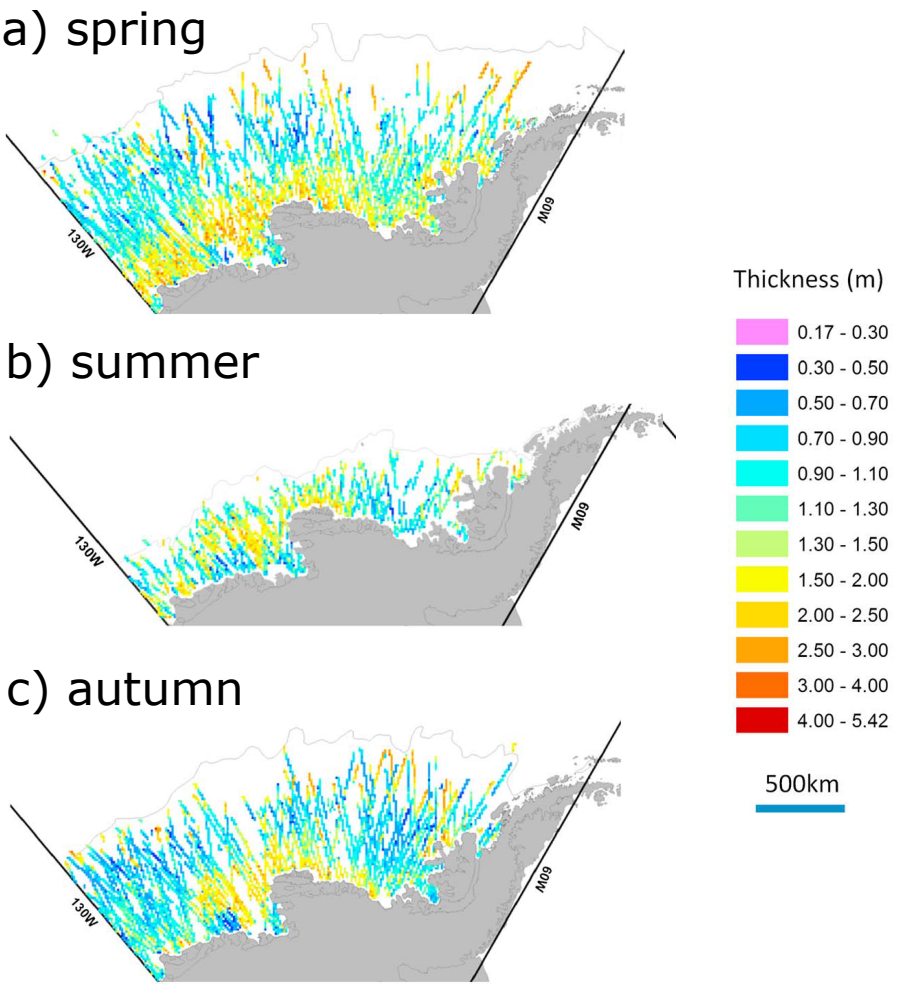

Figure 4.10: Sea ice thickness, taken from from Xie et al. (2013) for a) spring, b) summer, and c) autumn over 2003-2009. Thickness is calculated empirically using ICESat satellite data.

values of 0.6-2.3 metres found by repeat springtime measurements at 93 °W, 70 °S by Lewis et al. (2011). While quantitative comparisons with Xie et al. (2013) must be conducted with caution given that they include the Amundsen Sea, the thickness estimates are still much higher than what the model recreates. Potentially the underestimation by the model can be explained by the thick regions of ice occurring out of the domain and the differing time period of the averaging (the model values are averaged over 1989-2014, which will include interannual variability and decadal trends, while Xie et al. (2013) results are from 2003-2009). Additionally, taking an area average is not straightforward because it excludes the vast spatial variance in sea ice thickness. Figure 4.9 shows the seasonal cycle of the sea ice thickness, and Figure 4.10 shows the spring to autumn spatial variation in thickness found by Xie et al. (2011). In terms of distribution, the increase to the west of the region and by Alexander Island are recreated successfully, although an increase at the northern ice edge is not reproduced by the model. It should be noted here that the definition of seasons is slightly different, with autumn being classified as October-December, slightly misaligned with the definition by Xie et al. (2013) who use October, November and half of September and December.

Table 4.1: Ice shelf melt rates, averaged over the spatial area of each ice shelf and the time period 1989-2014, are shown, with error bars indicating 1 standard deviation of interannual variability. Also shown are the 2003-2008 average ice shelf melt rates from Rignot et al. (2013) and 1979-2010 melt rates from Depoorter et al. (2013) where available, with error bars showing observational error.

	Model (1989-2014)	Rignot et al. (2013) (2003-2008)	Depoorter et al. (2013) (1979-2010)
George VI	4.74±0.19	3.8±0.7	2.88±0.83
Wilkins	1.00±0.28	1.5±1	-
Bach	0.43±0.03	2.3±0.3	-
Stange	1.11±0.26	3.5±0.7	-
Venable	1.99±0.34	6.1±0.7	4.82±0.83
Abbot	2.26±0.19	1.7±0.6	2.72±0.70

4.1.3 Ice shelf model

As mentioned in section 2.7, reducing the ice shelf melt by improving the melting equations (section 2.6.4) caused the model to behave unrealistically in certain regions, but fixing the issue made the ice shelf melting increase; George VI increased to 6.18 m/yr. This was reduced to its final value by turning the ice-ocean drag coefficient c_d down to 0.001, the value used by Holland et al. (2010), from its arbitrary model default value of 0.0015. Jenkins et al. (2010) found that a value of 6.2×10^{-3} allowed good representation of the melting beneath Ronne Ice Shelf, but models use a wide range of values. Dansereau et al. (2014) explore the variation of c_d, noting that a) it varies strongly spatially in reality, but the model uses a constant value, b) it is very uncertain what the realistic value should be, and c) while the default is often used, some studies vary it in order to tune melt rates. This justifies the variation in the parameter from the default.

An assessment of the modelled ice shelf melt flux is an important requirement of this study. Table 4.1 summarises the six main ice shelves in the domain and their melt rates derived from both the model and glaciological mass budgets. Note that Abbot Ice Shelf is only partially covered by the model. George VI Ice Shelf (GVIIS) is the only ice shelf where there are additional data from oceanographic observations, summarised in Holland et al. (2010). The modelled GVIIS melting (4.74±0.19 m/yr) is within 3-5 m/yr, the range quoted by Jenkins and Jacobs (2008), but slightly higher than the values found by both Rignot et al. (2013) (3.8±0.7 m/yr) and Depoorter et al. (2013) (2.88±0.83 m/yr).

Concerning the other ice shelves, modelled Wilkins Ice Shelf melting is slightly too low compared to the data and Bach, Stange and Venable ice shelf melt rates are all underestimated by a larger margin. Only half of Abbot Ice Shelf is included in the model domain, but is in good agreement with Rignot et al. (2013) and Depoorter et al. (2013). It should be noted that the time period of averaging is important here: the latter two studies use different time periods than the model. Padman et al. (2012) find a 1992-2008

average for Wilkins Ice Shelf to be 1.3±0.4 m/yr, within bounds of the Bellingshausen Sea model, but if this is divided by the year 2000 the melt rates are 1.8±0.4 (1992-2000) and 0.75±0.55 m/yr (2001-2008) respectively; the earlier time period is well away from the model result but the 2001-2008 average is comparable, showing interannual variability in the melt rates that is dampened by averaging over longer time period. Similarly, Bach Ice Shelf was estimated to have a steady state melt rate of 0.65 m/yr in the 1970s (Woodruff and Doake; 1979), more in line with the value of the model (although still larger).

Relatively low model resolution and poorly-known ice-shelf cavity geometry are significant limiting factors and therefore it is hard to fully recreate ice shelf melt rates in these smaller, poorly sampled cavities. Future improvements to the model can be made once suitable surveys of the cavities have been conducted. Holland et al. (2010) find similar deviation from model results, suggesting the coarseness of the grid and ice shelf topography are limiters. While these are certainly factors to consider in results, the melt rates produced are still deemed reasonable enough for studying the behaviour of ice shelf melt on the peninsula; George VI, the most studied of the ice shelves, is accurate and the other values are either close to error bars or not well known in reality.

4.2 Spatial freshwater distribution

4.2.1 Spatial distribution

A first indication of the freshwater balance of the Bellingshausen Sea can be gained by looking at the surface freshwater fluxes. In the long-term mean, each freshwater source into the Bellingshausen Sea is of comparable magnitude (Figure 4.11), albeit with strong spatial variation. In particular, there is a clear difference between the north and south, separated by Alexander Island and GVIIS. In the north, there is a strong positive contribution of freshwater extending across the shelf break out into the ACC, comprising precipitation, sea ice melt, and imposed iceberg melt (the prescribed runoff field). Strong sea ice freezing results in a net loss of sea ice freshwater directly adjacent to the entire coastline. This is particularly apparent in the south, where it is only countered by ice shelf melt and imposed iceberg melt; the cooler climate reduces both the precipitation rate and the open ocean area into which it falls. The surface (top 10 m) tracer concentration fields (Figure 4.12) reflect the spatial distribution in freshwater fluxes, their relative magnitudes, and redistribution and mixing of the freshwater by ocean processes, and demonstrate that the freshwater composition in any particular location cannot in general be deduced from fluxes alone (or vice versa). Over the deep ocean, evaporation, precipitation, and sea ice melt dominate the total freshwater budget. On the wAP shelf all components have localised contributions, resulting in total traced freshwater content exceeding 3% concentration in coastal areas and 5% in Marguerite Bay. The local variations are explored below. Evaporation and precipitation tracers demonstrate the role of westward advection along the coastal current from their source regions in the north.

Sea ice meltwater accumulates in the far west despite this being a region of net freezing

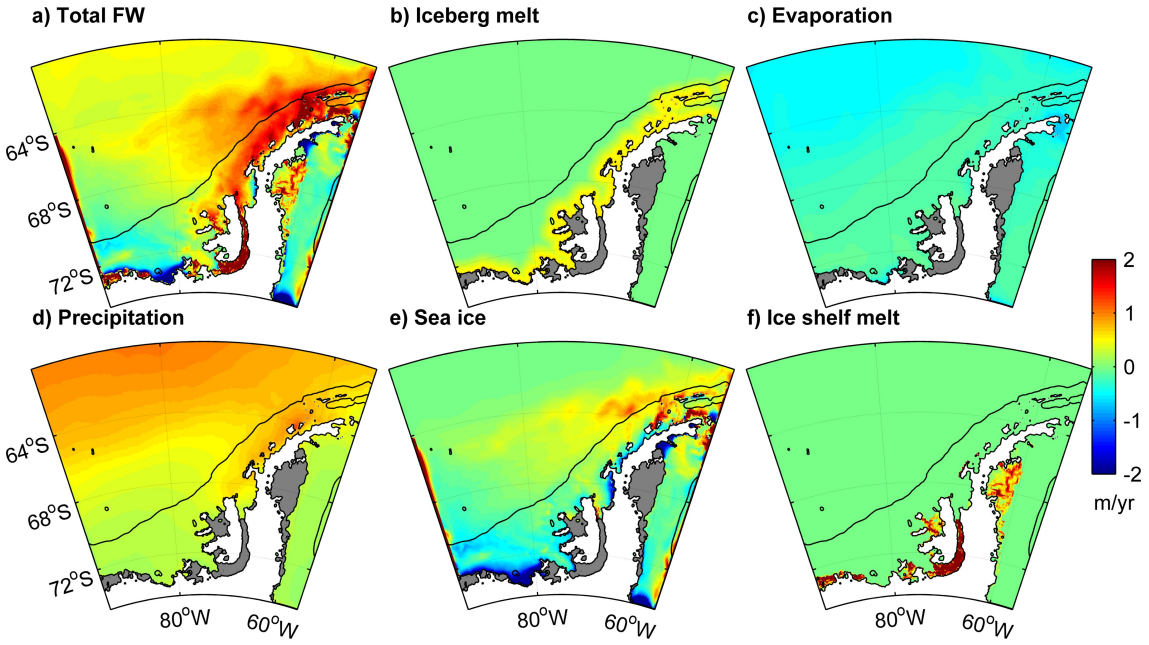

Figure 4.11: Mean (1989-2014) of freshwater fluxes (positive downwards) for a) total freshwater, b) iceberg melt, c) evaporation, d) precipitation, e) sea ice and f) ice shelf melt, all shown on the same scale. Grey regions indicate ice shelves, with the shelf break contoured at 1000 metres.

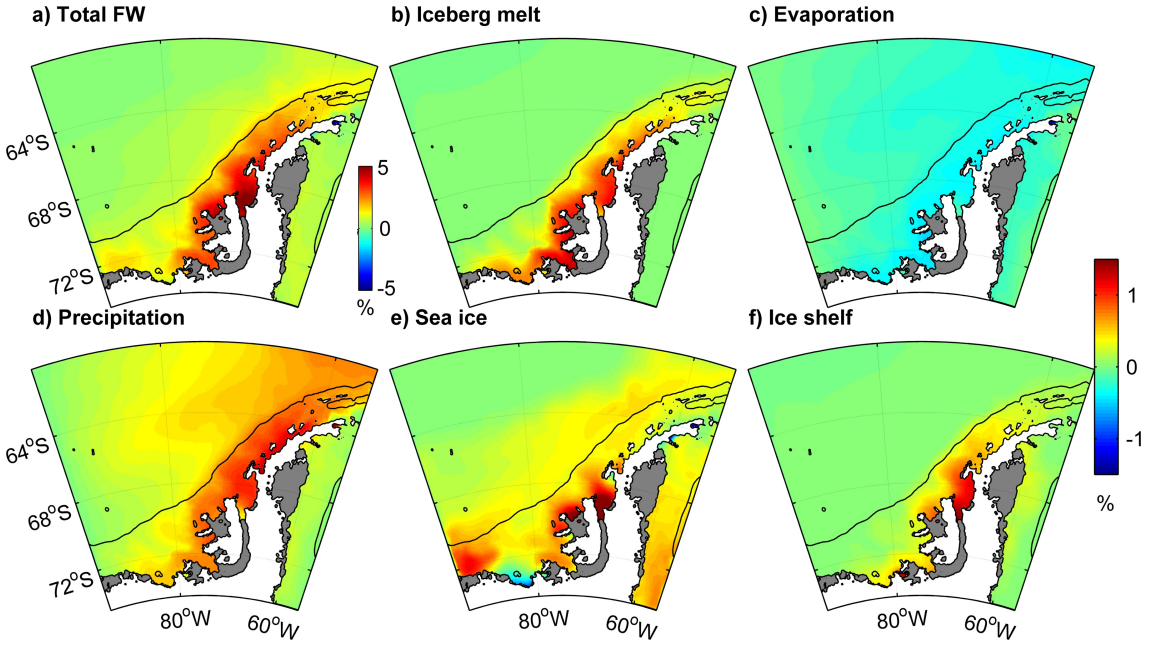

Figure 4.12: Mean (1989-2014) surface concentration of tracers for a) total freshwater, b) iceberg melt, c) evaporation, d) precipitation, e) sea ice and f) ice shelf melt. Grey regions indicate ice shelves, with the shelf break contoured at 1000 metres. Note the different colour scale for total freshwater.

(Figure 4.12e). Adjacent to this sea ice meltwater lies a pool of water depleted in sea ice tracer at the surface, due to strong ice growth in polynyas in Eltanin Bay (Holland et al.; 2010). This is countered by meteoric freshwater to result in a net positive concentration of freshwater tracer overall, masking the sea ice signal, which reaffirms the need to consider the behaviour of individual freshwater components rather than overall freshwater. All tracer concentrations are elevated east of Ronne Entrance, particularly in Marguerite Bay. Ice shelf melt reaches the surface in large volumes in Marguerite Bay but not elsewhere.

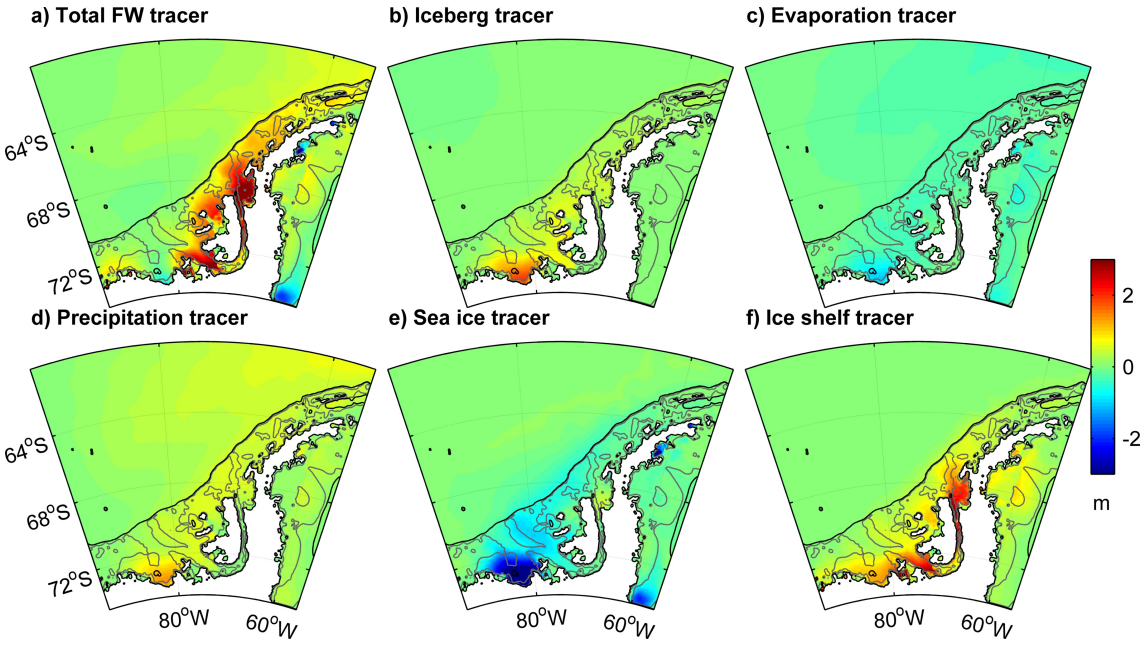

Figure 4.13: Mean (1989-2014) water-column integral of each tracer content, in metres. a) Total freshwater b) iceberg melt, c) evaporation, d) precipitation, e) sea ice and f) ice shelf melt all shown on the same scale. Bathymetry contours are shown at 100, 500, and 1000 metres.

The surface model layer accounts for less than 5% of the full water column tracer content and masks significant features at depth. Depth-integrals of the tracers (Figure 4.13) show that while surface freshwater is concentrated around the north of GVIIS and Alexander Island, the signals from surface inputs summed over all depths gather in Eltanin Bay. This occurs because the model predicts strong ice growth and convection in wintertime polynyas in this region (Holland et al.; 2010) which mix the surface tracers down through the water column. Convection does not reach the sea bed, so the model remains consistent with observations of a warm CDW layer in this region (Zhang et al.; 2016). However, the deep model mixed layer in some areas such as Eltanin Bay is unverified by observations and could be unrealistically deep.

The vertically-integrated tracers show that ice-shelf melting (Figure 4.13f) is the largest contributor to freshwater over the full water column. At both ends of GVIIS, the vertically integrated ice shelf meltwater shows a strong enhancement, and this water is also able to reach the surface ocean in the north in large quantities (Figure 4.12f). This sug-

gests buoyancy-driven flow occurring in Marguerite Bay and along the coast, in agreement with the finding of Talbot (1988) that upwelling of CDW is more significant to the north of GVIIS than in the southern BS. This result has important implications for the interpretation, and comparison, of geographically-separated sediment core δ^{18}O records that may be recording waters from different sources, or missing the bulk of some freshwater components, despite the δ^{18}O being measured on organisms living at the same depth and in the same ecological niche.

The spatial variation in freshwater content is clearly created by the fluxes into the ocean as well as the ocean processes active across the shelf. It is known that the AP shelf has a strong seasonal cycle in sea ice, and a buoyancy-driven summer coastal current (Moffat et al.; 2008), and thus the seasonal variation in both the flux and tracer content must be explored.

4.3 Freshwater seasonality

The annual average of freshwater quantities can provide an overview of the budget, but it does not indicate seasonal variation. Here, the seasons have been defined such that spring = October to December, summer = January to March, autumn = April to June, and winter = July to September. This choice of seasons is made to centre summer on the climatological sea ice minimum in February.

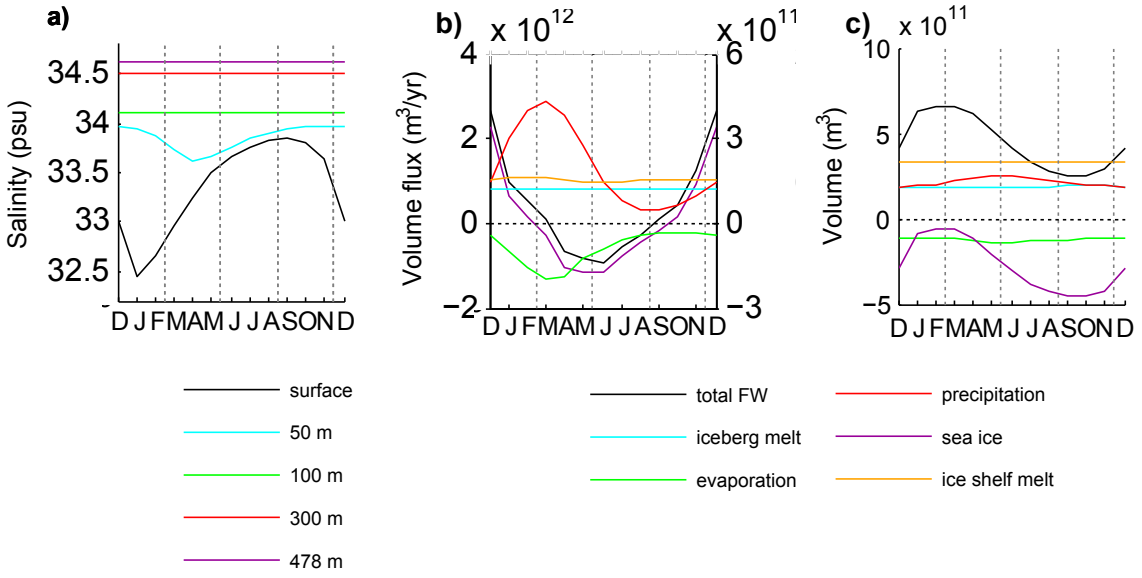

Figure 4.14: Seasonal variation of freshwater on the BS shelf (shallower than 1000 metres). Plots show seasonal cycles of a) mean salinity at different depths; b) area-integrated freshwater fluxes; and c) volume-integrated tracer content. Note that in panel b) the left y-axis is used for total freshwater and sea ice, while the right y-axis is used for all other fluxes.

The Bellingshausen Sea extends out to the ACC, and thus in this study is defined out

to the shelf break at 1000 metres. Here it should be noted that all quantification and analysis does not include the Weddell Sea as it is beyond the scope of the study.

On an annual mean, the magnitude of freshwater fluxes and their associated tracers are comparable. However, the seasonal variation differs markedly between tracers. The salinity at the surface, which receives the majority of freshwater inputs, has a strong seasonal cycle (Figure 4.14a), with less variability at depth. During winter, the upper ocean has relatively uniform salinity due to the deepened mixed layer. The onset of surface freshening occurs in October, with the minimum salinity occurring in January. At deeper levels the lowest salinities occur later in summer and are less pronounced.

The seasonal cycle in the sea ice flux is an order of magnitude larger than seasonal variation in other freshwater inputs (Figure 4.14b), with its maximum negative values in autumn showing a strong freezing occurring. Evaporation also has a negative sign as it reflects a negative freshwater input. Precipitation and evaporation peak in summer, once sea ice has melted. While the seasonal variability of these is higher than glacial inputs, their annual mean contribution is comparable.

The domination of sea ice variability over the seasonal flux cycle (Figure 4.14b) is reflected in the seasonality of its associated tracer concentration (Figure 4.14c). However, while instantaneous freshwater fluxes are dominated by sea ice, the annual-mean flux, and hence the total freshwater concentration, is a balance of all sources. Table 4.2 shows that precipitation is the biggest annual contributor, followed by ice shelf meltwater flux, with sea ice contributing the least on an annual mean, negative overall due to the large net freezing in the south (Figure 4.11). The associated precipitation and ice shelf tracers are similarly large, with ice shelf melt dominating as shown earlier.

The sea ice tracer content has a negative sign. This is because sea ice meltwater injects surface waters, while freezing results in brine-enhanced waters deepening the mixed layer, meaning they reside at depth. The surface waters are more rapidly exported off the shelf by surface currents, and out of the domain via the boundary conditions, meaning that on average the effect of freezing overrides the strong positive signal from surface meltwater. This indicates a high residence time of the subsurface brine-enhanced saline waters. The seasonal variability in freshwater tracers is lagged from the variability in its sources, with the peak sea ice and total freshwater tracer in February-March and peak precipitation tracer in June. This is because until the flux falls below average, the tracer content is influenced by above-average freshwater input, so continues to increase, and only when the flux drops below average does the freshwater content experience a big enough reduction in the influx to counter the influence of the previous input.

Maps of seasonal distribution explain the shelf-wide pattern. While sea ice tracer content has the most extreme magnitude in summer and winter (Figure 4.17), the sea ice freshwater flux is maximised in spring and autumn (Figure 4.15). Precipitation also shows seasonal variation in the form of a larger freshwater input in autumn than spring that extends further south, especially close to the peninsula. Glacial freshwater sources (ice shelf melt and prescribed iceberg melt) are seasonally uniform.

Table 4.2: Table showing the annual mean and seasonal variability of each flux ($\times 10^{11}$ m^3/y) and tracer on the shelf ($\times 10^{11}$ m^3) from Figure 4.14. The annual cycle was calculated by taking the average of each month over the 26 years, which was then averaged to produce the annual mean.

	Annual mean	Seasonal variability (1 sd)
Total FW flux	2.11	10.26
Sea ice flux	-0.79	9.95
Precipitation flux	2.04	1.49
Evaporation flux	-0.92	0.61
Iceberg flux	1.23	*N/A**
Ice shelf flux	1.53	0.06
Total tracer	4.41	1.62
Sea ice tracer	-2.77	1.57
Precipitation tracer	2.19	0.23
Evaporation tracer	-1.25	0.09
Iceberg tracer	1.89	0.01
Ice shelf tracer	3.30	0.01

*Not applicable as prescribed iceberg flux is temporally uniform

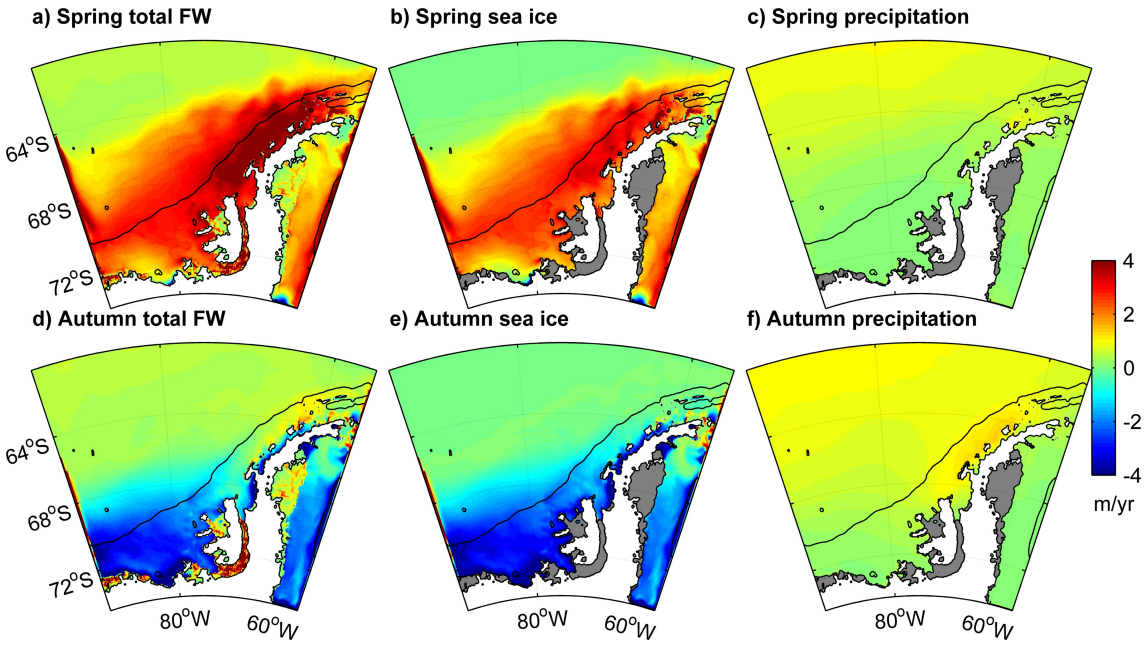

Figure 4.15: Seasonal distribution of fluxes of (a,d) total freshwater, (b,e) net sea ice melt/growth, and (c,f) precipitation for the spring (top) and autumn (bottom). Grey regions indicate ice shelves, with the shelf break contoured at 1000 metres.

Figure 4.16 shows the seasonal cycle in salinity at the surface, where the ocean interacts with the most seasonally-variable fluxes. The freshest waters occur in the summer near the coast, extending out to the shelf break, and to a lesser extent out to the maximum sea ice extent near 64 °S. Spring and autumn have similar salinity distributions, freshest in the north where there are multiple freshwater inputs. In the winter there is a net salinification, particularly in Eltanin Bay, which is also seen on a small scale in autumn and remains in spring.

Given that the sea ice flux dominates the seasonal cycle, the salinity variation (Figure 4.16) can be compared to the surface sea ice tracer. Figure 4.16 largely mirrors the distribution of the sea ice tracer (Figure 4.17), showing that the shelf-wide seasonal cycle of salinity and sea ice tracer are strongly linked in most locations. The autumn and spring sea ice tracers highlight the dominance of freezing in Eltanin Bay, and a large amount of sea ice melt remains close to Alexander Island late into autumn. High sea ice meltwater content in summer is offset by freezing in winter, providing opposing signals that compensate on an annual mean.

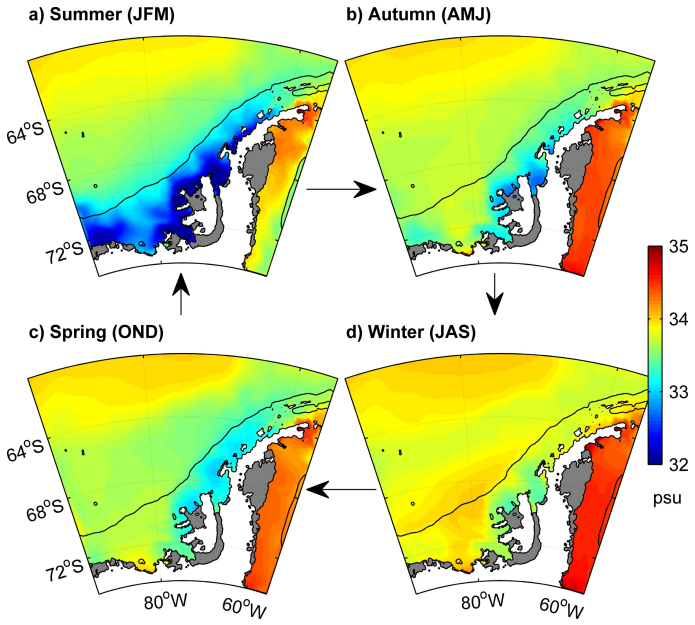

Figure 4.16: Average seasonal surface salinity, clockwise from top left: a) summer, b) autumn, d) winter and c) spring. Grey regions indicate ice shelves, with the shelf break contoured at 1000 metres.

The shelf-wide relationship between surface salinity and sea ice tracer is explored in Figure 4.18a. For each season, the surface salinity and sea ice tracer at each location on the shelf is correlated, with the magenta line showing the resulting linear fit. The heat map shows the distribution of salinity against sea ice tracer once the salinity-tracer space has been binned into a 100x100 grid. The same plots are shown for b) ice shelf tracer, c) iceberg melt tracer, d) evaporation tracer, and e) precipitation tracer.

It is clear that sea ice tracer dominates summer and autumn salinity, with the highest correlation of all plots and significant numbers of points exceeding the limits of the other tracers, as seen in Figure 4.14; in the other seasons, other tracers show higher correlation

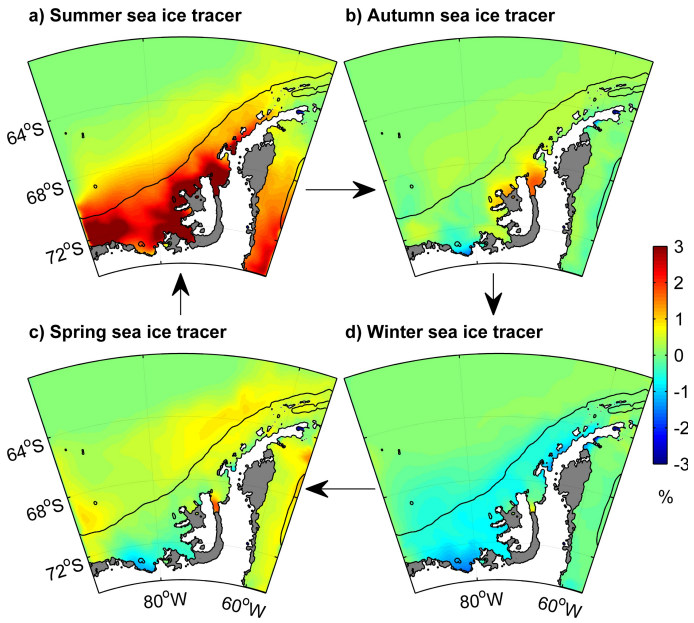

Figure 4.17: Seasonal distribution of sea ice tracer at the surface. Seasons are shown clockwise from top left: a) summer, b) autumn, d) winter and c) spring. Grey regions indicate ice shelves, with the shelf break contoured at 1000 metres.

but few exceed a correlation of 0.5. In all plots, there is a large spread away from the line of best fit. This highlights the important role of each freshwater component at the surface in all seasons, particularly winter where surface sea ice meltwater is diminished. This, in turn, suggests that caution must be taken when interpreting data collected in only one season. Evaporation (Figure 4.18d) has low tracer concentrations in a range of salinities, showing it has little influence on total surface salinity. The same can be said for precipitation and iceberg melt in winter and spring, when sea ice cover prevents access to the surface ocean. It should be noted that boundary conditions for salinity from the circumpolar model represent the effects of nonlocal salinity variations, while freshwater tracers are only based on local surface fluxes, and therefore a decoupling between the two fields is inevitable.

The fact that the correlations between sea ice tracer and salinity at the surface are highest in summer highlights the temporal variation in dominance of freshwater content distribution and the changes that can occur below the surface layer to affect the relationship. The effect of this at different geographical locations will be investigated in the next section.

4.4 Regional freshwater variation

The maps of freshwater distribution show that there is significant variation regionally, and therefore shelf-wide conclusions miss important features. In particular, there is a gradient of freshwater flux with latitude, with precipitation and net sea ice melt dominating in the north while ice shelf melt and sea ice freeze are large fluxes in the south. This translates to

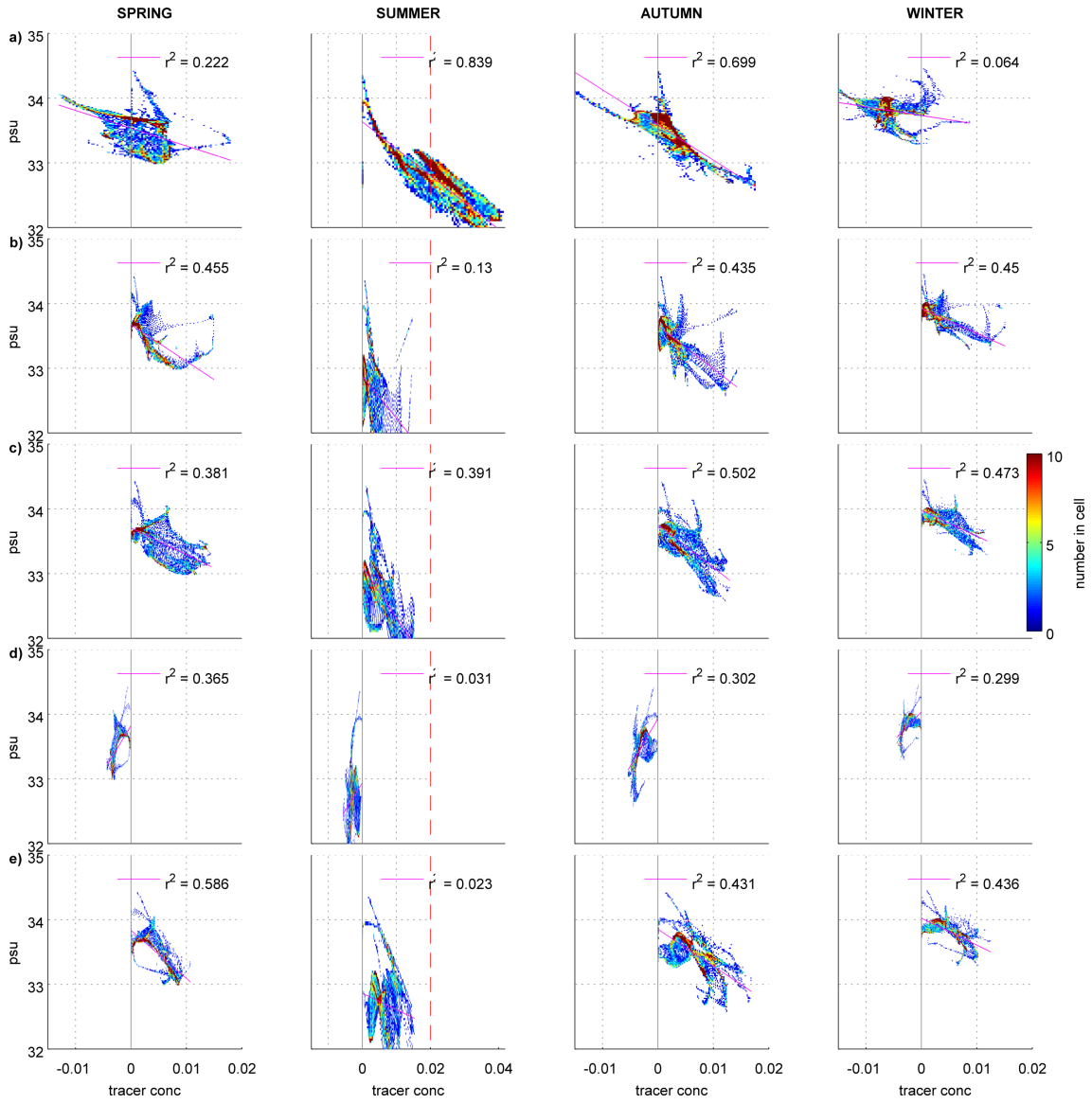

Figure 4.18: For each season, the surface salinity and tracer at each location on the shelf is correlated, with the magenta line showing the resulting linear fit. The heat map shows the distribution of salinity against tracer once the salinity-tracer space has been binned into a 100x100 grid. Plots are shown for a) sea ice tracer, b) ice shelf tracer, c) iceberg melt tracer, d) evaporation tracer, and e) precipitation tracer. Note that vertical lines are shown at 0 tracer (grey), and 0.02 tracer (red dotted) in the case of summer plots, for ease of comparison between each plot.

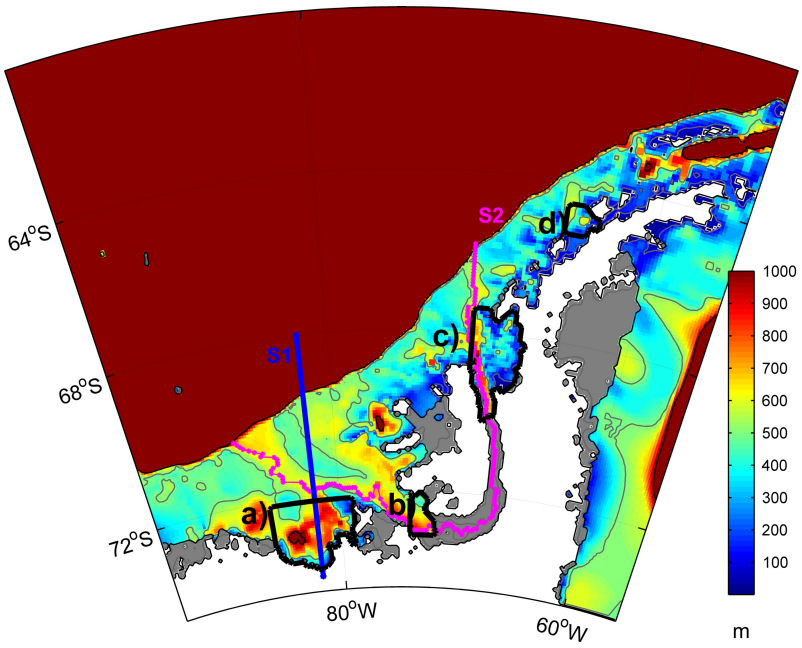

Figure 4.19: Map of the model bathymetry, with the four selected locations shown: a) Eltanin Bay, b) Ronne Entrance, c) Marguerite Bay, and d) Palmer. Also shown are locations where vertical sections are taken. S1 represents a south-north section through Eltanin Bay, and S2 is a section from the shelf break through Belgica Trough, under GVIIS and up to the shelf break via Marguerite Trough, following the deepest part of the channel.

a large positive signal of total surface freshwater tracer to the north of GVIIS in Marguerite Bay, dominated by sea ice melt and ice shelf melt, but less to the south, in Ronne Entrance, where iceberg melt and precipitation tracer appear highest at the surface. At depth the story is very different, with ice shelf melt being widespread and Eltanin Bay acting as a reservoir for freshwater. This section focuses on the exploration of these areas in detail, by quantifying the relative portions of freshwater in each, looking at their variation with depth, and investigating the variation in winds, ocean currents and sea ice distribution between these areas. The Palmer Station site, being a region which has enabled validation of the model and an area where palaeoclimate observations are frequently taken, is also displayed, resulting in the four boxes shown in Figure 4.19. Box (d) has been named the Palmer site as it is the location of Palmer Deep and the nearby Palmer Station.

4.4.1 Quantifying variation at specific locations

Figure 4.20 shows the relative contributions of freshwater to each region, and comparison with the entire shelf. Panel (a) shows average annual m/yr of each freshwater flux on the shelf in terms of its components, alongside the average flux of each freshwater component to the regions shown in 4.19, whilst (b) shows the average concentration, as a percentage, of each tracer in the surface layer for each site, and (c) shows the average depth-integrated tracer.

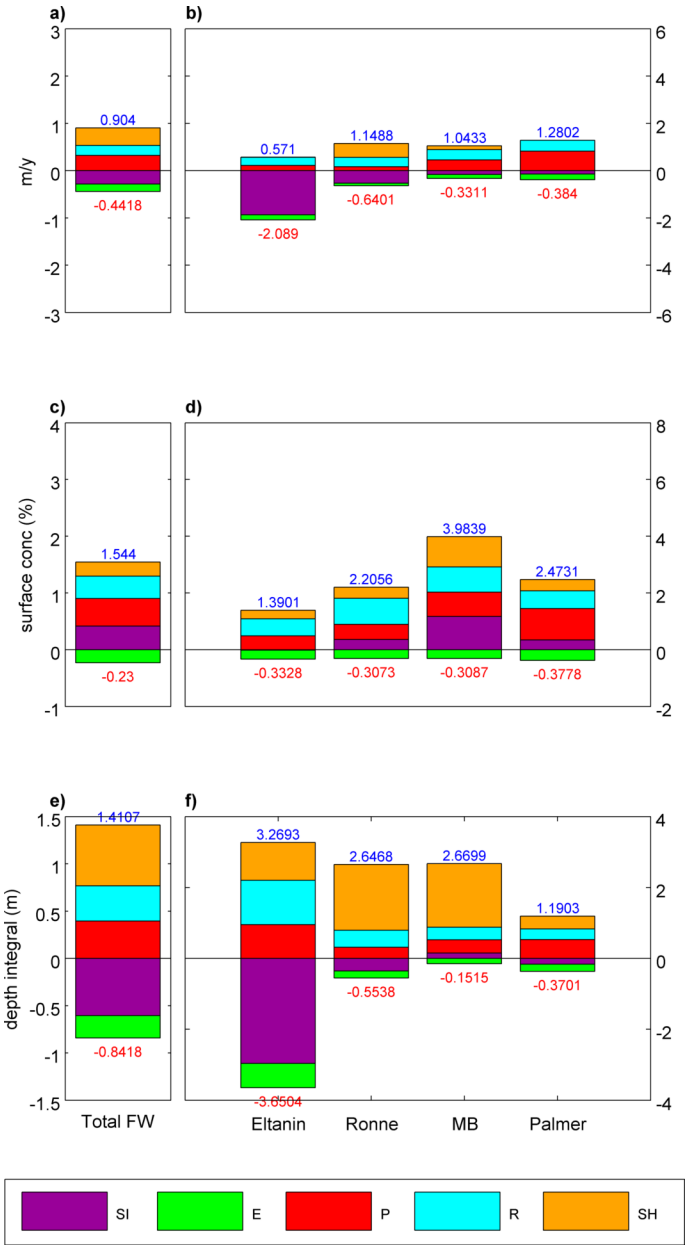

Figure 4.20: Bar graph showing a,b) average annual m/yr of each freshwater flux on the shelf in terms of its components (sea ice in purple, evaporation in green, precipitation in red, iceberg melt in blue, and ice shelf melt in orange), alongside the average flux of each freshwater component to the regions shown in Figure 4.19 (from left to right, west to east): Eltanin Bay, Ronne Entrance, Marguerite Bay and Palmer. c,d) shows the percentage concentration in the surface layer for each site, and e,f) shows the average depth-integrated tracer. Note that localised increased variability means that the axis of the individual sites is larger than the shelf average.

The net annual average freshwater flux on the shelf is around 0.5 metres per year, comprised of 0.9 m/y of positive freshwater flux and 0.44 negative (Figure 4.20a). Here ice shelf melt and precipitation are the largest terms in the budget, though all fluxes are comparable. When comparing this to individual locations (Figure 4.20b), a vastly different pattern is seen. The locations on Figure 4.20 move south-west to north-east, and this clearly reflects the shift from a region of net sea ice freezing to net melt on the annual average, as well as an increase in significance of precipitation moving northwards which is not mirrored in evaporation. This results in a general increase in positive freshwater flux and decrease in negative sources moving east and north.

The average tracer content on the shelf, at the surface (Figure 4.20c) and across the whole depth (Figure 4.20e), shows that there is variation with depth as well as spatially, with precipitation marginally greater at the surface and positive surface sea ice tracer (reflecting the pattern of the flux) and negative sea ice tracer and ice shelf melt dominating at depth.

The same ratio of sources in the overall depth-integrated shelf freshwater budget is not seen in individual locations. Ronne Entrance and Marguerite Bay are the only selected locations that have ice shelves in them, and thus are able to more closely reflect the overall shelf composition. However, whilst those sites are most aligned with the average total freshwater flux on the shelf, the depth-integrated content of Marguerite Bay (Figure 4.20f) is vastly different to the shelf-wide average (Figure 4.20e), with ice shelf melt contributing more than the other tracers combined, and very little sea ice melt. A similar story is seen at the other end of GVIIS, although the net freshwater content is lower due to an increased sea ice freezing signal at depth, and less surface tracer is retained due to less sea ice melting in the region and a lower ice shelf melt component. Figure 4.12f suggests this is because ice shelf melt from GVIIS does not reach the surface in large quantities here. Eltanin Bay is comprised of a completely different ratio to both the shelf and other selected sites, largely driven by a sea ice freezing component that alone exceeds the average freshwater content on the shelf.

Marguerite Bay exceeds the surface shelf average freshwater content (Figure 4.20d), particularly in its ice shelf melt and sea ice melt, while other tracer contributions are similar to the shelf average (Figure 4.20c). At the Palmer site, less total tracer content is present despite a large signal at the surface, suggesting surface waters are advected away quickly and replaced with large surface fluxes rather than remaining to be mixed down. All sites contain contributions from ice shelf melt despite their lack of presence in the north, which is in agreement with Nakayama et al. (2014a) who find that 30% of ice shelf meltwater from the Bellingshausen Sea heads northeast. Eltanin Bay shows some similarities to the average shelf content at depth, with a large reservoir of brine-enhanced water from freezing sea ice. Very little sea ice registers in the budget at the surface, despite there being a large negative flux here as indicated by the maps.

4.4.2 Comparison with observations

While there are rather few observations for constraining the freshwater budget of the Bellingshausen Sea, it can be helpful to view these numbers in the context of repeat measurements taken. Meredith et al. (2010) collected δ^{18}O profiles from the Rothera Time Series (RaTS) site, a year-round quasi-weekly sampling of Ryder Bay, adjacent to Rothera Station on Adelaide Island (the northern land border of Figure 4.19, area c) which has been taking oceanographic measurements since 1997. While this location is not resolved in the model (the closest grid cells are those bordering Adelaide Island), it can be helpful to see the model's prediction of the nearby Marguerite Bay freshwater content and the RaTS observations in the context of the model's shelf average. Samples were taken on an annual basis from 1999 to 2007 from various spring/summer months (Meredith et al. (2010), , shown in Figure 4.21). Those that were taken earlier in the year are more consistent with modelled summer values, both records showing an increase in positive freshwater composition during the year. Modelled values are generally lower than the record, both for positive and negative amounts of tracer content, and only one year from the RaTS observations sees a positive signal from sea ice. This emphasises the regional variability and the effects of local freshwater inputs. Both records have much more meteoric water than sea ice melt, showing the significance of glacial inputs despite the strong seasonal sea ice cycle in the area. The shelf average is not representative of the RaTS data, showing both limitations in extrapolating from data and the hidden information that can be lost from averaging.

Meredith et al. (2013) provide another record of oxygen isotope-derived freshwater composition from January 2011 in the region of the Palmer site analysed previously (Figure 4.21 b and c. The data uses near-surface values presented as percentages of total seawater volume, which when converted to a percentage of the surface layer, shows that the model generally aligns with the data. The model predicts 2.4% in spring and 3.8% in summer (not shown), which would suggest that winter and autumn have lower freshwater content in order to create the lower annual mean, as expected.. The study notes that concentrations are elevated near the coast, something the model will struggle to capture. The significance of meteoric water over sea ice melt in the Palmer site is represented well. . However, the previous comparison to the RaTS site, and the variability in data between the two, emphasises the significant spatial variability and the caution that must be taken when using discrete observations to infer regional patterns. This must also be considered in the context of palaeoceanographic records.

4.4.3 Variability with depth

Figure 4.20 highlights both the strong variation of freshwater content with depth and its spatial variation. To understand the variation with depth more thoroughly, vertical sections of each tracer can be viewed. Figure 4.22 shows vertical sections of the long-term mean of each tracer in Eltanin Bay (Figure 4.19, section S1). There is a freshwater layer at the surface, as expected in the Bellingshausen Sea, with all freshwater sources

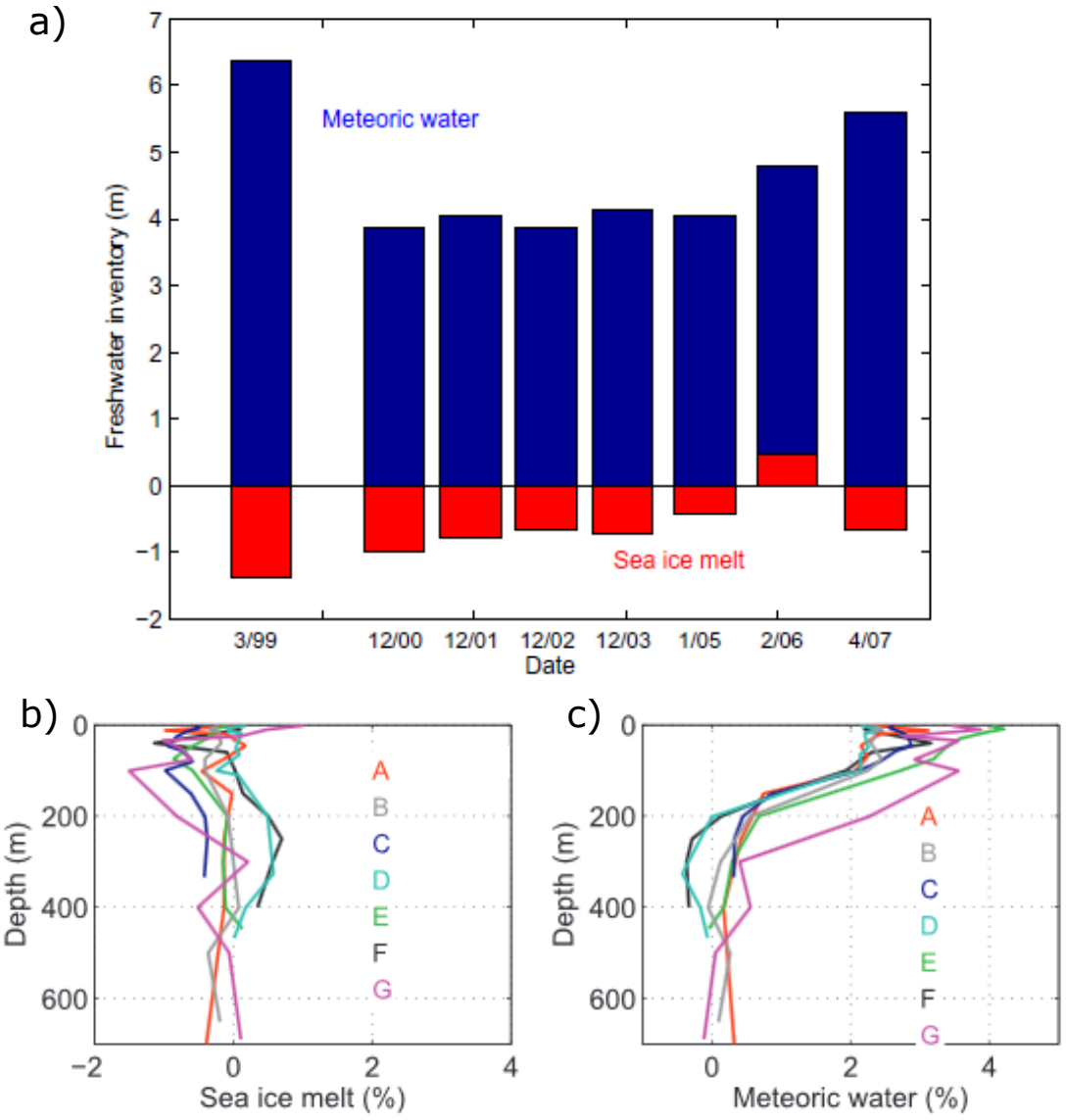

Figure 4.21: a) Bar chart taken from Meredith et al. (2010) showing meteoric water and sea ice meltwater content derived from from δ^{18}O concentrations from CTD casts at the RaTS site, Ryder Bay, adjacent to Rothera Station on Adelaide Island (the northern land border of Figure 4.19, area c), for 1999-2007 spring/summer months. Plots b) and c) taken from Meredith et al. (2013) show sea ice melt and meteoric water from the Palmer LTER grid, derived from δ^{18}O concentrations from CTD casts in January 2011.

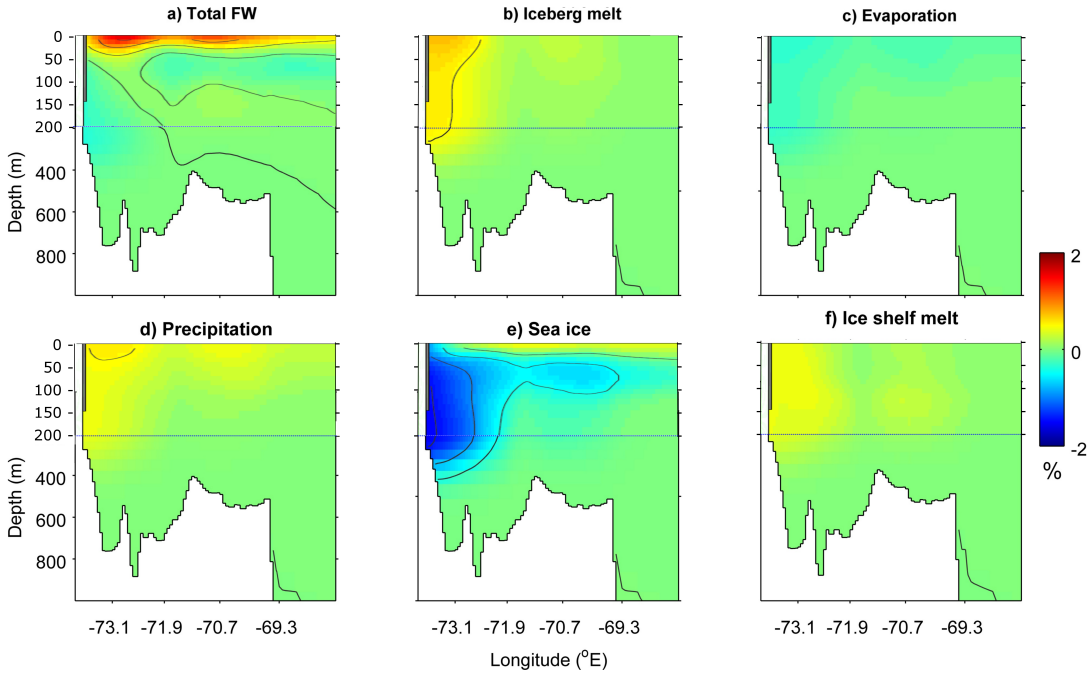

Figure 4.22: Vertical sections from south to north (Figure 4.19, section S1) in Eltanin Bay for the long-term means of a) total freshwater content, b) iceberg melt, c) evaporation, d) precipitation, e) sea ice and f) ice shelf melt. Contours are shown at 0.5% intervals. Top 200 metres (above blue dotted line) are enlarged to show the surface variation.

contributing. This is the AASW layer formed from increased summer freshwater inputs and solar radiation stratifying the water column. It can be seen that sea ice melt is dominant in forcing this layer at the very surface. The WW layer formed in winter can also be seen as a negative sea ice tracer, which maintains a presence on an annual basis. Freshwater content is strongly concentrated near the coast.

Figure 4.23 shows vertical sections from the shelf break, through Belgica Trough and Ronne Entrance, under GVIIS, and through Marguerite Trough to return to the shelf break further along the peninsula, along the section S2 in Figure 4.19. Either side of GVIIS, the AASW layer and WW layers can also be seen in the surface layers. Ice shelf meltwater tracer dominates under GVIIS. A sub-surface layer of brine-enhanced water (Figure 4.23e) is present, tracing the deeper winter water from sea ice formation and highlighting its importance on the annual mean; the magnitude of this exceeds 0.5% offshore in Ronne Entrance. More ice shelf meltwater reaches the surface in the north in Marguerite Bay, with the spatial extent exceeding that in Ronne Entrance, where other freshwater inputs at the coast reduce vertical mixing. This suggests that the surface waters are less dense than the ice shelf meltwater in Ronne Entrance than in Marguerite Bay.

In Marguerite Trough to the north of GVIIS, stratification of meltwater-enriched surface layers extends to the shelf break, but high levels of sea ice and ice shelf meltwater dominate at the ice shelf front. Ice shelf meltwater is able to reach the surface due to it being fresher than the ambient seawater. The concentration of sea-ice brine-enhanced

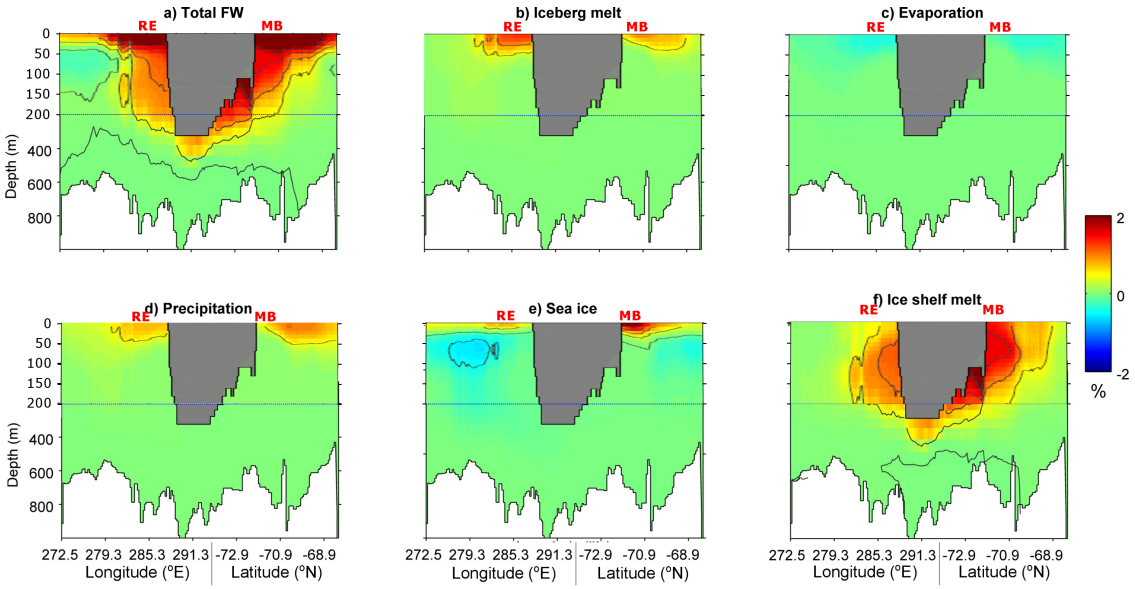

Figure 4.23: Vertical sections from the shelf break, through Belgica Trough and Ronne Entrance, under GVIIS, and through Marguerite Trough to return to the shelf break further along the peninsula, as shown in Figure 4.19, section S2. Fields shown are long-term means of a) total freshwater content, b) iceberg melt, c) evaporation, d) precipitation, e) sea ice and f) ice shelf melt. Contours are shown at 0.5% intervals. Top 200 metres (above blue dotted line) are enlarged to show the surface variation.

water is lower in Marguerite Trough than in Ronne Entrance, and the surface sea ice meltwater is stronger. Talbot (1988) proposes that the oceanic properties under GVIIS are similar to those in Marguerite Bay, and that ice shelf meltwater at the surface is a dominant source of freshwater. This was hinted at from the tracer maps, and the vertical sections here reinforce this view, backing the idea of a south-north throughflow through GVIIS (Jenkins and Jacobs; 2008) bringing large volumes of water into Marguerite Trough and onto into the shallower areas.

The sea ice tracer has a big presence at depth offshore, though the other tracers greatly reduce its influence in the total freshwater content. Close to the coast, ice shelf meltwater dominates the intermediate depths down to 400 metres, the bulk of which remains at depth below the sea ice signal as its salinity is higher than the surface layers, resulting in a second area of high freshwater concentration. The sea ice tracer shows a strong vertical gradient, with a large positive tracer concentration at the surface (Figure 4.12e), and a larger volume of brine-enhanced water at depth (Figure 4.13e) which deepens away from the coast in regions of net melt (Figure 4.23). With the simulations starting from zero sea ice tracer, positive meltwater fluxes are added to the surface in spring, and negative fluxes are extracted over a greater depth in autumn. This gradually forms the vertical structure in the model, with negative tracer residue. The overall dominance of negative tracer values (Figure 4.13e) is due to the preferential export of surface meltwater out of the domain by the coastal current. Apart from ice shelf meltwater, influence from surface-derived freshwater content is restricted to the top 200 metres through the GVIIS section (apart from very small amounts of negative sea ice tracer), while in Eltanin Bay the coastal areas experience strong mixing that deepens the mixed layer to 400 metres.

4.4.4 Oceanographic variation between locations

The evidence so far suggests that while Eltanin Bay has more freshwater content than the other selected locations, Marguerite Bay is comparable in summer and its ice shelf melt tracer is the largest of all sites, and vertical sections show key differences in meltwater composition. To understand the accompanying oceanography, the modelled ocean currents can be viewed. Figure 4.24 shows the surface layer streamfunction (a) and the barotropic streamfunction (b). For a), contours between -5 $\times$ 10^4 m^2 s^{-1} and 5 $\times$ 10^4 m^2 s^{-1} with 0.1 $\times$ 10^4 m^2 s^{-1} spacing are shown in grey, with black contours showing every 5 $\times$ 10^4 m^2 s^{-1}. In b), contours between -5 $\times$ 10^6 m^2 s^{-1} and 5 $\times$ 10^6 m^2 s^{-1} with 0.05 $\times$ 10^6 m^2 s^{-1} spacing are shown in grey, with black contours showing every 5 $\times$ 10^6 m^2 s^{-1}.

The magnitude of flow in the surface layer (a) is similar to Holland et al. (2010), and the cyclonic gyre to the north of Eltanin Bay is also present, though closer to the coast. The north of the region has higher fluxes because the boundary conditions force the Bellingshausen Sea model with the ACC. The general flow across seasons is from the southwest to the northeast on the shelf, with recirculations caused by islands and bathymetry at all depths (b). Notable recirculation areas are to the north and southwest of Adelaide Island at the surface and north of Eltanin Bay at depth, and to the west

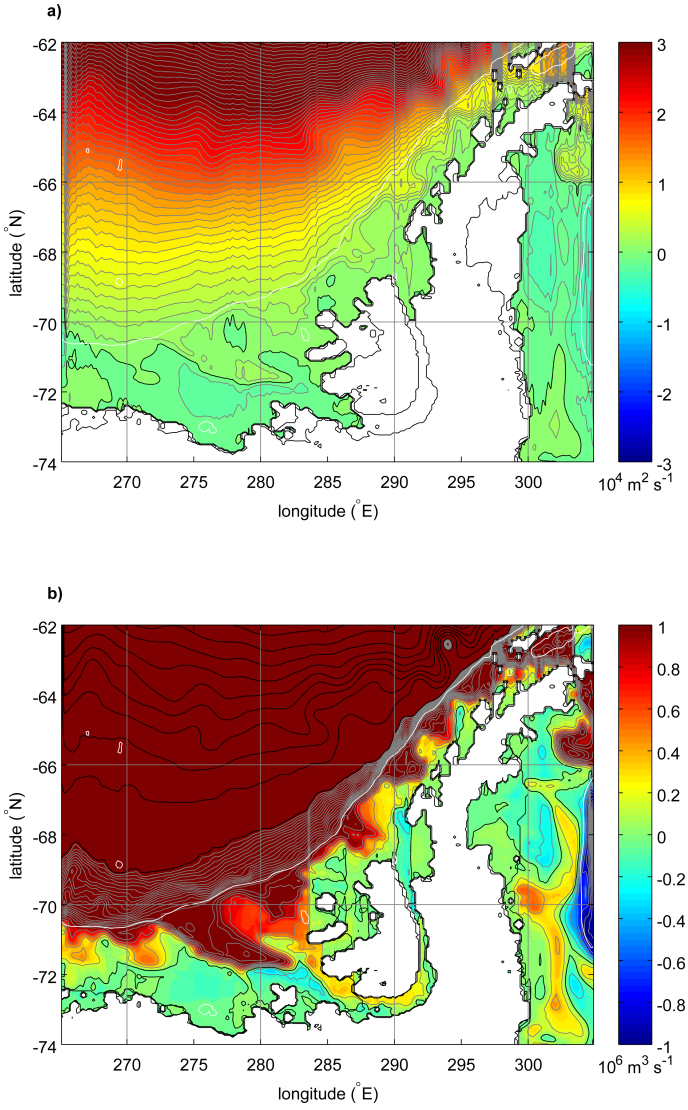

Figure 4.24: Shelf plots for a) the surface layer long-term mean streamfunction (10^4 m^2 s^{-1}), and b) the long-term mean barotropic streamfunction (10^6 m^3 s^{-1}).For a), contours between -5 $\times$ 10^4 m^2 s^{-1} and 5 $\times$ 10^4 m^2 s^{-1} with 0.1 $\times$ 10^4 m^2 s^{-1} spacing are shown in grey, with black contours showing every 5 $\times$ 10^4 m^2 s^{-1}. In b), contours between -5 $\times$ 10^6 m^2 s^{-1} and 5 $\times$ 10^6 m^2 s^{-1} with 0.05 $\times$ 10^6 m^2 s^{-1} spacing are shown in grey, with black contours showing every 5 $\times$ 10^6 m^2 s^{-1}. The shelf break is shown in white.

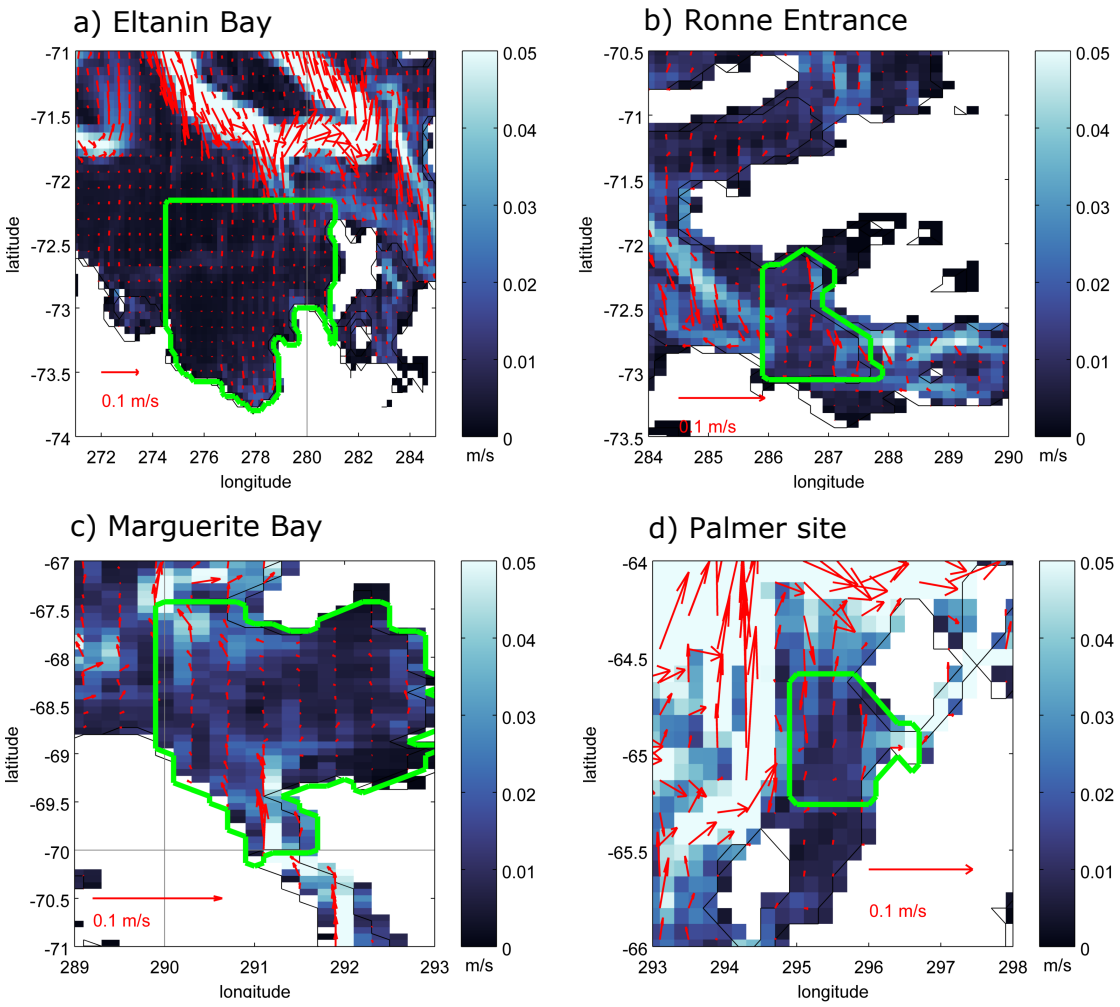

Figure 4.25: Long-term mean ocean velocities averaged over the full water column depth for a) Eltanin Bay, b) Ronne Entrance, c) Marguerite Bay, and d) Palmer. Vectors are shown every two grid points and overlaid onto gridded speed.

of Ronne Entrance. In the latter, a return flow is seen to head northwest and either rejoin the current near the shelf break or curve back round in front of Alexander Island and the Wilkins and Bach ice shelves to return to Ronne Entrance. At depth, the flow here develops as a throughflow from Ronne Entrance to Marguerite Bay under GVIIS, as in Jenkins and Jacobs (2008), which explains the increase in quantity of ice shelf melt in the latter over the former in Figure 4.20. At depth, the strongest parts of this flow are able to come further toward the coast in Marguerite Bay than at the surface where sea ice meltwater is prevalent. To the north of the region, strong flows are seen where the ACC regularly affects the shelf, but in the south all surface flows are weak near the coast where sea ice is often present.

Eltanin Bay is bounded by a strong inflow but its currents are low (Figure 4.25a) despite strong northwestward winds (Figure 4.26a) which export sea ice out of the region (Figure 4.27a), resulting in the creation of polynyas. It is this combination of sea ice export and atmospheric interaction that causes the deep mixing that is seen in Figure

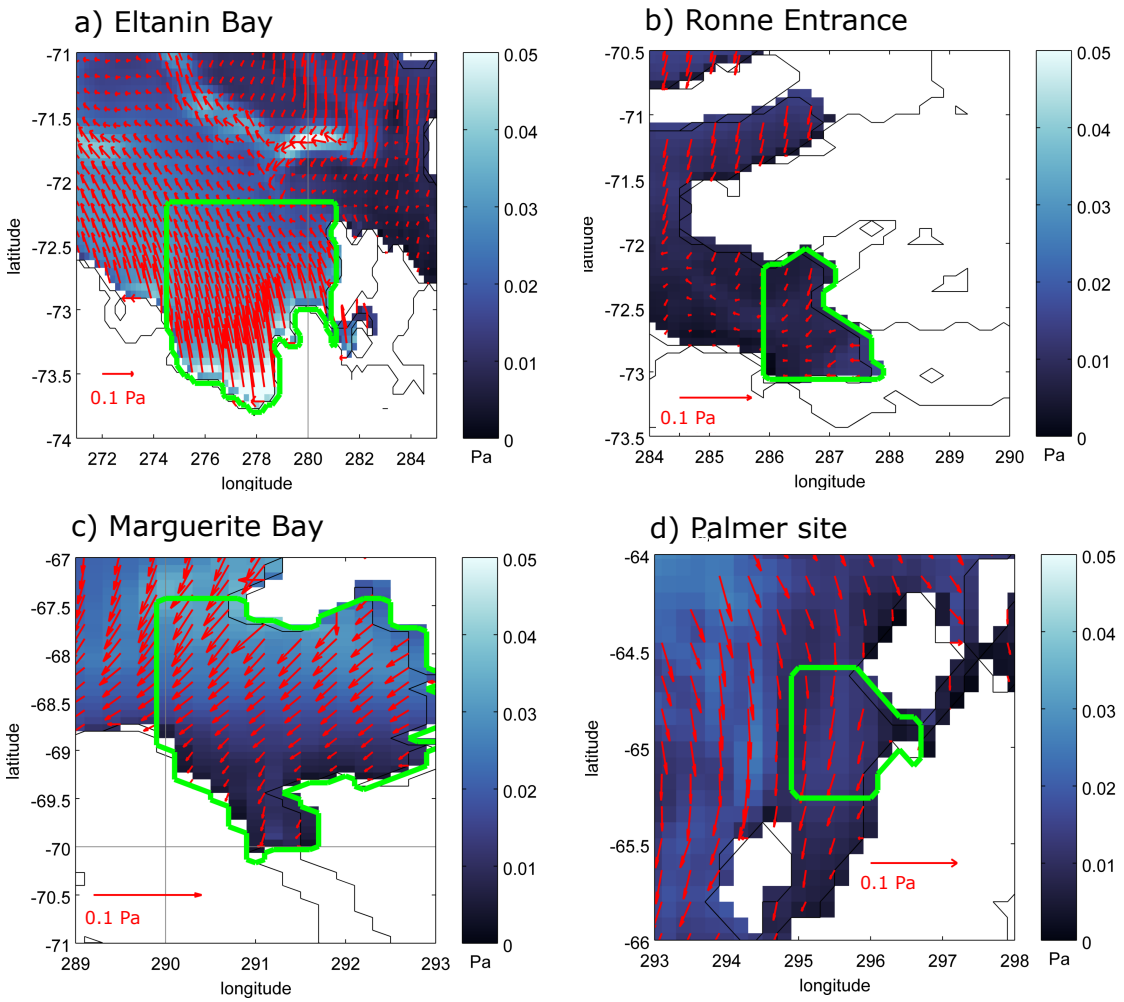

Figure 4.26: Long-term mean wind stress for a) Eltanin Bay, b) Ronne Entrance, c) Marguerite Bay, and d) Palmer. Vectors are shown every two grid points and overlaid onto gridded speed.

4.22.

The Palmer site selected covers Palmer Deep, another deep bathymetric feature on the peninsula. Like Eltanin Bay, it is bounded by strong currents to the north (Figure 4.25d), although a throughflow means that waters do not gather here like in Eltanin Bay. Strong flows from along the shelf break are brought inland by southerly winds, where they join a narrow north-eastward coastal current. So while at depth there is little motion, the surface waters are advected away quickly, aided by the complete loss of sea ice in summer (not shown). This explains the low retention of freshwater content seen in Figure 4.20. Wind stress on the ocean (Figure 4.26d) opposes the average ocean currents. Sea ice motion is more irregular than in Eltanin Bay. The Palmer site experiences very different conditions in general to Eltanin Bay, with higher air temperatures and precipitation rates and net melting of sea ice, and so these differences are to be expected.

Down the coast from the Palmer site, Marguerite Bay is more similar in terms of its atmospheric conditions (both temperatures, and wind stress and direction shown in Figure 4.26c). However, it is strongly influenced by the outflows of GVIIS, where its northward

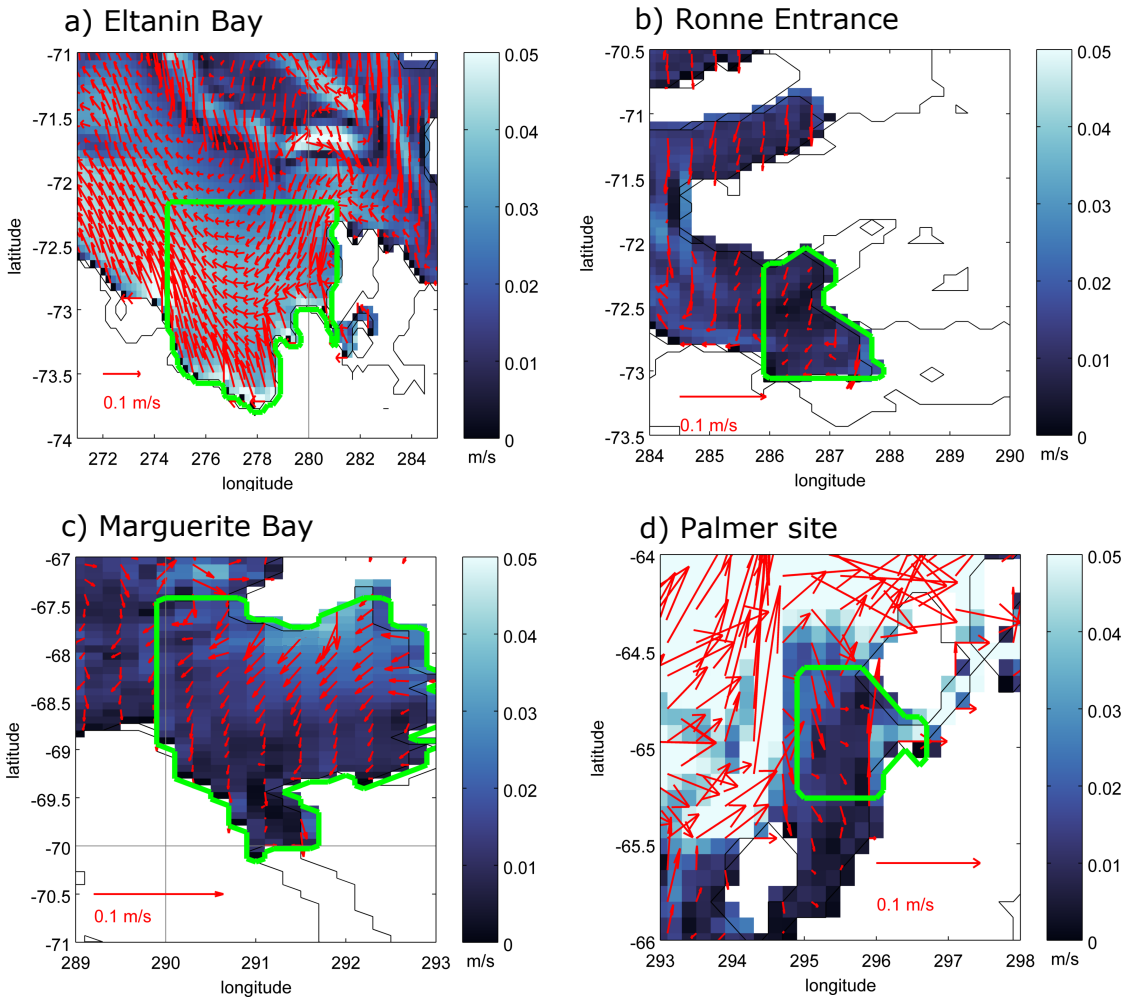

Figure 4.27: Long-term mean sea ice velocities for a) Eltanin Bay, b) Ronne Entrance, c) Marguerite Bay, and d) Palmer. Vectors are shown every two grid points and overlaid onto gridded speed.

velocities along the channel are able to influence surface flows as the meltwater rises, as seen in the vertical sections (Figure 4.23). Flow continues northwards slowly, but at the surface it enters the shallow regions of Marguerite Bay to the east and follows the coast, continuing northeast around Adelaide Island where it is joined by an eastward coastal current from Alexander Island, as seen in Figure 4.24. The wind stress forces sea ice across the entrance of GVIIS. Around Adelaide Island, south-westward winds oppose the ocean velocities, resulting in variable sea ice motion. Here, the ocean also flows faster than in the interior of Marguerite Bay.

At the other end of GVIIS, the Ronne Entrance site suffers significant sea ice compaction at the entrance to GVIIS. This was identified from Figure 4.24 as a region where recirculation along the coast is present, and this is apparent in surface patterns of all fields. There is a very narrow coastal current to the north of Ronne Entrance returning back along the coast, while the predominant flow continues under the ice shelf. This return flow up to Wilkins Ice Shelf shows that different ice shelf meltwater pathways can interact, and thus the ice shelf source cannot be deduced from proximity of meltwater.

4.4.5 Seasonality of ice shelf meltwater

The seasonal variation in freshwater fluxes is shown in Figure 4.14, with precipitation from atmospheric reanalyses and sea ice from the model having the biggest influences seasonally. Whilst ice shelf flux appears to not vary seasonally, the seasonal variation in flows observed in the southern locations (Eltanin Bay and Ronne Entrance) within the proximity of ice shelves could affect the melt rates. To investigate this, the seasonal cycle has been plotted in Figure 4.28a. Error bars are shown as 1 standard deviation from the mean seasonal cycle, derived from the timeseries after spinup. George VI Ice Shelf has the highest melt rates, with their average established during the model setup in Section 2. Those close to the western boundary, Abbot and Venable, also have reasonably high melt rates, while Stange, Bach and Wilkins surrounding Ronne Entrance have the lowest melt rates. However, it appears that Wilkins and Stange both peak when Venable and Abbot ice shelf melt rates lower.

Figure 4.28b shows the percentage change from the annual average for each season. This emphasises the patterns seen in the raw melt rates. In summer, Wilkins sees an almost 40% increase in its melt rates, with Stange over 10%, while Venable and Abbot melt rates in summer are over 5% lower than their annual average. Bach and George VI ice shelves also peak in summer but their melt rates vary less over time. The lowest seasonal melt rate for these occurs in autumn, as does that of Stange Ice Shelf, suggesting that there some link to ice shelf melt rate and other freshwater seasonality with these ice shelves. Venable and Abbot, however, peak in their melt rates in winter, showing an inverse relationship with other fluxes close to a region where a summer westward coastal current towards Abbot Ice Shelf is seen and southward flow towards the coast is seen in winter. This emphasises the different oceanographic conditions seen near Eltanin Bay compared to other regions, and the increased mixing activity, and therefore energy at the

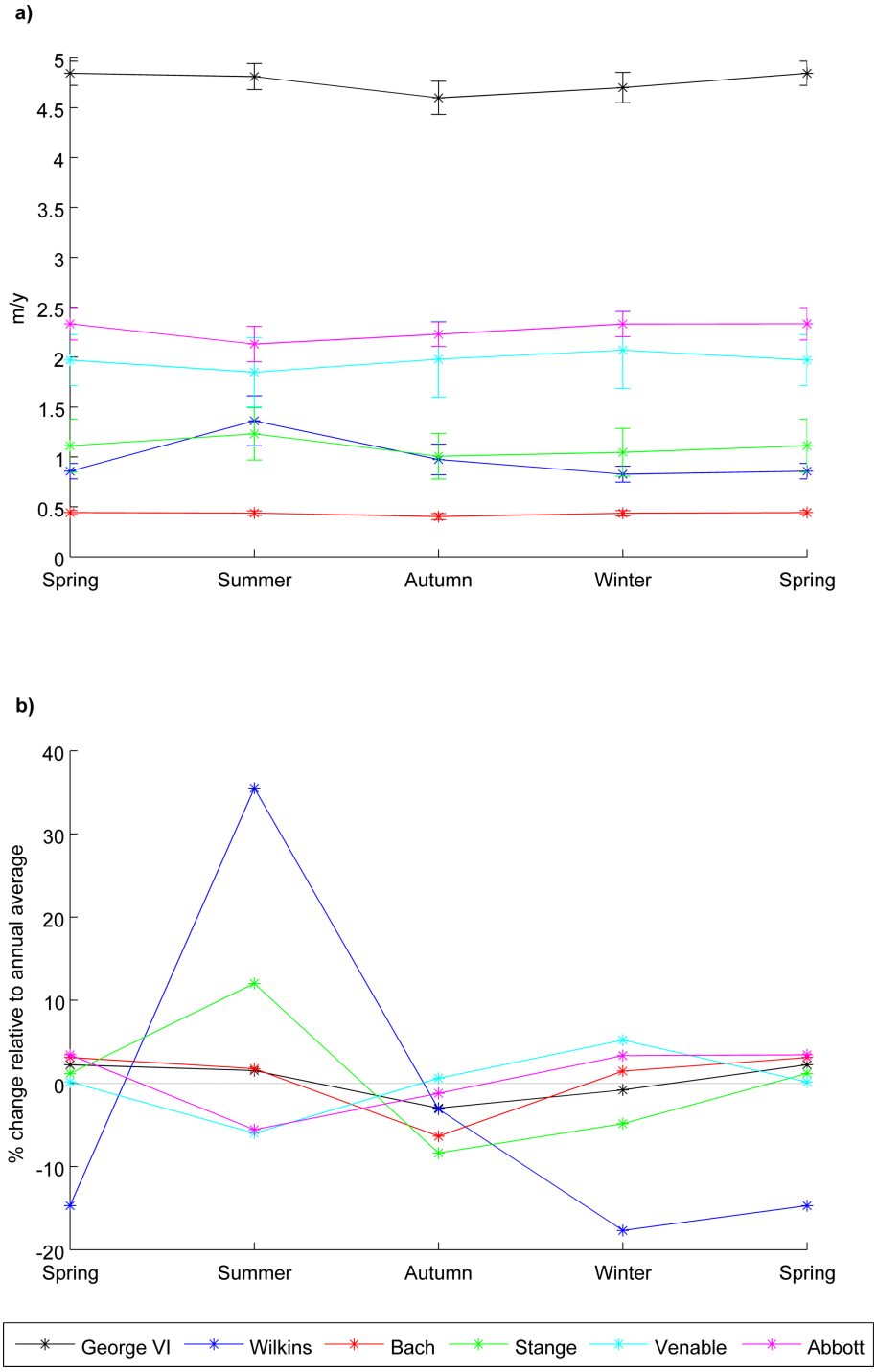

Figure 4.28: Ice shelf melt seasonal cycle shown for each ice shelf adjacent to the Bellingshausen Sea. a) shows the raw cycle in metre per year, and b) shows the relative percentage change in each season compared to the annual average melt rate.

coast, in winter. It should be noted that Abbot Ice Shelf is close to the boundary of the model domain and therefore caution needs to be taken when interpreting results here.

Stange, George VI and Bach ice shelves, those surrounding Ronne Entrance, all have minimum melt rates in autumn when the mixed layer deepens and WW begins to form close to the ice shelf base. They are also all affected by CDW inflow from Belgica Trough (Figure 4.24b). However, with the exception of Wilkins and Stange ice shelves the seasonal variation is low, which could suggest that they are more susceptible to seasonal changes to the mixed layer depth and increase in WW due to their shallow depth. The overall ice shelf flux is seasonally constant compared with other fluxes as it is forced by deep water that is less variable. For this reason, and given that ice shelves generally respond more slowly to change, the variability of ice shelf meltwater will be investigated more thoroughly when looking at the temporal evolution of freshwater in the next chapter.

4.5 Sensitivity to freshwater fluxes

Models are highly sensitive to input freshwater flux, as demonstrated by the convection problems discussed in Chapter 2. Given that salt stratification is so important, it is vital that the magnitude of freshwater flux is realistic. With this in mind, a number of cases were set up to see how sensitive the model is to choice of iceberg melt field. The motivation for this is because it is the most uncertain field used for freshwater forcings in the Bellingshausen Sea model. Whilst other fields are reanalyses and model output, thus also uncertain, they have been validated and used in numerous other studies. The iceberg melt field is known to be important from Chapter 1, and while temporal variation and meltwater injection at depth are not able to be tested without further modifications, the spatial variation and magnitude can be tested here.

Figure 4.29 shows the distribution of the test fields, alongside the surface tracer content of each freshwater component on the shelf and at each site from section 4.4.1 (Figure 4.19). The original setup uses a distribution of 130 Gt/yr spread along the coast, decreasing linearly from the coast to 100 km offshore, with the spatial extent set to be uniform along the coast. The first test case (second row of Figure 4.29) shows the same magnitude of runoff, but this time linearly decreasing out to 500 km offshore. The second test case (row 3 of Figure 4.29) shows the same magnitude again, but randomly distributed to 100 km offshore. Rows 4 and 5 of Figure 4.29 show the distribution when the original magnitude of 130 Gt/yr is doubled and halved respectively, with the original distribution maintained.

It is clear from Figure 4.29 that the overall freshwater content on the shelf is not significantly affected by the iceberg melt field changes in most cases. With the exception of doubling the magnitude of the flux, all cases retain a similar total shelf content, with the iceberg melt on-shelf reduction resulting in lower values when halving the magnitude and extending the iceberg melt out beyond the shelf break. In the latter two cases, this appears to enable some positive sea ice meltwater tracer to reside in Eltanin Bay. The other sites retain similar amounts of non-iceberg melt tracer as the standard run.

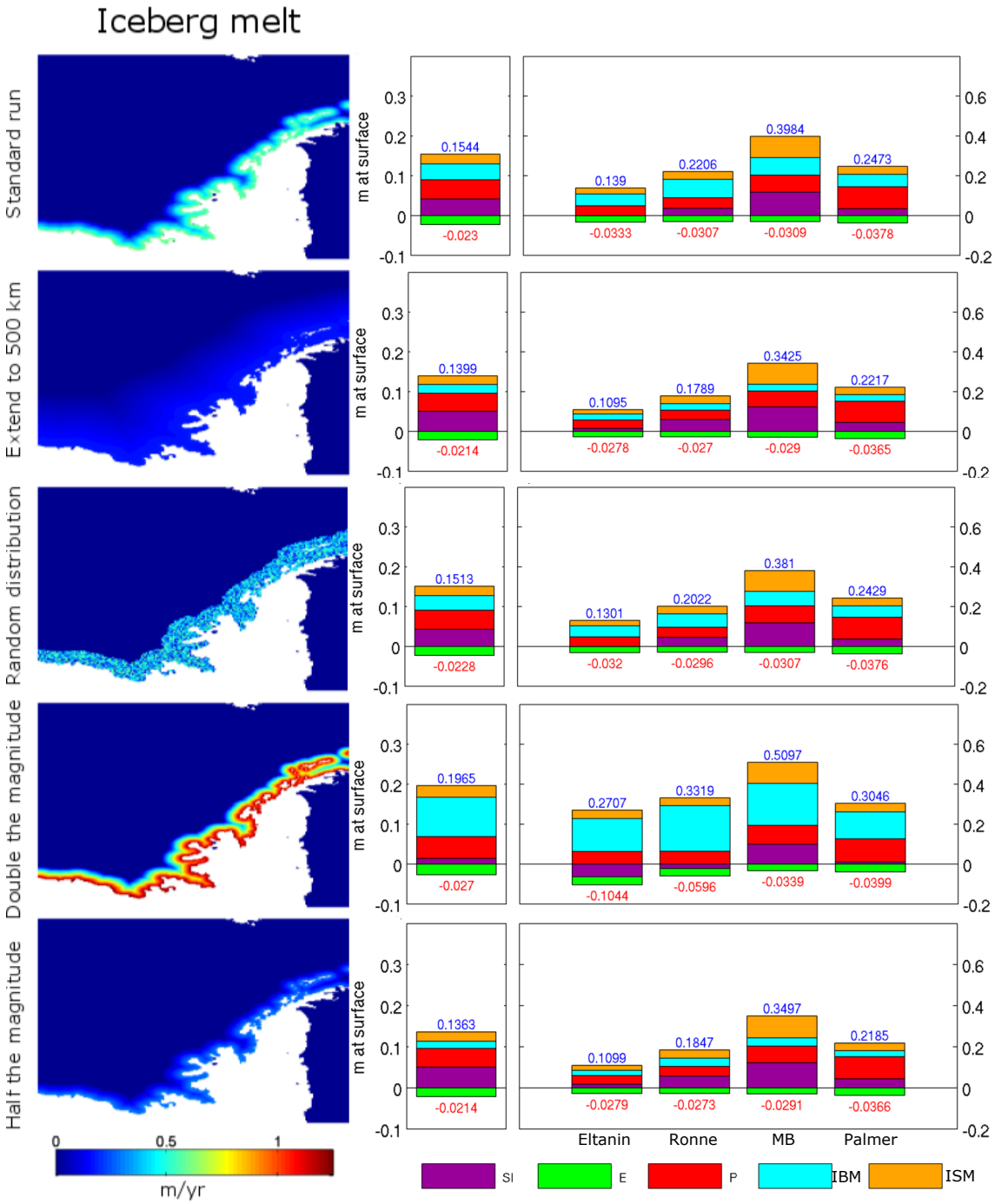

Figure 4.29: Figure showing (column 1) the five different iceberg melt settings, with the resulting surface tracer content for each freshwater component (SI = sea ice, E = evaporation, P = precipitation, IBM = iceberg melt, and ISM = ice shelf melt) on the shelf and at each site from section 4.4.1 (Figure 4.19) in metres (column 2).

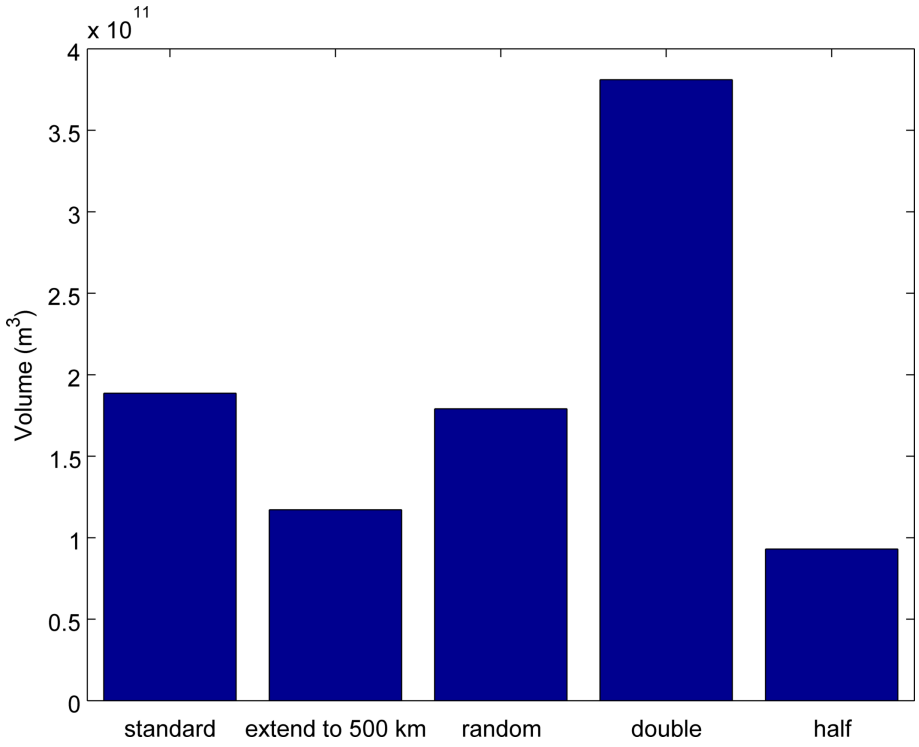

Figure 4.30: Long-term mean of total iceberg melt tracer on the shelf for each of the sensitivity runs.

In the case of doubling the magnitude of iceberg melt, the iceberg melt tracer has a large effect on the total freshwater on the shelf and at each site. Additionally, it affects the sea ice tracer markedly. Across the shelf, a large reduction in positive meltwater is seen, and this is reflected in changes at all sites, with Eltanin Bay and Ronne Entrance developing a negative sea ice meltwater tracer signature. In Chapter 2, convection problems were tested by doubling and quadrupling the iceberg melt field, and therefore it is known that significantly increasing the iceberg melt serves to stabilise the water column. This translates to a significant increase in tracer content (Figure 4.30) - 1.94 $\times$ 10^{11} m^3 compared to 3.85 $\times$ 10^{11} m^3. Additionally, halving the flux results in just under half the amount of tracer, suggesting the relationship between magnitude of flux and tracer is almost linear, and thus the distribution may be less important, as found in Chapter 1. This is backed by the randomised distribution having little effect.

Doubling and halving the flux is a significant change with little physical justification, and can result in vast changes to the water column which can affect the model performance (Chapter 2), therefore the difference seen in the freshwater content is not concerning. Spatial variation in the distribution has a big effect in the case of extending the flux to 500 km offshore, but it should be noted that this reaches beyond the shelf break and therefore the overall flux to the shelf is lessened; the lower tracer content on the shelf suggests that these waters will be entrained into the ACC instead of reaching the shelf. Therefore these results give confidence in the choice of field and the conclusions drawn about the significance of iceberg melt in the Bellingshausen Sea. However, it does suggest that better data is required in order to force this field suitably, given that the magnitude

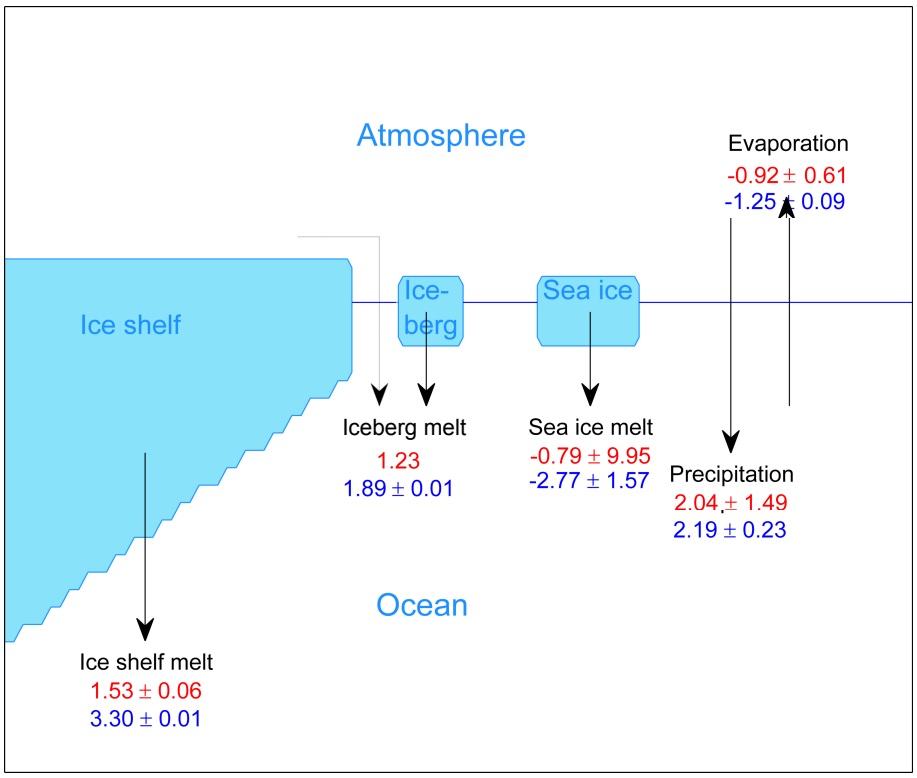

Figure 4.31: Schematic showing the fluxes (red, $\times 10^{11}$ m^3/y) and freshwater content (blue, $\times 10^{11}$ m^3) in the Bellingshausen Sea, with average on-shelf fluxes and tracers labelled from Table 4.2. Quantities show 1 standard deviation error bars indicating seasonal variability. Note that iceberg melt has no flux errorbar as it is temporally uniform.

is important. In addition to this, information of the temporal variability would allow inference of the seasonal importance of iceberg melt, identifying whether it behaves more like ice shelf melt or sea ice in its annual cycle. Whilst the lesser effect of spatial variation suggests high coastal values are less significant to represent, further testing in a higher resolution model would allow further insight into its importance.

4.6 Summary

This chapter has quantified the freshwater fluxes and resulting freshwater content across the Bellingshausen Sea. The findings are detailed below, in the context of the original aims:

1) **Validate the physical model.**
   Each of the model components (ocean, sea ice, and ice shelf) perform well against available data given the limitations of computational resources (and therefore resolution) and available bathymetry and forcings.

2) **Provide an overview of the mean freshwater contribution to the overall freshwater content, in the context of individual fluxes and total salinity.**
   The overall fluxes and freshwater content on the shelf are shown in Figure 4.31. On

an annual mean basis, all fluxes (precipitation, evaporation, sea ice, icebergs and ice shelves) are comparable. The on-shelf content of each tracer largely reflects this also. Ice shelf melt is the largest single contributor to mean freshwater content in the BS, thus it is vital that its contribution is further understood in light of recent changes to ice shelf melting. South of George VI Ice Shelf, the peak ice shelf meltwater resides at intermediate depths, while to the north it reaches the surface. This result has important implications for the interpretation, and comparison, of geographically-separated sediment core δ^{18}O records that may be recording waters from different sources, or missing the bulk of some freshwater components, despite the δ^{18}O being measured on organisms living at the same depth and in the same ecological niche.

3) **Understand the seasonality of freshwater fluxes and content, and how this affects the mean.**
Sea ice dominates the seasonal freshwater cycle such that sea ice fluxes are instantaneously an order of magnitude larger than any other source, while precipitation has a large magnitude peak in autumn when others reduce (Figure 4.14). Spatial variation is significant on the shelf, with the north being a region of strong precipitation and net sea ice melt in summer, while the south has a large winter sea ice freezing which dominates its annual signal. Thus seasonal and spatial variation in freshwater fields can be hidden in observations that only survey one time period. In Eltanin Bay, strong winter salinification from sea ice growth is masked by a net positive total freshwater content from meteoric sources, showing the importance of identifying the full regional composition of freshwater. Additionally, when assessing the freshwater balance, the different origins of freshwater content cannot be deduced from fluxes, or vice versa, since many freshwater constituents are far removed in space and time from their sources. This is particularly relevant for single site studies which infer conditions from past climates (e.g. Pike et al.; 2013; Swann et al.; 2013).

4 **Investigate regional differences and associated variations in oceanography; deduce how much can be inferred of the wider shelf from individual locations.**
There is significant spatial variability of freshwater in the Bellingshausen Sea. It is clear that, in addition to north-south variations, individual sites behave differently according to their proximity to gyres, deep currents or seasonally-enhanced coastal currents. This differing oceanography has an effect on both the input fluxes, through sea ice cover and changes to ice shelf melt, and the residence time of freshwater content at different depths. The resulting freshwater variation can maintain stratification, or in the case of Eltanin Bay, cause significant destabilisation. When selecting sites for taking freshwater samples, and representative depths, care must therefore be taken to account for the local oceanography.

5 **Perform sensitivity analysis on iceberg melt field to quantify uncertainty in the freshwater flux and test the effect of changing the magnitude and**

distribution of surface fluxes.

The Bellingshausen Sea model is sensitive to the magnitude of iceberg melt input but not its spatial distribution. While the finding gives confidence in the setup and results, a comprehensive set of observations would allow fewer assumptions to be made and add a temporal component to the field, strengthening results further.

The spatial variation in the Bellingshausen Sea suggests that small-scale features are significant when analysing the freshwater balance. Given that the shelf displays regional differences that are based on different freshwater components, each of which vary on different timescales, it is important to put these results in the context of temporal variation also. This will be explored in Chapter 5.

Chapter 5

Interannual changes to freshwater in the Bellingshausen Sea

The Bellingshausen Sea has seen a number of changes in recent years. As described in Chapter 1, until the late 1990s the Antarctic Peninsula (AP) warmed more rapidly than any other region in the Southern Hemisphere, with air temperatures increasing by nearly 3°C (Turner et al.; 2005a) and warming and salinification of the surface ocean in summer (Meredith and King; 2005). Recent changes to the air temperature trend complicate the long-term picture (Turner et al.; 2016). In conjunction with this, the freshwater system has altered, with an overall decrease in sea ice duration (Stammerjohn et al.; 2012) and extent (Parkinson and Cavalieri; 2012) over the satellite era, particularly in summer (Holland; 2014). Alongside these changes, increases in precipitation (Thomas et al.; 2008), and mass loss (Wouters et al.; 2015) and thinning (Paolo et al.; 2015) of the southern BS ice shelves has occurred, affecting the meteoric water flux into the ocean. Regional variation contributes to the overall shelf freshwater budget, and changes to each of these can have nonlocal effects, as seen in Chapter 4. The main aim of this section is therefore to explore the temporal changes of salinity on the wAP shelf and relate these to changes in freshwater sources and the resulting composition of freshwater content.

5.1 Shelf-wide overview

To motivate study into the temporal variation in the model, the shelf-wide temporal behaviour can be viewed in Figure 5.1. Here, the timeseries of average salinity, total of each freshwater flux and total of each tracer on the shelf have been calculated. The mean seasonal cycle has been removed from this (Figure 5.1a-c) to provide a timeseries of anomalies, shown as annual averages in Figure 5.1d-f. Table 5.1 shows the average seasonal and long-term mean from Table 4.2 (Chapter 4), alongside the interannual variability calculated from the model. Note that annual means, as opposed to monthly output, is shown for better clarity of interannual trends.

Surface salinity shows significant interannual variability (Figure 5.1d), while deeper layers show little deviation from the mean. Over most of the timeseries there is a freshen-

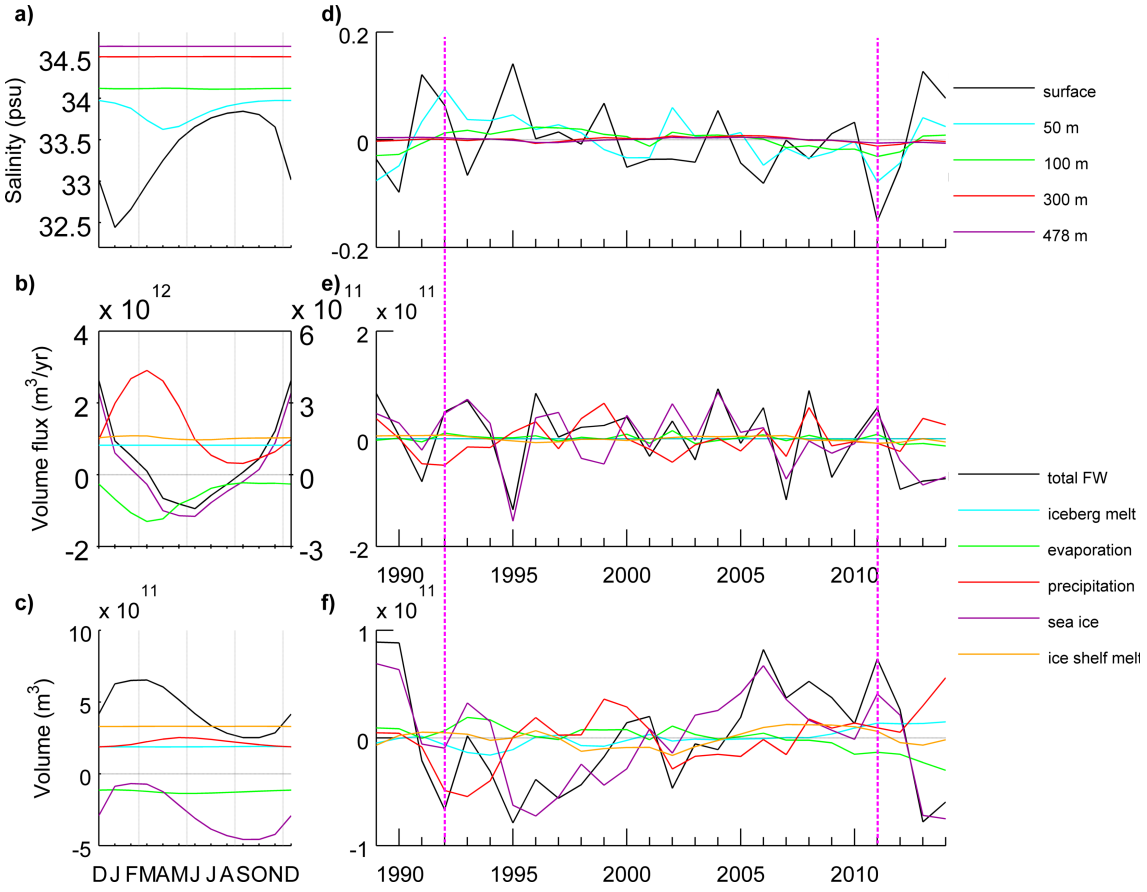

Figure 5.1: Temporal variation of freshwater on the BS shelf (shallower than 1000 metres). Plots on the left show (from top) seasonal cycles of a) mean salinity at different depths; b) area-integrated freshwater fluxes; and c) volume-integrated tracer content. Plots d)-f) on the right show the timeseries of deviations from the mean seasonal cycle, plotted as annual averages. Note the second y-axis in panel b) for iceberg melt, evaporation, precipitation and ice shelf melt. Magenta lines highlight the years 1992 and 2011 which are used for trend analysis.

Table 5.1: Table showing the annual mean, seasonal variability and interannual variability of each flux ($\times 10^{11}$ m^3/y) and tracer ($\times 10^{11}$ m^3) from Figure 5.1. The annual mean was calculated by averaging the seasonal cycle of Figure 5.1a-c, with the seasonal variability representing the seasonal deviation from this. Interanual variability was calculated by removing the annual cycle from the timeseries, taking the yearly averages and calculating the standard deviation of the result.

	Annual mean	Seasonal variability (1 sd)	Interannual variability (1 sd)
Total flux	2.11	10.26	0.67
Sea ice flux	-0.79	9.95	0.57
Precipitation flux	2.04	1.49	0.31
Evaporation flux	-0.92	0.61	0.07
Iceberg flux	1.23	*N/A**	*N/A**
Ice shelf flux	1.53	0.06	0.05
Total tracer	4.41	1.62	0.51
Sea ice tracer	-2.77	1.57	0.44
Precipitation tracer	2.19	0.23	0.25
Evaporation tracer	-1.25	0.09	0.12
Iceberg tracer	1.89	0.01	0.08
Ice shelf tracer	3.30	0.01	0.08

*Not applicable as prescribed iceberg flux is temporally uniform

ing, although this is not monotonic. This could reflect the feedbacks that can occur from one year to the next, such as a deeper winter mixed layer from reduced sea ice cover providing conditions that allow for increased freezing of sea ice the following winter (Venables et al.; 2013).

While the seasonal cycle of sea ice flux is an order of magnitude larger than the other freshwater sources (Figure 5.1b), the interannual changes of both sea ice and precipitation fluxes are an order of magnitude larger than the other variables (Figure 5.1e; Table 5.1). The dominance of these in flux anomalies is apparent to a lesser extent in interannual variability of tracer content, with ice shelf meltwater and iceberg meltwater content displaying more interannual variability (as a portion of the whole freshwater content) than the ratio of their associated fluxes to the total (Table 5.1).

A change in the flux leads to a change in the rate of change of tracer content, so a fixed flux anomaly leads to a fixed trend in tracer content (Figure 5.1f). The seasonality of salinity was shown to correlate with surface sea ice tracer in Chapter 4, and here a freshening seen over the majority of the time period is also closely linked to sea ice meltwater content changes over longer timescales. High sea ice melt tracer in 1989-1990 is followed by a period of low precipitation tracer in 1992-95. After a few years of relatively stable conditions, both the freshening and total freshwater trends accelerate rapidly after 1995, following a year of particularly low freshwater flux. This would suggest that conditions in individual years can have a subsequent effects on the overall system, as well as being a diagnostic for a change in circulation. From 1995, lower than average sea ice melt tracer broadly increases until 2012, becoming higher than average from 2002 onwards, and from 2006 the precipitation and ice shelf melt sustain high total freshwater content. After 2011 the model freshwater content decreases dramatically due to a large decrease in sea ice meltwater, despite an increase in freshwater content from precipitation and iceberg melt. The total freshwater tracer is mirrored by salinity at the surface (Figure 5.1d), highlighting the importance of the surface layer in determining changes to freshwater content across the water column. In general, sea ice is the strongest contributor to variability in both total freshwater flux and total tracer (Table 4.2); where there is a large difference this is due to precipitation.

To quantify the apparent changes to the freshwater budget over time in the Bellingshausen Sea, linear trends in salinity and freshwater tracers on the BS shelf are shown in Table 5.2. Over the full time period (1989-2014) there are no significant trends in salinity over most of the water column. However, there are compensating trends in the individual freshwater components. The precipitation flux from ERA-Interim in the model increases over time, as in observations (Thomas et al.; 2008), contributing to more precipitation tracer on the shelf (Figure 5.1f). Significantly, the iceberg melt tracer increases over the model period despite having a constant prescribed flux, showing that ocean dynamics are paramount; the input flux outweighs export from the shelf during this period. This is probably due to meltwater accumulation in regions with a long residence time, such as Eltanin Bay (see Chapter 4), and could have subsequent effects on the seasonal Antarctic Penin-

Table 5.2: Interannual trends in annual-mean anomaly from mean seasonal cycle shown for on-shelf salinity at various levels (y^{-1}), and in the total tracer content (km^3y^{-1}). Trends are shown for the full time period and 1992-2011, identified as a period of freshening. Confidence at the 90% (italic), 95% (bold) and 99% (bold, italic) levels are indicated.

	1989-2014	1992-2011
Salinity (surface)	-0.0011	**-0.0047**
Salinity (50 m)	-0.0015	***-0.0051***
Salinity (100 m)	-0.0005	***-0.0020***
Salinity (300 m)	-0.0001	-0.0001
Salinity (478 m)	**-0.0002**	0.0000
Total tracer	0.50	***6.02***
Sea ice	-0.56	**3.39**
Precipitation	**1.50**	*1.68*
Evaporation	***-1.19***	***-1.10***
Iceberg	***0.78***	***0.93***
Ice shelf	0.18	*0.61*

sula Coastal Current (Moffat et al.; 2008). Ice shelf meltwater content has an insignificant trend, despite observations suggesting an increase in melting in recent years (Paolo et al.; 2015).

The period of 1992-2011 was selected as it provides a case study of freshwater change, similar time periods have been studied by other authors (e.g. Parkinson and Cavalieri; 2012; Holland et al.; 2014; Holland; 2014), and it coincides with the maximum and minimum salinity between the start and end of the run. This period has been studied in the past. Shepherd et al. (2012) found a loss of Antarctic Peninsula ice mass (though mainly in the east), in conjunction with an increased rates of precipitation during the 1900s (Thomas et al.; 2008), and trends in sea ice cover have been observed over a similar time period (Holland; 2014). This suggests that the freshening seen is realistic. Wouters et al. (2015) find a loss of mass in southern Bellingshausen Sea ice shelves towards the end of the time period; (Cook et al.; 2005) suggest increased glacial melt in the northern AP is due to the ocean, highlighting the feedbacks associated with meltwater and melting conditions across the freshwater inputs. To quantify the changes, Table 5.2 also shows the linear trends in all components during this shorter time period. Comparisons can be made to investigate interannual variability over this period, allowing 1) comparison with the many previous studies that have examined these changes, and 2) a case study of strong decadal freshwater change.

The tracers associated with precipitation, evaporation, and iceberg melting show significant changes in freshwater from 1989-2014, but their sum does not create significant freshening. Over 1992-2011, however, the clear freshening can be attributed to significant increases in freshwater tracers, of which iceberg melt, evaporation and sea ice melt are

significant contributors at the 95% level (Table 5.2). Increases in precipitation and ice shelf melting also contribute to the freshening, albeit significant at only the 90% level. The main difference is sea ice; an increase in sea ice tracer contributes over half the total freshwater trend in 1992-2011, but has no significant trend over the whole model period.

This shelf-wide overview gives rise to a number of questions which will be investigated in the remainder of this chapter. The emphasis will be on the feedbacks associated with freshwater change, such as sea ice and ice shelf melt variation as highlighted earlier, rather than the effects of external inputs that are independent of the ocean model.

- What are the oceanographic conditions accompanying the time-varying freshwater content?
- Given the importance of sea ice to the seasonal cycle of freshwater in the Bellingshausen Sea, along with its domination of tracer content, how does it vary interannually, and why?
- Since ice shelf melting predicted by the model results in significant contributions to tracer content at depth, known to have a long residence time, how does this translate to change in freshwater content over time? Is there any link to the large surface changes?
- From Chapter 4, it is clear that spatial variation is a key feature of the Bellingshausen Sea. What is the role of this in temporal change, and how does it affect the shelf-wide quantification? Can the changes to flux and tracer content be reconciled?

5.2 Oceanographic conditions

It is known that freshwater inputs can influence currents (e.g. Moffat et al.; 2008) as well as being affected by changes in circulation. Figure 5.1 shows that there are various points over the period of 1989-2014 where key changes in behaviour are seen compared to previous years. Figure 5.2a) shows the long-term (1989-2014) depth-averaged currents in the Bellingshausen Sea. The on-shelf flow of CDW is observed through Belgica Trough, and further intrusions along the shelf break and influence of the ACC are seen all along the northern peninsula. Areas of low flow in Eltanin Bay, Marguerite Bay and Alexander Island, and a throughflow under GVIIS are also seen. To the north of the region, the influence of the ACC can be seen. Key recirculations around Alexander Island and under Stange and Wilkins ice shelves are not prominent.

Based on Figure 5.1, 1989 is a year of average salinity and freshwater addition, but high levels of freshwater content mainly forced by sea ice meltwater. The spatial distribution of freshwater in 1989, in total metres of the water column depth, is shown in Figure 5.3, showing the general heightened levels of freshwater around ice shelves as seen previously in Chapter 4.

Changes to the circulation, compared to the long-term mean, can be seen in Figure 5.2 for key years. These years have been selected as they represent the endpoints of

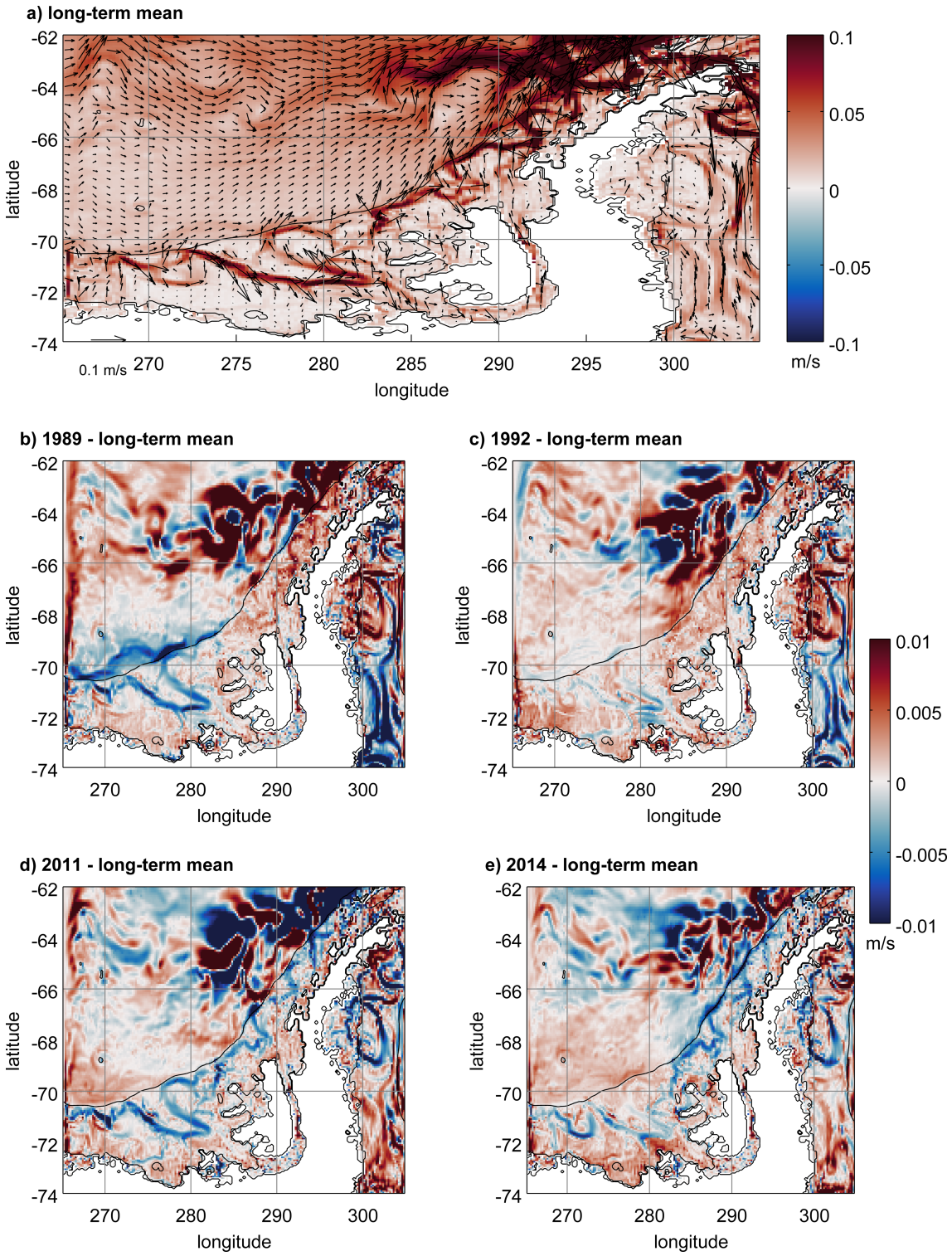

Figure 5.2: a) Long-term mean magnitude of depth-averaged currents in the Bellingshausen Sea in 1989, and the difference between this and the depth-averaged currents of b) 1989, c) 1992, d) 2011 and e) 2014, the end of the timeseries, where a positive value shows an increase in the magnitude over time. a) shows velocity vectors, and the shelf break (1000 metres) is shown in black.

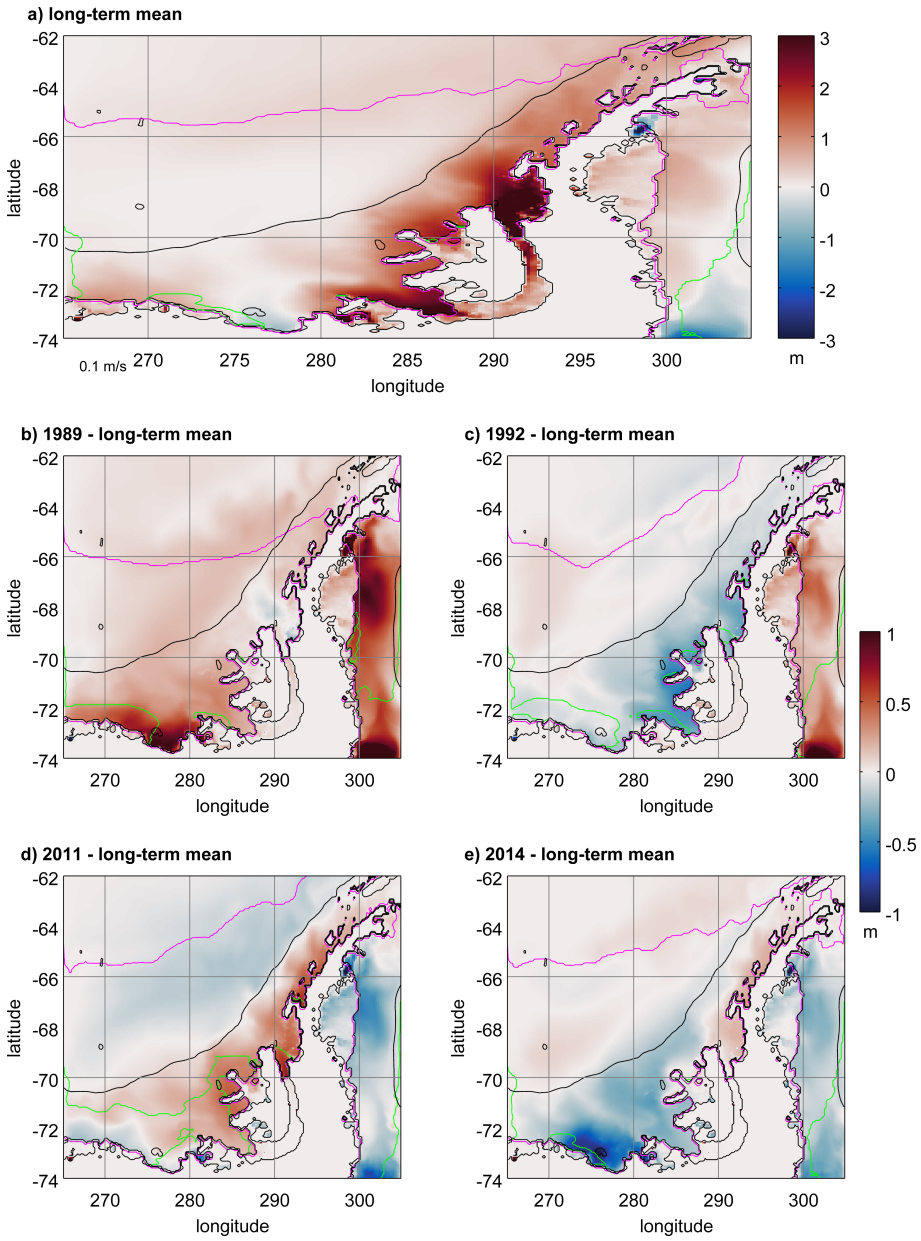

Figure 5.3: a) Long-term depth-integrated annual average of total freshwater content in the Bellingshausen Sea, and the difference between this and the annual average depth-integrated total freshwater content of b) 1989, c) 1992, d) 2011 and e) 2014, the end of the timeseries, where a positive value shows an increase in the magnitude over time. Plot a) shows velocity vectors, and the shelf break (1000 metres) is shown in black. Sea ice extent for the winter (magenta) and summer (green) of each year is shown, where extent below 15% is masked.

the freshening trends considered, and show peaks and troughs of total freshwater tracer (Figure 5.1) so can provide an insight into the ocean state before and after significant freshwater content change. In the case of 1992 and 2014, they follow rapid decreases in freshwater content despite differing salinities and freshwater fluxes.

In 1989, lower than average salinity results from high total freshwater flux. This results in high tracer content, which Figure 5.3b shows is due to higher than average freshwater tracer in Eltanin Bay. This region is usually occupied by brine-enhanced water (Figure 5.3a), suggesting that 1989 is a year of less sea ice formation in that area. This occurs alongside a reduction along the shelf break and in on-shelf flow of CDW through Belgica Trough. Given that a reduction of on-shelf flow would provide less on-shelf heat transport, more sea ice formation would be expected. This suggests that another process, such as a change in atmospheric conditions, is occurring. In terms of the tracer composition, the high freshwater flux translates to high tracer content everywhere except in Marguerite Bay (Figure 5.3b); to the north of this, the northeastward flow along the northern peninsula is enhanced. The reduction in Marguerite Bay could reflect a decrease in ice shelf melt water resulting from reduced CDW input.

A similar situation to 1989 is seen in 2011, in terms of high overall shelf flux and tracer content (Figure 5.1), which is accompanied again by weaker on-shelf flow, but here the reduction continues all along the shelf break to the north (Figure 5.2). The flow adjacent to the shelf break in the south is increased, but this does not increase the on-shelf flow. By this point in the time-series, the area has experienced 20 years of freshening, though the summer sea ice extent is larger than average. The regional spread of total tracer is different to 1989, with higher than average content concentrated towards the coast in large amounts everywhere except Eltanin Bay where a reduction is seen (Figure 5.3). Off the shelf, lower than average tracer content is observed.

1992 and 2014 are both low tracer content years (Figure 5.1). This is despite 1992 experiencing high freshwater fluxes, suggesting that the presence of more saline waters from previous years are still having an effect. Increases in CDW inflow to restore 1992 conditions to the long-term mean from reduced on-shelf flow in 1989 could explain this. The distribution of freshwater is a shelf-wide reduction in tracer content in all but Belgica Trough (Figure 5.3). In 2014, however, it is the result of opposing signals in the north and south, with increased brine-enhanced water in Eltanin Bay linked to low summer sea ice offsetting an increase to freshwater in the northern AP. The fact that 2011 also had a large increase in freshwater here could imply that residual freshwater here is still being seen. Meredith et al. (2013) find a net residence time of 3 years for meteoric water at the Palmer site, and Eltanin Bay retains more depth-integrated meteoric freshwater content (Chapter 4, figure 4.20), so residual freshwater after 3 years is not unreasonable.

In general, high fluxes translate to a high annual tracer content, but the effects of the high residence time of Eltanin Bay brine-enhanced water, along with residual freshwater from previous years, means that the conditions are not easy to interpret. Interannual variability of the currents alone is significant, explaining why the constant freshwater flux

from prescribed iceberg melt translates to a non-uniform freshwater content. Given that the model predicts ice shelf melting and sea ice melting based on feedbacks from the ocean, the next two sections will investigate their melting conditions in the context of these findings.

5.3 Sea ice variability

The total shelf freshwater content and surface salinity is closely related to sea ice (Figure 5.1; Tables 4.2 and 5.2). To compare the long-term trends, the model output of annual sea ice concentration is shown compared to observations (Cavalieri et al.; 1996) for both the full time period (1989-2014) and the period of freshening (1992-2011) in Figure 5.4. In both time periods, a significant loss of sea ice concentration is apparent, though in 1992-2011 the magnitude of this loss is much greater and significant at the 99% level. The model shows a similar distribution, though the magnitude of loss is reduced. Over the full time period, the model also predicts a reduction in the north, although the magnitude of loss in each region is small.

The previous chapter found that the seasonal cycle was significant, and thus temporal changes can be viewed in terms of trends for each season. Figure 5.5 shows the seasonal trends in sea ice concentration from observations (Cavalieri et al.; 1996) over the full time period 1989-2014, and the identified period of increased melting 1992-2011. Key similarities show a loss of sea ice over both time periods in summer and autumn. In winter and spring, however, 1989-2014 shows an increase in sea ice, though at an insignificant level, while 1992-2011 shows a general ice loss at the 90% significance level. This shows there are key changes in sea ice occurring within the trend years which are offsetting the opposite behaviour outside of the trend period. The strong summer-intensified ice loss from the BS (Holland; 2014) is robust for all time periods but during 1989-2014 the annual-mean trend (Figure 5.4) is greatly reduced because winter ice gain offsets summer ice loss.

The fact that observations also show changes between 1992 and 2011 gives confidence in the modelled changes. Figure 5.6a shows the modelled sea ice concentration trends, alongside drift, thickness (Figure 5.6b), and freshwater flux (Figure 5.6c) trends over the period of increased sea ice freshwater 1992-2011. Comparing the model to observations (Figure 5.5) shows that overall ice concentration trends are very generally captured, though the model ice loss is not focused on the coastline, and little ice exists in summer. The spring changes seen in observations in the northern peninsula are not significant in the model areal changes. Any model forced by coarse reanalysis winds can only be expected to reproduce the broad features of complex regional changes such as these, rather than small-scale details.

The 1992-2011 freshening can be explained by trends in seasonal ice motion and thickness (Figure 5.6). In autumn and winter, reduced sea ice extent across the BS is caused by strong northerly wind trends forcing the sea ice towards the BS coast, resulting in ice

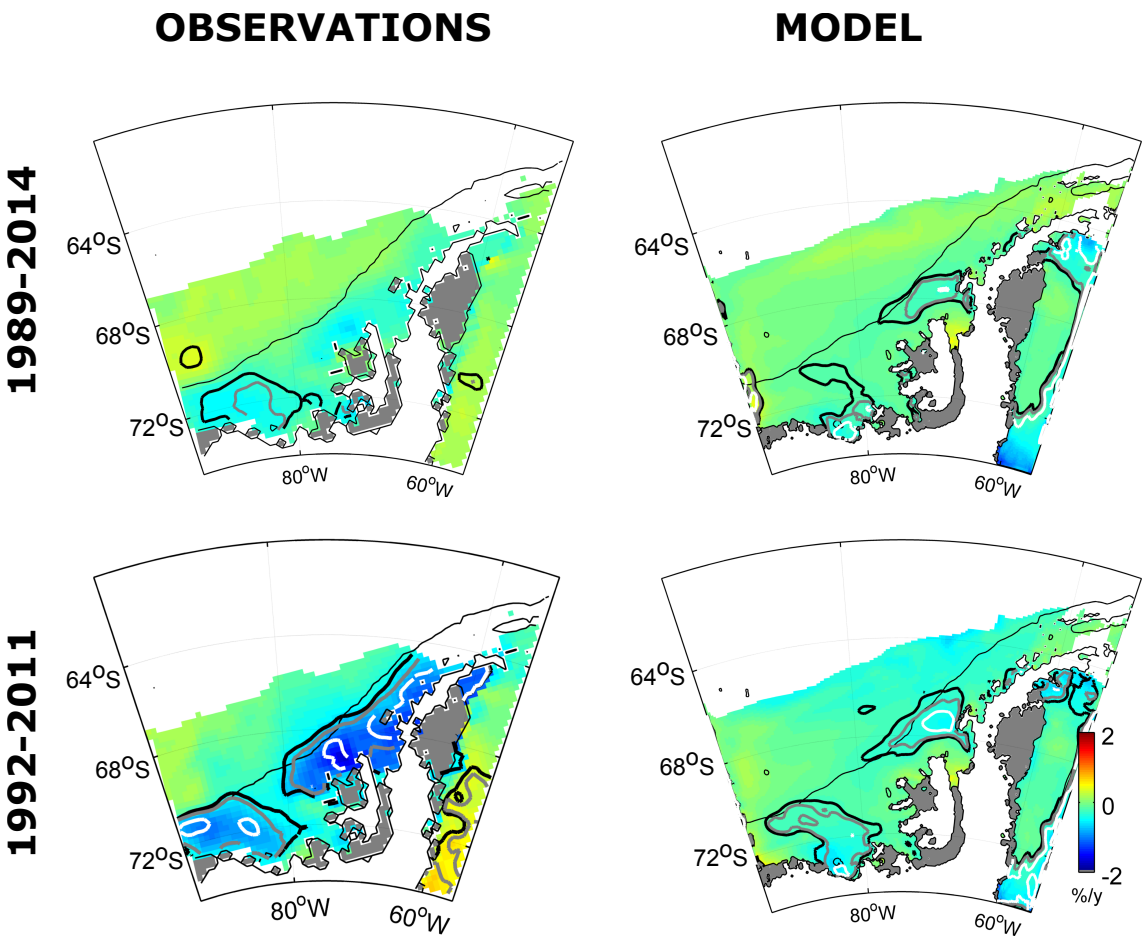

Figure 5.4: Trends of observed satellite-derived sea ice concentration from Cavalieri et al. (1996) (left) and the model output (right) for the full modelled period 1989-2014 (top) and period of increased sea ice flux, 1992-2011 (bottom). Confidence levels are shown at the 90% (black), 95% (grey) and 99% (white) levels. The shelf break is shown in black and ice shelves are in grey.

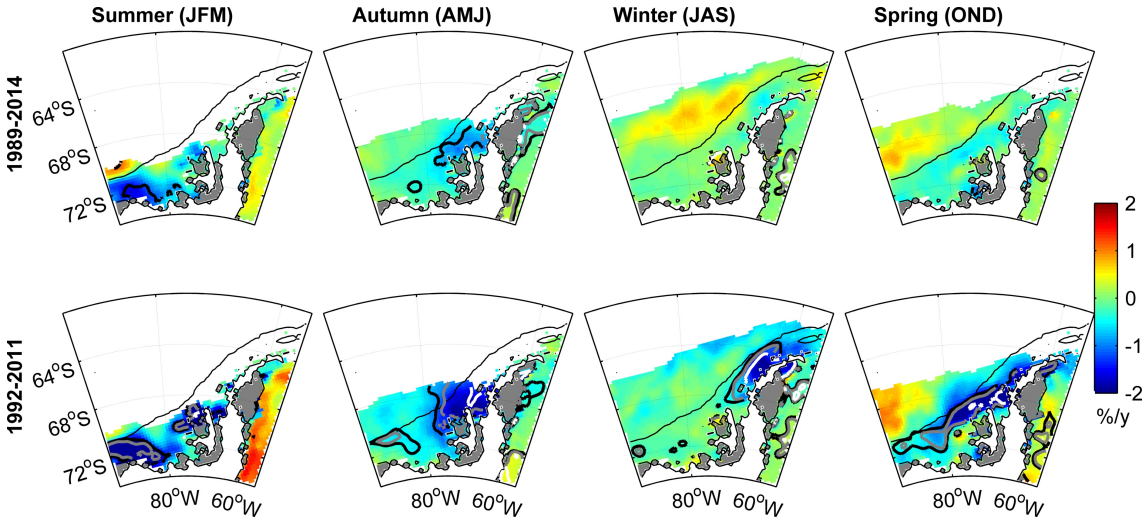

Figure 5.5: Trends of observed satellite-derived sea ice concentration from Cavalieri et al. (1996) for the full modelled period 1989-2014 (top) and period of increased sea ice flux, 1992-2011 (bottom). Confidence contours are shown at the 90% (black), 95% (grey) and 99% (white) levels. The shelf break is shown in black and ice shelves are in grey.

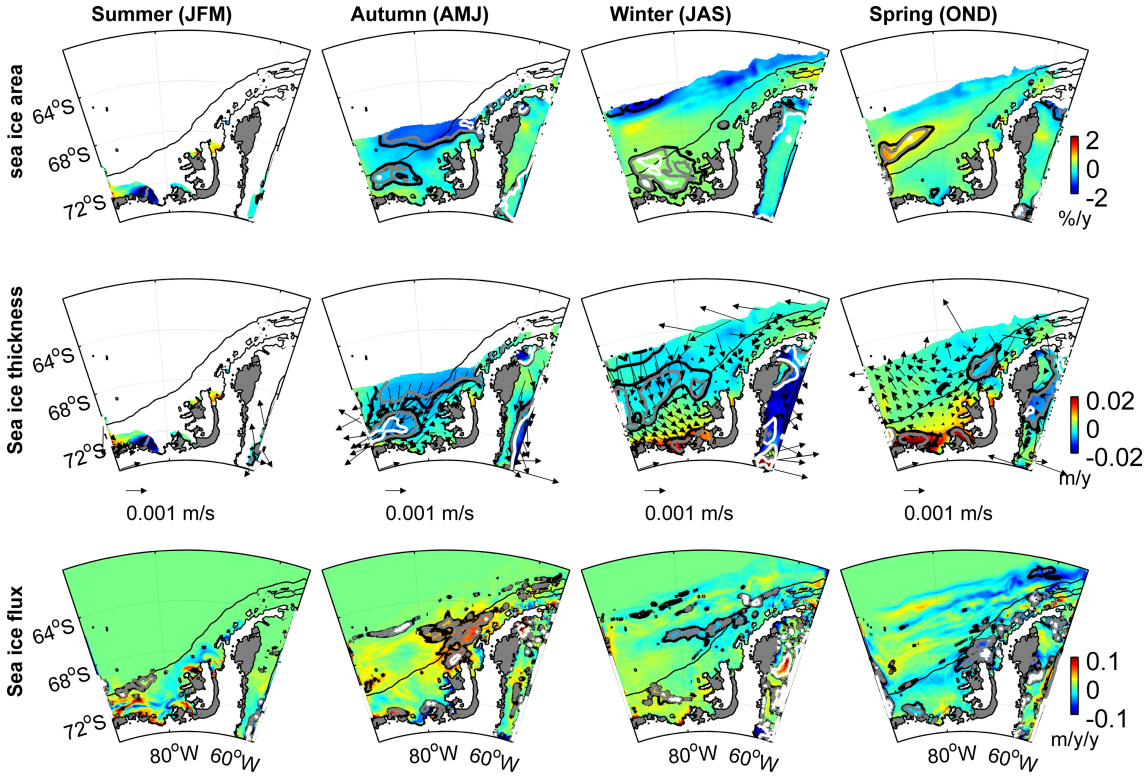

Figure 5.6: Modelled trends over the time period 1992-2011 in sea ice area (top), thickness and drift (middle), and sea ice freshwater flux (bottom, positive downward). Confidence interval contours are shown at the 90% (black), 95% (grey) and 99% (white) levels. The shelf break is shown in black and ice shelves are in grey.

thinning in the north and thickening at the southern coastline (Holland et al.; 2014). This wind-driven change remains into spring, resulting in a net loss of meltwater in the north of the region, particularly in Marguerite Bay, which is opposed by a significant reduction in freezing in autumn (indicated by an increase in meltwater flux) on the northern BS shelf. Consequently a reduction in autumn and winter ice concentration and thickness is seen. It is this reduction in brine rejection on the shelf that causes the increase in annual-mean sea ice freshwater content (Table 5.2).

The large net loss of meltwater in Marguerite Bay can be linked to a decrease in thickening on an annual mean basis, but this is the only location where a change occurs over all seasons (Figure 5.7a), with the coastal thickening having no significance annually. There is little change to sea ice motion on the shelf; a slight trend towards the southwestward motion in autumn, and along the northern AP in spring, is seen, and the outer limit of the ice pack is generally compacted towards the shelf break. This explains the annual decrease in thickness seen there. Figure 5.7b shows that whilst trends in each season are significant, leading to the increase in annual-mean sea ice freshwater content, the annual-mean sea ice flux shows no significant change apart from along the northern AP, northern Marguerite Bay, and western Eltanin Bay on the shelf. This highlights the importance of seasonality in affecting long-term change to freshwater content, as well as the important effect of small regions on wider shelf change.

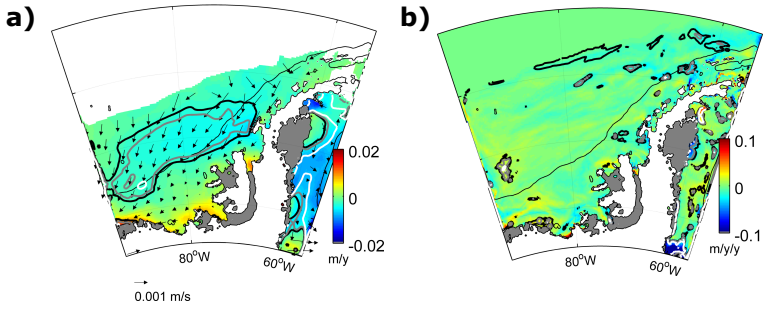

Figure 5.7: Modelled trends in a) annual sea ice thickness and drift, and b) annual sea ice freshwater flux (positive downward) from 1992-2011. Confidence interval contours are shown at the 90% (black), 95% (grey) and 99% (white) levels. The shelf break is shown in black and ice shelves are in grey.

5.4 Ice shelf melting

Ice shelf melting has the largest contribution to total freshwater content on the Antarctic Peninsula shelf, suggesting that any change to this will have a noticeable impact on the freshwater budget. Further, ice shelf meltwater is input at depth and therefore any change to its net flux, either from additional melting or changes to its export, could occur over long time periods as it is affected directly by deep waters rather than seasonal surface changes. Figure 5.1 shows that little variation in ice shelf melt flux still results in a change

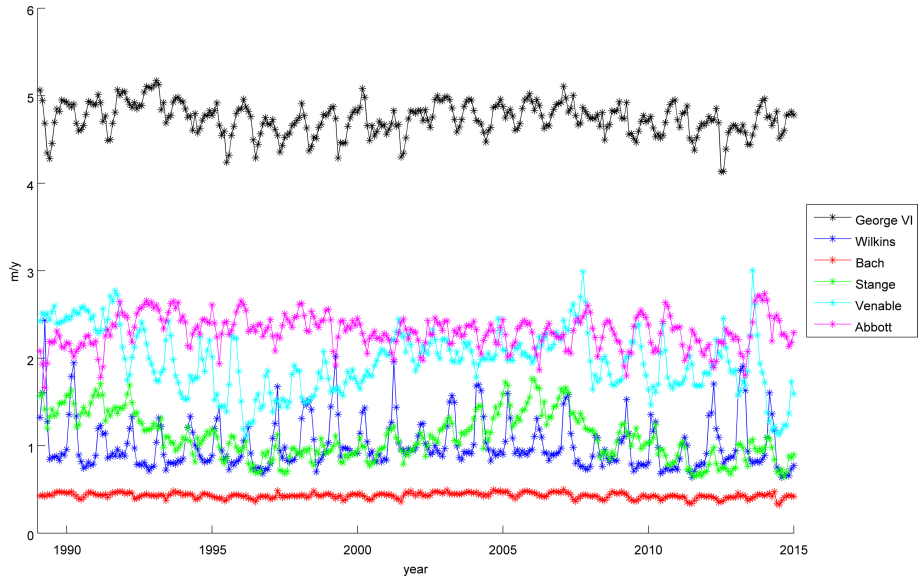

Figure 5.8: Timeseries of the average melt rate (in metres per year) of each ice shelf from the model over the full model time period, shown for each month.

in ice shelf meltwater on the shelf, albeit with a smaller variation than sea ice meltwater. This subsection will investigate individual ice shelves and their impact on the meltwater, in order to see how changes to the Bellingshausen Sea can affect its ice shelf meltwater content, both on local scales and further afield.

Figure 5.8 shows the interannual variability in melt rates for each ice shelf represented by the model. The dominant feature here is that George VI Ice Shelf melt rates are much higher than other ice shelves, though their variability is less than Wilkins, Stange and Venable ice shelves, which show differing behaviour on various time scales. All show some seasonality in their melting, though this is low compared to the seasonality of other freshwater inputs (Figure 5.1b). Bach Ice Shelf has low melt rates and little interannual variability so will not be discussed further; similarly, Abbot Ice Shelf intersects the model domain boundary so will not be investigated.

5.4.1 George VI Ice Shelf

George VI Ice shelf is the deepest of all the ice shelves on the wAP, and is uniquely placed with a strong throughflow of CDW. This results in its main melting being caused from basal processes rather than calving (Rignot et al.; 2013). The throughflow is generally from south to north (Jenkins and Jacobs; 2008), leading from a region of net sea ice freezing to net sea ice melt (Chapter 4), and therefore is likely to undergo melting changes with latitude.

Figure 5.9 shows that both sections of the ice shelf have seasonal variation in the surface waters and clear peaks in melting coinciding with a shallowing CDW layer in 1992 and 2006, which also has higher salinity and temperature, suggesting less mixing before reaching GVIIS. In the northern section, the maximum ice shelf depth is slightly deeper

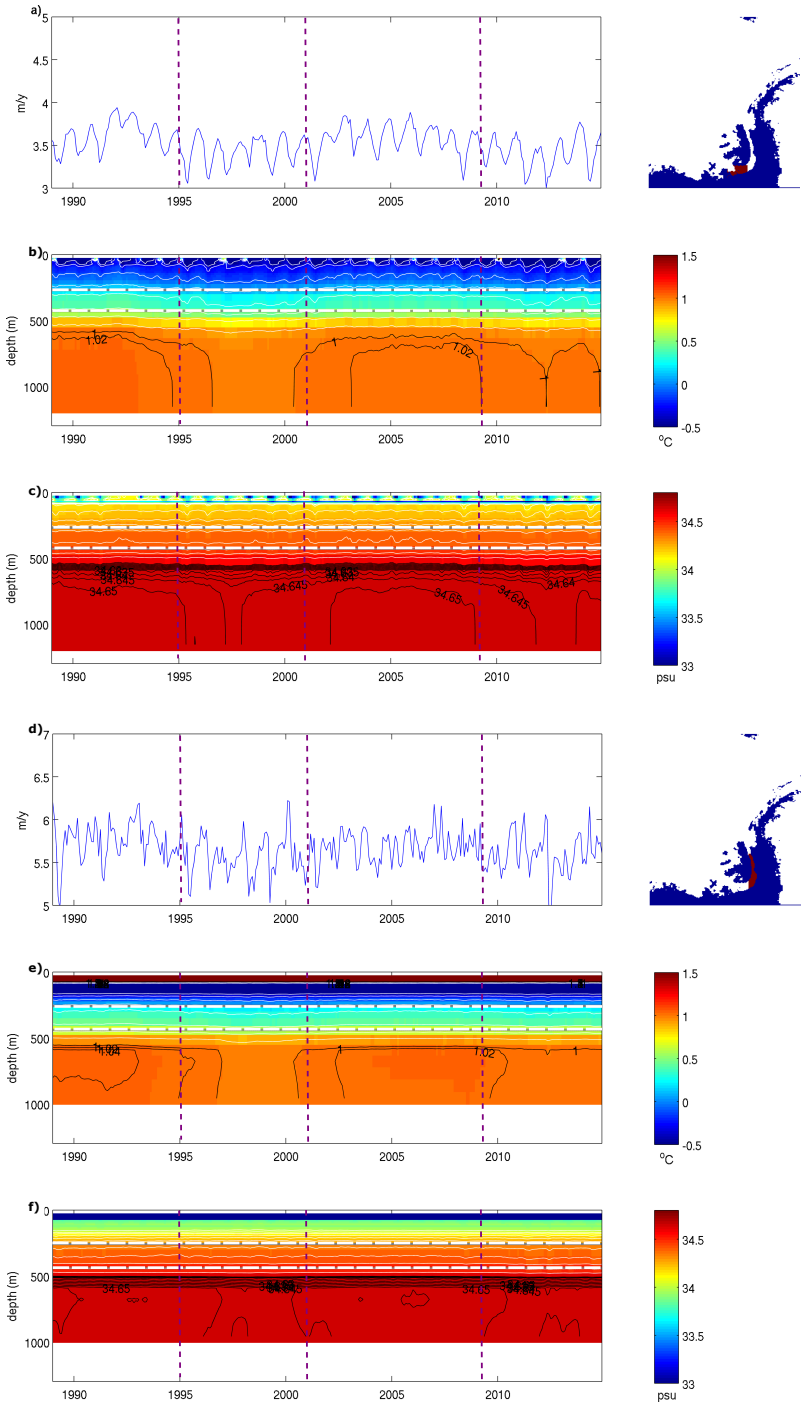

Figure 5.9: (a,d) Timeseries of average basal melt rate for the south and north of George VI Ice Shelf respectively (shown in map to the right), separated by 291 °E, as in Holland et al. (2010). Also shown are Hovmöllers of (b, e) horizontally-averaged temperature and (c, f) salinity under the south/north of the ice shelf over time. Due to the large difference between surface and deep values, black contours show changes to CDW. White lines show the average and maximum ice shelf depth, and vertical purple lines show where highest and lowest melting years fall.

than in the south, while the average is slightly shallower and the total water column is shallower. This shows that the ice shelf in the north is exposed to more of the water column. Increased stratification, along with warm, salty CDW reaching shallower depths (indicated by shallower contours) occur in conjunction with a higher and much more variable melt rate in the north. The presence of AASW at the surface in the north shows the influence of surface fluxes near the northern end of the ice shelf.

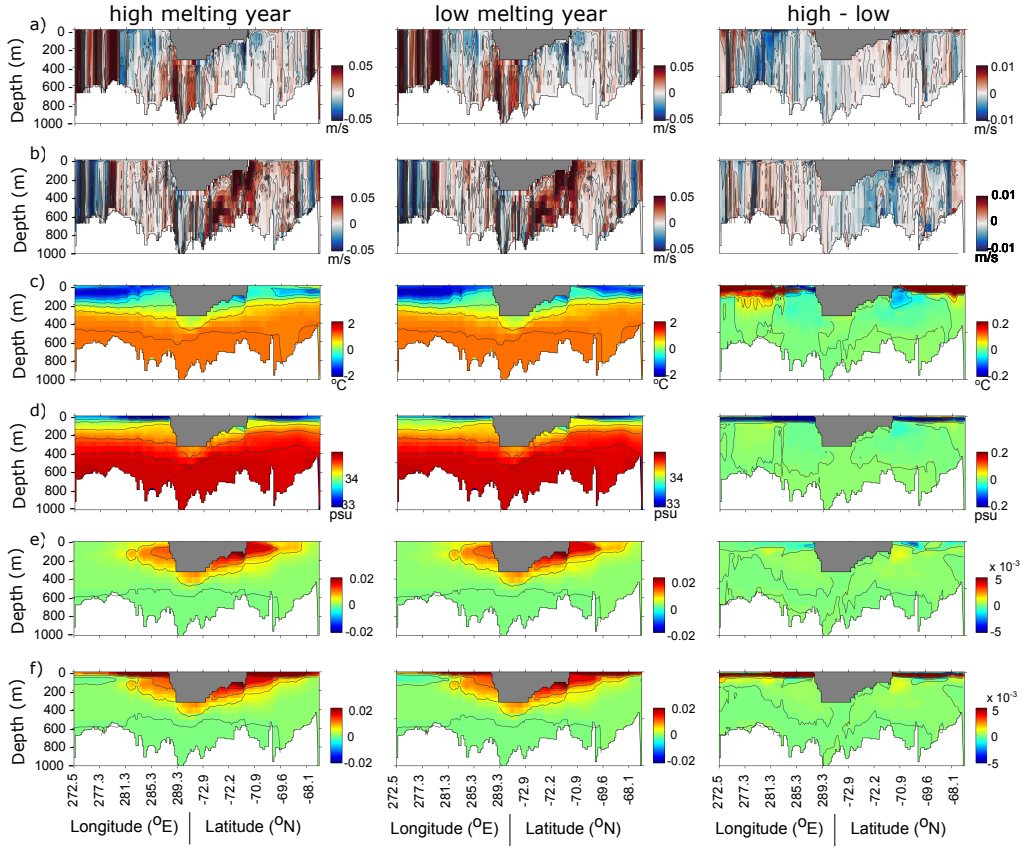

Figure 5.10: Annual melt rates categorised into high-melt years (1989-1994, and 2002-2008, first column) and low-melt years (1995-2001, and 2009-2014, second column) and associated fields then averaged.The third column shows the difference between the two categories. a) and b) show zonal and meridional velocities in high years and low years and the difference between the two under the section through the deepest part of Belgica Trough, under GVIIS and out through Marguerite Trough to the shelf break, as shown in 4.19. c) and d) show temperature and salinity and e) and f) show the ice shelf melt tracer and total freshwater tracer respectively.

To understand the discrepancy between Holland et al. (2010) and this model, the average melt rates for each year have been split into low and high years and the ocean properties of those years averaged for comparison. This binning results in high years being 1989-1994, and 2002-2008, the remaining years categorised as low-melt years. Figure 5.10 shows the resulting a) zonal and b) meridional velocities, c) temperature and d) salinity, e) ice shelf meltwater tracer and f) total tracer, from the shelf break, through the deepest

part of Belgica Trough, under GVIIS and out through Marguerite Trough to the shelf break.

In all years there is a clear stratification across the vertical section, with isopycnals rising towards the surface close to the coast due to freshwater inputs ((Figure 5.10c,d). In high-melting years, the flow through GVIIS is slightly reduced (via decreased eastward velocities in the southern portion, and decreased northward velocities out through Marguerite Trough, Figure 5.10a,b). In general, surface waters are warmer and fresher in high-melt years (Figure 5.10c,d).

Changes are particularly apparent at either end of GVIIS, where cooler, fresher water resides in high-melt years at depth. This is due to increased the ice shelf tracer content (Figure 5.10e) at depth, while at the surface, reduced ice shelf meltwater suggests influence of other freshwater components. This is clear from looking at the total tracer (Figure 5.10f), which shows a clear signal of increased surface inputs in high melt years. This suggests that melt rates of ice shelves are closely linked to surface freshwater content, potentially through temperature increase (Figure 5.10c), but also potentially a consequence of effects on all surface inputs and their resulting tracers. Holland et al. (2010) suggest that changes to sea ice at the southern end cause the increased interannual variability they see there, and whilst the opposite trend is seen in this model, it appears that sea ice (which dominates the surface, as seen in Chapter 4), does have a role in stratification and therefore presence of meltwater. However, the trend in sea ice flux does not directly align with that of the ice shelf melting patterns, highlighting the complexity of the variability. Future work would focus on deducing the cause and effect of ice shelf melting in the region.

5.4.2 Wilkins, Stange and Venable ice shelves

The remaining ice shelves on the peninsula are much smaller than GVIIS, and are generally shallower. Figure 5.11a shows the average melt rate of Wilkins Ice Shelf alongside average vertical metres of tracer under the ice shelf. A comparison with Padman et al. (2012) shows that their melt rate of 1.3 m/y is generally reproduced by the model. Although a decline from 2000 is seen until 2012. The melt rate found by Holland et al. (2010) of 0.7 m/y also fits the winter melt rates of this model. Oceanographic conditions (Figure 5.11c and d) also align with Padman et al. (2012), with a Winter Water layer varying between 100 and 200 metres, and CDW from 280 to 400 metres and below. Additionally, the finding of significant sensitivity of basal melt to surface processes is apparent in the model, with a strong seasonality in the melt rates and peaks in summer. Dinniman et al. (2012) found that Wilkins Ice Shelf is particularly sensitive to changes in winds at the shelf break, which shows the effect of nonlocal changes. The interannual variability in the modelled average melt rates is much smaller than Dinniman et al. (2012) found at particular locations.

Padman et al. (2012) found that the year 2000 was a turning point, with lower melt rates from 2000 onwards. Whilst the period of 1999-2001 in this model sees much larger summer melt rates which only occur again from 2012 onwards, this is at odds

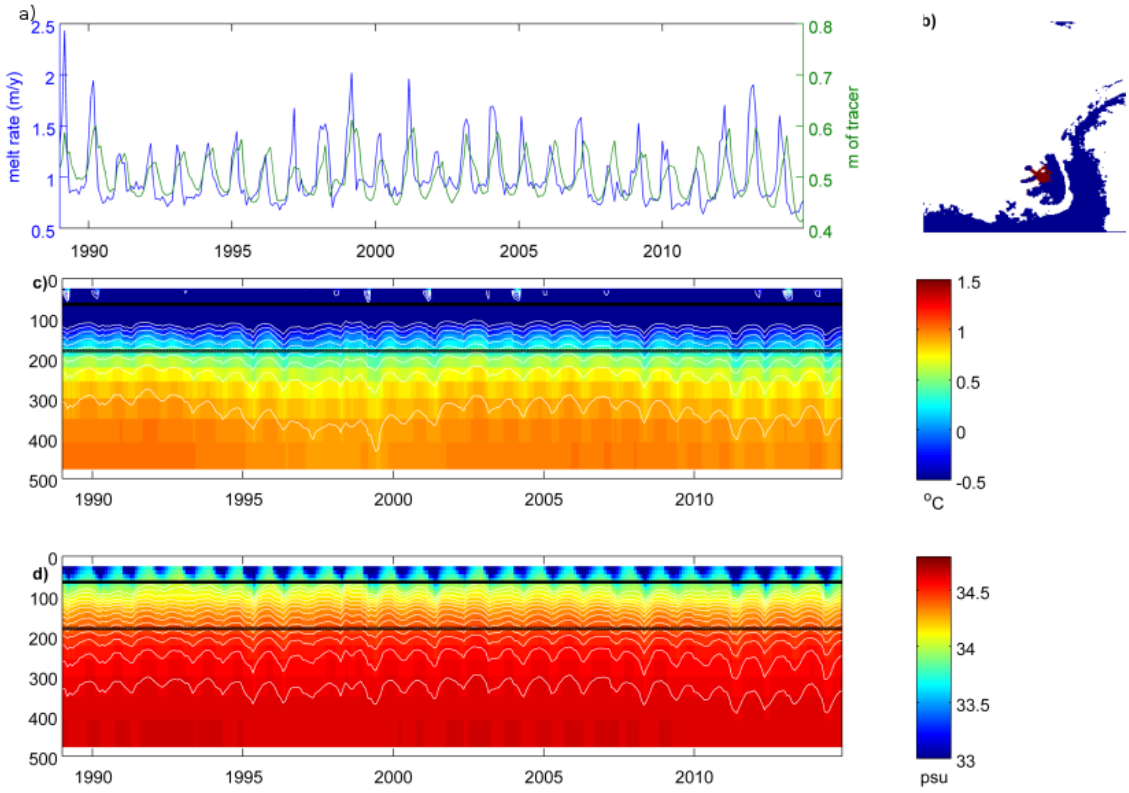

Figure 5.11: Timeseries of average basal melt rate (blue) alongside average metres of ice shelf tracer over the full water column (green) beneath the Wilkins Ice Shelf (b), and Hovmöller diagrams for the horizontally-averaged temperature (c) and salinity (d) under the Wilkins Ice Shelf over time. Black lines show the average and deepest depth of the ice shelf.

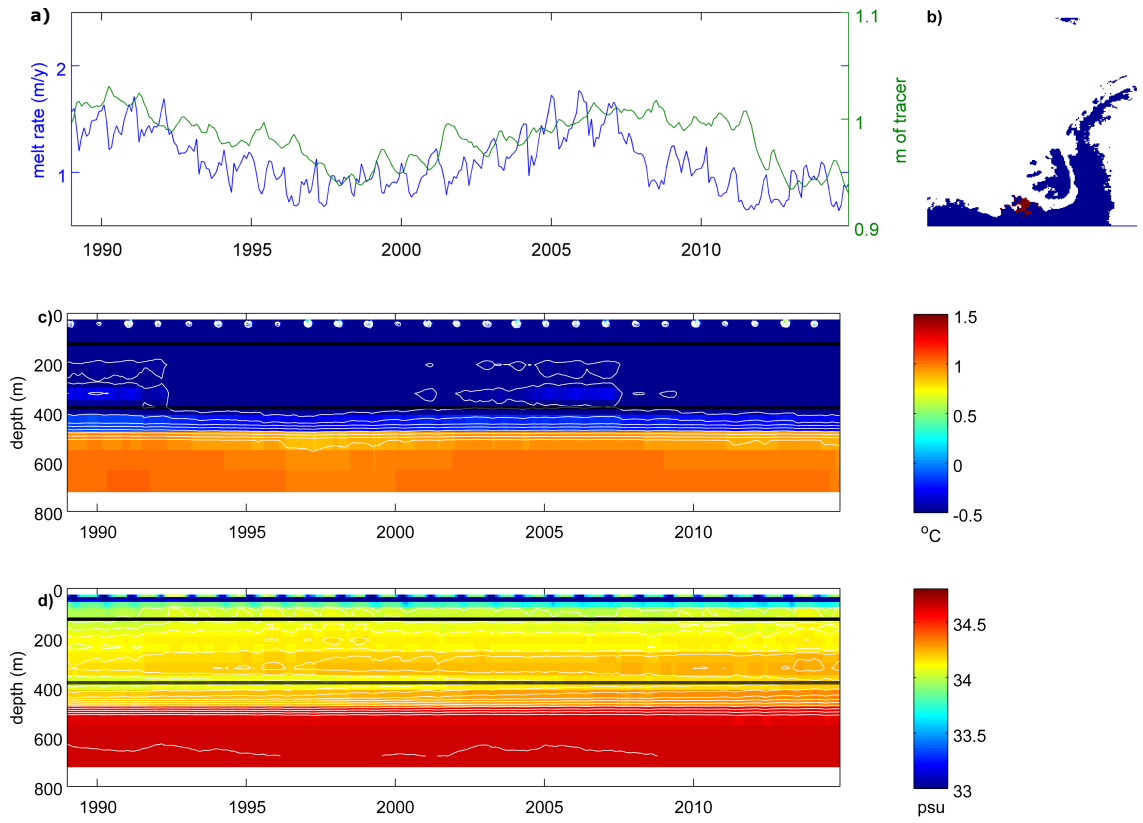

Figure 5.12: Timeseries of average basal melt rate (blue) alongside average metres of ice shelf tracer over the full water column (green) beneath the Stange Ice Shelf (b), and Hovmöller diagrams for the horizontally-averaged temperature (c) and salinity (d) under the Stange Ice Shelf over time. Black lines show the average and deepest depth of the ice shelf.

with the oceanographic setting where warmer CDW and thermocline waters in the model shoal upwards from 2000 (which would result in increased melting). Conversely, peaks in summer melting occur when the thermocline deepens. The Wilkins Ice Shelf meltwater contribution is dominated by basal melting over calving (Rignot et al.; 2013), but it is less dependent on CDW than deeper ice shelves as its average depth is partially in the mixed layer (Holland et al. (2010); Figure 5.11). Whilst the annual trend agrees with changes to thermocline depth, the seasonal melt rate does not, and therefore must be controlled by surface variations instead.

Dinniman et al. (2012) suggest that the core CDW properties are retained when reaching the Wilkins Ice Shelf as it is closer to the shelf break and has therefore experienced less mixing. There are similarities between the ocean properties under Wilkins Ice Shelf and GVIIS (Figure 5.9), suggesting that there is interannual variability in this mixing that is actually also seen under Stange and Venable ice shelves (Figures 5.12c,d and 5.13c,d). In all cases, melt rates are dominated more by seasonality than interannual variability, with the tracer content lagging the flux by varying degrees. On a seasonal basis, the content trend in both Venable and Stange Ice Shelf noticeably lags the ice shelf melt rate (Figures

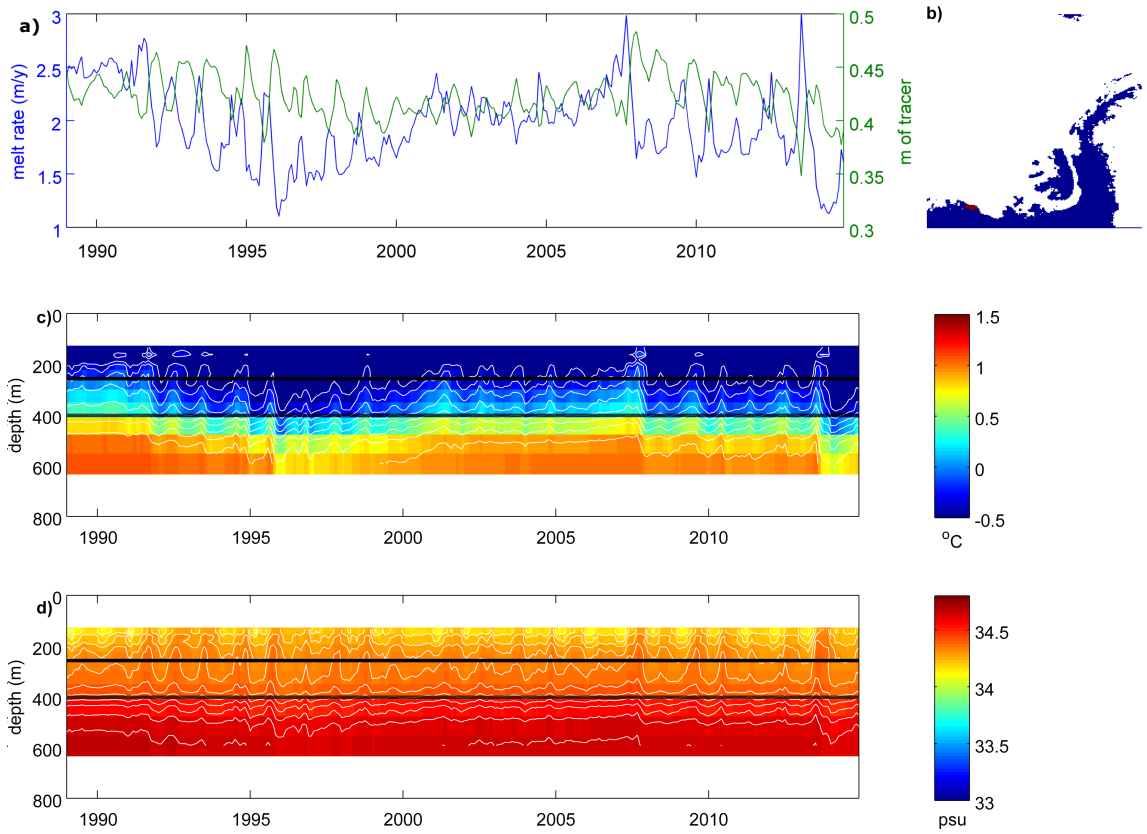

Figure 5.13: Timeseries of average basal melt rate (blue) alongside average metres of ice shelf tracer over the full water column (green) beneath the Venable Ice Shelf (b), and Hovmöuller diagrams for the horizontally-averaged temperature (c) and salinity (d) under the Venable Ice Shelf over time. Black lines show the average and deepest depth of the ice shelf.

5.12a and 5.13a) but they are consistent in long-term variability and the oceanographic conditions, with shallowing periods of CDW and the thermocline resulting in increases in melt rates, particularly between 1996 and 2007. CDW is able to reach the ice shelf base under Venable Ice Shelf, particularly in 2007 and 2012, causing large spikes in melt rates which does not transfer into the meltwater signal. Thus total meltwater content is more affected by longer-term variations than seasonality. In terms of wider oceanography, increased flow to Stange Ice Shelf is seen (Figure 5.2 in years of high melting, but Venable Ice Shelf has decreased flow in 1992 and 2011 when melt rates are high. Therefore the feedbacks associated with ice shelf melt and oceanography are key in determining the conditions.

5.5 Spatial variation in temporal change

The time series of freshwater change (Figure 5.1) provides an invaluable insight into the quantification of freshwater fields over time. However, further investigations have shown that this can mask spatial variation. For example, sea ice trends show key areas that have significant changes over 1992-2011 while other areas have remained constant, while an absence of clear link between ice shelf melt rates and resulting meltwater suggest that the spatial distribution of glacial freshwater flux could be of importance. This section aims to investigate this.

Figure 5.14 shows a map of the correlation between interannual anomalies of local flux and the shelf-average depth-integrated tracer content (the latter from Figure 5.1c) for each freshwater component over the time period 1989-2014, in order to understand the temporal link between the two fields. This provides the following information:

- 1: Flux and tracer content covary, and therefore it is likely the local flux has a significant effect on the shelf-wide tracer content of that freshwater component over the correlated time period. This is therefore likely to be a key region of input freshwater flux.
- 0: No covariance between flux and tracer, so the flux into the area has little effect on the shelf-wide tracer content.
- -1: The source of freshwater has an inverse relationship with the amount of tracer, so that when positive flux is high, the freshwater content reduces. This suggests that there is at least one other process that is having the opposite effect on each.

Thus, whilst an individual point is unlikely to provide much insight, regions with similar correlation can allow deduction of the local interplay between oceanography and meltwater.

Figure 5.14 shows that, in general, whilst there is a positive correlation on the majority of the shelf, in most locations this is not significant, suggesting that temporal variability in tracer content is not clearly linked with its flux. However, there are some key regions where this does not hold. Away from the coastal regions, evaporation and precipitation are significant, with precipitation more important north of Alexander Island and evaporation

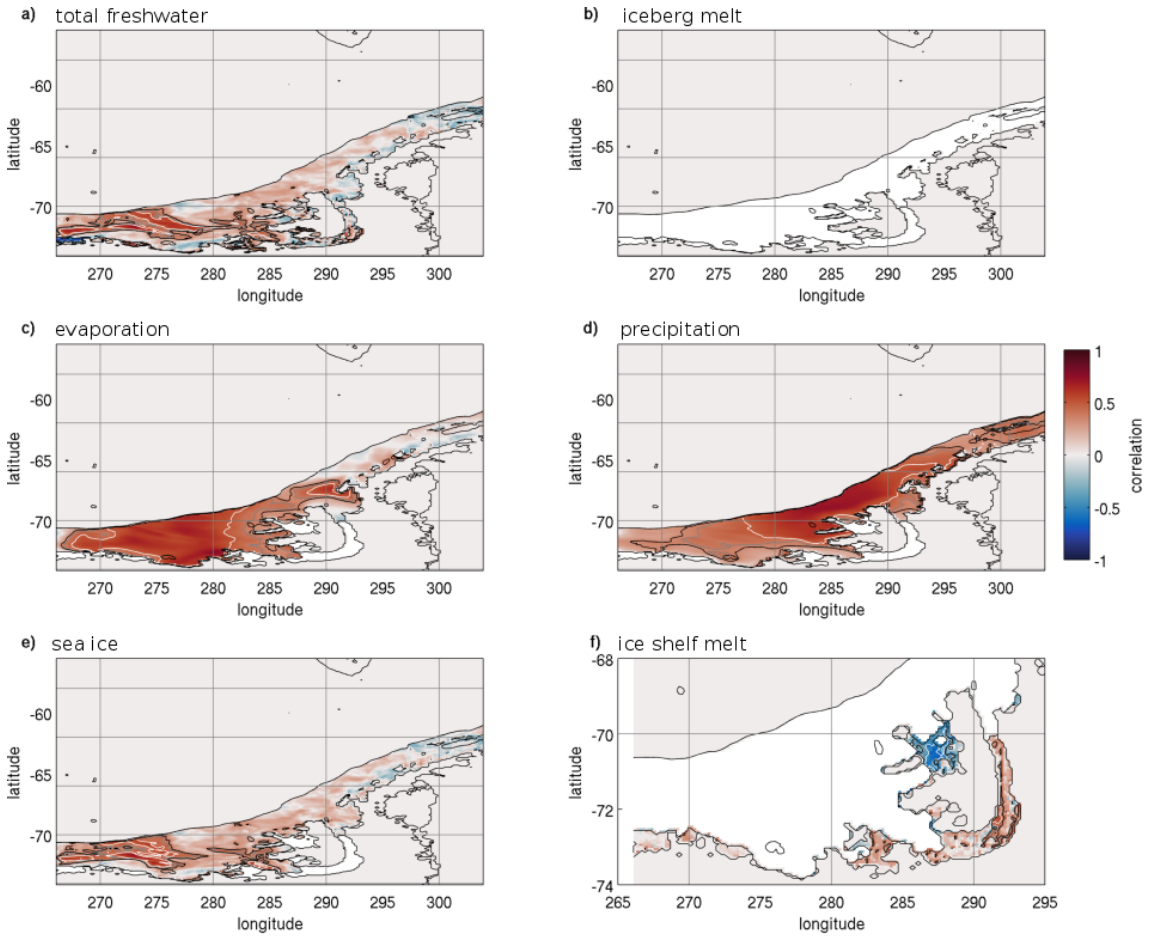

Figure 5.14: Figure showing the correlation between the shelf-mean interannual anomaly timeseries of shelf-wide depth-integrated tracer content and the local flux at each grid point, for each freshwater component. Correlations were carried out for the full anomaly (1989-2014). Areas with correlation at the 90%, 95% and 99% confidence limits are shown in black, grey and white contours respectively.

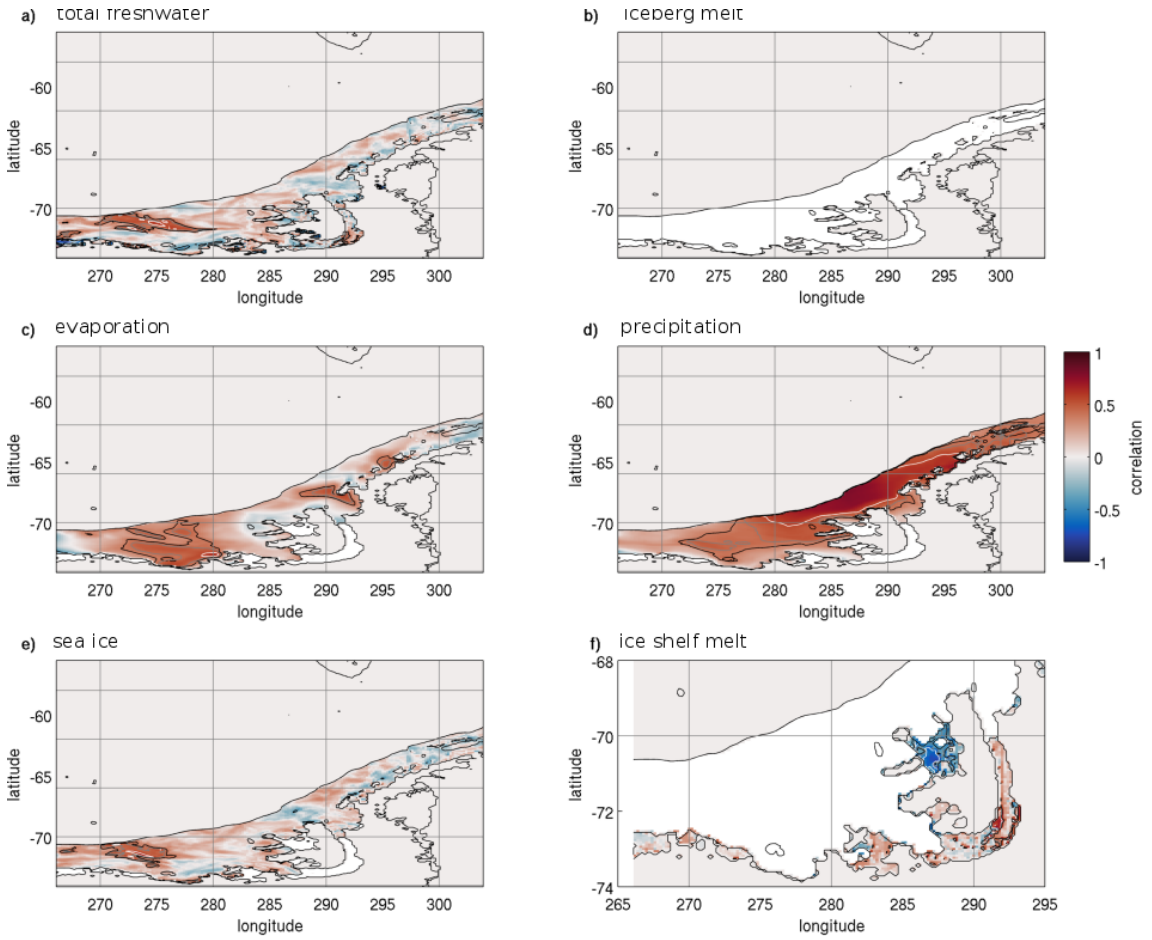

Figure 5.15: Figure showing the correlation between the shelf-mean interannual anomaly timeseries of shelf-wide depth-integrated tracer content and the local flux at each grid point, for each freshwater component. Correlations were carried out for the freshening-trend subset of the anomaly (1992-2011). Areas with correlation at the 90%, 95% and 99% confidence limits are shown in black, grey and white contours respectively.

more important west of 280 °E and in a small region west of Adelaide Island. This suggests that regions of lower summer sea ice cover are significantly affected by atmospheric inputs. Sea ice in the south shows significant correlation, especially along the inflow of CDW onto the shelf. This suggests that the flux in this region is affected by this inflow, which then carries the tracer further onto the shelf. This is backed by a further region of high correlation (significant at the 90% level) occurring close to Ronne Entrance in the return flow region. The lack of correlation elsewhere for sea ice, despite its shelf-wide link with total freshwater tracer content over time and thus the similarity between 5.14a and e, emphasises its strong regional variability year-on-year and its delicate balance of freezing and melting resulting in a changeable annual average that is not as consistent as other fluxes.

Ice shelf melting is generally positively correlated to the ice shelf meltwater shelf content, highlighting the role of each ice shelf in the annual freshwater budget is important over time. This is particularly strong at the centre of GVIIS. However, this is at odds with Wilkins Ice Shelf, the only region of anticorrelation on the shelf. This suggests that a shallowing thermocline that increased melt rates there (as shown in the previous section) is controlled by processes that serve to reduce tracer content elsewhere. For example, Dinniman et al. (2012) found that increased winds at the shelf break served to increase Wilkins Ice Shelf basal melt rates but decrease GVIIS because of increased mixing before reaching the base of the ice. The resulting meltwater content of GVIIS outweighs the opposing effect of Wilkins Ice Shelf. Note that iceberg melting shows no correlation as its flux is temporally uniform.

Since the correlation is linking the temporal variation of tracer and flux, which are known to have trends in interannual variability, it can be helpful to look at the correlation between the local flux anomaly and total shelf anomaly of Figure 5.1 over the freshening period of 1992-2011. The resultant correlations in Figure 5.15 show little deviation from the trends over 1989-2014. This suggests that key flux regions are established on the shelf and are relatively insensitive to change despite variations in oceanography, which further implies that any oceanographic change and resulting freshwater content is closely related to the flux input. A slight reduction in the correlation of evaporation is seen, with some negative areas appearing and a significant area forming around the Palmer site. The strongly-correlated region of precipitation flux and content has shifted northwards, and more anti-correlation is observed in both the sea ice and total freshwater plots. This means that when temporal change occurs, the shelf-wide freshwater content is more sensitive to change to all fluxes across the whole shelf rather than it being attributable to one particular flux or one area. This emphasises the non-local nature of freshwater content on the shelf.

5.6 Summary

The findings of this chapter suggest that temporal variability is significant in a range of contexts. Key findings are outlined below in the context of the original lines of investiga-

tion.

1 **What are the oceanographic conditions in the context of time-varying salinity and freshwater content?**

In general, high fluxes translate to a high annual tracer content, but the effects of the high residence time of Eltanin Bay brine-enhanced water, along with residual freshwater from previous years, means that the conditions are not straightforward to interpret. Interannual variability of the currents alone is significant, explaining why the constant freshwater flux from prescribed iceberg melt translates to a non-uniform freshwater content and suggesting that there is no simple relationship between the strength of the main currents and freshwater distribution.

2 **Given the importance of sea ice on the seasonal cycle of freshwater in the Bellingshausen Sea, along with its domination of tracer content, how does it vary temporally, and why? What is the significance of the trend in the sea ice freshwater content?**

Over the full model period (1989-2014) there are no overall salinity trends despite increasing precipitation, evaporation, and iceberg melt tracers (the latter increasing despite a constant prescribed flux). However, a strong surface freshening occurs during 1992-2011, a period studied by several previous authors. In the model, a strong decrease in ice growth in autumn causes this freshening, driven by northerly wind trends. This illustrates the importance of sea ice to decadal freshwater change.

3 **Since ice shelf melting predicted by the model results in significant contributions to tracer content at depth, known to have a long residence time, how does this translate to change in freshwater content over time? Is there any link to the large surface changes?**

Ice shelf melting displays little interannual variability despite their large contribution to the long-term mean. Shallower ice shelves are more affected by surface processes, with tracer content lagging the flux due to seasonal processes. GVIIS displays more links with longer-term variation to CDW inflow, though differing behaviour in the north and south disagrees with previous analyses (Holland et al.; 2010), and whilst both studies suggest sea ice could be a factor, the present model finds that the north section shows more variation in both melt rates and resulting local tracer content. It is not easy to deduce whether the flow is affecting the melt rates or vice versa due to the feedbacks in the system, but increases in other surface tracers occurs alongside increased melt rates.

4 **What is the spatial variation in temporal change? Can the changes to flux and tracer content be reconciled?**

In general, changes in shelf-wide tracer content over time do not result from changes to their corresponding local flux in one particular region, highlighting the significance

of all fluxes over the entire shelf in driving temporal change in freshwater content. However, key regions have more influence than others, with evaporation in the south and precipitation in the north dominating their overall tracer content, and ice shelf melt in GVIIS having a big effect on its tracer content. Sea ice only contributes significantly to tracer content in the south, highlighting the importance of this region in sea ice flux over time and the strong temporal variability of annual sea ice flux that prevents a coherent relationship at individual locations.

It is clear that whilst sea ice is a key driver of temporal variability in the Bellingshausen Sea freshwater budget, other components must not be dismissed as they contribute locally and can result in feedbacks affecting the sea ice flux. In particular, ice shelf melting has complex links which need to be understood further. Whilst sea ice dominates the temporal trend, its strong seasonality and regional variability mean that its effects are hard to deduce. This is an important consideration for future climate scenarios.

Chapter 6

Conclusions

There are multiple drivers of ocean circulation and transport on the Antarctic Peninsula shelf, and these vary locally and over time. The ocean is affected by freshwater inputs from both sea ice and meteoric sources, the balance of which is variable and insufficiently understood, but the overall composition of which is thought to be changing. Whilst oxygen isotope data can be used to identify the relative contributions of sea ice and meteoric water sources at a particular location and time, data is sparse and generally more obtainable in summer, something that is problematic since the ocean system has very seasonal behaviour. This paucity of data makes interpretation difficult, particularly in the past.

Chapter 1 found that it is clear the changes to the freshwater budget of the Bellingshausen Sea could have profound changes on its circulation and associated feedbacks, both regionally and beyond, but there are still many questions surrounding the quantification of the variation in the freshwater flux and content. Motivated by this, the aim of this thesis was to develop a new model of the Bellingshausen Sea to investigate the temporal and spatial variation in each freshwater source (sea ice melt/freeze, precipitation/evaporation, iceberg melt, ice shelf melt and glacier melt), and their overall importance in the freshwater budget. Chapter 2 demonstrated the creation of a high resolution model of the Bellingshausen Sea with realistic inputs and a setup that runs from 1989-2014. Noting that Chapter 1 identified a need to look in detail at the behaviour of individual freshwater sources, Chapter 3 developed the MITgcm code to enable detailed tracking of the fate of each individual freshwater source so that the model was able to deduce the relative composition of each to the overall freshwater budget. The model output was then validated against available data in Chapter 4. Throughout the remainder of the thesis, the developed Bellingshausen Sea model was used to investigate the long-term mean and interannual variability of these, with the results summarised in Figure 6.1. Key findings are summarised below.

6.1 Long-term mean spatial distribution

On an annual mean basis, all freshwater fluxes (precipitation, evaporation, sea ice, icebergs and ice shelves) are comparable, and this is largely reflected in the on-shelf content of each

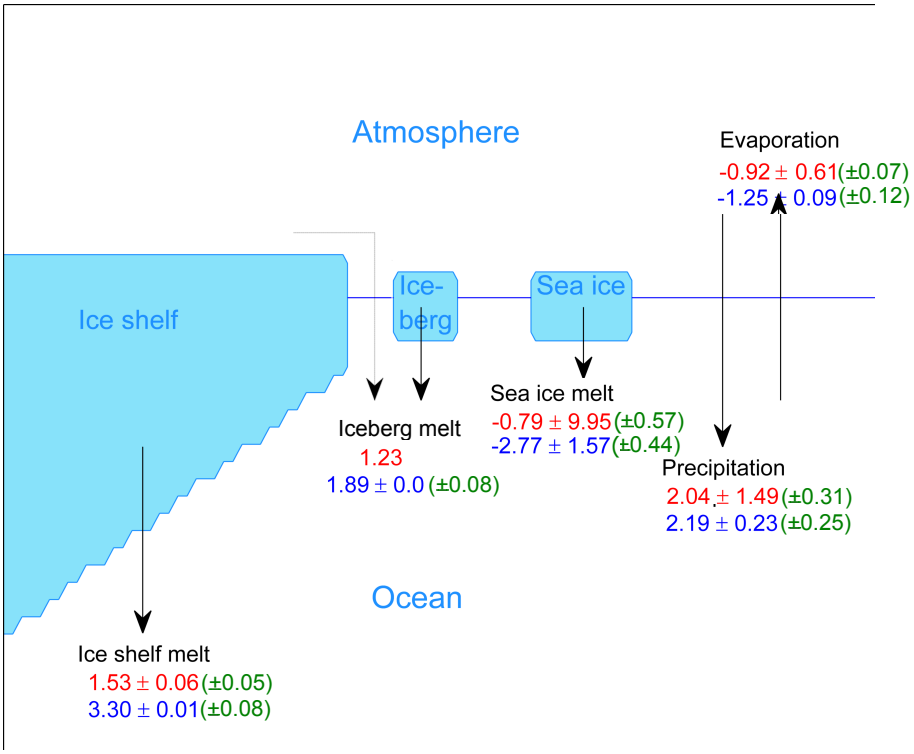

Figure 6.1: Schematic showing the fluxes (red, $\times$ 10^{11} m^3/y) and freshwater content (blue, $\times$ 10^{11} m^3) in the Bellingshausen Sea, along with interannual variability shown in green. Average on-shelf fluxes and tracers labelled from Table 5.1. Quantities show 1 standard deviation error bars indicating seasonal variability.

(Figure 6.1). Ice shelf melt is the largest single contributor to mean freshwater content in the BS, thus it is vital that its contribution is further understood in light of recent changes to ice shelf melting. South of George VI Ice Shelf, the peak ice shelf meltwater resides at intermediate depths, while to the north it reaches the surface (section 4.2, Figures 4.12-4.13), highlighting the differing conditions in the north and southern regions of the Bellingshausen Sea.

Significant spatial variability of freshwater is seen in the Bellingshausen Sea (section 4.4, Figure 4.20). It is clear that, in addition to north-south variations, individual sites behave differently according to their proximity to gyres, deep currents or seasonally-enhanced coastal currents. This has an effect on both the input fluxes, through sea ice cover and changes to ice shelf melt, and the residence time of freshwater content at different depths. It will also maintain stratification, or in the case of Eltanin Bay, cause significant destabilisation. When selecting water column sample sites, and representative depths, care must therefore be taken to account for the local oceanography. Additionally, caution must be used in the interpretation, and comparison, of geographically-separated sediment core δ^{18}O records that may be recording waters from different sources, or missing the bulk of some freshwater components, despite the δ^{18}O being measured on organisms living at the same depth and in the same ecological niche.

6.2 Seasonality

Sea ice dominates the seasonal freshwater cycle such that sea ice fluxes are instantaneously an order of magnitude larger than any other source, while precipitation has a large magnitude peak in autumn when others reduce (section 4.3, Figure 4.14). Spatial variation is significant on the shelf, with the north being a region of strong precipitation and net sea ice melt in summer, while the south has a large winter sea ice freezing (section 4.3, Figure 4.15) which dominates its annual signal. Thus seasonal and spatial variation in freshwater fields can be hidden in observations that only span one time period. In Eltanin Bay, strong winter salinification from sea ice growth is masked by a net positive total freshwater content from meteoric sources, showing the importance of identifying the full regional composition of freshwater. Additionally, when assessing the freshwater balance, the different origins of freshwater content cannot be deduced from fluxes, or vice versa, since many freshwater constituents are far removed in space and time from their sources. This is particularly relevant for single site studies which infer conditions from past climates (e.g. Pike et al.; 2013; Swann et al.; 2013).

6.3 Interannual variability

While the seasonal cycle of sea ice flux is an order of magnitude larger than the other freshwater sources, the interannual changes of both sea ice and precipitation fluxes are an order of magnitude larger than the other variables (section 5.1, Figure 5.1e; Table 5.1). Over the full model period (1989-2014) there are no overall salinity trends despite increas-

ing precipitation, evaporation, and iceberg melt tracers (the latter increasing despite a constant prescribed flux). However, a strong surface freshening occurs during 1992-2011 (section 5.1, Table 5.2), a period studied by several previous authors. In the model, a strong decrease in ice growth in autumn causes this freshening, driven by northerly wind trends (section 5.3, Figure 5.6). This illustrates the importance of sea ice to decadal freshwater change, as well as emphasising the importance of regional variation on the overall shelf-wide changes. This raises the question of how important sea ice trends could be in other areas of sea ice decline, and the effects of sea ice growth in the freshwater budget in other areas of Antarctica.

Despite the significance of sea ice meltwater, changes in shelf-wide tracer content over time do not easily occur from changes to the local flux in one particular region, highlighting the significance of all fluxes over the entire shelf in driving temporal change in freshwater content and the complexity of isolating key regions or processes. In particular, the local influence of sea ice is complicated by the seasonal effects on the annual-mean flux. However, some regions have more influence than others, with evaporation in the south and precipitation in the north dominating offshore links with flux and ice shelf melt in GVIIS having a big effect on its overall tracer content.

In general, high fluxes translate to a high annual tracer content, but the effects of the high residence time of Eltanin Bay brine-enhanced water, along with residual freshwater from previous years, means that the conditions are complex and challenging to interpret. Interannual variability of the currents alone is significant, explaining why the constant freshwater flux from prescribed iceberg melt translates to a non-uniform freshwater content and suggesting that there is no simple relationship between the strength of the main currents and freshwater distribution.

Ice shelves display little interannual variability in both their flux and resulting meltwater despite their large contribution to the long-term mean. Whilst there is a clear link to shallower ice shelves and surface processes, the northern end of GVIIS displays sensitivity to the surface ocean in addition to longer-term variation to CDW inflow. This means that change to surface ocean processes could have effects on ice shelf melting, which is significant given the importance of ice shelves in the long-term mean and their potential effects beyond the Bellingshausen Sea (e.g. Nakayama et al.; 2014a).

6.4 Implications and future work

The creation, development and analysis of a high-resolution model of the Bellingshausen Sea has yielded some important results. The significance of sea ice trends in forcing long-term freshwater variability has been demonstrated, along with the importance of ice shelf meltwater which had not previously been quantified. This has been documented in Regan et al. (Submitted), which highlights the need for year-round observations and understanding of features at depth as well as surface change.

In addition to the scientific output of the model, this Bellingshausen Sea modelling

study has developed a useful tool, both by creating a model for use in other fields (for example, collaborations with scientists at Woods Hole Oceanographic Institution, who are now adding biological components to the model developed), and development of the method to trace individual freshwater components in the ocean from their source which has subsequently been implemented in an Amundsen Sea model (Kimura et al.; Submitted).

Whilst the model has successfully recreated a realistic setup of the Bellingshausen Sea, perhaps its biggest limitation is the uniform iceberg melt field. In the absence of data, it would be difficult to impose a realistic temporal field, and the study finds that the Bellingshausen Sea model is sensitive to magnitude of iceberg melt input but not spatial distribution. While the finding gives confidence in the setup and results, a comprehensive set of observations would allow fewer assumptions to be made and add a temporal component to the field, strengthening results further. The use of an interactive iceberg model could be implemented in future studies to allow some temporal evolution of the field and feedbacks from the model; here, observations would still be useful for validation purposes.

A choice that was made in the model setup was to ascribe purely local forcing to each freshwater field, setting zero tracer content on the boundaries. This was to quantify the local effects, but therefore does not account for any freshwater inputs from elsewhere, despite the ACC entering the domain along the western boundary. To reasonably force the model with nonlocal conditions, the model would need to be provided with accurate boundary conditions which could be derived from a Southern Ocean model run. If this were to be done, the model could feasibly be set up with the new code to enable a whole Southern Ocean modelling study of freshwater. However, this would still require northern precipitation and evaporation tracer boundary conditions to allow for their nonlocal representation. As such, scaling the model up would require significant additional computing power and time, though it would provide a unique insight into the whole Antarctic freshwater balance. A further step of adding a δ^{18}O tracer would also provide further insight into changes to freshwater content in the Bellingshausen Sea.

Another key next step would be to trace individual ice shelves. During the analysis, it was useful to attribute freshwater into its components, but non-local ice shelf melt was hard to analyse given that there is significant advection of tracers from their source, both in this study and others (e.g. Nakayama et al.; 2014a). Given that pathways of GVIIS, Wilkins and Bach are often shared (Jenkins and Jacobs; 2008), and it would be useful to diagnose the contribution from each and their fate. In conjunction with this, tagging certain areas of sources would allow further investigation into the pathways on the shelf and the fate of waters, such as those that are fluxed into Eltanin Bay. However, as noted above, this would require significant increases in computational development, time and storage, and therefore was not feasible for this study.

An investigation into both the importance of higher resolution (e.g. Graham et al.; 2016) and the model's ability to resolve coastal features better, given the link between coastal regions and freshwater input (e.g. Meredith et al.; 2016) would be desirable. This would allow more geographical effects to be deduced. Additionally, analysis of the effect

of freshwater on the ocean (e.g. as in Abernathey et al.; 2016) would further develop understanding of the implications of the changes occurring to the freshwater balance of the Bellingshausen Sea.

Chapter 7

References

Abernathey, R., Cerovecki, I., Holland, P., Newsom, E., Mazloff, M. and Talley, L. (2016). Water-mass transformation by sea ice in the upper branch of the Southern Ocean overturning, *Nature Geoscience* **9**: 596–601.

Adcroft, A., Hill, C. and Marshall, J. (1997). The representation of topography by shaved cells in a height coordinate model, *Monthly Weather Review* **125**(9): 2293–2315.

Annett, A. L., Skiba, M., Henley, S. F., Venables, H. J., Meredith, M. P., Statham, P. J. and Ganeshram, R. S. (2015). Comparative roles of upwelling and glacial iron sources in Ryder Bay, coastal western Antarctic Peninsula, *Marine Chemistry* **176**: 21–33.

Barbara, L., Crosta, X., Schmidt, S. and Massé, G. (2013). Diatoms and biomarkers evidence for major changes in sea ice conditions prior the instrumental period in Antarctic Peninsula, *Quaternary Science Reviews* **79**: 99–110.

Bhatt, V. (2009). T-S diagram. MATLAB Central File Exchange. Retrieved: 08/04/2017. **URL:** *mathworks.com/matlabcentral/fileexchange/23796*

Bintanja, R., van Oldenborgh, G. J., Drijfhout, S. S., Wouters, B. and Katsman, C. A. (2013). Important role for ocean warming and increased ice-shelf melt in Antarctic sea-ice expansion, *Nature Geoscience* **6**(5): 376–379.

Böning, C. W., Dispert, a., Visbeck, M., Rintoul, S. R. and Schwarzkopf, F. U. (2008). The response of the Antarctic Circumpolar Current to recent climate change, *Nature Geoscience* **1**(12): 864–869.

Boyer, T. P., Antonov, J. I., Baranova, O. K., Garcia, H. E., Johnson, D. R., Locarnini, R. A., Mishonov, A. V., O'Brien, T. D., Seidov, D., Smolyar, I. V. and Zweng, M. M. (2009). World Ocean Database 2009, Chapter 1: Introduction, *in* S. Levitus (ed.), *NOAA Atlas NESDIS 66*, World Ocean Database 2009, U.S. Gov. Printing Office, Wash. D.C., p. 216.

Carmack, E. C. (2007). The alpha/beta ocean distinction: A perspective on freshwater fluxes, convection, nutrients and productivity in high-latitude seas, *Deep Sea Research Part II: Topical Studies in Oceanography* **54**: 2578–2598.

Carter, L., McCave, I. and Williams, M. J. (2008). Chapter 4 - Circulation and Water Masses of the Southern Ocean: A Review, *in* F. Florindo and M. Siegert (eds), *Antarctic Climate Evolution*, Vol. 8 of *Developments in Earth and Environmental Sciences*, Elsevier, pp. 85–114.

Cavalieri, D. J., Parkinson, C. L., Gloerson, P. and Zwally, H. J. (1996). Sea Ice Concentrations from Nimbus-7 SMMR and DMSP SSM/I-SSMIS Passive Microwave Data, Version 1. [1989-2014]. Accessed 23 June 2016, *NASA DAAC at the National Snow and Ice Data Center, Boulder, Colorado USA.* .

Chassignet, E. P., Smith, L. T., Bleck, R. and Bryan, F. O. (1996). A model comparison: numerical simulations of the north and equatorial Atlantic Ocean circulation in depth and isopycnic coordinates, *Journal of Physical Oceanography* **26**(1): 1849–1867.

Chelton, D. B., de Szoeke, R. A., Schlax, M. G., El Naggar, K. and Siwertz, N. (1998). Geographical variability of the first baroclinic rossby radius of deformation, *Journal of Physical Oceanography* **28**: 433–460.

Clarke, A., Murphy, E. J., Meredith, M. P., King, J. C., Peck, L. S., Barnes, D. K. A. and Smith, R. C. (2007). Climate change and the marine ecosystem of the western Antarctic Peninsula, *Philosophical transactions. Series B, Biological sciences.* **362**(1477): 149–166.

Cook, A. J., Fox, A. J., Vaughan, D. G. and Ferrigno, J. G. (2005). Retreating glacier fronts on the Antarctic Peninsula over the past half-century., *Science* **308**(5721): 541–544.

Cook, A. J., Holland, P. R., Meredith, M. P., Murray, T., Luckman, A. and Vaughan, D. G. (2016). Ocean forcing of glacier retreat in the western Antarctic Peninsula, *Science* **353**(6296): 283–286.

Cook, A. J. and Vaughan, D. G. (2010). Overview of areal changes of the ice shelves on the Antarctic Peninsula over the past 50 years, *The Cryosphere* **4**(1): 77–98.

Craig, H. and Gordon, L. (1965). Deuterium and oxygen 18 variations in the ocean and the marine atmosphere, *in* E. Tongiorgi (ed.), *Stable Isotopes in Oceanographic Studies and Paleotemperatures*, Consiglio nazionale delle richerche, Laboratorio de geologia nucleare, Pisa, pp. 9–130.

Cunningham, S. A. (2005). Southern Ocean circulation, *Archives of Natural History* **32**(2): 265–280.

Dansereau, V., Heimbach, P. and Losch, M. (2014). Simulation of subice shelf melt rates in a general circulation model: Velocity-dependent transfer and the role of friction, *Journal of Geophysical Research* **119**(3): 1765–1790.

de Jong, J., Schoemann, V., Lannuzel, D., Croot, P., de Baar, H. and Tison, J. L. (2012). Natural iron fertilization of the Atlantic sector of the Southern Ocean by continental shelf sources of the Antarctic Peninsula, *Journal of Geophysical Research* **117**: 1–25.

De Rydt, J., Holland, P. R., Dutrieux, P. and Jenkins, A. (2014). Geometric and oceanographic controls on melting beneath Pine Island Glacier, *Journal of Geophysical Research: Oceans* **119**(4): 2420–2438.

Dee, D. P., Uppala, S. M., Simmons, A. J., Berrisford, P., Poli, P., Kobayashi, S., Andrae, U., Balmaseda, M. A., Balsamo, G., Bauer, P., Bechtold, P., Beljaars, A. C. M., van de Berg, L., Bidlot, J., Bormann, N., Delsol, C., Dragani, R., Fuentes, M., Geer, A. J., Haimberger, L., Healy, S. B., Hersbach, H., Hólm, E. V., Isaksen, L., Kållberg, P., Köhler, M., Matricardi, M., McNally, A. P., Monge-Sanz, B. M., Morcrette, J.-J., Park, B.-K., Peubey, C., de Rosnay, P., Tavolato, C., Thépaut, J.-N. and Vitart, F. (2011). The ERA-Interim reanalysis: configuration and performance of the data assimilation system, *Quarterly Journal of the Royal Meteorological Society* **137**(656): 553–597.

Delaygue, G., Jouzel, J. and Dutay, J.-C. (2000). Oxygen 18-salinity relationship simulated by an oceanic general circulation model, *Earth and Planetary Science Letters* **178**(1-2): 113–123.

Depoorter, M. A., Bamber, J. L., Griggs, J. A., Lenaerts, J. T. M., Ligtenberg, S. R. M., van den Broeke, M. R. and Moholdt, G. (2013). Calving fluxes and basal melt rates of Antarctic ice shelves., *Nature* **502**(7469): 89–92.

Dierssen, H. M., Smith, R. C. and Vernet, M. (2002). Glacial meltwater dynamics in coastal waters west of the Antarctic Peninsula., *Proceedings of the National Academy of Sciences of the United States of America* **99**(4): 1790–1795.

Dinniman, M. S. and Klinck, J. M. (2004). A model study of circulation and cross-shelf exchange on the west Antarctic Peninsula continental shelf, *Deep Sea Research Part II: Topical Studies in Oceanography* **51**(17-19): 2003–2022.

Dinniman, M. S., Klinck, J. M. and Hofmann, E. E. (2012). Sensitivity of Circumpolar Deep Water transport and ice shelf basal melt along the West Antarctic Peninsula to changes in the winds, *Journal of Climate* **25**(14): 4799–4816.

Dinniman, M. S., Klinck, J. M. and Smith, W. O. (2003). Cross-shelf exchange in a model of the Ross Sea circulation and biogeochemistry, *Deep Sea Research Part II: Topical Studies in Oceanography* **50**(22-26): 3103–3120.

Dinniman, M. S., Klinck, J. M. and Smith, W. O. (2011). A model study of Circumpolar Deep Water on the West Antarctic Peninsula and Ross Sea continental shelves, *Deep Sea Research Part II: Topical Studies in Oceanography* **58**(13-16): 1508–1523.

Eicken, H. (1992). Salinity profiles of Antarctic sea ice: field data and model results, *Journal of Geophysical Research* **97 (C10)**: 15545–15557.

England, M. H. and Maier-Reimer, E. (2001). Using chemical tracers to assess ocean models, *Reviews of Geophysics* **39**(1): 29–70.

Epstein, S. and Mayeda, T. (1953). Variation of O^{18} content of waters from natural sources, *Geochemica et Cosmochimica Acta* **4**(5): 213–224.

Fretwell, P., Pritchard, H. D., Vaughan, D. G., Bamber, J. L., Barrand, N. E., Bell, R., Bianchi, C., Bingham, R. G., Blankenship, D. D., Casassa, G., Catania, G., Callens, D., Conway, H., Cook, A. J., Corr, H. F. J., Damaske, D., Damm, V., Ferraccioli, F., Forsberg, R., Fujita, S., Gim, Y., Gogineni, P., Griggs, J. A., Hindmarsh, R. C. A., Holmlund, P., Holt, J. W., Jacobel, R. W., Jenkins, A., Jokat, W., Jordan, T., King, E. C., Kohler, J., Krabill, W., Riger-Kusk, M., Langley, K. A., Leitchenkov, G., Leuschen, C., Luyendyk, B. P., Matsuoka, K., Mouginot, J., Nitsche, F. O., Nogi, Y., Nost, O. A., Popov, S. V., Rignot, E., Rippin, D. M., Rivera, A., Roberts, J., Ross, N., Siegert, M. J., Smith, A. M., Steinhage, D., Studinger, M., Sun, B., Tinto, B. K., Welch, B. C., Wilson, D., Young, D. A., Xiangbin, C. and Zirizzotti, A. (2013). Bedmap2: improved ice bed, surface and thickness datasets for Antarctica, *The Cryosphere* **7**(1): 375–393.

Fyfe, J. C. and Saenko, O. (2005). Human-induced change in the Antarctic Circumpolar Current, *Journal of Climate* **18**: 3068–3073.

Gent, P. R. and McWilliams, J. C. (1990). Isopycnal mixing in ocean circulation models, *Journal of Physical Oceanography* **20**: 150–155.

Gent, P. R., Willebrand, J., McDougall, T. J. and McWilliams, J. C. (1995). Parameterizing eddy-induced tracer transports in ocean circulation models, *Journal of Physical Oceanography* **25**: 463–474.

Gill, A. E. (1982). *Atmosphere-Ocean Dynamics*, 1st edn, Vol. 30 of *International Geophysics*, Academic Press, p. 662.

Gille, S. T. (2008). Decadal-scale temperature trends in the Southern Hemisphere ocean, *Journal of Climate* **21**(18): 4749–4765.

Gladstone, R. M., Bigg, G. R. and Nicholls, K. W. (2001). Iceberg trajectory modeling and meltwater injection in the Southern Ocean, *Journal of Geophysical Research* **106**(C9): 19903–19915.

Gnanadesikan, A., Dixon, K. W., Griffies, S. M., Balaji, V., Barreiro, M., Beesley, J. A., Cooke, W. F., Delworth, T. L., Gerdes, R., Harrison, M. J., Held, I. M., Hurlin, W. J., Lee, H.-C., Liang, Z., Nong, G., Pacanowski, R. C., Rosati, A., Russell, J., Samuels, B. L., Song, Q., Spelman, M. J., Stouffer, R. J., Sweeney, C. O., Vecchi, G., Winton, M., Wittenberg, A. T., Zeng, F., Zhang, R. and Dunne, J. P. (2006). GFDL's CM2 global coupled climate models. Part II: the baseline ocean simulation, *Journal of Climate* **19**(5): 675–697.

Goosse, H. and Fichefet, T. (1999). Importance of ice-ocean interactions for the global ocean circulation: a model study, *Journal of Geophysical Research* **104**(C10): 23337–23355.

Graham, J. A., Dinniman, M. S. and Klinck, J. M. (2016). Impact of model resolution for on-shelf heat transport along the West Antarctic Peninsula, *Journal of Geophysical Research: Oceans* **121**(10): 7880–7897.

Grotov, A. S., Nechaev, D. A., Panteleev, G. G. and Yaremchuk, M. I. (1998). Large scale circulation in the Bellingshausen and Amundsen seas as a variational inverse of climatological data, *Journal of Geophysical Research* **103**(C6): 13011–13022.

Hattermann, T. and Levermann, A. (2010). Response of Southern Ocean circulation to global warming may enhance basal ice shelf melting around Antarctica, *Climate Dynamics* **35**(5): 741–756.

Hellmer, H. H. (2004). Impact of Antarctic ice shelf basal melting on sea ice and deep ocean properties, *Geophysical Research Letters* **31**(10): L10307.

Hellmer, H. H. and Olbers, D. J. (1989). A two-dimensional model of the thermohaline circulation under an ice shelf, *Antarctic Science* **1**: 325–336.

Hibler, W. D. (1980). Modeling a variable thickness sea ice cover, *Monthly Weather Review* **108**: 1943–1973.

Hofmann, E. E., Klinck, J. M., Lascara, C. M. and Smith, D. A. (1996). Water mass distribution and circulation west of the Antarctic Peninsula and including Bransfield Strait, *in* R. M. Ross, E. E. Hofmann and L. B. Quetin (eds), *Foundations for Ecological Research West of the Antarctic Peninsula*, Vol. 70 of *Antarctic Research Series*, American Geophysical Union, Washington, D. C., pp. 61–80.

Holland, D. M. and Jenkins, A. (1999). Modeling thermodynamic ice-ocean interactions at the based of an ice shelf, *Journal of Physical Oceanography* **29**: 1787–1800.

Holland, P., Bruneau, N., Enright, C., Losch, M., Kurtz, N. and Kwok, R. (2014). Modelled trends in Antarctic sea ice thickness, *Journal of Climate* **27**(10): 3784–3801.

Holland, P. R. (2014). The seasonality of Antarctic sea ice trends, *Geophysical Research Letters* **41**: 4230–4237.

Holland, P. R., Jenkins, A. and Holland, D. M. (2010). Ice and ocean processes in the Bellingshausen Sea, Antarctica, *Journal of Geophysical Research* **115**(C5): C05020.

Holland, P. R. and Kimura, N. (2016). Observed concentration budgets of Arctic and Antarctic sea ice, *Journal of Climate* **29**(14): 5241–5249.

Holland, P. R. and Kwok, R. (2012). Wind-driven trends in Antarctic sea-ice drift, *Nature Geoscience* **5**(12): 872–875.

Inoue, M. (1985). Model decomposition of the low-frequency currents and baroclinic instability at Drake Passage, *Journal of Physical Oceanography* **15**: 1157–1181.

Ishman, S. E. and Sperling, M. R. (2002). Benthic foraminiferal record of Holocene deep-water evolution in the Palmer Deep , western Antarctic Peninsula, *Geology* **30**: 435–438.

Jacobs, S. S. and Comiso, J. C. (1993). A recent sea-ice retreat west of the Antarctic Peninsula, *Geophysical Research Letters* **20**(12): 1171–1174.

Jacobs, S. S. and Comiso, J. C. (1997). Climate variability in the Amundsen and Bellingshausen seas, *Journal of Climate* **10**: 697–709.

Jenkins, A. (1999). The impact of melting ice on ocean waters, *Journal of Physical Oceanography* **29**(3): 2370–2381.

Jenkins, A., Hellmer, H. H. and Holland, D. M. (2001). The role of meltwater advection in the formulation of conservative boundary conditions at an ice-ocean interface, *Journal of Physical Oceanography* **31**: 285–296.

Jenkins, A. and Jacobs, S. (2008). Circulation and melting beneath George VI Ice Shelf, Antarctica, *Journal of Geophysical Research* **113**(C4): C04013.

Jenkins, A., Nicholls, K. W. and Corr, H. (2010). Observation and parameterization of ablation at the base of Ronne Ice Shelf, Antarctica, *Journal of Physical Oceanography* **40**: 2298–2312.

Khim, B.-K., Yoon, H. I., Kim, Y. and Shin, I. C. (2001). Late Holocene stable isotope chronology and meltwater discharge event in Maxwell and Admiralty bays, King George Island, Antarctica, *Antarctic Science* **13**(02): 167–173.

Kimmritz, M., Danilov, S. and Losch, M. (2015). On the convergence of the modified elastic-viscous-plastic method for solving the sea ice momentum equation, *Journal of Computational Physics* **296**: 90–100.

Kimura, S., Jenkins, A., Regan, H., Holland, P., Assmann, K., Whitt, D., van Wessem, M., van de Berg, W., Reijmer, C. and Dutrieux, P. (Submitted). Oceanographic controls on the variability of ice-shelf basal melting and circulation of glacial meltwater in the Amundsen Sea Embayment, Antarctica.

King, J. C. (1994). Recent climate variability in the vicinity of the Antarctic Peninsula, *International Journal of Climatology* **14**: 357–369.

Kjellsson, J., Holland, P. R., Marshall, G. J., Mathiot, P., Aksenov, Y., Coward, A. C., Bacon, S., Megann, A. P. and Ridley, J. (2015). Model sensitivity of the Weddell and Ross seas, Antarctica, to vertical mixing and freshwater forcing, *Ocean Modelling* **94**: 141–152.

Klinck, J. M. and Dinniman, M. S. (2010). Exchange across the shelf break at high southern latitudes, *Ocean Science* **6**(2): 513–524.

Klinck, J. M., Hofmann, E. E., Beardsley, R. C., Salihoglu, B. and Howard, S. (2004). Water-mass properties and circulation on the west Antarctic Peninsula continental shelf in austral fall and winter 2001, *Deep Sea Research Part II: Topical Studies in Oceanography* **51**(17-19): 1925–1946.

Large, W. G., Danabasoglu, G., Doney, S. C. and McWilliams, J. C. (1997). Sensitivity to surface forcing and boundary layer mixing in a global ocean model: annual-mean climatology, *Journal of Physical Oceanography* **27**: 2418–2447.

Large, W. G. and Pond, S. (1982). Sensible and latent heat flux measurements over the ocean, *Journal of Physical Oceanography* **12**: 464–482.

Large, W., McWilliams, J. and Doney, S. (1994). Oceanic vertical mixing: A review and a model with nonlocal bounday layer parameterization, *Review of Geophysics* **32**: 363–403.

Leith, C. E. (1996). Stochastic models of chaotic systems, *Physica D* **98**: 481–491.

Lennon, P. W., Loynes, J., Paren, J. G. and Potter, J. R. (1982). Oceanographic observations from George VI Ice Shelf, Antarctic Peninsula, *Annals of Glaciology* **3**: 178–183.

Leventer, A., Domack, E. W., Ishman, S. E., Brachfeld, S., Mcclennen, C. E. and Manley, P. (1996). Productivity cycles of 200-300 years in the Antarctic Peninsula region: understanding linkages among the sun, atmosphere, oceans, sea ice, and biota, *Geological Society of America Bulletin* **108**(12): 1626–1644.

Lewis, M. J., Tison, J. L., Weissling, B., Delille, B., Ackley, S. F., Brabant, F. and Xie, H. (2011). Sea ice and snow cover characteristics during the winter-spring transition in the Bellingshausen Sea: An overview of SIMBA 2007, *Deep-Sea Research Part II: Topical Studies in Oceanography* **58**(9-10): 1019–1038.

Liu, J. (2003). Sensitivity of sea ice to physical parameterizations in the GISS global climate model, *Journal of Geophysical Research* **108**(C2): 3053.

Losch, M. (2008). Modeling ice shelf cavities in a z coordinate ocean general circulation model, *Journal of Geophysical Research* **113**(C8): C08043.

Losch, M., Menemenlis, D., Campin, J.-M., Heimbach, P. and Hill, C. (2010). On the formulation of sea-ice models. Part I: effects of different solver implementations and parameterizations, *Ocean Modelling* **33**(1-2): 129–144.

Lumpkin, R. and Speer, K. (2007). Global Ocean Meridional Overturning, *Journal of Physical Oceanography* **37**(10): 2550–2562.

Maddison, E. J., Pike, J., Leventer, A. and Domack, E. W. (2005). Deglacial seasonal and sub-seasonal diatom record from Palmer Deep, Antarctica, *Journal of Quaternary Science* **20**(5): 435–446.

Manabe, S., Spelman, M. J. and Stouffer, R. J. (1992). Transient responses of a coupled ocean-atmosphere model to gradual changes of atmospheric CO_2, part II, Seasonal response, *Journal of Climate* **5**: 105–126.

Marsh, R., Ivchenko, V. O., Skliris, N., Alderson, S., Bigg, G. R., Madec, G., Blaker, A. T., Aksenov, Y., Sinha, B., Coward, A. C., Sommer, J. L., Merino, N. and Zalesny, V. B. (2015). NEMOICB (v1.0): interactive icebergs in the NEMO ocean model globally configured at eddy-permitting resolution, *Geosci. Model Dev* **8**: 1547–1562.

Marshall, J., Adcroft, A., Hill, C., Perelman, L. and Heisey, C. (1997a). A finite-volume, incompressible Navier Stokes model for studies of the ocean on parallel computers, *Journal of Geophysical Research* **102**(C3): 5753–5766.

Marshall, J., Hill, C., Perelman, L. and Adcroft, A. (1997b). Hydrostatic, quasi-hydrostatic, and nonhydrostatic ocean modeling, *Journal of Geophysical Research: Oceans* **102**(C3): 5733–5752.

Marsland, S. and Wolff, J. O. (2001). On the sensitivity of Southern Ocean sea ice to the surface freshwater flux: a model study, *Journal of Geophysical Research* **106**(C2): 2723–2741.

Martinson, D. G., Stammerjohn, S. E., Iannuzzi, R. A., Smith, R. C. and Vernet, M. (2008). Western Antarctic Peninsula physical oceanography and spatio-temporal variability, *Deep Sea Research Part II: Topical Studies in Oceanography* **55**(18-19): 1964–1987.

Massom, R. A., Hill, J., Lytle, V. I., Worby, A. and Allison, I. (2001). Snow on Antarctic sea ice, *Reviews of Geophysics* **39**(3): 413–445.

Mastumoto, K., Lynch-Stieglitz, J. and Anderson, R. F. (2001). Similar glacial and Holocene Southern Ocean hydrography, *Paleoceanography* **16**(5): 445–454.

Mathieu, R., Pollard, D., Cole, J. E., White, J. W. C., Webb, R. S. and Thompson, S. L. (2002). Simulation of stable water isotope variations by the GENESIS GCM for modern conditions, *Journal of Geophysical Research* **107**(D4): 4037.

McDougall, T. J. and Barker, P. M. (2011). Getting started with TEOS-10 and the Gibbs Seawater (GSW) Oceanographic Toolbox. 28pp., SCOR/IAPSO WG127, ISBN 978-0-646-55621-5.

McDougall, T. J., Jackett, D. R., Wright, D. G. and Feistel, R. (2003). Accurate and computationally efficient algoriths for potential temperature and density of seawater, *Journal of Atmospheric and Oceanic Technology* **20**: 730–741.

Meredith, M. P. and Brandon, M. A. (2017). Oceanography and sea ice in the Southern Ocean, *in* D. Thomas (ed.), *Sea ice*, 3rd edn, Wiley, pp. 216–238.

Meredith, M. P., Brandon, M. A., Wallace, M. I., Clarke, A., Leng, M. J., Renfrew, I. a., van Lipzig, N. P. and King, J. C. (2008). Variability in the freshwater balance of northern Marguerite Bay, Antarctic Peninsula: Results from δ^{18}O, *Deep Sea Research Part II: Topical Studies in Oceanography* **55**(3-4): 309–322.

Meredith, M. P. and Hogg, A. M. (2006). Circumpolar response of Southern Ocean eddy activity to a change in the Southern Annular Mode, *Geophysical Research Letters* **33**(16): 2–5.

Meredith, M. P. and King, J. C. (2005). Rapid climate change in the ocean west of the Antarctic Peninsula during the second half of the 20th century, *Geophysical Research Letters* **32**(19): L19604.

Meredith, M. P., Renfrew, I. A., Clarke, A., King, J. C. and Brandon, M. A. (2004). Impact of the 1997/98 ENSO on upper ocean characteristics in Marguerite Bay, western Antarctic Peninsula, *Journal of Geophysical Research* **109**(C9): C09013.

Meredith, M. P., Stammerjohn, S. E., Venables, H. J., Ducklow, H. W., Martinson, D. G., Iannuzzi, R. A., Leng, M. J., van Wessem, J. M., Reijmer, C. H. and Barrand, N. E. (2016). Changing distributions of sea ice melt and meteoric water west of the Antarctic Peninsula, *Deep-Sea Research Part II: Topical Studies in Oceanography* .

Meredith, M. P., Venables, H. J., Clarke, A., Ducklow, H. W., Erickson, M., Leng, M. J., Lenaerts, J. T. M. and van den Broeke, M. R. (2013). The freshwater system west of the Antarctic Peninsula: Spatial and temporal changes, *Journal of Climate* **26**(5): 1669–1684.

Meredith, M. P., Wallace, M. I., Stammerjohn, S. E., Renfrew, I. A., Clarke, A., Venables, H. J., Shoosmith, D. R., Souster, T. and Leng, M. J. (2010). Changes in the freshwater composition of the upper ocean west of the Antarctic Peninsula during the first decade of the 21st century, *Progress in Oceanography* **87**(1-4): 127–143.

Merino, I., Le Sommer, J., Durand, G., Jourdain, N. C., Madec, G., Mathiot, P. and Tournadre, J. (2016). Antarctic icebergs melt over the Southern Ocean: climatology and impact on sea ice, *Ocean Modelling* **104**: 99–110.

Meyer, A., Phillips, H. E., Sloyan, B. M. and Polzin, K. L. (2014). Mixing (MX) Oceanographic Toolbox for EM-APEX* float data applying shear-strain finescale parameterization, *Technical report*. 69pp., Institude for Marine and Antarctic Studies, University of Tasmania, Hobart.

Moffat, C., Beardsley, R. C., Owens, B. and van Lipzig, N. (2008). A first description of the Antarctic Peninsula Coastal Current, *Deep Sea Research Part II: Topical Studies in Oceanography* **55**(3-4): 277–293.

Nakayama, Y., Timmermann, R., Rodehacke, C. B., Schröder, M. and Hellmer, H. H. (2014a). Modeling the spreading of glacial meltwater from the Amundsen and Bellingshausen seas, *Geophysical Research Letters* **41**: 7942–7949.

Nakayama, Y., Timmermann, R., Schröder, M. and Hellmer, H. (2014b). On the difficulty of modeling Circumpolar Deep Water intrusions onto the Amundsen Sea continental shelf, *Ocean Modelling* **84**: 26–34.

Noon, P. E., Leng, M. J. and Jones, V. J. (2003). Oxygen-isotope (δ^{18}O) evidence of Holocene hydrological changes at Signy Island, maritime Antarctica, *The Holocene* **13**(2): 251–263.

Nowlin, W. D. and Klinck, J. M. (1986). The physics of the Antarctic Circumpolar Current, *Reviews of Geophysics* **24**(3): 469.

Nurser, A. J. G. and Bacon, S. (2014). The Rossby radius in the Arctic Ocean, *Ocean Sciences* **10**: 967–975.

Orsi, H., Whitworth, T. and Jr, W. D. N. (1995). On the meridional extent and fronts of the Antarctic Circumpolar Current, *Deep-Sea Research I* **42**(5): 641–673.

Padman, L., Costa, D. P., Dinniman, M. S., Fricker, H. A., Goebel, M. E., Huckstadt, L. A., Humbert, A., Joughin, I., Lenaerts, J. T. M., Ligtenberg, S. R. M., Scambos, T. and van den Broeke, M. R. (2012). Oceanic controls on the mass balance of Wilkins Ice Shelf, Antarctica, *Journal of Geophysical Research* **117**(C1). C01010.

Paolo, F. S., Fricker, H. A. and Padman, L. (2015). Volume loss from Antarctic ice shelves is accelerating, *Science* **348**(6232): 327–331.

Parkinson, C. L. (2004). Southern Ocean sea ice and its wider linkages: insights revealed from models and observations, *Antarctic Science* **16**(4): 387–400.

Parkinson, C. L. and Cavalieri, D. J. (2012). Antarctic sea ice variability and trends, 1979-2010, *The Cryosphere* **6**(4): 871–880.

Pawlowicz, R. (1997). M_Map: a mapping package for Matlab. Retrieved: 3rd October 2013.
URL: *http://www.ldeo.columbia.edu/˜pco2/data_process/processing/m_map/private/mapug.html*

Petty, A. A., Feltham, D. L. and Holland, P. R. (2013). Impact of atmospheric forcing on Antarctic continental shelf water masses, *Journal of Physical Oceanography* **43**(5): 920–940.

Pike, J., Allen, C. S., Leventer, A., Stickley, C. E. and Pudsey, C. J. (2008). Comparison of contemporary and fossil diatom assemblages from the western Antarctic Peninsula shelf, *Marine Micropaleontology* **67**(3-4): 274–287.

Pike, J., Swann, G. E. A., Leng, M. J. and Snelling, A. M. (2013). Glacial discharge along the west Antarctic Peninsula during the Holocene, *Nature Geoscience* **6**(3): 199–202.

Potter, J. R. and Paren, J. G. (1985). *Interaction between ice shelf and ocean in George VI Sound, Antarctica*, Antarctic Research Series, American Geophysical Union, pp. 35–58.

Pritchard, H. D., Ligtenberg, S. R. M., Fricker, H. A., Vaughan, D. G., van den Broeke, M. R. and Padman, L. (2012). Antarctic ice-sheet loss driven by basal melting of ice shelves., *Nature* **484**(7395): 502–5.

Pritchard, H. D. and Vaughan, D. G. (2007). Widespread acceleration of tidewater glaciers on the Antarctic Peninsula, *Journal of Geophysical Research* **112**(F3): F03S29.

Redi, M. H. (1982). Oceanic isopycnal mixing by coordinate rotation, *Journal of Physical Oceanography* **12**: 1154–1158.

Regan, H., Holland, P., Meredith, M. and Pike, J. (Submitted). Sources, variability and fate of freshwater in the Bellingshausen Sea, Antarctica.

Rignot, E., Jacobs, S., Mouginot, J. and Scheuchl, B. (2013). Ice-shelf melting around Antarctica., *Science* **341**(6143): 266–270.

Rintoul, S. R., Hughes, C. W. and Olbers, D. (2001). The Antarctic Circumpolar Current system, *in* G. Siedler, J. Church and J. Gould (eds), *Ocean Circulation and Climate*, 103 edn, Academic Press, London, chapter 4.6, pp. 271–302.

Rohling, E. (2007). Paleoceanography, physical and chemical proxies - oxygen isotopic composition of seawater, *in* S. A. Elias (ed.), *Encyclopedia of Quaternary Science*, Elsevier, Oxford, pp. 1748–1756.

Rooth, C. (1982). Hydrology and ocean circulation, *Progress in Oceanography* **11**: 131–149.

Roquet, F., Madec, G., Brodeau, L. and Nycander, J. (2015). Defining a simplified yet "realistic" equation of state for seawater, *Journal of Physical Oceanography* **45**: 2564–2579.

Rye, C. D., Naveira Garabato, A. C., Holland, P. R., Meredith, M. P., Nurser, A. J. G., Hughes, C. W., Coward, A. C. and Webb, D. J. (2014). Rapid sea-level rise along the Antarctic margins in response to increased glacial discharge, *Nature Geoscience* **7**: 732–735.

Saha, S., Moorthi, S., Pan, H.-L., Wu, X., Wang, J., Nadiga, S., Tripp, P., Kistler, R., Woollen, J., Behringer, D., Liu, H., Stokes, D., Grumbine, R., Gayno, G., Wang, J., Hou, Y.-T., Chuang, H.-Y., Juang, H.-M. H., Sela, J., Iredell, M., Treadon, R., Kleist, D., Delst, P. V., Keyser, D., Derber, J., Ek, M., Meng, J., Wei, H., Yang, R., Lord, S., van den Dool, H., Kumar, A., Wang, W., Long, C., Chelliah, M., Xue, Y., Huang, B., Schemm, J.-K., Ebisuzaki, W., Lin, R., Xie, P., Chen, M., Zhou, S., Higgins, W., Zou, C.-Z., Liu, Q., Chen, Y., Han, Y., Cucurull, L., Reynolds, R. W., Rutledge, G. and Goldberg, M. (2010). The ncep climate forecast system reanalysis, *Bulletin of the American Meteorological Society* **91**: 1015–1057.

Savidge, D. K. and Amft, J. A. (2009). Circulation on the West Antarctic Peninsula derived from 6 years of shipboard ADCP transects, *Deep Sea Research Part I: Oceanographic Research Papers* **56**(10): 1633–1655.

Schlosser, P., Bayer, R., Foldvik, A., Gammelsrød, T., Rohardt, G. and Münnich, K. O. (1990). Oxygen 18 and helium as tracers of ice shelf water and water/ice interaction in the Weddell Sea, *Journal of Geophysical Research* **95**(C3): 3253–3263.

Schmidt, G. A., LeGrande, A. N. and Hoffmann, G. (2007). Water isotope expressions of intrinsic and forced variability in a coupled ocean-atmosphere model, *Journal of Geophysical Research* **112**(D10): D10103.

Schmidt, M., Botz, R., Stoffers, P., Anders, T. and Bohrmann, G. (1997). Oxygen isotopes in marine diatoms: A comparative study of analytical techniques and new results on the isotope composition of recent marine diatoms, *Geochemica et Cosmochimica Acta* **61**(11): 2275–2280.

Semtner, A. J. J. (1976). A model for the thermodynamic growth of sea ice in numerical investigations of climate, *Journal of Physical Oceanography* **6**(5): 379–389.

Shepherd, A., Ivins, E. R., A, G., Barletta, V. R., Bentley, M. J., Bettadpur, S., Briggs, K. H., Bromwich, D. H., Forsberg, R., Galin, N., Horwath, M., Jacobs, S., Joughin, I., King, M. A., Lenaerts, J. T. M., Li, J., Ligtenberg, S. R. M., Luckman, A., Luthcke, S. B., McMillan, M., Meister, R., Milne, G., Mouginot, J., Muir, A., Nicolas, J. P., Paden, J., Payne, A. J., Pritchard, H., Rignot, E., Rott, H., Sørensen, L. S., Scambos, T. A., Scheuchl, B., Schrama, E. J. O., Smith, B., Sundal, A. V., van Angelen, J. H., van de Berg, W. J., van den Broeke, M. R., Vaughan, D. G., Velicogna, I., Wahr, J., Whitehouse, P. L., Wingham, D. J., Yi, D., Young, D. and Zwally, H. J. (2012). A reconciled estimate of ice-sheet mass balance, *Science* **338**(6111): 1183–1189.

Silva, T. a. M., Bigg, G. R. and Nicholls, K. W. (2006). Contribution of giant icebergs to the Southern Ocean freshwater flux, *Journal of Geophysical Research* **111**(C3): C03004.

Smith, D. A., Hofmann, E. E., Klinck, J. M. and Lascara, C. M. (1999). Hydrography and circulation of the West Antarctic Peninsula continental shelf, *Deep Sea Research Part I: Oceanographic Research Papers* **46**(6): 925–949.

Smith, D. A. and Klinck, J. M. (2002). Water properties on the west Antarctic Peninsula continental shelf: a model study of effects of surface fluxes and sea ice, *Deep Sea Research Part II: Topical Studies in Oceanography* **49**(21): 4863–4886.

Sokolov, S. and Rintoul, S. R. (2009). Circumpolar structure and distribution of the Antarctic Circumpolar Current fronts: 1. Mean circumpolar paths, *Journal of Geophysical Research: Oceans* **114**(11): 1–19.

St-Laurent, P., Klinck, J. M. and Dinniman, M. S. (2013). On the role of coastal troughs in the circulation of warm Circumpolar Deep Water on Antarctic shelves, *Journal of Physical Oceanography* **43**(1): 51–64.

Stammerjohn, S., Massom, R., Rind, D. and Martinson, D. (2012). Regions of rapid sea ice change: an inter-hemispheric seasonal comparison, *Geophysical Research Letters* **39**: L06501.

Swann, G. E., Pike, J., Snelling, A. M., Leng, M. J. and Williams, M. C. (2013). Seasonally resolved diatom δ^{18}O records from the West Antarctic Peninsula over the last deglaciation, *Earth and Planetary Science Letters* **364**: 12–23.

Talbot, M. (1988). Oceanic environment of George VI Ice Shelf, Antarctic Peninsula, *Annals of Glaciology* **11**: 161–164.

Talley, L. D., Pickard, G. L., Emery, W. J. and Swift, J. H. (2011a). Chapter 13 - Southern Ocean, *in* L. D. Talley, G. L. Pickard, W. J. Emery and J. H. Swift (eds), *Descriptive Physical Oceanography*, 6th edn, Academic Press, Boston, pp. 437 – 471.

Talley, L. D., Pickard, G. L., Emery, W. J. and Swift, J. H. (2011b). Chapter 3 - Physical Properties of Seawater, *in* L. D. Talley, G. L. Pickard, W. J. Emery and J. H. Swift (eds), *Descriptive Physical Oceanography*, 6th edn, Academic Press, Boston, pp. 29 – 65.

Thoma, M., Jenkins, A., Holland, D. and Jacobs, S. (2008). Modelling Circumpolar Deep Water intrusions on the Amundsen Sea continental shelf, Antarctica, *Geophysical Research Letters* **35**(18): L18602.

Thomas, E. R., Marshall, G. J. and McConnell, J. R. (2008). A doubling in snow accumulation in the western Antarctic Peninsula since 1850, *Geophysical Research Letters* **35**(1): L01706.

Timmermann, R., Le Brocq, A. M., Deen, T. J., Domack, E. W., Dutrieux, P., Galton-Fenzi, B., Hellmer, H. H., Humbert, A., Jansen, D., Jenkins, A., Lambrecht, A., Makinson, K., Niederjasper, F., Nitsche, F.-O., Nøst, O. A., Smedsrud, L. H. and Smith, W. (2010). Antarctic ice sheet topography, cavity geometry, and global bathymetry (RTopo 1.0.5-beta). Supplement to: Timmermann, R et al. (2010): A consistent dataset of Antarctic Ice Sheet topography, cavity geometry, and global bathymetry. Earth System Science Data, 2(2), 261-273, doi:10.5194/essd-2-261-2010.

Tiwari, M., Nagoji, S. S., Kartik, T., Drishya, G., Parvathy, R. and Rajan, S. (2013). Oxygen isotope—salinity relationships of discrete oceanic regions from India to Antarctica vis-à-vis surface hydrological processes, *Journal of Marine Systems* **113-114**: 88–93.

Tournadre, J., Bouhier, N., Girard-Ardhuin, F. and Rémy, F. (2015). Large icebergs characteristics from altimeter waveforms analysis, *Journal of Geophysical Research: Oceans* **120**: 1954–1974.

Tournadre, J., Bouhier, N., Girard-Ardhuin, F. and Remy, F. (2016). Antarctic icebergs distributions 1992-2014, *Journal of Geophysical Research: Oceans* **121**: 327–349.

Turner, J., Bracegirdle, T. J., Phillips, T., Marshall, G. J. and Hosking, J. S. (2013b). An initial assessment of Antarctic sea ice extent in the CMIP5 models, *Journal of Climate* **26**(5): 1473–1484.

Turner, J., Colwell, S. R., Marshall, G. J., Lachlan-Cope, T. A., Carleton, A. M., Jones, P. D., Lagun, V., Reid, P. A. and Iagovkina, S. (2005a). Antarctic climate change during the last 50 years, *International Journal of Climatology* **25**(3): 279–294.

Turner, J., Lachlan-Cope, T., Colwell, S. and Marshall, G. J. (2005b). A positive trend in western Antarctic Peninsula precipitation over the last 50 years reflecting regional and Antarctic-wide atmospheric changes, *Annals of Glaciology* **41**: 85–91.

Turner, J., Lu, H., White, I., King, J. C., Phillips, T., Hosking, J. S., Bracegirdle, T. J., Marshall, G. J., Mulvaney, R. and Deb, P. (2016). Absence of 21st century warming on Antarctic Peninsula consistent with natural variability, *Nature* **535**(7612): 411–415.

Turner, J., Maksym, T., Phillips, T., Marshall, G. J. and Meredith, M. P. (2013a). The impact of changes in sea ice advance on the large winter warming on the western Antarctic Peninsula, *International Journal of Climatology* **33**(4): 852–861.

van Meijgaard, E., van Ulft, L. H., van de Berg, W. J., Bosveld, F. C., van den Hurk, B., Lenderink, G. and Siebesma, A. P. (2008). The KNMI regional atmospheric climate model RACMO version 2.1, *Technical report*, KNMI, De Bilt.

van Wessem, J. M., Ligtenberg, S. R. M., Reijmer, C. H., van de Berg, W. J., van den Broeke, M. R., Barrand, N. E., Thomas, E. R., Turner, J., Wuite, J., Scambos, T. and van Meijgaard, E. (2016a). The modelled surface mass balance of the Antarctic Peninsula at 5.5 km horizontal resolution, *The Cryosphere* **10**: 271–285.

van Wessem, J., Meredith, M., Reijmer, C., van den Broeke, M. and Cook, A. (2016b). Characteristics of the modelled meteoric freshwater budget of the western Antarctic Peninsula, *Deep Sea Research Part II: Topical Studies in Oceanography* .

Vaughan, D. G. (2006). Recent trends in melting conditions on the Antarctic Peninsula and their implications for ice-sheet mass balance and sea level, *Arctic, Antarctic, and Alpine Research* **38**(1): 147–152.

Venables, H. J., Clarke, A. and Meredith, M. P. (2013). Wintertime controls on summertime stratification and productivity at the western Antarctic Peninsula, *Liminology and Oceanography* **58**(3): 1035–1047.

Watkins, A. B., Simmonds, I. and Morgan, V. (1998). Relationships between Antarctic sea-ice concentration, wind stress and temperature temporal variability, and their changes with distance from the coast, *Annals of Glaciology* **27**(1): 409–412.

Woodruff, A. H. W. and Doake, C. S. M. (1979). Depolarization of radio waves can distinguish between floating and grounded ice sheets, *Journal of Glaciology* **23**: 223–232.

Worby, A. P., Geiger, C. A., Paget, M. J., Van Woert, M. L., Ackley, S. F. and DeLiberty, T. L. (2008). Thickness distribution of Antarctic sea ice, *Journal of Geophysical Research: Oceans* **113**(5): 1–14.

Wouters, B., Martin-Espanol, A., Helm, V., Flament, T., van Wessem, J. M., Ligtenberg, S. R. M., van den Broeke, M. R. and Bamber, J. L. (2015). Dynamic thinning of glaciers on the Southern Antarctic Peninsula, *Science* **348**(6237): 899–903.

Wyrtki, K. (1961). The thermohaline circulation in relation to the general circulation in the oceans, *Deep-Sea Research* **8**: 39–64.

Xie, H., Ackley, S., Yi, D., Zwally, H., Wagner, P., Weissling, B., Lewis, M. and Ye, K. (2011). Sea-ice thickness distribution of the Bellingshausen Sea from surface measurements and ICESat altimetry, *Deep Sea Research Part II: Topical Studies in Oceanography* **58**(9-10): 1039–1051.

Xie, H., Tekeli, A. E., Ackley, S. F., Yi, D. and Zwally, H. J. (2013). Sea ice thickness estimations from ICESat Altimetry over the Bellingshausen and Amundsen Seas, 2003-2009, *Journal of Geophysical Research: Oceans* **118**(5): 2438–2453.

Yin, J., Overpeck, J. T., Griffies, S. M., Hu, A., Russell, J. L. and Stouffer, R. J. (2011). Different magnitudes of projected subsurface ocean warming around Greenland and Antarctica, *Nature Geoscience* **4**(8): 524–528.

Zhang, X., Thompson, A. F., Flexas, M. M., Roquet, F. and Bornemann, H. (2016). Circulation and meltwater distribution in the Bellingshausen Sea: from shelf break to coast, *Geophysical Research Letters* **43**(12): 6402–6409.

Zwally, H. J., Comiso, J. C., Parkinson, C. L., Cavalieri, D. J. and Gloerson, P. (2002). Variability of Antarctic sea ice 1979-1998, *Journal of Geophysical Research* **107**(C5).